PREPARATION AND CHARACTERIZATION OF SOLUTION PROCESSED KESTERITE Cu_2ZnSnS_4 THIN FILMS FOR PHOTOVOLTAIC APPLICATIONS

Thesis submitted to
University of Calicut, Kerala
in partial fulfillment of the requirements for the award of the degree of

DOCTOR OF PHILOSOPHY IN PHYSICS
under the Faculty of Science

By

PRABEESH. P.

Under the supervision of

Dr. S. Sankara Narayanan Potty

CENTRE FOR MATERIALS FOR ELECTRONICS TECHNOLOGY [C-MET]
(Scientific Society, Ministry of Electronics and Information Technology (MeitY)
Govt. of India, M.G. Kavu, Athani P.O, Thrissur 680581, Kerala, India
www.cmet.gov.in
October 2018

सेन्टर फॉर मेटिरियल्स फॉर इलेक्ट्रॉनिक्स टेक्नोलॉजी (सी-मेट)
(वैज्ञानिक संस्था, इलेक्ट्रॉनिक्स और सूचना प्रौद्योगिकी मंत्रालय, भारत सरकार)
षोरनूर रोड, मुलॅगुन्नतुकावु पोस्ट, अत्तानि, त्रिशूर - 680 581, केरला, भारत
CENTRE FOR MATERIALS FOR ELECTRONICS TECHNOLOGY
(Scientific Society, Ministry of Electronics and Information Technology, Government of India)
Shoranur Road, P.O. Mulangunnathukavu, Athani, Thrissur - 680 581, Kerala, India
Tel : EPABX : 91-487-2201156-59 (4 LINES). Fax : 91-487-2201347
E-mail : cmett@cmet.gov.in URL : www.cmet.gov.in

Date.....

CERTIFICATE

This is to certify that the thesis titled "**PREPARATION AND CHARACTERIZATION OF SOLUTION PROCESSED KESTERITE Cu_2ZnSnS_4 THIN FILMS FOR PHOTOVOLTAIC APPLICATIONS**" submitted to University of Calicut in partial fulfilment of the requirements for the award of the degree of **Doctor of Philosophy in Physics** under the Faculty of Science, University of Calicut, is a record of the authentic work carried out by **Mr.Prabeesh. P.**, at Centre for Materials for Electronics Technology (C-MET), Thrissur, under my guidance. The work presented in this thesis has not been submitted for any other degree or diploma of this or any other University and has been found to have no plagiarism using the software approved by the UGC/University.

Thrissur

Dr. S. Sankara Narayanan Potty
Supervising Guide

सेन्टर फॉर मेटिरियल्स फॉर इलेक्ट्रॉनिक्स टेक्नोलॉजी (सी-मेट)
(वैज्ञानिक संस्था, इलेक्ट्रॉनिक्स और सूचना प्रौद्योगिकी मंत्रालय, भारत सरकार)
षोरनूर रोड, मुलॅगुन्नतुकावु पोस्ट, अत्तानि, त्रिशूर - 680 581, केरला, भारत

CENTRE FOR MATERIALS FOR ELECTRONICS TECHNOLOGY
(Scientific Society, Ministry of Electronics and Information Technology, Government of India)
Shoranur Road, P.O. Mulangunnathukavu, Athani, Thrissur - 680 581, Kerala, India
Tel : EPABX : 91-487-2201156-59 (4 LINES). Fax : 91-487-2201347
E-mail : cmett@cmet.gov.in URL : www.cmet.gov.in

Dr. S N Potty
Scientist
snpotty@cmet.gov.in

08.03.2019

The Director of Research
University of Calicut
Calicut University PO
Thenhipalam, Kerala 673635

Dear Sir,

Sub: Open Defence & Public viva-voce in r/o Prabeesh-Physics – reg.
Ref No: 199239/RESEARCH-C-ASST-1/2018/Admn dated 23.02.2019

Kindly refer to the above letter received from the Director of Research, University of Calicut. Please find enclosed two copies of the thesis entitled "Preparation and Characterization of Solution Processed Kesterite Cu_2ZnSnS_4 Thin Films for Photovoltaic Applications", along with one soft copy of the same in PDF (on CD). We hereby certify that the typographical errors pointed out by the adjudicators have been incorporated in the thesis. As intimated, the open defence and public viva-voce will be conducted on 20th March 2019 at 2.00 PM at the seminar hall of Department of Physics, University of Calicut.

Thanking you,

Yours Sincerely,

Dr. S. Sankara Narayanan Potty
(Supervising Guide)

DECLARATION

I hereby declare that the dissertation entitled "**Preparation and characterization of solution processed kesterite Cu_2ZnSnS_4 thin films for photovoltaic applications**" submitted to **University of Calicut** in partial fulfillment of the requirement for the award of the **degree of DOCTOR OF PHILOSOPHY in PHYSICS** is a record of original work done by me under the supervision and guidance of **Dr. S Sankara Narayanan Potty, Scientist, C-MET Thrissur** and it has not formed the basis for the award of any Degree/ Diploma/ Associateship/ Fellowship or any other similar title to any candidate of any university.

Thrissur **Prabeesh. P.**

ACKNOWLEDGEMENT

In pursuit of this academic endeavour I feel that I have been especially fortunate as inspiration, guidance, direction, co-operation, love and care all came in my way in abundance and it seems almost an impossible task for me to acknowledge the same in adequate terms.

On this auspicious moment I give profound thanks to all concerned who have extended their selfless guidance to assist in completing my research work. First my most sincere gratitude and deep devotion goes to my supervisor Dr. S. N. Potty, who by the most sincere care gave to me rays of hope and aspiration to accomplish this work. I thank him for giving the appearance of unswerving confidence that I knew what I was doing at every stage of this research work.

I am thankful to Dr N. Raghu, Director C-MET, Thrissur for his continues support and encouragement. I am also thankful to former directors, Dr K. R. Dayas for providing permission to carry out this work and permitting to use the research facilities in the C-MET, and Dr V. Kumar for his support and encouragement.

I am intensely indebted to Mr I. Packia Selvam for his very helpful assistance and counselling in overcoming various bottlenecks during the course of the work and for his comments during my work presentation and drafting my thesis. I deeply appreciate his incessant encouragement.

I am also grateful to Dr R. Ratheesh, Director C-MET Hyderabad for helpful discussions in Raman Spectroscopy and providing access to the X-ray diffraction facilities at C-MET Hyderabad. I am grateful to Prof. (Dr.) Mohan Rao IISc Banglore for extending the RF sputtering facilities at a crucial time and Dr.V. Raghavendra Reddy, UGC-DAE Consortium for Scientific Research, Indore for the high resolution GIXRD measurements.

Then I want to extent my thanks to Prof. (Dr.) P.P Pradyumnan, Department of Physics, University of Calicut; Prof (Dr.) P. Raveendran, Department of Chemistry, University of Calicut; Prof (Dr.) P A Abraham,

Dean, Faculty of Science, University of Calicut; Prof. (Dr.) N.V. Unnikrishnan, Dr. P.R. Biju, Dr. Cyriac Joseph and Dr. Santhosh Kumar, School of Pure and Applied Physics, Mahatma Gandhi University, Kottayam for both technical support and scientific discussion during my research work.

Various people have been invaluable for their help including research scholars at Department of Physics, University of Calicut for XRD measurement. My special thanks to Mr Shabeer for the continuous support; my colleagues at C-MET Mrs. Priyadarshini for Raman analysis, Mr. Arun & Mr. Albin Antony for SEM analysis, Mr. Manoj Nageri for UV-Vis spectroscopic analysis, and Miss Divya (IISc Banglore) for RF sputtering. Acknowledgements are also due the project students Mrs. Saritha, Mrs. Divya, Mrs. Sravani, Miss. Anagha, Mr Vysakh, Mr. Sajeesh, Mr. Vivek, Mr. Sarath, Mr. Yadukrishnan, Mrs. Arathi, Mrs. Jijisha, Miss Krishnapriya and Miss Harsha during the period. I also convey my sincere thanks to my labmate Mrs Soumya Kannoth, the lunchmates, friends especially Mr Ranjth, Mr Anil and Mr Suresh and well wishers in and out of C-MET for their continuous support, encouragement and motivation towards the journey of research carrier.

I would like to thank Department of Science and Technology (DST), Government of India for the financial support during the research period.

I have no words to explain the love, blessing, affection, inspiration, motivation and patience shown by my parents P. Narayanan (achan), Padmini V V (amma), Prasanth P Nair (ettan), Nishitha Prasanth (ettathi), Rithunandh and Rithupravana were great factors of success.

*Last but not the least, I praise and indebted to **ALMIGHTY** for being the unfailing source of support, comfort and strength throughout the completion of my research work.*

PRABEESH P.

Dedicated to
All
Who inspired me to choose
Research career

PREFACE

For the past several decades, the world is searching for cleaner and sustainable alternatives to conventional fossil fuels, such as solar, wind, ocean, hydrothermal etc. Among these, solar photovoltaic (PV) is the most effective, because solar energy is abundant and free from pollution. Thin film solar cells, frequently referred to as second generation solar cells, have an advantage over the conventionally used wafer based solar cells in terms of production cost. Three materials are currently in the market for thin film technologies; they are amorphous silicon (a-Si), cadmium telluride (CdTe) and copper indium gallium selenide (CIGS). Of these, CIGS has shown the highest efficiency of above 20% for laboratory scale cells, while CdTe has the highest market share among the thin film technologies. A drawback with CIGS and CdTe technologies is the use of scarce and expensive elements indium and tellurium. In addition to this, cadmium is toxic.

It is therefore clear that there are issues of long term sustainability in terms of cost and availability in the case of the aforementioned CdTe and CIGS technologies. It is in this context, investigations have been initiated all over the world for an alternative non-toxic absorber material. Cu_2ZnSnS_4 (CZTS) and $Cu_2ZnSnSe_4$ (CZTSe) are two promising absorber materials for thin film photovoltaic cells due to their *p*- type nature, high absorption coefficient ($>10^4 cm^{-1}$) and optimum direct band gap (~1.5eV). The occurrence of kesterite mineral was first discovered in 1958 in the Kester deposit in Russia. The mineral is usually seen in quartz-sulphide hydrothermal veins in ore deposits. The copper zinc tin

sulphide consists of earth abundant, non-toxic and inexpensive elements. Though this material possesses ideal characteristics, the cells based on CZTS reached only 9.1% efficiency so far. This material is little investigated on the basic research side. The fabrication of a quaternary material in phase pure form is a challenge. There is a small formation region for Cu_2ZnSnS_4 at 670K, where both the Cu/(Zn+Sn) and the Zn/Sn ratio may vary between 0.94 and 1.07, based on the available phase diagram. Outside this small area, Cu_2ZnSnS_4 co-exists with a number of different phases such as $Cu_2ZnSn_3S_8$, ZnS, Cu_2S, Cu_4SnS_4 and Cu_2SnS_3, etc. This suggests the importance of pursuing research into the formation aspects of this material. Ultimately, this will lead to phase pure CZTS with optimised photovoltaic properties.

P type conductivity in CZTS absorber is mainly due to its intrinsic point defects. These defects play very important role to yield efficient solar cells by influencing generation, separation and recombination of electron hole pair. Since CZTS forms in a very small window, it is very important to control the deposition conditions. The films have to be grown under Cu-poor and Zn-rich conditions, which will yield the necessary defects in the system. However, the formation of secondary phases has to be avoided during fabrication of the films.

Previously, CZTS thin film solar cells have been fabricated using vacuum based co-evaporation and multilayer evaporation processes and have achieved an efficiency of 6.7%. However, these methods are complex due to high cost, difficult process steps and low yield and poor reproducibility. For this reason, solution based CZTS fabrication routes are becoming increasingly important to reduce

manufacturing cost significantly with high-throughput fabrication for large area solar cells. To date, spin coated and electrodeposited CZTS thin film solar cells have yielded maximum efficiencies of 2.0% and 3.4%, respectively. More recently, two approaches have yielded significantly higher efficiencies. In the first approach, $Cu_2ZnSn(S_x,Se_{1-x})_4$ solar cells were fabricated by nanocrystal-ink based solution process. By optimizing Cu/(Zn+Sn) and Zn/Sn ratios, cells with 7.2% efficiency has been achieved after selenization. In the other approach, hybrid solution particle approach is used to form CZTS directly. This approach has yielded the highest efficiency of 9.7% among all CZTS fabrication process to date. However, toxicity of the solvent hydrazine used in this process for dissolving constituent materials is a major safety concern for large scale manufacturing.

The thesis entitled "Preparation and characterization of solution processed kesterite Cu_2ZnSnS_4 thin films for photovoltaic applications" is a detailed study of the fabrication of CZTS absorber films by inexpensive solution based dip, spin and spray coating techniques and investigation of their properties. Two different approaches were used to prepare precursor films by dip coating, while three routes were used in the spin and spray coatings. The as-coated films from these routes were annealed in inert or sulphur atmospheres at various temperatures and studied the effect of sulphurization on the structural, surface morphological, optical and electrical properties of CZTS thin films. After optimizing coating conditions, prototype CZTS solar cell was fabricated with non-toxic ZnS buffer layer.

The studies included in the thesis are divided into seven chapters and the contents of each chapter are summarised as follows.

Chapter 1 is a general introduction to solar cells based on silicon, thin films, organic and chemical. It also discusses a detailed introduction of kesterite material including a brief history and review of literature. CZTS thin films already deposited by various groups using different techniques were addressed in this chapter. The objectives of the work carried out are briefed at the end of the chapter 1.

Chapter 2 is describes the experimental and characterization techniques used to fabricate and characterize CZTS thin films. Techniques employed for prototype solar cell fabrication and its evaluation are also described in this section. Details of solution based routes, such as, spin, dip and spray coatings used for fabricating CZTS thin films, and x-ray diffractometer, Raman spectroscopy and rietveld refinement technique used to study the structural properties and phase purity of the films are also discussed. Elemental compositions were analysed by energy dispersive x-ray spectroscopy and optical properties by UV-visible spectroscopy. Surface morphology of the films were analysed by scanning electron microscope. Hall Effect measurement system was used for electrical properties measurement. Finally, prototype of CZTS solar cell fabricated was tested using solar simulator under standard test conditions. The techniques employed for the fabrication and testing are briefly described in this chapter.

Chapter 3 the first working chapter, describes the fabrication of Cu_2ZnSnS_4 precursor films by dip coating and the studies carried out to investigate the structural, morphological, optical and electrical

properties of the films annealed at different temperatures. Two types of stable precursor solutions, without and with sulphur, were prepared for dip coating. The precursor films coated from solutions without and with sulphur were referred to as CZT and CZTS, respectively. In the first route, the dip coated CZT precursor films were sulphurized at different temperatures to optimize the phase formation conditions. In addition to X-ray diffraction and Raman analysis, rietveld refinement technique using the GSAS software was also used to extract the structural properties. The studies confirmed the formation of phase pure kesterite for the film annealed at 550°C. The absorption co-efficient calculated from the UV-visible spectra was found to be $\sim 10^4 cm^{-1}$ in the visible region and the optical band gap estimated was 1.48 eV. SEM, FESEM, Hall measurement studies were also used to characterize the films. In the second route, CZTS precursor films dip coated from solution containing sulphur were annealed at various temperatures and studied the effect of sulphurization on the properties of CZTS thin films. A band gap of 1.43 eV and absorption coefficient of $\sim 10^5$ cm^{-1} in the visible region was obtained for the film sulphurized at 550°C. The investigations indicated optimum material properties required for thin film solar absorber materials in the dip coated film annealed in sulphur atmosphere at 550°C. EDXS results indicated Cu poor and Zn rich compositions for the Cu_2ZnSnS_4 films fabricated by sulphurizing dip coated precursor films by two different approaches.

The fabrication of phase pure CZTS thin films by spin coating and post-annealing/ sulphurization forms the theme of **Chapter 4**. As in the case of dip coating, two different precursor solutions with and without sulphur, were used for spin coating. Precursor films were

sulphurized or annealed in three different routes. In the first method, precursor films without sulphur (CZT) coated on pre-cleaned glass substrates were converted to Cu_2ZnSnS_4 by annealing in sulphur environment at various temperatures. No impurity phases were detected for the precursor film sulphurized at 500°C. Elemental composition ratios of both films were calculated and Cu/(Zn+Sn) and Zn/Sn ratio of films sulphurized at 500°C were 1.00 and 1.16 respectively. Film thickness obtained from SEM cross section was ~1.5μm. Optical absorption coefficient was ~$10^4 cm^{-1}$ in the visible region. Optical band gap estimated was ~1.47eV, which is quite close to the optimum band gap energy for thin film photovoltaic cells. Highest carrier mobility of 48.20 cm^2/Vs was observed in this route. In the second route, precursor films with sulphur (CZTS) were annealed further in sulphur atmosphere at various temperatures to compensate possible sulphur loss, which may occur during annealing process. Films sulphurized at 500°C were found to be phase pure from the XRD and Raman studies. Dense, uniform and improved crystallite structure was obtained for the film sulphurized at 500°C. The films exhibited optical bandgap of 1.45eV and absorption coefficient of >$10^5 cm^{-1}$. In the third route, Cu_2ZnSnS_4 precursor films fabricated using sulphur containing solution were annealed in inert (nitrogen) atmosphere and studied the effect of annealing temperature in the range 350-550°C. Good crystallinity, dense structure, ideal band gap (1.49eV) and good absorption coefficient (10^4 cm^{-1}) were obtained for the film annealed at 500°C for 30 minutes in nitrogen. The film possessed optimum properties required of thin film absorber. The phase pure Cu_2ZnSnS_4 films prepared by annealing sulphur containing precursor films in

nitrogen and sulphur environments (second and third routes) exhibited the required Cu poor and Zn rich compositions. Hall measurement indicated *p* type conduction for all films.

Chapter 5 describes the properties of CZTS thin films coated by spray coating. As in the previous cases, two different precursor solutions, with and without sulphur, were used for spray coating. The spray coated precursor films were converted to phase pure CZTS through three different temperature treatments. In the first approach, spray coated CZT precursor films were sulphurized at various temperatures and studied the effect of sulphurization temperature on their structural and various other optoelectronic properties. The studies indicated phase pure nature of the film sulphurized at 550°C. Sulphurization at other temperatures resulted in the formation of secondary or ternary phases, along with CZTS. Rietveld refinement technique was further used to investigate the structural properties. The film thickness was found to be ~1.9μm; good surface morphology with large grains were observed in the films sulphurized at 550°C. Band gap and absorption coefficient were 1.47eV and $8\times10^{4}cm^{-1}$ respectively. In the second approach, CZTS precursor films prepared by spray coating were sulphurized at various temperatures from 400°C to 600°C. Though XRD and Raman studies revealed phase pure kesterite phase at 500°C and 550°C, better crystallinity was observed for the film sulphurized at higher temperature. Further structural studies were carried out with rietveld refinement. SEM image exhibited dense grain structure for the film sulphurized at 550°C. The thickness of the film was found to be ~2μm from the cross-sectional image. The absorption coefficient estimated from UV-visible spectra was ~$10^{5}cm^{-1}$in the visible region

and the optical band gap calculated was 1.49eV. In the third approach, precursor films fabricated by spray coating were further annealed in inert (nitrogen) atmosphere. The study indicated dense and improved grain structure with proper phase and crystallinity for the film annealed at 500°C. The absorption co-efficient was found to be ~$10^5 cm^{-1}$ in the visible region and the optical band gap estimated was 1.51 eV. The Cu_2ZnSnS_4 absorber films fabricated in this route possesses required photovoltaic properties. Hall measurements indicated *p* type nature for all the films. The coating procedure was optimized upto a substrate size of 2 inch by 2 inch by this technique. The spray coating technology can be easily up-scaled to any size.

Chapter 6 focuses on the fabrication of prototype CZTS solar cells with device structure SLG/Mo/CZTS/ZnS/AZO/Ag, where SLG stands for soda lime glass. Non-toxic ZnS was used as buffer layer instead of the commonly used CdS. Solar cells were also fabricated with different absorber layer thicknesses (1.8µm, 2.2µm and 2.7µm). Photovoltaic properties such as open circuit voltage, close circuit current, efficiency, fill factor, series resistance and shunt resistance were measured using solar simulator under standard test condition. The prototype cell was fabricated without intrinsic ZnO layer and anti-reflection coating. Highest efficiency of 3.02% was observed for cell fabricated with lower thickness (1.8µm) CZTS film. Efficiency of the cell was found to decrease when the absorber layer thickness was increased. The study was extended further to find out the possible reason for the observed low efficiency of solar cell. In order to see whether the substrates play any significant issues on the structural properties, the films were coated on glass and Mo coated SLG substrates by spin

coating, followed by sulphurization at 500°C for 30 min. Phase purity of these films was analyzed and confirmed by glancing incidence XRD and Raman spectroscopy. In addition to these, the films were further characterized with Rietveld refinement technique using GSAS package. χ^2 for films on glass substrate is 1.294 and on Mo coated SLG is 1.256. Different structural parameters were observed for the films on these substrates. The study indicates that it is important to optimize the properties of CZTS film on Mo coated SLG substrate separately, without following the same preparation conditions used for coating film on glass substrates.

Chapter 7 concludes the major findings of the thesis work to fabricate phase pure Cu_2ZnSnS_4 thin films through solution based approaches. Also, proposed future direction of the research work to be implemented to improve the efficiency of solar cell.

List of Papers Published in International Journals

1. Cu_2ZnSnS_4 thin films by dip coating from metal-thiourea precursor solution: effect of sulphurization temperature on the formation and structural, optical and electrical properties, P. Prabeesh, K. V. Vysakh, I. P. Selvam, S. N. Potty, Journal of Electronic Materials. 47 (2018) 5396.

2. Structural properties of CZTS thin films on glass and Mo coated glass substrates: a Rietveld refinement study, P. Prabeesh, I. Packia Selvam, S. N. Potty, Applied Physics A: Material Science and Processing 124 (2018) 225.

3. Fabrication of CZTS thin films by dip coating technique for solar cell applications, P. Prabeesh, P. Saritha, I. P. Selvam, S. N. Potty, Materials Research Bulletin 86, (2017) 295.

4. Effect of annealing temperature on a single step processed Cu_2ZnSnS_4 thin film via solution method, P. Prabeesh, I. Packia Selvam, S. N. Potty, Thin Solid Films, 606 (2016) 94.

List of Conference Proceedings

1. Fabrication of kesterite absorber films by spray pyrolysis: effect of annealing temperature on the phase formation, P. Prabeesh, P. Saritha, I Packia Selvam, S. N. Potty, Advanced Materials Proceedings 2 (2017) 46.

2. Development of Cu_2ZnSnS_4 thin-film absorber on glass and Mo coated glass substrates by solution process, P. Prabeesh, I. Packia Selvam, and S. N. Potty, IEEE International Conference on Electrical, Electronics, and Optimization Techniques (ICEEOT), (2016) 4431.

List of Paper Presented in Seminar / Conferences

1. Presented a paper "Development of Non-Toxic Earth Abundant Kesterite Absorber for Thin Film Solar Cell Applications", P. Prabeesh, I. P. Selvam, S. N. Potty in the 27th Kerala Science Congress held at Alappuzha. *This paper bagged the Young Scientist Best Paper Award for the oral presentation.*

2. Presented a poster "Development of Cu_2ZnSnS_4 thin-films on glass and mo coated glass substrates by solution process" P. Prabeesh, I. P. Selvam, S. N. Potty, in the International Conference on Energy Harvesting Storage and Conversion (IC-EEE 2015), Organized by Cochin University of Science and Technology (CUSAT) during 5 - 7 Feb 2015.

3. Presented a paper "Fabrication of kesterite absorber films by spray pyrolysis: effect of annealing temperature on the phase formation", P. Prabeesh, P Saritha, I. P. Selvam, S. N. Potty in the International Conference on Material Science and Technology (ICMTech 2016), Organized by University of Delhi during 1 - 4 Mar 2016.

4. Presented a poster "Fabrication of nanostructured CZTS absorber films by dip coating: Effect of annealing temperature on phase formation", P. Prabeesh, I. P. Selvam, S. N. Potty in the international conference on sustainable energy technologies for smart and clean cities (SETS&CC) organized by IIT Thirupati during July 27-29 2016. *This paper bagged third prize for poster presentation.*

5. Presented a paper "Spray coated kesterite absorber thin film for photovoltaic application", P. Prabeesh, I. P. Selvam, S. N. Potty in the UGC Sponsored National Seminar on Recent trends in nano and other materials for energy efficient devices by St. Aloysius college Edathua During 20-22 July 2017. *This paper bagged first prize for the oral presentation.*

6. Presented a paper "Effect of sulphurization temperature on CZTS phase formation and fabrication of thin film CZTS solar cell with Cd free buffer layer", P. Prabeesh, I. P. Selvam, S. N. Potty in the National Seminar on Recent thin film technology and applications by School of Pure and Applied Physics, M.G

University Kottayam During 15-17 February 2018. *This paper bagged first prize for the oral presentation.*

7. Presented a poster "Effect of drying temperature on structural optical and electrical properties of CZTS thin films fabricated by spin coating " P. Prabeesh, I. P. Selvam, S. N. Potty, in the International Conference on Advanced semiconductor materials and devices (ICASMD-2018), Organized by Centre for Materials for Electronics Technology (C-MET) during 8-10 Mar 2018.

CONTENTS

LIST OF FIGURE

LIST OF TABLES

Chapter 1
Introduction and Motivation

1.1 Energy Resources

Energy is necessary to sustain everything in the universe. Energy resources have been divided into two: renewable and non-renewable. Entire world depends mainly on non-renewable energy resources. A non-renewable resource has economic value that cannot be readily replaced by natural means on a level equal to its consumption. Most fossil fuels, such as oil, natural gas and coal are considered non-renewable and their use is not sustainable since their formation takes billions of years. Fossil fuels being used today were formed hundreds of millions of years ago during the carboniferous period [1,2]. It is hard to meet energy needs of future with the available non-renewable energy sources.

Non-renewable sources also have a large negative effect on the environment when mined, extracted and consumed. Coal processing plants leach toxic materials into groundwater, while gasoline burnt in combustion engines emit carbon dioxide and other pollutants contributing to global climate change. Natural gas is mainly methane, as a greenhouse gas, it is twenty times more effective in trapping heat in the atmosphere than carbon dioxide. Hence we need to move towards renewable energy resources and this indicates the importance of effective energy conversion control, including power generation

from renewable and environmentally clean energy sources, in view of rising energy demand [3,4].

1.2 Energy Crisis

Energy crisis is the concern that the world's demands on the limited natural energy recourses that are used to power industrial society are diminishing as the demand increases [5]. The world uses energy at the rate of ~4.7×10^{20} J/year (2012 report), which is equivalent to 15 terawatts (TW) [6]. World population is increasing exponentially and the energy demand is also increasing. The forecast is that by the end of 2025 energy demand will become ~30TW [7-10]. The energy demand is at present satisfied by fossil fuels, mainly coal, oil and natural gases. As pointed out, natural non-renewable resources are limited in supply. Renewable energy sources such as solar, wind, hydropower, biomass etc., are constantly replenished and will never run out. In order to address the energy crisis problem, it is necessary to find and exploit clean and environment friendly renewable energy sources. Among the renewable energy sources, solar energy is one of the most abundant and clean source of energy. Energy from the sun captured by the earth is about 1.8×10^{11} MW, which is larger than the present energy consumption for a year [11]. The main advantage of solar power as energy source is that it can be easily deployed by both home and business users as it does not require any huge machinery or other set up like in the cases of wind or geothermal power. Solar energy benefits not only individual owners, but environment as well.

1.3 Solar photovoltaic technologies

Solar energy is the powerful renewable source and the energy falls from the sun on the earth in day is enough to use everyone in the world in one year [4,12]. It can be used directly or indirectly for energy generation. Photovoltaic is the direct conversion of photons in to useful forms of energy (mainly in the form of electricity), using semiconductor materials that exhibit photovoltaic effect [4]. The photovoltaic effect was first introduced by A. E Bacquerel in 1839 [13,14]. After a long research in this field, researchers could convert photon into electron (light into electricity). Mainly, solar cell is a *p-n* junction under illumination. The operation of a photovoltaic cell or solar cell requires three basic attributes,

- *Excitation of charge carrier*

When solar cell is illuminated under sunlight, free electrons or holes in the ground state (valance band) absorbs light energy and goes to its higher energy levels (conduction band) and thus free them. Light absorption on both regions will cause production of electron-hole pair.

- *Separation of charge carrier*

Light absorption increases electron density in *p* region and hole density in *n* region [4]. Excited charge carriers were separated at the *p-n* junction by drift mechanism. Drift and diffusion are the two major mechanisms in a *p-n* junction. Minority carriers, electrons, in *n* side drift in to *p* side and minority holes in *n* side drift in to *p* side through the junction [4].

- *Collection of charge carrier*

Separated electrons and holes move through front and back contacts and power the external circuits.

Competitive materials are already in market with good performance, however there are rooms for novel materials with high efficiency and certain other materials with low cost. In *p-n* junction solar cell, absorber material is the heart of it, where the main part of electron- hole pair production takes place [4]. Solar cells are named on the basis of its absorber material. For example, Si, CdTe, CIGS, etc.

1.4 Solar cell classification

Solar cells are generally classified into three types based on the technology adopted; they are silicon based, thin film, and organic and chemical solar cells [15]. Fig. 1.1 shows the classification of solar cells on the basis of technology and materials.

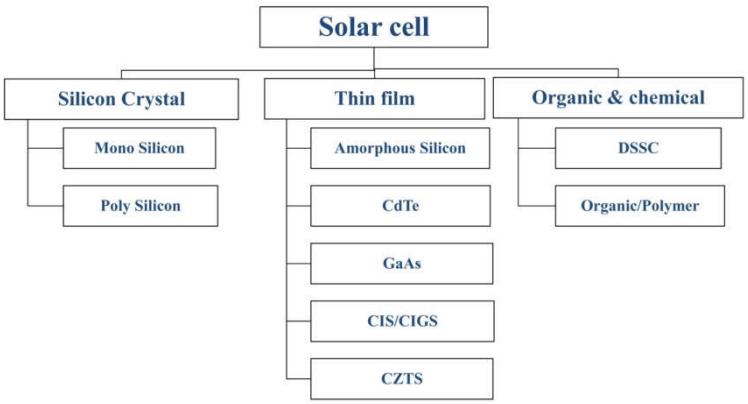

Fig. 1.1 Classification of solar cells

1.4.1 Silicon based solar cells

Silicon is group IV element in the periodic table and has certain special properties. Atomic number of silicon is 14 and its outer orbit contains 4 valance electrons. The four electrons in its valance shell shares with other Si atom and forms crystalline structure. The crystalline structure turns out to be important for photovoltaic applications. Pure crystalline silicon is an intrinsic semiconductor and proper doping can turn the material to *n* type or *p* type semiconductor. The first practical solar cell developed in 1954 at BEL laboratory in United States was based on Si [11]. In 1950's, solar cells are used for space application to generate electricity. Crystalline silicon solar cells are used later for home and industrial applications due to dramatic improvement in the silicon manufacturing process. Silicon solar cells are available in two types, with mono-crystalline silicon (single crystal) and multi-crystalline silicon (poly-crystalline).

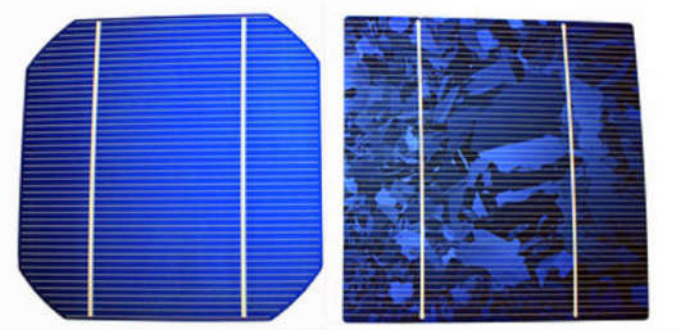

Fig. 1.2 A moncrystalline (a) and a polycrystalline (b) solar cell [16]

Single crystal solar cells are relatively expensive, since it uses thick Si wafers but they are high efficient devices. One of the major

issues of Si absorber is its indirect band gap, it shows lower absorption coefficient in the visible region of solar spectrum [4,16]. Thick Si wafer (~230μm) is required to absorb most of the incident photons, due to its lower absorption coefficient. Higher thickness of the device increases material usage and thus requires high production cost. Monocrystalline Si wafers are made by wire cutting of Si ingots. Czochralski process was used to grow Si ingots [17]. The highest efficiency reported in laboratory for a single junction crystalline solar cell with inter-digitated back contact is 26.7±0.5 under standard test conditions [18]. In the case of industrially sized silicon wafers, Panasonic Japan certified an efficiency of 25.6% [17]. As a result, silicon technology rules the entire solar cell industry for more than 30 years.

Silicon single crystals are produced through a complicated process [18]. Major cost of silicon cell comes from the wafer production cost. To reduce production cost, polycrystalline Si (p-Si) are also used by compromising on efficiency. Polycrystalline Si wafers are made by cutting of cast Si blocks [19,20]. Grain and grain boundaries in p-Si reduce the life time of electron-hole pair, which drops open circuit voltage (V_{oc}) of the cell. The larger the grain size the larger the V_{oc}. Polycrystalline Si solar cells are already in the market. The highest conversion efficiency reported for p-Si solar cells is 21.9% with an active area of 4cm^2 under standard test condition [21]. Fig. 1.2 shows the images of monocrystalline and polycrystalline solar cell.

The material wastage during wafering can be avoided by directly preparing silicon in the form of ribbon or sheets [22]. When compared to other silicon processing techniques, this method reduces the production cost considerably. Several approaches were implemented to produce silicon wafers in the form of ribbon or sheets. Edge-defined film-fed growth (EFG) is the most successful growth technology implemented for commercial production of silicon ribbon/sheets [23,24].

1.4.2 Thin Film Solar cells

Thin film solar cells are considered as second generation solar cells. Thin films are layer of material having thickness in the range of few nanometers to few micrometers. Cost of solar cell reduces when thickness of layers are decreased. Absorption coefficient of the material, which is the measure of the fraction of incident light energy absorbed per unit mass or thickness of an absorber layer, defines the thickness of the absorber layer [4,16]. In the case of crystalline silicon based solar cells, absorption coefficient of the material is very low due to its indirect bandgap. Hence, this open up a new door to the area of novel absorber materials with improved material properties. Currently thin film solar cells are commercialized with four different types of absorber materials, they are CdTe, CIGS, GaAs and amorphous silicon based solar cells [3,4,16,20].

1.4.2.1 Amorphous Silicon

Absorption characteristics of silicon is changed by eliminating its crystalline lattice structure (non-crystalline silicon) [11,23,25]. This new material is called amorphous silicon (a-Si) [23]. a-Si is different from crystalline silicon, with increased absorption coefficient, increased band gap (from 1.1eV to 1.7eV) and improved electrical properties [4,11,23]. The improvement in absorption characteristics of silicon helps to reduce to its thickness to few microns [16,25]. Due to its amorphous nature, recombination loss in the *p-n* interface is higher; in order to reduce recombination loss, the amorphous solar cell employs *p-i-n* structure. A thick intrinsic film (*i* layer) is placed in between thin *p* layer and *n* layer. Fig. 1.3 shows typical structure of amorphous silicon based solar cell. The built in electric field controls the charge carrier transport in the intrinsic layer [25]. Solar cells are stacked to improve the efficiency. The highest conversion efficiency reported by Matsui et al. [21] for amorphous Si solar cell is 10.2%. An attractive roll-to-roll process has also been developed for the manufacturing of a-Si solar cell.

The main issues of a-Si solar cell are its low efficiency and also the degradation of cell efficiency after continues use. Solar cell efficiency is degraded about 20% of its initial value by illuminating the solar cell continuously for a long time [25]. It is needed to adopt complicated manufacturing processes in order to fabricate multilayer stacked structure.

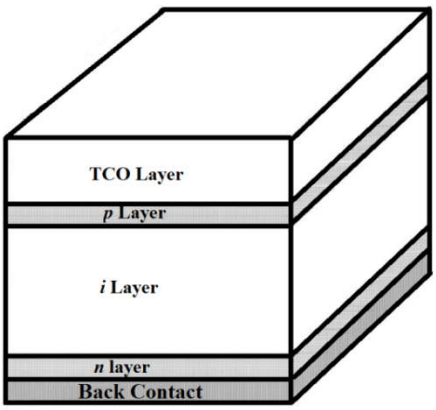

Fig. 1.3 *p-i-n* solar cell structure with a-Si

1.4.2.2 Cadmium telluride solar cell

CdTe is the most attractive compound semiconductor photovoltaic material. CdTe has direct band gap in the range 1.4-1.5eV, considered as the optimum value for a single junction solar cell [25]. High absorption coefficient of CdTe absorber controls its thickness to ~1μm. CdTe technology has been demonstrated with low cost cost/watt among all the photovoltaic technologies. *n* and *p* type conductivity in CdTe has been obtained by doping or non-stoichiometry [26]. CdTe is a stable compound and different methods were already adopted for fabricating CdTe solar cells [26]. Fist CdTe solar cell was made by a three step process including high temperature vapour phase deposition and reported a conversion efficiency of 6% in 1972 [27]. Different techniques were tried later and improved the conversion efficiency up to 21% [25-27]. Fig. 1.4 shows the schematic diagram of CdTe solar cell. The main difference between CdTe cells

with other thin film solar cells is that CdTe solar cells are manufactured in superstrate configuration. The term superstrate refers to a configuration, where the substrate is a supporting structure and also acting as window for the illumination. In this configuration, the substrate is "above" the actual solar cell. If the glass is placed bottom of the solar cell (only act as a supporting structure), then it refers as substrate configuration [4,16,28].

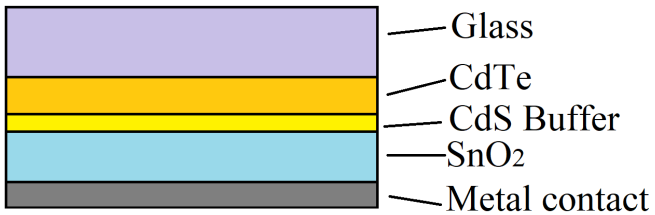

Fig. 1.4 Schematic diagram of CdTe solar cell

Along with these advantages, CdTe solar cells have certain disadvantages also. Cd is a heavy metal and the abundance of Te in earth crust is low, only 0.001 ppm [27]; in view of this, the production of CdTe solar cell in large scale is limited.

1.4.2.3 GaAs solar cell

Amongst different solar cell materials and technologies GaAs solar cells are receiving more attention worldwide. Highest efficiency reported so far is for GaAs absorber layer [21, 29]. Technologies currently used for space application and concentrated solar cells are based of gallium arsenide. It has a direct band gap with 1.42 eV. The

theoretical conversion efficiency predicted for GaAs solar cell is about 33% [29]. The highest efficiency reported for GaAs thin film solar cell is 28.8% [21]. Due to its tunable band gap property, GaAs can be used in multi-junction solar cell for proper bandgap utilization [30]. However, due to limited availability, the element Ga has high material cost. Hence, the multi-junction GaAs solar cells are used for specific high end applications.

1.4.2.4 CIGS solar cell

Copper indium selenide ($CuInSe_2$ or CIS) is I-III-VI ternary compound and crystallizes in tetragonal chalcopyrite structure [31,32]. CIS is a direct bandgap semiconductor with band gap energy of 1.04eV. Kazmerski et al. [33] demonstrated first CIS/CdS solar cell with a conversion efficiency of 4-5% by evaporating CuInSe powder in the presence of excess Se vapour. The real breakthrough began after alloying CIS with Ga, [31]. $Cu(In,Ga)Se_2$ (CIGS) is a compound semiconductor with ideal bandgap and high absorption coefficient [31,32]. Typical CIGS is heterogeneous and hence the physical properties of this material is rather complex. The parent compounds in the system are $CuInSe_2$ (Eg=1.04eV), $CuInGaSe_2$ (Eg=1.5eV) and $CuGaSe_2$ (Eg=1.7eV); the possible materials in this system cover a wide range of bandgap and lattice constant [34,35]. It is a direct band gap semiconductor and has large absorption coefficient; thickness in the range 1-2μm is sufficient to absorb all the incident photons. Typically CIGS is seen in polycrystalline alpha phase (Fig. 1.5). The band gap of the material can be varied 1 to 1.7eV by changing In/Ga

ratio in $CuIn_xGa_{1-x}Se$ (x=0 to 1) [34,35]. CIGS is a *p* type semiconductor, intrinsic defect Cu vacancy in the crystal make the material *p* type [31,36].

Hahn et al. [37] first reported CISe material in 1953 with band gap of 1.04eV. In 1981 Mickelson reported an efficiency of 9.4% for the film deposited by co-evaporation from elemental sources [38]. After this, CIS solar cell had greater impact in thin film solar cell industry. Fig. 1.6 shows the typical structure adopted for CIGS solar cells.

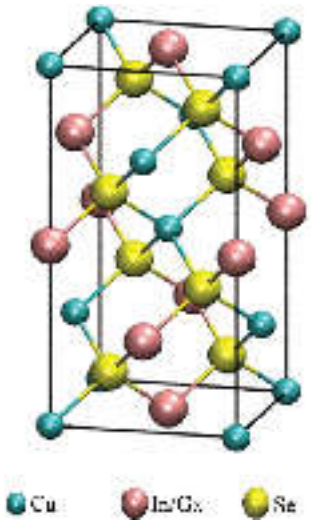

Fig. 1.5 Crystal structure of tetragonal chalcopyrite CIGS unit cell [31]

In the basic structure, molybdenum coated soda lime glass (SLG) substrates were used as back contact, then *p* type absorber film is deposited on this Mo substrate to make good ohmic contact. Several deposition techniques were developed for coating CIGS [31-38]. To

make *p-n* junction, very thin layer of *n* type CdS layer is normally deposited by chemical bath deposition on to the CIGS film. This layer is also known as buffer layer [33]. An intrinsic ZnO layer is then deposited over this *n* type film. Finally, Al doped ZnO film is coated, which act as the top contacting electrode. Several modifications were carried out by different groups and a few other layers were also included in this structure to improve efficiency [31-38]. Ga/(In+Ga) and Cu/(Ga+In) ratios have to be around 0.26 and 0.88-0.92 respectively, to obtain higher efficiency [31]. Change in ratios is found to increase number of defects in the crystalline lattice [36]. Leading solar cell manufacturing company "Solar frontier" reported CIGS solar cell with 22.8% efficiency; however in the case of commercial modules the efficiency is only 16% [31]. A large difference in terms of efficiency is existed between laboratory cells and commercial modules. In large scale production, the efficiency decreases due to the differences in the growth kinetics [16,31]. In addition, there are a few issues in CIGS solar cell production, such as

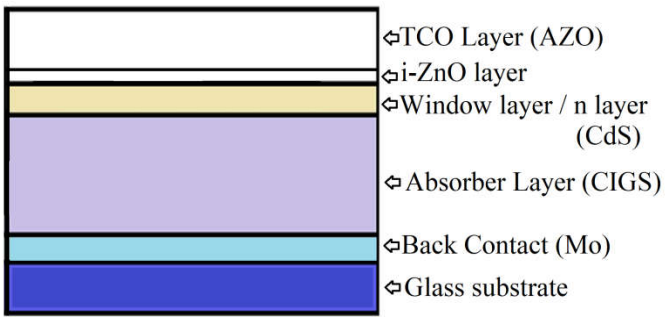

Fig. 1.6 Schematic diagram of CIGS solar cell

1) Large scale production of CIGS solar cell is limited due to the availability of indium and gallium.

2) CdS is used as a buffer layer in CIGS solar cell. Disposal of Cd containing product causes adverse effect in environment.

3) Module efficiency in large area cell is limited to 16%, hence the cost/watt ratio is increased.

4) Encapsulation of CIGS solar cell is one the major problem. CIGS materials are highly sensitive to moisture.

1.4.2.5 CZT(S,Se) solar cell

The I-II-IV-VI quaternary compound, kesterite Cu_2ZnSnS_4 (CZTS), is a promising absorber material for low-cost thin film solar cells. This material is having a band gap of 1.4 - 1.5eV and absorption coefficient of $>10^4$ cm^{-1} in the visible region [39-43]. CZTS based solar cell is expected to have a theoretical efficiency of more than 30%, and is being extensively investigated in recent years.

One can obtain CZTS from the chalcopyrite CIGS, by substituting the trivalent In/Ga with a bivalent Zn and tetravalent Sn. Each components of CZTS is abundant in earth's crust (Cu: 50ppm, Zn: 75ppm, Sn: 2.2ppm, S: 260ppm) and these elements possess extremely low toxicity [6,39,40]. On the other side, in the case of CIS/CIGS, the abundance of indium and selenium in the earth's crust are very low [6].

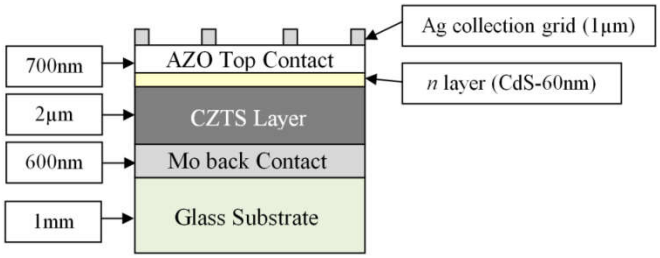

Fig. 1.7 Schematic diagram of a Cu_2ZnSnS_4 solar cell.

Fig.1.7 represents a typical CZTS solar cell. The substrate in the figure is glass, it can also be a flexible plastic substrate [44]. *p-n* junction is formed by combining *p* type CZTS layer and *n* type CdS layer and the junction is sandwiched between the bottom (Mo metal contact) and top electrical contacts; top contact consists of an n-type Al-doped ZnO contact, and patterned metal electrode provides contact to the external circuit. An antireflective coating is also used in this type of cells. All these layers contain abundant elements and can be deposited using thin film technologies. Highest conversion efficiency reported for CZTSSe solar cell is 12.6% by IBM [45]. The research area of this work is based on CZTS absorber and will be discussed later.

1.4.3 Organic and chemical solar cells

Several photovoltaic technologies have emerged that have high potential, such as dye sensitised solar cells (DSSC), organic solar cells, perovskite solar cells, quantum dot solar cells [21-26]. These solar cells have advantages and certain disadvantages.

1.4.3.1 Dye sensitised solar cell

Michael Gratzel in 1990s demonstrated inexpensive and easily producible devices that can harvest electricity in appreciable quantity [46]. These are known as dye sensitized solar cells (DSSC). A typical DSSC has a sandwich structure; a dye sensitised semiconductor with electrolyte is placed between a transparent conducting electrode and a counter electrode [46, 47]. The mainly used counter electrode is platinum, which has high conductivity and electro-catalytic activity. But Pt is scarce and expensive, which makes solar cell expensive. The highest certified conversion efficiency reported for DSSC is around 11.9% [48]. A few companies, eg. Solaronix, Fujikura, commercialised DSSC technology. The main advantage with this technology is its ability to integrate in various part of buildings shell, not just the roof top [46,48]. The main issue which limit the production of DSSC is the dyes used in the cell. Commonly used dyes are ruthenium complexes which is corrosive, volatile, and issues with long term stability [46,47].

1.4.3.2 Organic solar cell

Organic solar cells are thin, light weight and flexible. They are mainly a mixture of light sensitive polymer and fullerene like compounds to absorb light [49]. Highest conversion efficiency reported for organic solar cell is 11.5% [50]. Solar manufacturing companies tried to make flexible solar panels for portable powering applications [11]. Similar to valance band and conduction band in inorganic semiconductor materials, organic materials have LUMO

(lowest unoccupied molecular orbital level) and HOMO (highest occupied molecular orbital level) levels [51]. The difference between HOMO and LUMO is referred to as band gap of organic material and is typically in the range of 1-4eV [49,51]. The main disadvantages with organic solar cells are low efficiency, stability, toxicity and reproducibility [11,51].

1.4.3.3 Perovskite solar cell

In the recent years, perovskite solar cells made remarkable advances in the field of photovoltaics. The highest conversion efficiency of 22.1% is reported under laboratory conditions [26]. Perovskite materials have ABX_3 structure, where A is an organic cation, B is an inorganic cation and X is a halide [26,51]. Band gap of these materials can be tuned from 1.6eV to 3.2eV [52-54]. The main advantages are low material cost, band gap tunability, low recombination losses and higher carrier diffusion length [51,52]. Most studied example of perovskite material is $(CH_3NH_3)PbI_3$, which absorb light and produce electron-hole pair [20]. The main disadvantages with perovskite materials are use of toxic Pb, instability of material, highly sensitive to moisture, lack of fill factor due to non-uniformity in absorber layer, etc [26]. It is necessary to carry out further research in this material to address all those issues. Perovskites are expected to make breakthrough in the solar cell industry.

1.4.3.4 Quantum dot solar cell

Quantum dot solar cells are the low cost emerging technology. Quantum dot photovoltaics use metal chalcogenide nanocrystals as

light absorbing material [21]. Mainly used nanocrystals are CdS, CdSe, PbS, PbSe etc [51]. Du et al. reported [55] highest conversion efficiency of 11.6% for colloidal quantum dot solar cell. The main advantage with quantum dot solar cell is the easy of manufacturing process. Roll to roll printing techniques can be implemented for solar cell fabrication. Usage of Cd and Pb are restricted the research in the field of quantum dot solar cells [11,54]. A new approach developed by Du and his co-workers gives further attention in quantum dot solar cells [55]. They developed quantum dot solar cell by using less toxic Zn-Cu-In-Se, with highest conversion efficiency.

1.5 Kesterite (Cu_2ZnSnS_4) absorber

Kesterite is a chalcogenide mineral from Kester (place in Russia) deposit with chemical formula $Cu_2(Zn,Fe)SnS_4$ [56,57]. In the mineral form of kesterite, Zn and Fe atoms share the same lattice site [58,59]. Cu_2ZnSnS_4 and $Cu_2ZnSnSe_4$ are the synthetic form of kesterite mineral. There are in general three types of kesterite absorbers, Cu_2ZnSnS_4 (CZTS), $Cu_2ZnSnSe_4$ (CZTSe) and $Cu_2ZnSn(S,Se)_4$ (CZTSSe) [60,61]. Copper zinc tin sulphide (CZTS), kesterite, is a well known absorber material for photovoltaic cells because of its optimum band gap of 1.5eV and high absorption coefficient ($>10^4 cm^{-1}$) [57,60,61]. They exist in two forms, Zn rich mineral is called kesterite and Zn poor mineral is called stannite [56-58]. Kesterite is also called isostannite, because kesterite and stannite are structurally similar. Due to the structural similarities of CZTS with CIGS, researchers are interested in this material also. As described

earlier, chalcopyrites based CIGS already demonstrated with higher efficiency (22.8%) for laboratory scale and with 16% for production scale. As pointed out, large scale manufacturing of CIGS solar cell is limited due to the scarcity of indium and gallium. Cost of indium is very high due to the demand from display industry. Table 1.1 shows the abundance and price range of major elements used in electronic industries (the price as on 2017 October and the abundance as on 2007 April). As seen in the table, the abundance of In and Te are very low compared to the other metals.

Table 1.1 Abundance of elements and its price list

Element	Price (USD/Kg)*	Abundance in earth crust (in ppm)
Copper	6.504	68
Zinc	3.314	79
Tin	20.954	2.2
Sulphur	-----	420
Selenium	319670	0.05
Indium	2000000	0.160
Cadmium	1.8739	0.15
Tellurium	400000	0.001

(Source: "Abundance in Earth's Crust". WebElements.com. and *prize list as on 4th Oct 2017; ** from *http://mineralprices.com/)*

Those emerging photovoltaic technologies, which use earth abundant and non-toxic materials are more attractive now a days. As shown in the table, the constituent elements in CZTS are earth abundant with low cost. As per Shockley-Queisser photon balance, the theoretical conversion efficiency of CZTS(Se) solar cell is 32.2% [62].

Due to the admirable properties, kesterite compounds are promising candidate for photovoltaic applications.

1.5.1 Crystal structure

The two CZTS crystal structures reported, kesterite and stannite, are difficult to distinguish due to similar crystallographic structure. Fig. 1.8 shows kesterite and stannite crystal structures for CZTS drawn with PowderCell software using their mineral data [56]. The difference between these two phases is in the distribution of cations in the tetrahedral voids [56-58, 60,61].

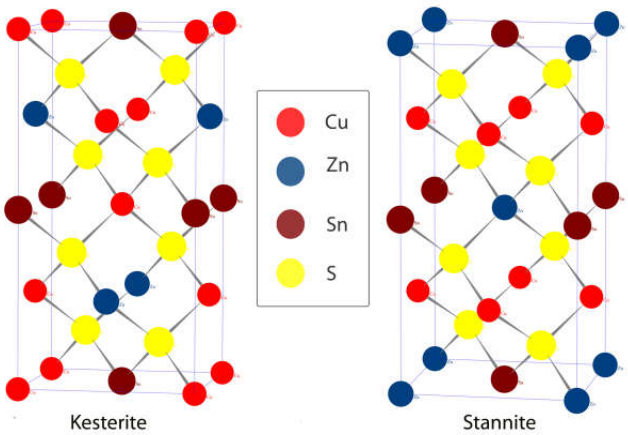

Fig. 1.8 Kesterite and Stannite crystal structure for CZTS. Structures drawn with PowderCell (V 2.4) Software [63]

These two structures are derived from basic chalcopyrite structure. In CIGS, half of the In replaced with Zn and another half by Sn to form CZTS. Kesterite and stannite are structurally similar but they differ in its space group [60,61]. Kesterite has a space group of I4 (S.G No 82)

while stannite has space group of I42m (S.G No 121) [60,61,64]. Stannite structure consists of a layer of copper alternates with layer of zinc and tin, zinc and tin switch their position layer by layer [56,65]. Kesterite structure consists of two alternating cation layer, each containing Cu and Zn or Cu and Sn along the c axis [65]. Due to the structural similarities and iso electronic nature of Cu^{+} and Zn^{2+}, it is difficult to differentiate these two phases by X-ray diffraction techniques [61]. Neutron diffraction and Raman spectroscopic technique are more useful in this case [61,64].

There is a probability to co-exist kesterite with stannite phase during crystallization process; there is only a small difference in lattice parameter for both phases [61]. Recent works in this area predicted that kesterite structures are dominant at temperature below 876°C, and that the kesterite structure are thermodynamically more stable than the stannite phase [65-70].

1.5.2 Phase Diagram

Several vacuum and solution based techniques are used for coating CZTS thin films [71-90]. Most of these articles are describing the phase purity of CZTS thin films. It is extremely difficult to form quaternary semiconductor in single phase [69]. Phase diagrams are helpful to identify the possible secondary or ternary phases. Fig. 1.9 shows ternary phase diagram for CZTS formation [71]. Abermann constructed CZTS phase diagram including expected secondary phases [71]. The phase diagram is constructed in such a way that it is valid at 400°C. Sulphur concentration is assumed to be 50%. As seen in the

phase diagram, CZTS is formed only at specific points, outside this region it coexists with other secondary or ternary phases.

In the case of CZTS formation, only 1-2% deviation from the ideal stoichiometry is allowed, compared to other chalcopyrite systems, where up to 4% deviation is acceptable [71,72]. Hence the formation of this compound in single phase is an exciting challenge. In this connection, phase diagram can be used for better understanding of secondary phases.

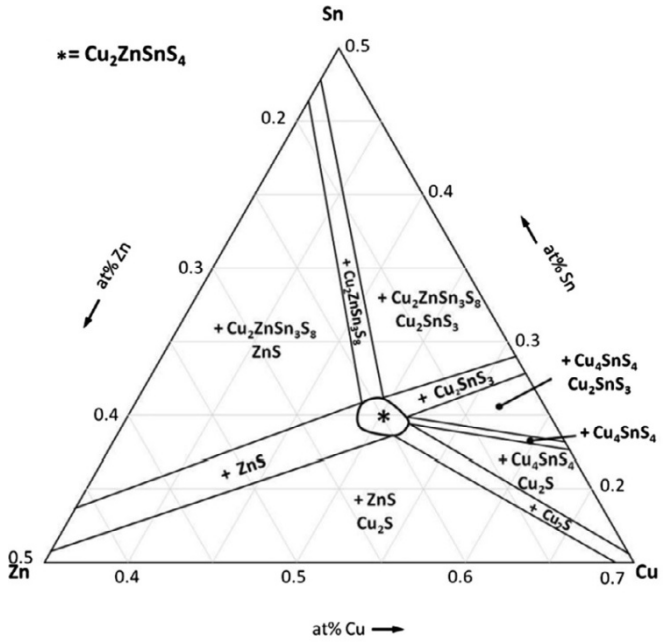

Fig. 1.9 Ternary phase diagram exhibiting CZTS formation including expected secondary phases [71]

1.5.3 Secondary or ternary phases

Presence of secondary or ternary phases in CZTS absorbers greatly deteriorates cell performance [71]. Generally observed phases are ZnS, SnS_2, Cu_2SnS_3, Cu_2S, SnS, etc. High efficiency CZTS solar cell reported so far were slightly off-stoichometric [73]. The stoichometry of the CZTS composition is mainly analysed based on the Cu/(Zn+Sn) and Zn/Sn ratios. Composition ratios for the high efficient CZTS solar cell reported by Katagiri et al. were Cu/(Zn+Sn)=0.87 and Zn/Sn=1.15 [73]. Cu poor Zn rich conditions are more favourable in CZTS crystal, this point will be discussed in detail in section 3.1.6 of this thesis. However, deviation from stoichiometry may lead to secondary phases. The secondary phases in CZTS absorber create shunting current path and/or act as recombination centre [74-79]. Secondary phases affect energy band gap of the material and limit the open circuit voltage of cells [80]. Hence a detailed balance in stoichiometry and proper identification of secondary or ternary phases is important to obtain phase pure CZTS absorber films with optimum photovoltaic properties.

1.6 Kesterite (Cu_2ZnSnS_4) - a review

This direct band gap, *p* type, less expensive, non-toxic semiconductor has recently received wide attention as absorber layer in thin film solar cells. Nitche et al. in 1966 developed quaternary CZTS material via iodine vapor transport [81]. Ito and Nakazawa in 1988 reported formation of CZTS and they verified its potential as a thin

film absorber material [82]. Several types of growth techniques were adopted for CZTS absorber layer coating after this report.

Katagiri in 1997 introduced first vacuum based CZTS solar cell with 0.66% efficiency [83]. Generally vacuum based techniques give higher device performance compared to solution based approaches [21-25]. However, record efficient devices are developed by solution based approaches for CZTS solar cells from 2009 onwards. The current record efficiency of 12.6% was reported in 2013 for CZTSSe solar cell using solution approach with hydrazine, and the absorber used in this cell was in Cu poor and Zn rich condition [45]. In the last few years, several approaches were tried to coat phase pure CZTS thin film and to develop solar cells exhibiting higher efficiency.

1.6.1 CZTS thin film by vacuum based approaches

Vacuum techniques include sputtering, thermal evaporation, pulsed laser deposition chemical vapour deposition etc. Several parameters are to be controlled depending on the technique to obtain desired stoichiometry and phase purity. In general, two approaches are used for CZTS thin film preparation, (i) formation of CZTS by single step process; this process is more preferable because CZTS film is formed in a single equipment [84] and (ii) In this case, in a two step process, a post annealing treatment is required after coating CZTS precursor film [83]. In 1997, Katagiri et al. prepared CZTS thin film via vapour phase sulphurization of electron beam evaporated precursor film, and reported a conversion efficiency of 0.66% with

ZnO:Al/CdS/CZTS/Mo/SLG device structure [83]. The same group in 2001 improved the conversion efficiency to 2.63% [85], in 2003 to 5.45% [86] and in 2008 to 6.7% [87]. The group made a remarkable contribution in the field of CZTS solar cell fabricated by vacuum based technique. Both co-sputtering and CZTS single target sputtering were used for coating CZTS thin film.

CZTS sputtering target is suitable for large area manufacturing process and also useful for depositing high quality of CZTS thin films. In sputtering process with single stage CZTS target, composition deviation can be minimised; this approach was proposed by Kusano et al.[88] This is relatively simple, cost effective and can be used to coat film over large area. Lin et al. [89] and Sun et al. [90] studied the effect of stoichiometry in CZTS thin films and obtained higher efficiency of 5.2% by varying stoichometric ratios. Nakamura et al. compared CZTS thin film obtained by co-sputtering and single target sputtering and found that both films exhibited similar properties at 500°C sulphurization temperature [91]. Wang et al. prepared absorber film by prolonged sulphurization of stacked precursor layers, but observed cracks and small holes on the grain boundaries due to the evaporation of Sn [92]. He demonstrated a method to reduce Sn evaporation by annealing metal stacked precursor before sulphurization. Gang et al. introduced another method to avoid Sn loss during sulphurization by increasing sulphur partial pressure [93]. Feng et al. fabricated CZTS thin film solar cell with conversion efficiency of 8.58% by co-sputtering and sulphurization [94]. The highest conversion efficiency reported so far by sputtering techniques is also based on this method.

Tajima et al. reported the highest conversion efficiency of 9.4% for CZTS cell by co-sputtering of metal targets followed by sulphurization in H_2S atmosphere [95]. There are several articles that studied the different parameters that control CZTS film properties [96].

Schubert et al. in 2011 [97] reported 4.1 % efficient CZTS solar cell by co-evaporation of ZnS, Sn, Cu and S sources and the process was performed at substrate temperature of 550°C and with sulphur partial pressure of $2\text{-}3\times10^{-3}$Pa. Repins et al. [98] in 2012 demonstrated CZTSe solar cell with 9.15% efficiency by co evaporation method. They adopted standard CIGS coating procedure and changed In and Ga shots with Zn and Sn. This is the highest conversion efficiency reported so far by co-evaporation method. Higher efficiency of 8.4% was reported by shin et al. by growing CZTS film using co-evaporation followed by sulphurization [99]. Mise et al. [100] studied the effect of Na incorporation in the device fabrication and studied its effect on efficiency. Both selenization and sulphurization effects were studied by Gao et. al. [101] and observed significant effect of temperature and atmosphere on the morphology and crystallinity of CZTSe films.

Pulsed laser deposition is another major technique used for coating CZTS film. Phase pure CZTS target is required for PLD technique and further processing is also required to improve the crystallite properties. 5.85% conversion efficiency is reported for cells with PLD coated CZTS film [102]. Several studies are made by various groups using this technique [103]. Vanalakar et al. [104] studied the effect of annealing atmosphere on the properties of PLD

deposited CZTS film. Mohoikar et al. [105] studied the effect of variation in compositional ratios and reported how this affects the film's structural, electrical and optical properties. Byeon et al. [106] studied the influence of deposition time on the structural and optical properties of CZTS film deposited by PLD. CZTS thin films fabricated by PLD technique were also used for DSSC application [107]. The group replaced the conventionally used Pt electrode by CZTS film.

1.6.2 CZTS thin film by non-vacuum approaches

Record conversion efficiency of 12.6% has been reported using by cheap and economic solution based technique [45]. It demonstrates the importance of solution based routes for CZTS thin film solar cells development. Major non-vacuum approaches include spin coating, dip coating, spray coating etc. Non-vacuum based approaches are cost effective; consume very less energy and give uniform films.

Several studies using solution based methods are available in literature [21,26,62]. Wang et al. reported 12.6% efficiency CZTSSe thin film solar cell by spin coating of hydrazine based precursor solution [45]. Tanaka et al. developed CZTS film by sulphurizing spin coated precursor film containing Cu, Zn and Sn [108] and studied its pre-annealing effects. In another article, Yeh et al. [41] prepared CZTS films using thiourea as sulphur source and metal chlorides in de-ionized water/ethanol, and studied the effect of annealing in air in the temperature range 160°C-320°C. Fischereder et al. [42] prepared CZTS thin films using thioacetamide as sulphur source, and dissolved metal salts in pyridine. The group studied the effects of annealing in

vacuum and concentration of thioacetamide in the precursor solution on the structural, surface morphological and optical properties of CZTS thin films. Kahraman et al. [43] prepared CZTS thin films using thiourea, but sulphurized again in elemental sulphur atmosphere to tolerate sulphur loss during annealing. Most of the works done so far were by spin coating [109]. However, for bifacial solar cell applications, the most widely used technique is dip coating; this route helps to deposit films on both surfaces simultaneously. Only a few groups investigated the potential of CZTS prepared by dip coating for bifacial solar cells applications [110-114]. Tapas Kumar et al. deposited phase pure CZTS films by dip coating from methanolic solution of metal-thiourea complex [110]. Yuxin et al. coated CZTS films by this route using ethylene glycol and metal-thioacetamide system [111]. Ferhat et al. studied the influence of pH on structural, optical and electrical properties of CZTS absorber film coated by dip technique [112]. Patel et al. prepared CZTS thin films by dip coating using thiourea as the sulphur source and investigated the effect of annealing in sulphur atmosphere at different temperatures [113]. In bifacial device configuration, Ge et al. [114] reported a conversion efficiency of 3.4%.

Among the non-vacuum techniques, spray pyrolysis is the easiest method for large area deposition. Nakayama and Ito reported fabrication of sprayed films of Cu_2ZnSnS_4 for the first time in 1996 and the raw materials used were chlorides and thiourea [115]. They dissolved precursors in deionised water and sprayed onto the soda lime

glass substrate heated by a nichrome heater indirectly. Later, several groups investigated the effects of various parameters, such as substrate temperature, pH of the solution, etc [116-122]. In another work, Rodriez et al. sprayed films with $CuCl_2$, $Zn(CH_3COO)_2.2H_2O$, $SnCl_4$ and $SC(NH_2)_2$ precursors in an $Ar/Ar+H_2$ atmosphere followed by annealing in sulphur atmosphere [116]. Certain groups reported the deposition of CZTS using chloride precursors and annealing in different sulphur environments [116,118,119]. Tanaka et al. reported annealing of the CZTS thin films by placing precursor films of Sn and S face to face during the annealing process to suppress the evaporation of S and Sn [123]. Highest conversion efficiency of 8.1% is reported by Nguyen et al. for spray coated CZTS film with Cu poor and Zn rich composition [124].

Screen printing is another type of large area thin film coating technique. Zhoue et al., fabricated CZTS thin film by screen printing technique on polyamide substrate and fabricated solar cell with conversion efficiency of 0.49% [125]. Kermadi et al., used ultrasonic spray pyrolysis technique to coat CZTS film and studied its Cu content and sulphurization process [126]. In another work, Araki et al., prepared CZTS film by sulphurizing electroplated precursors and studied the effect of sulphurization temperature [127]. Saraswat et al.,[128] and Pawar et al.,[129] studied the properties of electrochemically deposited CZTS thin films.

1.6.3 CZTS nanoparticles synthesis

In an another approach in non-vacuum based technique uses CZTS nanoparticles prepared by solution routes [130-133]. Synthesis and characterization of semiconductor nanoparticles has generated vast amount of interest in recent years due to their attractive properties. Guo et al. prepared CZTS nanoparticles by hot injection method for using as an absorber material [132]. Kameyama et al., synthesised CZTS nanoparticles by thermal reaction of metal acetate with elemental sulphur in an oleylamine solution at different temperatures [133]. Using CZTS nanoparticles, Guo et al., constructed CZTSSe solar cell with conversion efficiency of 7.2% [131].

1.7 Objectives of the Thesis

It is clear that there are issues of long term sustainability in terms of cost and availability for the CdTe and CIGS based PV technologies. It is in this context, investigations have been initiated all over the world for an alternative non-toxic absorber material. Cu_2ZnSnS_4 (CZTS) and $Cu_2ZnSnSe_4$ (CZTSe) are two promising absorber materials for thin film photovoltaic cells due to their *p*- type nature, high absorption coefficient ($>10^4 cm^{-1}$) and optimum direct band gap (~1.5eV). CZTS consists of earth abundant, non toxic and inexpensive elements. Even with these ideal characteristics, the CZTS cells reached only 9.1% efficiency so far. There are wide variations in CZTS solar cell efficiencies reported so far. The low device efficiency in CZTS solar cell may be due to the difficulty in forming CZTS in

single phase. In view of this, a detailed study on absorber film fabrication is important. Technology Information, Forecasting and Assessment Council (TIFAC) in its report projected development of CZTS thin film technology with efficiency 15% and above as one of the major R&D thrust areas, which need to be undertaken by Indian R&D fraternity to make India a leading nation in photovoltaic technology and its applications [10].

Various approaches were made by different groups on vacuum and solution based techniques. In this work, simple and cost effective solution based techniques were used for preparing phase pure CZTS absorber films. The films were coated on glass substrates by three different solution based techniques (spin, dip and spray coating). After coating precursor films by these techniques, the films were further annealed/ sulphurized at different temperature to study the effect of annealing conditions on structural, surface morphological, optical and electrical properties of CZTS thin films. A prototype of the CZTS solar cell has also been fabricated in this study.

The main objectives of the proposed works are,

a. To develop kesterite (CZTS) thin films by chemical solution deposition methods (Eg. Spin/dip coating, spray pyrolysis).

b. To study the structural, morphological and optical properties of the kesterite films.

c. To fabricate and characterize a prototype solar cell using the kesterite absorber.

1.8 References

1) McGlade C, Ekins P, The geographical distribution of fossil fuels unused when limiting global warming to 2 C, Nature. 17 (2015) 187.

2) Dresselhaus M S, Thomas I L, Alternative energy technologies, Nature. 414 (2001) 332.

3) Green M A, Third generation photovoltaics: solar cells for 2020 and beyond, Physica E: Low Dimens. Syst. Nanostruct. 14 (2002) 65.

4) Chopra K L, Paulson D, Dutta V, Thin film solar cells: an overview, Prog. Photovolt: Res. Appl. 12 (2004) 69.

5) Ragauskas A J, Williams C K, Davison B H, Britovsek G, Cairney J, Eckert C A, Frederick W J, Hallett J P, Leak D J, Liotta C L, Mielenz J R, The path forward for biofuels and biomaterials, Science. 311 (2006) 484.

6) Suryawanshi M P, Agawane G L, Bhosale S M, Shin S W, Patil P S, Kim J H, Moholkar A V, CZTS based thin film solar cells: a status review, Mater. Technol. 28 (2013) 98.

7) Kydes A S, Impacts of a renewable portfolio generation standard on US energy markets, Energy Policy. 35 (2007) 809.

8) Goswami D Y. A review and future prospects of renewable energy in the global energy system, Proceedings of ISES World Congress. Springer, Berlin, Heidelberg, 1-5 (2008) 3.

9) Kiani B, Rowe A, Wild P, Pitt L, Sopinka A, Pedersen T F, Optimal electricity system planning in a large hydro jurisdiction: Will British Columbia soon become a major importer of electricity?, Energy Policy. 54 (2013) 311.

10) Solar PV technology foresight for India, Technology Information, Forecasting & Assessment Council (TIFAC) Government of India (2015).

11) Parida B, Iniyan S, Goic R, A review of solar photovoltaic technologies, Renewable Sustainable Energy Rev. 15 (2011) 1625.

12) King R R, Bhusari D, Larrabee D, Liu X Q, Rehder E, Edmondson K, Cotal H, Jones R K, Ermer J H, Fetzer C M, Law D C, Solar cell generations over 40% efficiency, Prog. Photovoltaics Res. Appl. 20 (2012) 801.

13) Palz, Wolfgang, Power for the World - The Emergence of Electricity from the Sun. *Bel*gium: Pan Stanford Publishing. (2010) *6*.

14) Becquerel E. On electric effects under the influence of solar radiation. Compt. Rend. 9 (1839) 561.

15) Kirchartz T, Bisquert J, Mora-Sero I, Garcia-Belmonte G, Classification of solar cells according to mechanisms of charge separation and charge collection, Phys. Chem. Chem. Phys. 17 (2015) 4007.

16) Fonash S, Solar cell device physics. Elsevier; 2012.

17) Battaglia C, Cuevas A, De Wolf S. High-efficiency crystalline silicon solar cells: status and perspectives, Energy Environ. Sci. 9 (2016) 1552.

18) Yoshikawa K, Kawasaki H, Yoshida W, Irie T, Konishi K, Nakano K, Uto T, Adachi D, Kanematsu M, Uzu H, Yamamoto K, Silicon heterojunction solar cell with interdigitated back contacts for a photoconversion efficiency over 26%, Nat. Energy. 2 (2017) 17032.

19) Aberle A G, Surface passivation of crystalline silicon solar cells: a review, Prog. Photovoltaics: Res. Appl. 8 (2000) 473.

20) Goetzberger A, Hebling C, Photovoltaic materials, past, present, future, Sol. Energy Mater. Sol. Cells. 62 (2000) 1.

21) Green M A, Hishikawa Y, Warta W, Dunlop E D, Levi D H, Hohl-Ebinger J, Ho-Baillie AW, Solar cell efficiency tables (version 50). Prog. Photovoltaics. 25 (2017) (NREL/JA-5J00-68932).

22) Schmidt W, Woesten B, Kalejs J P, Manufacturing technology for ribbon silicon (EFG) wafers and solar cells, Prog. Photovoltaics Res. Appl. 10 (2002) 129.

23) Green M A, Crystalline and thin-film silicon solar cells: state of the art and future potential, Sol. Energy. 74 (2003) 181.

24) Hegedus S S, Luque A, Status, trends, challenges and the bright future of solar electricity from photovoltaics, Handbook of photovoltaic science and engineering. 25 (2003) 1.

25) Shah A, Torres P, Tscharner R, Wyrsch N, Keppner H, Photovoltaic technology: the case for thin-film solar cells, Science. 285 (1999) 692.

26) Lee T D, Ebong A U, A review of thin film solar cell technologies and challenges, Renewable Sustainable Energy Rev. 70 (2017) 1286.

27) Bonnet D, Rabenhorst H, New results on the development of a thin-film p-CdTe-n- CdS heterojunction solar cell, Photovoltaic Specialists Conference, 9th, silver Spring, (1972).

28) Poortmans J, Arkhipov V, Thin film solar cells: fabrication, characterization and applications, John Wiley & Sons; (2006).

29) Makableh Y F, Vasan R, Sarker J C, Nusir A I, Seal S, Manasreh M O, Enhancement of GaAs solar cell performance by using a ZnO sol–gel anti-reflection coating, Sol. Energy Mater. Sol. Cells. 123 (2014) 178.

30) Kurtz S R, Allerman A A, Klem J F, Jones E D, inventors; National Technology, Engineering Solutions of Sandia LLC, assignee. InGaAsN/GaAs heterojunction for multi-junction solar cells, (2001) United States patent US 6,252,287.

31) Ramanujam J, Singh U P, Copper indium gallium selenide based solar cells–a review, Energy Environ. Sci. 10 (2017) 1306.

32) Jeyakumar R, Ramamurthy S, Jayachandran M, Chockalingam M J, Electrochemical preparation and characterization of copper indium diselenide thin films, Mater. Res. Bull. 29 (1994) 195.

33) Kazmerski L L, White F R, Morgan G K, Thin-film $CuInSe_2$/CdS heterojunction solar cells, Appl. Phys. Lett. 29 (1976) 268.

34) Wang Y C, Shieh H P, Improvement of bandgap homogeneity in $Cu(In,Ga)Se_2$ thin films using a modified two-step selenization process, Appl. Phys. Lett. 103 (2013) 153502.

35) Cui X, Yun D, Zhong C, Chen W, Cheng Q, Feng J, Zhang F, A facile route for synthesis of $CuIn_xGa_{1-x}Se_2$ nanocrystals with tunable

composition for photovoltaic application, J. Sol-Gel Sci. Technol. 76 (2015) 469.

36) Zhang S B, Wei S H, Zunger A, Katayama-Yoshida H, Defect Physics of the $CuInSe_2$ Chalcopyrite Semiconductor, Phys. Rev. B. 57 (1998) 9642.

37) Hahn H, About some ternary chalcogenides with chalcopyrite structure, Z. Anorg. Allg. Chem. 271 (1953) 153.

38) Mickelsen R A, Chen W S, Development of a 9.4% efficient thin-film $CuInSe_2$/CdS solar cell, 15th photovoltaic specialists conference 15 (1981) 800.

39) Tanaka K, Moritake N, Oonuki M, Uchiki H, Pre-annealing of precursors of Cu_2ZnSnS_4 thin films prepared by sol–gel sulfurizing method, Jpn. J. Appl. Phys. 47 (2008) 598.

40) Chaudhuri T K, Tiwari D, Earth-abundant non-toxic Cu_2ZnSnS_4 thin films by direct liquid coating from metal–thiourea precursor solution, Sol. Energy Mater. Sol. Cells. 101 (2012) 46.

41) Yeh M Y, Lee C C, Wuu D S, Influences of synthesizing temperatures on the properties of Cu_2ZnSnS_4 prepared by sol–gel spin-coated deposition, J. Sol-Gel Sci. Technol. 52 (2009) 65.

42) Fischereder A, Rath T, Haas W, Amenitsch H, Albering J, Meischler D, Larissegger S, Edler M, Saf R, Hofer F, Trimmel G, Investigation of Cu_2ZnSnS_4 formation from metal salts and thioacetamide, Chem. Mater. 22 (2010) 3399.

43) Kahraman S, Cetinkaya S, Podlogar M, Bernik S, Cetinkara H A, Güder H S, Effects of the sulfurization temperature on sol gel-processed Cu_2ZnSnS_4 thin films, Ceram. Int. 39 (2013) 9285.

44) Peng C Y, Dhakal T P, Rajbhandari P, Garner S, Cimo P, Lu S, Westgate C R, Flexible CZTS solar cells on flexible Corning Willow Glass substrates, Photovoltaic Specialist Conference (PVSC), IEEE 40 (2014) 0409.

45) Wang W, Winkler M T, Gunawan O, Gokmen T, Todorov T K, Zhu Y, Mitzi D B, Device characteristics of CZTSSe thin film solar cells with 12.6% efficiency, Adv. Energy Mater. 4 (2014) 1301465.

46) Grätzel M, Dye-sensitized solar cells, J. Photochem. Photobiol. C. 4 (2003) 145.

47) Hagfeldt A, Grätzel M, Molecular photovoltaics, Acc. Chem. Res. 33 (2000) 269.

48) Ahmad M S, Pandey A K, Rahim N A, Advancements in the development of TiO_2 photoanodes and its fabrication methods for dye sensitized solar cell (DSSC) applications. A review, Renewable Sustainable Energy Rev. 77 (2017) 89.

49) Cui Y, Yao H, Gao B, Qin Y, Zhang S, Yang B, He C, Xu B, Hou J, Fine-tuned photoactive and interconnection layers for achieving over 13% efficiency in a fullerene-free tandem organic solar cell, J. Am. Chem. Soc. 139 (2017) 7302.

50) Li M, Gao K, Wan X, Zhang Q, Kan B, Xia R, Liu F, Yang X, Feng H, Ni W, Wang Y, Solution-processed organic tandem solar cells with power conversion efficiencies >12%, Nat. Photonics. 11 (2017) 85.

51) Kaushika N D, Mishra A, Rai A K, High Performance Solar Cells. Solar Photovoltaics, Springer, Cham. (2018) 139.

52) Zweibel K, Reducing ES & H impacts from thin PV in environmental aspects of PV power systems, The Netherlands: Utrecht University; 1997.

53) Green Martin A, Ho-Baillie Anita, Snaith Henry J, The emergence of perovskite solar cells, Nat. Photonics. 8 (2014) 506.

54) Snaith Henry J, Perovskites: the emergence of a new era for low-cost, high efficiency solar cells, J Phys Chem Lett 4 (2013) 3623.

55) Du J, Du Z, Hu JS, Pan Z, Shen Q, Sun J, Long D, Dong H, Sun L, Zhong X, Wan L J, Zn–Cu–In–Se quantum dot solar cells with a certified power conversion efficiency of 11.6%, J. Am. Chem. Soc. 138 (2016) 4201.

56) Hall S R, Szymanski J T, Stewart J M, Kesterite, ($Cu_2(Zn, Fe)SnS_4$), and stannite, ($Cu_2(Fe,Zn)SnS_4$), structurally similar but distinct minerals, Can. Mineral. 16.2 (1978) 131.

57) Wallace S K, Mitzi DB, Walsh A, The steady rise of kesterite solar cells, ACS Energy Lett. 2 (2017) 776.

58) Sarker, Pranab, Mowafak M, Al-Jassim, Muhammad N, Huda, Theoretical limits on the stability of single-phase kesterite-Cu_2ZnSnS_4, J. Appl. Phys. 117.3 (2015) 035702.

59) Kumar M, Dubey A, Adhikari N, Venkatesan S, Qiao Q, Strategic review of secondary phases, defects and defect-complexes in kesterite CZTS–Se solar cells, Energy. Environ. Sci. 8 (2015) 3134.

60) Schorr S, Weber A, Honkimäki V, Schock H W, In-situ investigation of the kesterite formation from binary and ternary sulphides, Thin Solid Films. 517 (2009) 2461.

61) Schorr, Susan, Hans-Joachim Hoebler, Michael Tovar, A neutron diffraction study of the stannite-kesterite solid solution series, Eur. J. Mineral. 19.1 (2007) 65.

62) Shockley W, Queisser H J, Detailed balance limit of efficiency of p n junction solar cells, J. Appl. Phys. 32 (1961) 510.

63) Kraus W, Nolze G, POWDER CELL – a program for the representation and manipulation of crystal structures and calculation of the resulting Xray powder patterns, J. Appl. Crystallogr. 29 (1996) 301.

64) Dumcenco D, Huang YS, The vibrational properties study of kesterite Cu_2ZnSnS_4 single crystals by using polarization dependent Raman spectroscopy, Opt. Mater. 35 (2013) 419.

65) Schorr, S, The crystal structure of kesterite type compounds: a neutron and X-ray diffraction study, Sol. Energy Mater. Sol. Cells. 95 (2011) 1482.

66) Persson C, Electronic and optical properties of Cu_2ZnSnS_4 and $Cu_2ZnSnSe_4$, J. Appl. Phys. 107 (2010) 053710.

67) Raulot J M, Domain C, Guillemoles J F, Ab initio investigation of potential indium and gallium free chalcopyrite compounds for photovoltaic application, J. Phys. Chem. Solids. 66 (2005) 2019.

68) Nozaki H, Fukano T, Ohta S, Seno Y, Katagiri H, Jimbo K, Crystal structure determination of solar cell materials: Cu_2ZnSnS_4 thin films using X-ray anomalous dispersion, J. Alloy. Compd. 524 (2012) 22.

69) Siebentritt S, Schorr S, Kesterites - a challenging material for solar cells, Prog. Photovoltaics Res. Appl. 20 (2012) 512.

70) Chen S, Gong X G, Walsh A, Wei S H, Electronic structure and stability of quaternary chalcogenide semiconductors derived from cation cross-substitution of II–VI and I–III–VI2 compounds, Phys. Rev. B 79 (2009) 165211.

71) Stephan Abermann, Non-vacuum processed next generation thin film photovoltaics: Towards marketable efficiency and production of CZTS based solar cells, Sol. Energy. 94 (2013) 37.

72) Dudchak I V, Piskach L V, Phase equilibria in the Cu_2SnSe_3– SnSe–ZnSe system, J. Alloys Compd. 351 (2003) 145.

73) Katagiri H, Jimbo K, Yamada S, Kamimura T, Maw WS, Fukano T, Ito T, Motohiro T, Enhanced conversion efficiencies of Cu_2ZnSnS_4-based thin film solar cells by using preferential etching technique, Appl. Phys. Express. 1 (2008) 041201.

74) Redinger A, Hönes K, Fontané X, Izquierdo-Roca V, Saucedo E, Valle N, Pérez-Rodríguez A, Siebentritt S, Detection of a ZnSe secondary phase in coevaporated $Cu_2ZnSnSe_4$ thin films, Appl. Phys. Lett. 98 (2011) 101907.

75) Berg D M, Djemour R, Gütay L, Zoppi G, Siebentritt S, Dale P J, Thin film solar cells based on the ternary compound Cu_2SnS_3, Thin Solid Films. 520 (2012) 6291.

76) Fontané X, Calvo-Barrio L, Izquierdo-Roca V, Saucedo E, Pérez-Rodriguez A, Morante J R, Berg D M, Dale P J, Siebentritt S, In-depth resolved Raman scattering analysis for the identification of secondary phases: characterization of Cu_2ZnSnS_4 layers for solar cell applications, Appl. Phys. Lett. 98 (2011) 181905.

77) Choubrac L, Lafond A, Guillot-Deudon C, Moëlo Y, Jobic S, Structure flexibility of the Cu_2ZnSnS_4 absorber in low-cost photovoltaic cells: from the stoichiometric to the copper-poor compounds, Inorg. chem. 51 (2012) 3346.

78) Cheng A J, Manno M, Khare A, Leighton C, Campbell S A, Aydil ES, Imaging and phase identification of Cu_2ZnSnS_4 thin films using confocal Raman spectroscopy, J. Vac. Sci. Technol., A. 29 (2011) 051203.

79) Mousel M, Redinger A, Djemour R, Arasimowicz M, Valle N, Dale P, Siebentritt S, HCl and Br_2-MeOH etching of $Cu_2ZnSnSe_4$ polycrystalline absorbers, Thin Solid Films. 535 (2013) 83.

80) Siebentritt S, Why are kesterite solar cells not 20% efficient?, Thin Solid Films. 535 (2013) 1.

81) Nitsche R, Sargent D F, Wild P, Crystal Growth of Quaternary $I_{(2)}$-II-IV-$VI_{(4)}$ Chalcogenides by Iodine Vapor Transport, J. Cryst. Growth. 1 (1967) 52.

82) Ito K, Nakazawa T, Elecrical and optical properties of stannite-type quarternary semiconductor thin films, Jpn. J. Appl. Phys. 27 (1988) 2094.

83) Hironori Katagiri, Nobuyuki Sasaguchi, Shima Hando, Suguru Hoshino, Jiro Ohashi, Takaharu Yokota, Preparation films by and evaluation of Cu_2ZnSnS_4 thin sulfurization of E-B evaporated precursors, Sol. Energy Mater. Sol. Cells 49 (1997) 407.

84) Moholkar A V, Shinde S S, Babar A R, Sim K U, Kwon Y B, Rajpure K Y, Patil P S, Bhosale C H, Kim J H, Development of CZTS thin films solar cells by pulsed laser deposition: influence of pulse repetition rate, Sol. Energy. 85 (2011) 1354.

85) Hironori Katagiri, Kotoe Saitoh, Tsukasa Washio, Hiroyuki Shinohara, Tomomi Kurumadani, hinsuke Miyajima, Development of thin film solar cell based on Cu_2ZnSnS_4 thin flms, Sol. Energy Mater. Sol. Cells 65 (2001) 141.

86) Hironori Katagiri, Kazuo Jimbo, Katsuhiko Monya, Kazuyuki Tsuchida, Solar cell without environmental pollution by using CZTS thin film, 3rd World Conference on Photovoltaic Energy Conversion Osaka. Jopan (2003).

87) Hironori Katagiri, Kazuo Jimbo, Satoru Yamada, Tsuyoshi Kamimura, Win Shwe Maw, Tatsuo kano, Tadashi Ito, and Tomoyoshi Motohiro1, Enhanced Conversion Efficiencies of

Cu_2ZnSnS_4-Based Thin Film Solar Cells by Using Preferential Etching Technique, Appl. Phys. Express. 1 (2008) 041201.

88) Kusano E, Sakamoto M, Control of composition and properties by the use of reflector wall in RF sputter deposition of Cu_2ZnSnS_4 thin films, Thin Solid Films 589 (2015) 433.

89) Lin Y P, Chi Y F, Hsieh T E, Chen Y C, Huang K P, Preparation of Cu_2ZnSnS_4 (CZTS) sputtering target and its application to the fabrication of CZTS thin-film solar cells, J. Alloy. Compd. 654 (2016) 498.

90) Sun R, Zhao M, Zhuang D, Gong Q, Xie M, Ouyang L, Guo L, Zhang L, Effects of selenization on phase transition and S/(S+Se) ratios of as-deposited Cu_2ZnSnS_4 absorbers sputtered by a quaternary target, Mater. Lett. 164 (2016) 140.

91) Ryota N, Kunihiko T, Hisao U, Kazuo J, Tsukasa W, Hironori K, Cu_2ZnSnS_4 thin film deposited by sputtering with Cu2ZnSnS4 compound target, Jpn. J. Appl. Phys. 53 (2014) 02BC10.

92) Wang W, Shen H, Jin J, Li J, Ma Y, Effect of thermal pretreatment of metal precursor on the properties of Cu_2ZnSnS_4 films, Chin. Phys. B 24 (2015) 479.

93) Gang M G, Gurav K V, Shin S W, Hong C W, Min J H, Suryawanshi M P, Vanalakar S A, Lee D S, Kim J H, A 5.1% efficient kesterite Cu_2ZnSnS_4 (CZTS) thin film solar cell prepared using modified sulfurization process, Phys. Status Solidi Curr. Top. Solid State Phys. 12 (2015) 713.

94) Feng Y, Lau TK , Cheng G, Yin L, Li Z, Luo H, Liu Z, Lu X, Yang C, Xiao X, A low-temperature formation path toward highly efficient Se-free Cu_2ZnSnS_4 solar cells fabricated through sputtering and sulfurization, Cryst. Eng. Comm.18 (2016) 1070-7.

95) Tajima S, Itoh T, Hazama H, Ohishi K, Asahi R, Improvement of the open circuit voltage of Cu_2ZnSnS_4 cells using a two-layered process, Proceedings of the 40th IEEE Photovolt. Spec. Conference (PVSC), 40 (2014) 431.

96) Zhuk S, Kushwaha A, Wong T K, Masudy-Panah S, Smirnov A, Dalapati G K, Critical review on sputter-deposited Cu_2ZnSnS_4

(CZTS) based thin film photovoltaic technology focusing on device architecture and absorber quality on the solar cells performance, Sol. Energy Mater. Sol. Cells. 171 (2017) 239.

97) Schubert B A, Marsen B, Cinque S, Unold T, Klenk R, Schorr S, Schock H W, Cu_2ZnSnS_4 thin film solar cells by fast coevaporation, Prog. Photovoltaics Res. Appl. 19 (2011) 93.

98) Repins I, Beall C, Vora N, DeHart C, Kuciauskas D, Dippo P, To B, Mann J, Hsu WC, Goodrich A, Noufi R, Co-evaporated $Cu_2ZnSnSe_4$ films and devices, Sol. Energy Mater. Sol. Cells. 101 (2012) 154.

99) Shin B, Gunawan O, Zhu Y, Bojarczuk NA, Chey S J, Guha S, Thin film solar cell with 8.4% power conversion efficiency using an earth-abundant Cu_2ZnSnS_4 absorber, Prog. Photovolt. Res. Appl. 21(2013)72.

100) Mise T, Tajima S, Fukano T, Higuchi K, Washio T, Jimbo K, Katagiri H, Improving the photovoltaic performance of co evaporated Cu_2ZnSnS_4 thin film solar cells by incorporation of sodium from NaF layers, Prog. Photovoltaics Res. Appl. 24 (2016) 1009.

101) Gao C, Schnabel T, Abzieher T, Ahlswede E, Powalla M, Hetterich M, Preparation of $Cu_2ZnSnSe_4$ solar cells by low-temperature co-evaporation and following selenization, Appl. Phys. Lett. 108 (2016) 013901.

102) Nandur A, White B, Growth of Cu_2ZnSnS_4 (CZTS) by Pulsed Laser Deposition for Thin film Photovoltaic Absorber Material, Bull. Am. Phys. Soc. 59 (2014) 24.

103) Vanalakar S A, Agawane G L, Shin S W, Suryawanshi M P, Gurav K V, Jeon K S, Patil P S, Jeong C W, Kim J Y, Kim J H, A review on pulsed laser deposited CZTS thin films for solar cell applications, J. Alloys Compd. 619 (2015) 109.

104) Vanalakar S A, Shin S W, Agawane G L, Suryawanshi M P, Gurav K V, Patil P S, Kim J H, Effect of post-annealing atmosphere on the grain-size and surface morphological properties of pulsed laser deposited CZTS thin films, Ceram. Int. 40 (2014) 15097.

105) Moholkar A V, Shinde S S, Agawane G L, Jo S H, Rajpure K Y, Patil P S, Bhosale C H, Kim J H, Studies of compositional dependent

CZTS thin film solar cells by pulsed laser deposition technique: An attempt to improve the efficiency, J. Alloys Compd. 544 (2012) 145.

106) Byeon M, Bae J S, Hong T E, Jeong E D, Kim S, Kim Y, Effect of the Deposition Time onto Structural Properties of Cu_2ZnSnS_4 Thin Films Deposited by Pulsed Laser Deposition, Korean J. Mater. Res. 23 (2013) 7.

107) Wozny S, Wang K, Zhou W, Cu_2ZnSnS_4 nanoplate arrays synthesized by pulsed laser deposition with high catalytic activity as counter electrodes for dye-sensitized solar cell applications, J. Mater. Chem. A. 1 (2013) 15517.

108) Tanaka K, Moritake N, Oonuki M, Uchiki H, Pre-annealing of precursors of Cu_2ZnSnS_4 thin films prepared by sol–gel sulfurizing method, Jpn. J. Appl. Phys. 47 (2008) 598.

109) Tanaka K, Moritake N, Oonuki M, Uchiki H, Preparation of Cu_2ZnSnS_4 thin films by sulfurizing sol–gel deposited precursors, Sol. Energy Mater. Sol. Cells. 91 (2007) 1199.

110) Chaudhuri T K, Tiwari D, Earth-abundant non-toxic Cu_2ZnSnS_4 thin films by direct liquid coating from metal–thiourea precursor solution, Sol. Energy Mater. Sol. Cells. 101 (2012) 46.

111) Sun Y, Zong K, Zheng H, Wang H, Liu J, Yan H, Zhu M, Ethylene glycol-based dip coating route for the synthesis of Cu_2ZnSnS_4 thin film, Mater. Lett. 92 (2013)195.

112) Aslan F, Göktaş A, Tumbul A, Influence of pH on structural, optical and electrical properties of solution processed Cu_2ZnSnS_4 thin film absorbers, Mater. Sci. Semicond. Process, 43 (2016) 139.

113) Patel K, Kheraj V, Shah D V, Panchal C J, Dhere N G, Cu_2ZnSnS_4 thin-films grown by dip-coating: Effects of annealing, J. Alloys. Compd. 663 (2016) 842.

114) Ge J, Chu J, Jiang J, Yan Y, Yang P, Characteristics of In-Substituted CZTS Thin Film and Bifacial Solar Cell, ACS Appl. Mater. Interfaces. 6 (2014) 21118.

115) Nakayama N, Ito K, Sprayed films of stannite Cu_2ZnSnS_4, Appl. Surf. Sci. 92 (1996) 171.

116) Rodriguez M E, Sylla D, Sanchez Y, López-Marino S, Fontané X, López-García J, Placidi M, Pérez-Rodríguez A, Saucedo E, Pneumatically sprayed Cu_2ZnSnS_4 films under Ar and Ar–H_2 atmosphere, J. Phys. D: Appl. Phys. 47 (2014) 245101.

117) Aono M, Yoshitake K, Miyazaki H, XPS depth profile study of CZTS thin films prepared by spray pyrolysis, Phys. Status Solidi C. 10 (2013) 1058.

118) Kumar Y B, Bhaskar P U, Babu G S, Raja V S, Effect of copper salt and thiourea concentrations on the formation of Cu_2ZnSnS_4, Thin films by spray pyrolysis, Phys. Status Solidi A, 207 (2010) 149.

119) Rajeshmon V G, Kartha C S, Vijayakumar K P, Sanjeeviraja C, Abe T, Kashiwaba Y, Role of precursor solution in controlling the opto-electronic properties of spray pyrolysed Cu_2ZnSnS_4 thin films, Sol. Energy, 85 (2011) 249.

120) Zeng X, Tai K F, Zhang T, Ho CW, Chen X, Huan A, Sum T C, Wong L H, $Cu_2ZnSn(S,Se)_4$, Kesterite solar cell with 5.1% efficiency using spray pyrolysis of aqueous precursor solution followed by selenization, Sol. Energy Mater. Sol. Cells. 124 (2014) 55.

121) Ki W, Hillhouse H W, Earth abundant element photovoltaics directly from soluble precursors with high yield using a non toxic solvent, Adv. Energy Mater., 1 (2011) 732.

122) Patel M, Mukhopadhyay I, Ray A, Structural, optical and electrical properties of spray-deposited CZTS thin films under a non-equilibrium growth condition, J. Phys. D: Appl. Phys. 45 (2012) 445103.

123) Tanaka K, Kato M, Goto K, Nakano Y, Uchiki H, Face-to-face annealing process of Cu_2ZnSnS_4 thin films deposited by spray pyrolysis method, Jpn. J. Appl. Phys. 51 (2012) 10NC26.

124) Nguyen T H, Harada T, Nakanishi S, Ikeda S, Cu_2ZnSnS_4 -based thin film solar cells with more than 8% conversion efficiency obtained by using a spray pyrolysis technique, Photovoltaic Specialists Conference (PVSC), IEEE (2016) 0470.

125) Zhou Z, Wang Y, Xu D, Zhang Y, Fabrication of Cu_2ZnSnS_4 screen printed layers for solar cells, Sol. Energy Mater. Sol. Cells. 94 (2010) 2042.

126) Kermadi S, Sali S, Ameur F A, Zougar L, Boumaour M, Toumiat A, Melnik N N, Hewak D W, Duta A, Effect of copper content and sulfurization process on optical, structural and electrical properties of ultrasonic spray pyrolysed Cu_2ZnSnS_4 thin films. Mater, Chem. Phys. 169 (2016) 96.

127) Araki H, Kubo Y, Mikaduki A, Jimbo K, Maw WS, Katagiri H, Yamazaki M, Oishi K, Takeuchi A, Preparation of Cu_2ZnSnS_4 thin films by sulfurizing electroplated precursors, Sol. Energy Mater. Sol. Cells. 93 (2009) 996.

128) Sarswat P K, Free M L, Tiwari A, Temperature dependent study of the Raman A mode of Cu_2ZnSnS_4 thin films, Phys. Status Solidi B. 248 (2011) 2170.

129) Pawar B S, Pawar S M, Shin S W, Choi D S, Park C J, Kolekar S S, Kim J H, Effect of complexing agent on the properties of electrochemically deposited Cu_2ZnSnS_4 (CZTS) thin films, Appl. Surf. Sci. 257 (2010) 1786.

130) Ramasamy K, Malik M A, O'Brien P, Routes to copper zinc tin sulfide Cu_2ZnSnS_4 a potential material for solar cells, Chem. commun. 48 (2012) 5703.

131) Guo Q, Ford G M, Yang W C, Walker B C, Stach E A, Hillhouse H W, Agrawal R, Fabrication of 7.2% efficient CZTSSe solar cells using CZTS nanocrystals, J. Am. Chem. Soc. 132 (2010) 17384.

132) Guo Q, Hillhouse H W, Agrawal R, Synthesis of Cu_2ZnSnS_4 nanocrystal ink and its use for solar cells, J. Am. Chem. Soc. 131 (2009) 11672.

133) Kameyama T, Osaki T, Okazaki K I, Shibayama T, Kudo A, Kuwabata S, Torimoto T, Preparation and photoelectrochemical properties of densely immobilized Cu_2ZnSnS_4 nanoparticle films, J. Mater. Chem. 20 (2010) 5319.

Chapter 2
Thin film deposition and characterization techniques

This chapter describes coating techniques used for fabricating CZTS absorber thin films along with the characterization techniques used for studying their structural, surface morphological, optical and electrical properties. In addition to this, this chapter explains the preparation details of other layers used for prototype solar cell fabrication. CZTS solar cell was constructed by adopting standard device structure used for fabricating Copper Indium Gallium Selenide (CIGS) based solar cell; and its photovoltaic properties were studied under standard photovoltaic test conditions.

2.1 Methods for thin film coating

There are different techniques available for fabricating thin films. All those techniques are broadly categorised into two groups: vacuum based and non-vacuum based techniques. There are advantages and disadvantages to both techniques. Among the available routes, non-vacuum techniques are considered to be cheap and are relatively easy to scale up [1-8].

2.1.1 Vacuum based techniques

Majority of the thin film technologies are developed on the basis of vacuum based techniques [1,3,7,9-11]. Major vacuum based techniques are sputtering, thermal evaporation, chemical vapour deposition (CVD), pulsed laser deposition (PLD), etc. These routes

require vacuum in the range 10^{-3} to 10^{-8} Torr. In the present study, sputtering technique was used for depositing top layer, aluminium doped zinc oxide (AZO).

2.1.1.1 Sputtering

In sputtering, target material is bombarded with high energetic particle to eject atoms onto the substrate on which film has to be coated. Main process involved is the momentum exchange between particles and electrons [12,13]. Generally, a voltage is applied between target material and substrate. Sputtering can be classified into two categories based on the power source used on this technique: direct current (DC) and radio frequency (RF) sputtering techniques. DC sputtering uses DC voltage, whereas AC voltage is used in RF sputtering. Conducting metal targets can only be used in DC sputtering, however both conducting and non-conducting targets can be used in RF sputtering [14-17].

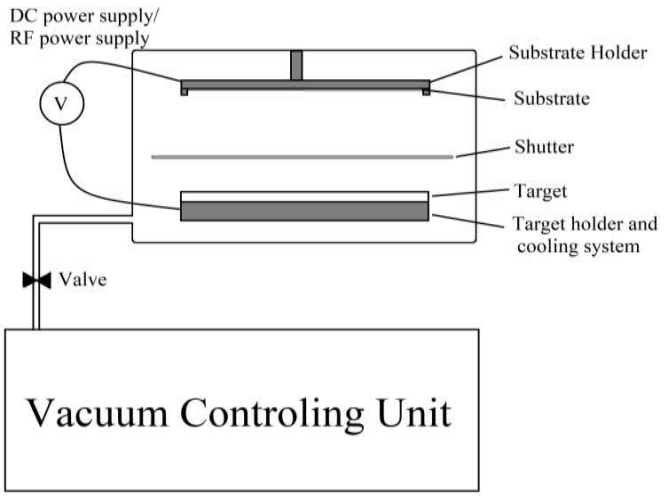

Fig. 2.1 Schematic diagram indicating sputtering unit

Fig. 2.1 shows a sputtering unit in which substrates to be coated are placed in a vacuum chamber containing an inert gas, usually Argon, and a negative electric charge is placed on the target material to be deposited causing plasma in the chamber to glow. Atoms are "sputtered off" the target by collisions with Argon gas atoms, carrying these particles across the vacuum chamber and are deposited as thin film on the substrate. In DC and RF sputtering routes, efficiency of ionization from energetic collisions between electrons and gas atoms is low.

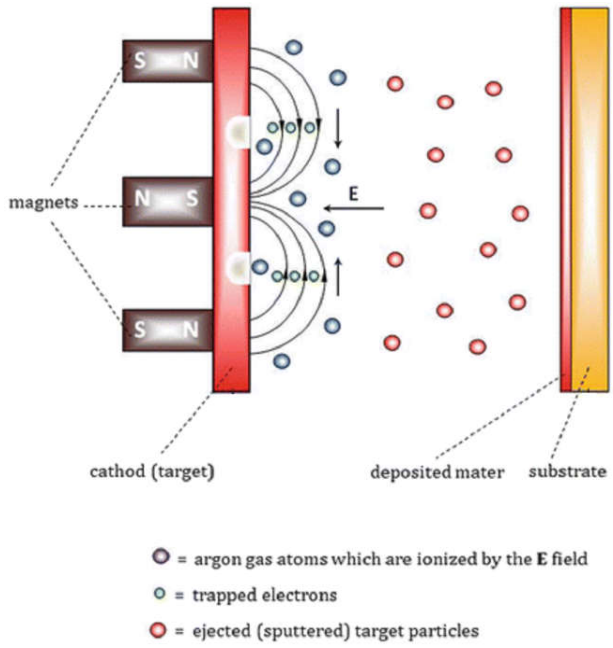

Fig. 2.2 Magnetron sputtering system [18]

In normal sputtering, ions are produced far away from the target and they are easily lost to chamber wall due to the larger mean free path of electrons at low gas pressure with a glow discharge.

Similarly, primary electrons may reach the anode without producing gas ionization. Hence the overall ionization efficiency becomes low and deposition rate also comes down. In order to increase the ionization efficiency, magnetron design was later introduced [19].

In order to enhance deposition rates, magnets are used to increase the percentage of electrons that take part in ionization events. In magnetron sputtering, a magnetic field is applied at right angles to the electric field by placing large magnets behind the target material, so that the cathode surface is immersed in magnetic field and thus electron traps are created. This cause ionization in the vicinity of the cathode, which further increase the sputtering yield. Magnetron sputtering can be done in DC or RF, but more often it is done in DC as cooling of insulating targets is difficult in RF systems [18,19].

The advantages of sputtering technique are [18],

- A wide variety of materials, such as metals, insulators, alloys, composites can be deposited.
- Replication of target composition in the films coated.
- Better film quality and step coverage.
- Reproducibility
- Possibility to deposit over large area.

However, there are a few disadvantages also,

- High energy ion bombardment or UV generated by plasma may damage substrate.
- Ultra clean gases and targets are required to avoid contamination.
- Deposition rate depends on material type.
- Heating due to ion bombardment may damage the target

Different methods of sputtering are widely used, including ion beam and ion-assisted sputtering, reactive sputtering, co-sputtering etc. [19-23]. In the present work, RF magnetron sputtering system (Hind High Vacuum, Bangalore) was used for coating top electrode, aluminium doped ZnO, in the prototype solar cell fabricated. ZnO target with 2wt% Al was used for sputtering.

2.1.2. Solution based techniques

Solution based routes are simple and cost effective compared to vacuum based techniques. In the case of CZTS, material coating solution based techniques shows better performance than vacuum based techniques. Solution based methods provide better mixing and distribution of elements at molecular level, which enable precise control of stoichiometry at molecular level [24]. The advantages of solution based techniques over vacuum based techniques are 1) it is simple and cost effective 2) it requires low energy consumption 3) it is

appropriate for large area coatings, etc [25,26]. CZTS thin films have been successfully deposited by various chemical based techniques [26,27]. The highest conversion efficiency of 12.6% was reported for solution processed solar cells by Wang et al. [27] for their CZTSSe absorber layer prepared by spin coating using hydrazine as a solvent.

In general, solution based techniques for CZTS involves four basic steps,

- Preparation of stable and homogenous precursor solution.
- Thin film coating on to substrates using solutions, with desired coating route.
- Heat treatment of films to evaporate solvents of other volatile constituents.
- Final annealing at suitable atmosphere to complete phase formation and to improve crystallinity

There are different types of coating techniques are currently available. Spin coating, dip coating and spray coating techniques were used for the present work to coat CZTS absorber films.

2.1.2.1 Dip coating technique

Dip coating is the simple and cost effective technique with feasibility for large area manufacturing [28]. In dip coating process, the substrate to be coated is immersed in a precursor solution where a wet layer is formed and then it is withdrawn at a well defined velocity.

Dipping speed, withdrawal speed, solution concentration, dipping delay and drying temperature are the parameters generally influence the final film properties. Schematic diagram describing dip coating process is shown in Fig. 2.3, along with the image of the dip coater used for the present study.

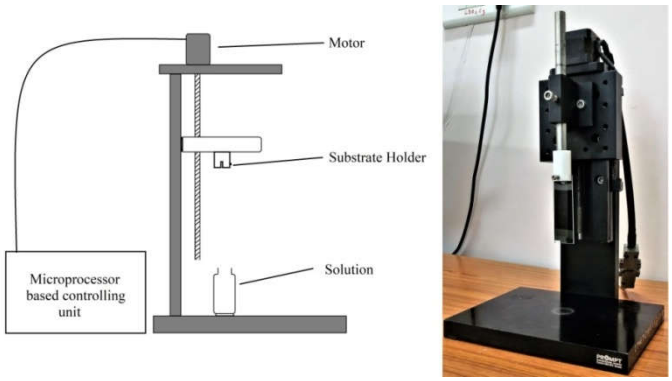

Fig. 2.3 Schematic diagram of the dip coater and image of the unit

The first patent based on this process was issued to Jenaer Glaswerk Schott and Gen. in 1939 for coating silica films [29]. The process of a liquid film deposition onto a solid surface has enormous practical significance, especially in applications such as protective coatings, adhesives, photographic films, and microelectronics [30-32].

Process of dip coating can be broadly separated into four important technical stages [29-32]. Fig. 2.4 shows the process steps involved in dip coating.

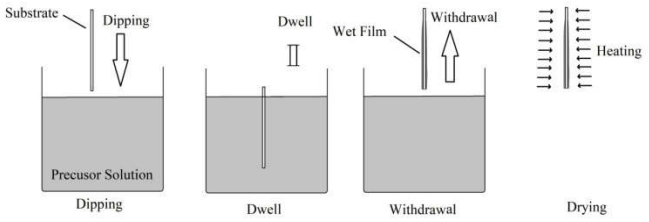

Fig. 2.4 Major four stages in dip coating process

Immersion speed: The substrate is immersed into the precursor solution at a constant speed. If substrate is immersed very fast, air bubbles will be formed in the precursor solution and affect the film quality.

Dwell time: Substrates immersed in solution for long time get sufficient time for complete wetting with the coating solution.

Withdraw speed: The next process is to pull the substrate upward at a constant speed. Thin layer of precursor solution is coated and drain the excess liquid from the surface. In some cases, thickness of the film directly depends on withdrawal speed.

Evaporation: Thin film is formed after solvent evaporation. For evaporation, wet film is subjected to heat treatment in furnace or oven. Drying temperature greatly influence the final film properties. Evaporation of organic residuals and crystallization of films occur in this stage.

The dip coating process can be repeated several times to increase film thickness. Dip coating is one of the simplest thin film processing techniques. This technique coats films on both sides of

substrate. However, it has disadvantages too [31,32]. The main disadvantage is the thickness variation from one end to other end due to gravity effect.

2.1.2.2 Spin coating technique

Spin coating is a widely used thin film coating technique to deposit film over a flat surface. In spin coating process, substrate spins around an axis, which is perpendicular to the coating area [33]. A typical process involves depositing a small amount of a fluid material onto the centre of a substrate and then spinning the substrate at high speed (typically around 3000-5000 rpm). The flow of the liquid is governed by a balance between centrifugal driving force and viscous resisting force [32,34,35]. Centripetal acceleration will cause most of the solution to spread to, and eventually off, the edge of the substrate, leaving a thin film of material on the surface. Final film thickness and other properties depend on the nature of the fluid material (viscosity, drying rate, concentration of solids, surface tension, etc.) along with the parameters, such as spinning speed, spinning time, etc chosen for the spin process. Factors such as final rotation speed, acceleration and fume exhaust affect properties of the coated films [35,36]. One of the most important advantages of spin coating is repeatability; suitable variations in the parameters that define spin coating can result in drastic variations in the coated film and its properties.

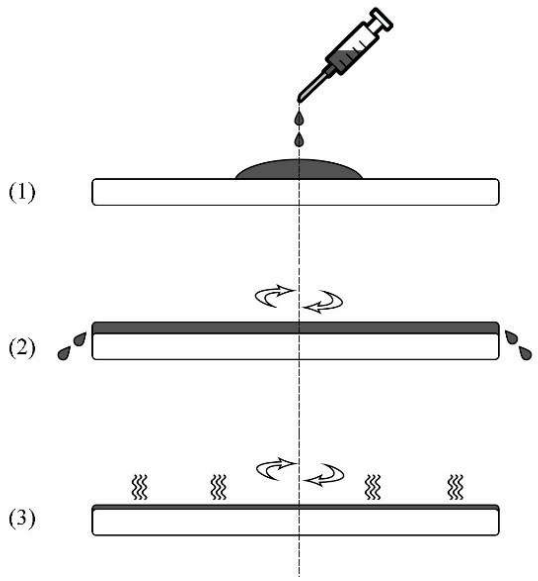

Fig. 2.5 Various steps in spin coating process [28]

Fig. 2.5 shows important steps involved in the spin coating process [15,28,35,36], as described below.

Solution dispensing

Solution dispensing is one of the important steps in spin coating process. Two types of dispensing techniques are generally used for this purpose; static and dynamic. In static dispense, a small puddle of fluid is placed on or near the centre of substrate. This can range from 1 to 10 cc depending on the viscosity of the fluid and the size of the substrate to be coated. Higher viscosity of fluid or bigger substrates typically requires larger puddle to ensure full coverage on the substrate during high speed spin step. Dynamic dispense is the process of dispensing fluid while substrate is rotating at low speed. This serves to spread the fluid over the substrate and can result in less waste of resin material.

Spinning of substrate

After dispense step, it is accelerated to a higher speed to thin the fluid to near its desired thickness. Typical spin speeds range from 3000-5000 rpm, depending on the properties of the fluid as well as the substrate. Spinning time is an important parameter in the coating process. This step can take from 10 seconds to several minutes. The combination of spinning speed and time selected for this step will generally define the final film thickness. In general, higher spin speeds and longer spin times create thinner films.

In general, thickness of spin coated film is inversely proportional to the square root of the spinning speed, as given in equation 2.1 below, where t is the thickness and ω is the angular velocity [15].

$$t \propto \frac{1}{\sqrt{\omega}} \quad \ldots\ldots\ldots\ldots (2.1)$$

This equation indicates that the thickness of the film will become half if it is spin coated at four times speed. The exact thickness of the film formed will depend on material concentration and solvent evaporation rate.

Drying (Solvent evaporation)

A drying step is optional and added after high speed spin step to dry the coated film without substantially thinning it. This is advantageous for thick films, in this case long drying times may be required to increase the physical stability of the film. In certain cases, hotplates are used for thin film drying.

Fig. 2.6 Spin coater (Chemat KW4) used for the present study along with hot plate

For the present work, Chemat Technology KW-4A spin coater is used. KW-4A is compact and easy to use spin coater for precise and uniform deposition of thin films and coatings. Fig.2.6 represents the spin coater and hotplate used in this work.

The disadvantages of spin coating techniques are [15,32,37]:

1) Only a single film can be coated at a time; relatively low throughput compared to roll-to-roll processes.
2) Fast drying time can lead to lower performance for certain applications in nanotechnology.
3) Material used is typically very low, ~10% or less; the remaining is wasted.

However, spin coating is considered as starting point and benchmark for most academic and industrial processes requiring thin and uniform coatings.

2.1.2.3 Spray coating technique

Compared to spin and dip coating techniques, spray coating is a promising route used in research and industry to fabricate thin films. In spray coating, precursor solution is sprayed on to a heated substrate to evaporate off volatile by-products and excess solvents. Fig. 2.7 shows schematic diagram of spray coating setup used for the present study. The main components in spray coating unit are spray nozzle, movement head, hot plate with temperature controller, flow meter and carrier gas.

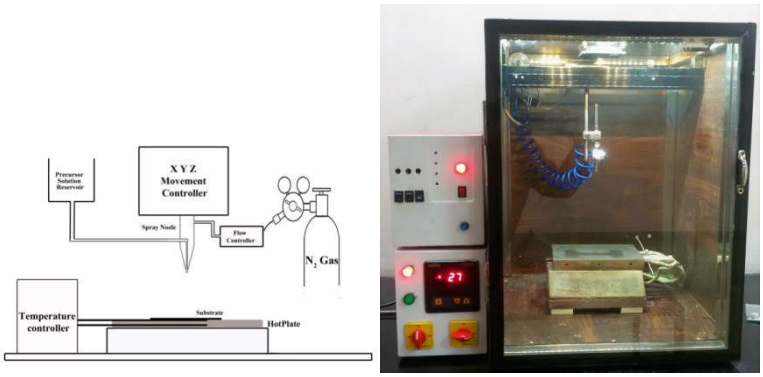

Fig. 2.7 Schematic diagram of spray coater and image of the spray coating unit used for the study

Substrate temperature determines film morphology and properties of coated film [38]. Film morphology changes from cracked to porous microstructure with increase in temperature. Solution used for spray pyrolysis has major role in the film formation. Solutions, colloidal dispersions, emulsions and sols are used as precursors in spray coating. Morphology of thin films can be changed considerably by adding additives to precursor solutions [39]. Solution pH, solution concentration, solvent type, etc., are also influencing the film

properties [40]. Aqueous solutions of desired materials are normally used due to its ease of handling. Metal chlorides and oxy-chlorides have better water solubility and hence widely used for industrial production. [41].

In spray coating, atomization is used to produce uniform and fine droplets by thermal decomposition [39,40]. This is a critical operation in this process. Air blast (liquid is exposed to a stream of air) [42], ultrasonic (ultrasonic frequencies produce short wavelengths necessary for fine atomization), [43]and electrostatic (liquid is exposed to high electric field) [44] are usually adopted in spray coating as atomizers. These atomizers differ in droplet size, rate of atomization and droplet velocity. The velocity of the droplet when it leaves atomizer is important. The charecteristics of the droplet from an atomizer depends on solution density, viscosity and surface tension [38-40].

The quality of film also depends on the inlet gas pressure used to guide the solution from the nozzle. When gas pressure is more, smaller droplets are likely to be formed. However, this may drop the substrate temperature due to rapid splashing of smaller droplets. On the other hand, larger droplets fall onto the substrates, if gas pressure is too small. This indicates that optimatisation of the gas flow is necessary in this process.

Thin film deposition by spray coating includes mainly three processes:

- Atomization of precursor solution.
- Aerosol transport of droplet.
- Decomposition of precursor

Precursor solution gets atomized through the nozzle and forms small droplets known as aerosols. These aerosols are allowed to incident on preheated substrate and form thin film through pyrolytic decomposition. During this transportation, the droplet is generally experienced by gravitational force, stokes force, thermophoretic force and electrical force [38-40]. These four forces control the trajectory of solution droplet. As it moves through the heated ambient, the precursor undergoes various changes such as evaporation, precipitate formation and vaporization, depending on the droplet size and ambient temperature. For better dense films, solvent has to be evaporated before it reaches the substrate [45].

The main advantages of spray coating are:

- Simple and cost effective
- Capability to produce uniform films over large area
- No need of high quality targets or vacuum
- Can be operated over moderate temperatures

2.1.2.4 Chemical bath deposition (CBD)

Chemical bath deposition is another simplest solution based technique used for coating thin films having thickness in the range of nanometres, with good surface coverage. Due to this advantage,

chemical bath deposition technique is widely used for solar cell application [46]. The requirements for this technique are (i) a vessel containing solution, (ii) stirring mechanism, (iii) heating mechanism with thermostat and (iv) suitable substrate on which deposition is to be carried out. In 1835, Liebig used CBD technique for coating silver on glass substrate to make mirrors [47]. Fig. 2.8 presents schematic diagram of the set up used for chemical bath deposition.

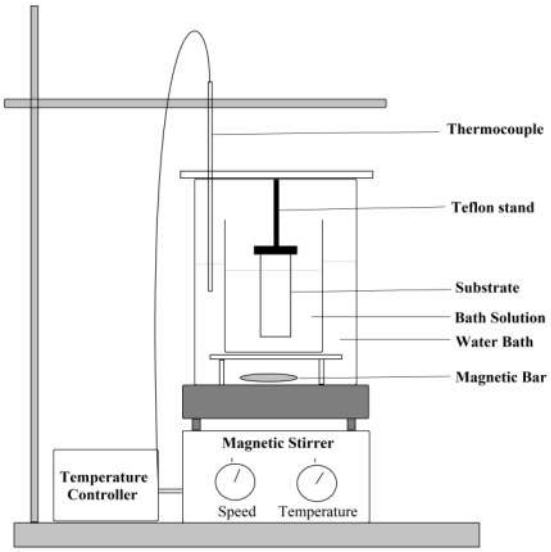

Fig. 2.8 Schematic diagram of chemical bath deposition technique

The basic principle in chemical bath deposition technique is controlled precipitation of the desired compound from a solution of its constituents [39,47-49]. Generally, three stages are involved in chemical bath deposition,

1. Creation of atomic/molecular/ionic species in the solution

2. Transport of the species through the solution

3. Condensation of the species

Thin film is coated on substrates by ion-ion condensation [50]. For this, the ionic product of anions and cations must exceed their solubility product. The solubility product of the compound plays an important role in thin film deposition. Various properties such as stoichiometry, homogeneity and adhesiveness are mainly dependent upon the solubility product [51]. The details of ionic product (IP) and solubility product (SP) are described below.

When a sparingly soluble salt AB is added to water, some of it dissolves to form a solution containing A^+ and B^- ions along with un-dissolved solid 'AB' is obtained, establishing an equilibrium between the solid phase and a solution of its ions as;

$$AB_{(s)} \leftrightarrow A^+_{(sol)} + B^-_{(sol)} \qquad \text{----- (2.2)}$$

Applying law of mass action [50,51], we get

$$K = {(a_{A^+} \times a_{B^-})}/{a_{AB}} \qquad \text{----- (2.3)}$$

Where, a_{A+}, a_{B-} and a_{AB} are activities of A^+, B^- and un-dissolved AB in the solution, respectively. The mean-activity coefficient of ions (*C*) are considered to be unity due to low concentrations, and therefore,

$$K = {(C_{A^+} \times C_{B^-})}/{C_{AB}} \quad \text{----- (2.4)}$$

However, the concentration of pure solid is constant and taken as K'. Therefore, the above equation can be written as;

$$C_{A+} \times C_{B-} = K.K' = K_{sp} \quad \text{-----(2.5)}$$

Both K and K' are constant, and hence the product of K.K' is also a constant and known as solubility product. The product $C_{A+} \times C_{B-}$ is called ionic product. The solution becomes saturated when the ionic product is equal to the solubility product (IP=SP). Solution become supersaturated when ionic product exceeds solubility product (IP/SP = S>1, where S is the degree of supersaturation. In this condition, ions in the solution combine on the surface of the substrates and form thin film on it. There major factors, temperature, solvent and particle size, affect the solubility product [47-49].

Typically, chemical bath deposition solution contains one or more metal salts; a chalcogenide source and a complexing agent. Complexing agents are required to slow down the rate of solid formation. The complexation provides required small metal cation concentration to produce controlled homogenous precipitation on substrate. Thin film formation proceeds through various reaction steps at the substrate surface [52]. Nucleation takes place on substrate surface initially. A particle already deposited on the substrate, or adsorbed cation, anion or particle on substrate surface in contact with reaction mixture can act as nucleation centres. Once the layer of

material is formed, further growth takes place by adsorbing more and more ions from the solution giving uniform and continuous film [52]. However, as deposition proceeds, the concentration of ions decreases, and hence the growth rate decreases.

In the present study, CBD was used to coat ZnS thin film on the SLG/Mo/CZTS solar cell device structure. ZnS layer act as buffer layer in thin film solar cell. As mentioned earlier, CBD gives complete surface coverage with minimum thickness, which is essentially required for the buffer layer. Fig. 2.9 shows the chemical bath deposition system used for ZnS thin films in the present work. Teflon holder and glass vessels were used for setting up chemical bath deposition coating system.

Fig. 2.9 Chemical bath deposition system used the present study

2.2. Characterization techniques

2.2.1 X-ray diffractometer (XRD)

X-ray diffraction is a powerful technique to analyse the crystal structure of a material. It is a fingerprint tool to identify materials and its phase purity. X-ray diffraction technique was used in the present study to confirm phase purity of the CZTS thin films [53]. Electromagnetic radiation of wavelength λ incident on a crystalline solid will be diffracted by the crystallographic planes in periodic lattice structure. X-rays are commonly used for diffraction because its wavelength is comparable to the inter-planar spacing of crystals. X-ray diffraction equipments normally use wavelengths such as, CuKα (λ- 1.54056Å, MoKα (λ- 0.7093Å), etc.

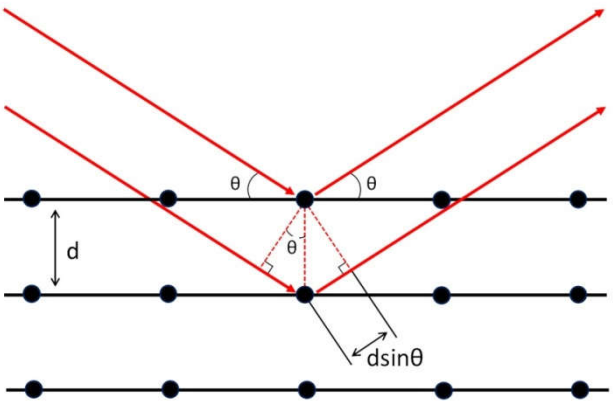

Fig. 2.10 Schematic diagram describing diffraction in crystals

If the crystallites are placed in the path of X-ray beam, diffraction will occur from the planes in the crystallites, which are oriented at the correct angle to fulfil a condition known as Bragg's law

[53]. Fig. 2.10 shows the schematic diagram of interaction between two x-rays with repeating planes of atoms. θ is the angle of incidence and *d* is the inter-planar spacing of crystal. Braggs diffraction criteria for obtaining diffraction pattern is,

$$2d\sin\theta = n\lambda \quad \text{---- (2.6)}$$

Where *n* is an integer representing order of diffraction, λ is the incident x-ray wavelength. X-ray diffraction analysis provides a diffraction pattern that shows constructive interference peaks from different crystal planes in the form of graph. Each characteristic peaks in the diffraction pattern can be correlated with set of planes in crystal lattice [54].

X-ray techniques are generally used for bulk samples. Thin films can also be characterized by this technique. However, grazing (glancing) incidence x-ray diffraction (GI-XRD) is good technique for thin film sample analysis due to its higher penetration depth. GI-XRD records XRD pattern of film with minimum contribution from the substrate by varying the grazing angle [53]. In GI-XRD, x-ray penetration depth is limited to 10-100Å for grazing angle < 5°. Penetration depth of a sample can be determined by using the relation [53]

$$D = \left(\frac{\sin\propto}{\mu}\right) \quad \text{----- (2.7)}$$

Where μ is the linear mass absorption coefficient of the material being analysed and α is the angle of incident (grazing angle).

To confirm phase purity, *d* values obtained from the diffraction pattern are compared with standard ICDD (International Centre for Diffraction Data) pattern of the material. In the present study, normal X-ray diffractometers (Rigaku Miniflex 600, Japan and Bruker D5005, Germany) and GI-XRD (Bruker D8 Advanced, Germany) were used.

Apart from phase formation and crystal structure studies, XRD pattern can also be used to calculate average crystallite size, lattice parameter, strain on the film, dislocation density etc. [53]

The average crystallite size is calculated using Scherrer's formula [53],

$$\boldsymbol{D_{hkl} = \frac{k\lambda}{\beta cos\theta}} \quad \text{----- (2.8)}$$

Where k is the constant depending on crystallite shape, usually taken as 0.9, λ is the wave length of x-rays, β is the full width half maximum (FWHM) and θ is the Bragg angle. Lattice constants (*a*, *b*, *c*) can be estimated from the *d* values obtained from XRD pattern, using standard formula of the *crystal system*. Cu_2ZnSnS_4, the material studied in this work, possesses tetragonal structure ($a \neq b=c$) and hence the lattice constants were calculated using the equation,

$$\frac{1}{d^2} = \frac{h^2+k^2}{a^2} + \frac{l^2}{c^2} \quad \text{----- (2.9)}$$

Where *h, k* and *l* are the miller indices. Lattice parameter *a* and *c* can be calculated by solving the above.

Broadening of peaks in XRD pattern depends not only on the size of crystallites but on strain of lattice also [53]. In this case,

average crystallite size obtained using Scherrer's may be incorrect. However, Williamson-Hall method considers the broadening of peak due to strain also [55,56]. The method is more effective to estimate average crystallite size [57,58]. This method is attributed to G K Williamson and his student, W H Hall. According to their principle, broadenings due to size (β_D) and strain (β_e) vary quite differently with respect to the Bragg angle, θ;

$$\beta_D = K\lambda/Dcos\theta \quad \text{----- (2.10)}$$

$$\beta_e = 4\varepsilon tan\theta \quad \text{----- (2.11)}$$

Where, ε is the induced strain

Total broadening due to strain and size is [56]

$$\beta_{tot} = \beta_D + \beta_e = K\lambda/Dcos\theta + 4\varepsilon tan\theta \quad \text{----- (2.12)}$$

by multiplying with cosθ .

$$\beta_{tot}cos\theta = K\lambda/D + 4\varepsilon sin\,\theta \quad \text{----- (2.13)}$$

The crystallite size and strain on the film can be calculated by plotting 4sinθ and βcosθ along the x and y axes, respectively. From the linear fit to the data, crystallite size can be estimated from the y intercept; strain (ε) is obtained from the slope of the fit [56].

2.2.2. Rietveld refinement using GSAS software

Most of the novel materials are prepared as polycrystalline nature due to the difficulty in preparing their single crystal materials. Understanding the structural properties of polycrystalline samples are important because of the correlation with its electrical, optical and magnetic properties. After its discovery, x-ray diffraction is used for the identification of crystal phase and calculation of lattice parameter. In 1969, Hugo Rietveld [59,60] introduced novel idea for extracting structural information from neutron diffraction data. This technique was later extended to structural studies using high resolution x-ray diffraction data. Rietveld refinement is fundamentally a structural refinement process and is not a structural solution technique [61-66]. Information such as, bonding angle, atom position, accurate lattice parameter, thermal parameters, occupancies, etc., can be extracted using this refinement analysis [59,60,62-66].

For structural refinement, a wide variety of licenced and free software are available. Full proof [67], Rietan [68], Topas [69], JANA [70], GSAS/EXPGUI [59,60] etc. are a few examples. In this work, EXPGUI, the graphical user interface version of General Structure Analysis System (GSAS) is used for the structural refinement [59,60]. The main requirement for the refinement is high resolution x-ray diffraction data and standard crystallographic information file (CIF). In Rietveld refinement procedure, all structural parameters such as, atomic positions, scale factor, lattice parameters, occupancy, preferred orientation correction, isotropic atomic displacement parameters, peak

width and shape functions were refined until the goodness of fit (χ^2) becomes an acceptable value (ideally, 1), or a good fit between observed and calculated x-ray diffraction pattern is observed [63-66]. In the refinement, pseudo-Voigt profile shape was assumed [63-66, 71],

$$\chi^2 = \sum \frac{(\sigma_{ip}^2 - \sigma_{ib}^2)^{-1} \times (y_{io} - y_{ic})^2}{(N-P)} \quad \text{----- (2.14)}$$

Where, σ_{ip} is the standard deviation associated with peak, σ_{ib} is the standard deviation associated with background intensity, y_{io} is the observed intensity, y_{ib} is the background intensity, y_{ic} is the calculated intensity, N is the total number of observations and P is the number of variables in least square refinement.

y_{ic} can be calculated using the equation,

$$y_{ic} = S \sum_j M_j PL_j \left|F_j\right|^2 G(\Delta\theta_{ij}) + y_{ib} \quad \text{----- (2.15)}$$

Where, M_j is multiplicity factor, PL_j is Lorentz polarization factor, F_j is structure factor, S is scale factor, G is reflection factor and $\Delta\theta_{ij}$ is calculated position of Bragg peak. After refinement process, the structural informations were extracted by running the program DISAGL in GSAS software [59,60]. The main disadvantage of this technique is the lack of availability of CIF file. However, crystallographic files are available for CZTS system.

2.2.3 Raman spectroscopy

Major secondary phases observed along with the formation of CZTS are ZnS and Cu_2SnS_3 [72]. X-ray diffraction patterns of these secondary phases overlap with that of CZTS. Hence identifying the presence of these impurities by XRD technique is difficult. However, Raman spectroscopy is a power tool route to analyse phase purity of CZTS films [73-76].

Raman spectroscopy involves inelastic scattering of light with matter [77,78]. It is used to study vibrational, rotational and other low-frequency modes in a system [77,78]. When electromagnetic radiation interacts with an atom, the electric field of the radiation displaces the electron and positively charged nucleus in opposite directions. This is known as polarization, and hence the atom has an induced dipole moment.

The polarization, P, is

$$P = \propto_0 E_0 \cos 2\pi \upsilon_0 t + \frac{1}{2}\left(\frac{\partial \propto}{\partial Q}\right) Q_0 E_0 [\cos 2\pi(\upsilon_0 + \upsilon_m)t + \cos 2\pi(\upsilon_0 - \upsilon_m)t] \quad \text{------ (2.16)}$$

Where α is the polarizability, Q is the normal coordinate associated with a particular mode of vibration frequency υ_m of the molecule and E is the applied electric field.

The polarization thus induced contains the three distinct frequency components [77-79];

$\upsilon=\upsilon_0$ Rayleigh line

$\upsilon=\upsilon_0-\upsilon_m$ Raman stokes line

$\upsilon=\upsilon_0+\upsilon_m$ Raman anti-stokes line

Raman spectroscopy relies on inelastic (Raman) scattering of monochromatic light, usually from a laser in the visible, near infrared, or near ultraviolet range. The laser light interacts with molecular vibrations, phonons or other excitations in the system, resulting in the energy of the laser photons being shifted up or down [80]. The shift in energy gives information about the vibrational modes in the system. Stokes lines are more intense than anti stocks lines and hence stokes lines are detected during Raman analysis.

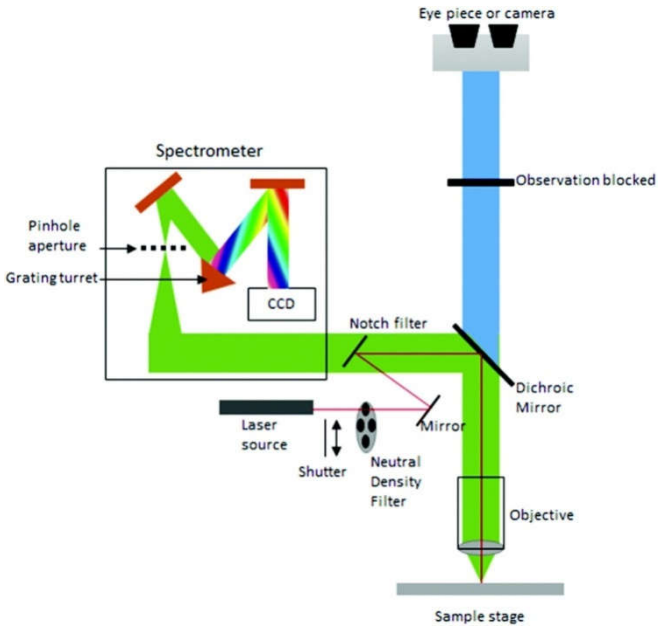

Fig. 2.11 Schematic diagram of confocal Raman spectrometer [55]

In Raman spectroscopic analysis, sample is normally illuminated with a laser beam; a lens collects the scattered light and then sent it through interference filter or spectrophotometer to obtain Raman spectra of the sample. Figure 2.11 shows the schematic diagram of confocal Raman spectrometer. Filters are included in the Raman spectrometer to separate weak modes from the intense Rayleigh scattering. Selection of laser wavelength is important in Raman spectroscopy. Light penetration depth is inversely proportional to the absorption coefficient [81];

$$d \sim 1/(2\alpha) \text{ ----- } (2.17)$$

Where d is the penetration depth and α is the absorption coefficient of the material. The Raman analysis of the present work was carried out with Raman microscope (Thermo Scientific DXR) with 532 nm semiconductor laser source.

2.2.4 Scanning Electron Microscope (SEM)

Study of surface morphology of absorber film is important since grain size and grain boundary effects greatly influence solar cell performance [82]. Grain boundaries in absorber films act as trap for electron-hole pair and also creating a resistive barrier for the transport of charges from one grain to another. Scanning electron microscope is used to analyse surface morphology, chemical composition, and orientation of the materials [83]. SEM has a focused beam of high energy electrons to generate surface image. Wide varieties of signals are produced when high energy electrons interact with the sample

surface. These signals include secondary electrons, backscattered electrons, photos and heat. Secondary electrons are detected and used for creating surface images. Backscattered electrons are detected and analysed to examine multiphase samples. Certain characteristic x-rays are produced during the interaction of high energy electrons, which can provide information about the atom. These characteristic x-rays can be used for qualitative and quantitative measurements [84]. Fig. 2.12 shows the schematic diagram of a scanning electron microscope; it includes electron source, detectors, electron lenses, vacuum pumps and sample stage. Sensors and cameras are also incorporated in the equipment.

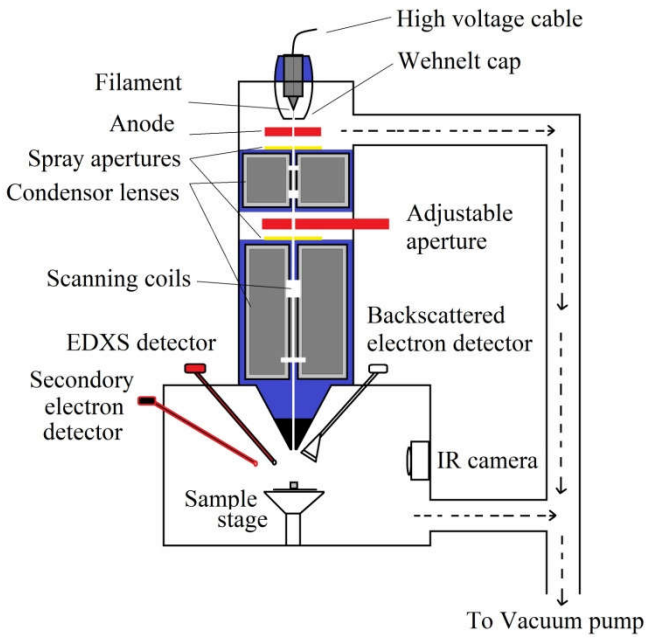

Fig. 2.12 Schematic diagram of Scanning Electron Microscope

Capability of an instrument is defined in terms of resolution. It is the ability to distinguish two adjacent points or objects. Resolution can be improved by changing accelerating voltage and initial cross over diameter [85]. Commonly used accelerating voltage is the range of 0.5-30kV. Higher voltage gives better resolution due to its shorter wavelength. For better resolution, diameter of an incident wave will have a smaller diameter than the object (Initial cross over diameter) and the wave should contain sufficient electrons to generate acceptable amount of signals. In field emission scanning electron microscope (FESEM), a field emission cathode in the electron gun provides a narrow beam at low and high electron energies [84]. This gives better image with higher resolution [86]. In this work, both SEM (Zeiss Evo18, USA) and FESEM (FEI Novo Nano SEM-450, USA) were used for surface morphology studies and also for film thickness measurements.

2.2.5 Energy dispersive x-ray spectroscopy (EDXS)

Earlier reported works on CZTS film revealed the influence of elemental composition ratios Cu/(Zn+Sn) and Zn/Sn on the solar cell performance. Most of the high performance devices based on CZTS are slightly off-stoichiometric [87-91]. Off-stoichiometry in films increases free carriers in the film; however, wide variations in the stoichiometry may lead to the formation of secondary phases. In view of this, elemental composition study is important for good quality absorber films. Energy dispersive x-ray spectroscopy provides information about the elements present, both qualitatively and

quantitatively. Most of the EDXS systems are attached to scanning electron microscopes. As discussed in the previous section, characteristic x-rays produced from sample surface are analysed by a detector, and elements are detected based on its intensity and energy [83]. Accuracy of EDXS technique depends on several factors; generally on the nature of the sample. The main disadvantages of EDXS analysis is that, for a few elements, x-ray emission peaks are overlapped with those of other elements (for example, Ti Kβ and V Kα) [92]. Solid state array detectors are widely used for detection. When characteristic x-rays incident on the detector it creates a charge pulse proportional to the energy of characteristic x-rays. The signals will be analysed by computer and create energy versus count plot. Evaluation of energy and its count will detect element and its quantification. In this work, EDXS equipped with SEM was used to study the chemical compositions of CZTS thin films coated by various techniques. The solid state detector used in the SEM was capable to measure maximum energy of 15keV. In order to identify chemical compositions of CZTS, K lines were used for Cu ($K_{\alpha 1}$-8.04778), Zn ($K_{\alpha 1}$-8.63886) and S ($K_{\alpha 1}$-2.30784), and L lines were used for Sn ($K_{\alpha 1}$-25.2713, $K_{\alpha 2}$-25.0440, $K_{\beta 1}$-28.4860, $L_{\alpha 1}$-3.44398) [93].

2.2.6 Inductively coupled plasma –Atomic emission spectroscopy

Inductively coupled plasma-Atomic emission spectroscopy (ICP-AES) is a sensitive technique used for qualitative and quantitative identification of elements in a sample. The sample is injected in to argon plasma with very high magnetic field [94]. The high energy

beam thermally excites outer-shell electrons of the elements in the sample and de-excited by emitting energy at a characteristic wavelength of the particular element. However, the excited species in the plasma emit light at different wavelengths and hence polychromatic. The polychromatic light has to be separated into individual wavelengths, and the emission from each element can be identified and its intensity can be measured. The separation of light according to wavelength is generally done using a monochromator spectrometer. This technique is known as inductively coupled plasma-atomic emission spectroscopy. A polychromator can be used to measure light at several different wavelengths simultaneously and this helps to analyse multiple elements at a time. The main advantage of ICP technique is its accuracy level, it can detect elements from ppm to ppb range. In this work, ICP-AES spectrometer (Thermo Electron IRIS Intrepid II XPS DUO) was used for elemental analysis.

2.2.7 UV-Visible spectroscopy

Band gap measurement is important for characterising absorber layer. For an ideal solar cell, the ideal band gap of absorber material is considered as 1.5eV to absorb maximum photons [88-91]. In order to study the band gap of absorber materials, absorption coefficient of the materials is investigated first. The *absorption coefficient* determines how far into a material light of a particular wavelength can penetrate before it is *absorbed.* Absorption coefficient of the material is thus important in determining the thickness of the absorber. The absorption coefficient is inversely proportional to the thickness of the film [95]. If

the absorption coefficient is higher, absorber layer can have minimum thickness. UV-Vis spectroscopy is a versatile technique used for optical and electronic properties of various materials such as, films, powders, monolithic solids and liquids. This technique has become the most important tool because of its simplicity, accuracy and cost effectiveness. Absorption of visible and ultraviolet radiations is associated with excitation of electrons, in both atoms and molecules, from lower to higher energy levels. This is associated with a few humps in the spectrum. Fig. 2.13 shows the schematic diagram of UV-visible spectrometer. The equipment consists of light source, sample stage, detector and related optics.

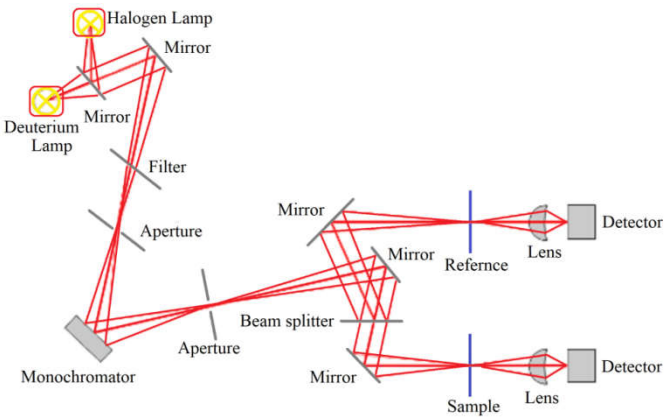

Fig. 2.13 Schematic diagram of UV-Visible spectrophotometer

Two types of light sources, as seen in the schematic diagram, are used to cover the entire UV-visible spectral range. The light sources are split into two by a prism or grating and pass through the reference and the sample to be analysed. Reference is used to nullify

the absorption by the substrate or the sample dispersing solution. Finally, detectors measure the light intensity and absorbance is calculated by comparing these two signals. Absorbance of the material can be expressed as

$$A = log_{10}\left(\frac{I}{I_0}\right) = -log_{10}T \text{ ----- (2.18)}$$

Where, A is the absorbance, I is the intensity of transmitted light, I_0 is the intensity of incident light and T is the transmittance. Absorption coefficient (α) of the thin film can be calculated from transmittance data

$$\alpha = -\frac{\ln\left(\%T/100\right)}{d} \qquad \text{----- (2.19)}$$

Where, *d* is the thickness of the film.

Band gap can be estimated using the Tauc's relation [95],

$$\alpha = \frac{A(h\nu - E_g)^n}{h\nu} \qquad \text{----- (2.20)}$$

Where, A is a constant, *h* is the planks constant, ν is frequency and E_g is the energy band gap. *n* characterize the transition process, which take up values 2, 2/3, 1/2 and 1/3 for the probability transitions of direct allowed, direct forbidden, indirect allowed and indirect forbidden transitions, respectively [96]. CZTS, being a direct band gap material, *n* is taken as 2 and the band gaps of the films in the present work were estimated by extrapolating the linear portion of the $(\alpha h\nu)^2$ versus hν plot to the x intercepting point at y=0. A UV-visible

spectrometer (Perkin Elmer: Lambda 35) was used for the present study.

2.2.8 Hall Effect measurement

Carrier concentration, mobility and resistivity are important electrical properties of materials. Mobility of the film defines the quality of the absorber layer [97,98]. Series resistance of the solar affects fill factor and efficiency of solar cells. Resistivity of absorber layer also influences the total series resistance of the device [97]. For high performance of the photovoltaic device, the resistivity of the absorber film should be low and the mobility should be high [99]. Hall Effect is a basic phenomenon in solid state physics and is an important diagnostic tool for the electrical characterization of materials, particularly semiconductors [86]. It provides a direct determination of the type of charge carriers, carrier density, mobility and resistivity in a given sample.

Hall voltage is the generation of transverse voltage across a current carrying conductor in the presence of external magnetic field [100,101]. In the presence of external magnetic field acting perpendicular to the direction of motion, an electron will experience Lorentz force normal to both the directions. The resulting Lorentz force is given by [101]

$$F = q(E + V \times B) \text{ ----- (2.21)}$$

Where q is the particle charge, E is the electric field, V is the particle velocity, and B is the magnetic field. If we consider a semiconductor

with bulk density n, the Lorentz force drifts the electrons away from the current direction. This lead to a potential drop across the conductor, called Hall voltage which is given by

$$V_H = \frac{I \times B}{q \times n \times d} \qquad \text{----- (2.22)}$$

Where I is the current through the conductor, B is the magnetic field, d is the thickness and q is the charge. From the above expression sheet density can be found,

$$n_s = n \times d \times n_s = \frac{I \times B}{q \times V_H} \qquad \text{----- (2.23)}$$

The Hall voltage V_H will be positive for p type semiconductor and negative for n type semiconductor. The Hall mobility (μ) is given by

$$\mu = \frac{V_H}{R_S \times I \times B} = \frac{1}{q \times n_s \times R_S} \qquad \text{----- (2.24)}$$

Where the sheet resistance R_S is measured using van der Pauw technique. This is a method to obtain resistivity of arbitrary shapes. The sheet resistance can be determined from the famous van der Pauw relation, [102]

$$e^{\left(-\pi \frac{R_A}{R_S}\right)} + e^{\left(-\pi \frac{R_A}{R_S}\right)} = 1 \qquad \text{----- (2.25)}$$

Where

$$R_A = \frac{V_{43}}{I_{12}} \text{ ----- (2.26)} \quad \text{and} \quad R_B = \frac{V_{43}}{I_{23}} \text{ ----- (2.27)}$$

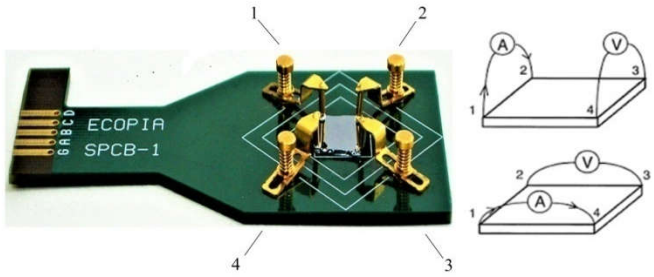

Fig. 2.14 Image of the sample holder used and schematic diagram of sample with four leads 1, 2, 3 and 4.

I_{12} is the DC current entering through contact 1 and leaves through contact 2 of the sample, I_{23} is the DC current entering through contact 2 and leaves through contact 3 of the sample, V_{43} is the voltage from contact 4 to 3 and V_{14} is the voltage from the contact 1 to 4. (Fig.2.14). By solving R_A and R_B in the above van der Pauw equation, R_s can be calculated. Thus, from Hall measurements, mobility, carrier concentration, Hall voltage and resistivity can be determined.

CZTS is a intrinsically doped *p* type semiconductor. The stoichiometric variation is responsible for the acceptor doping in CZTS material. Optimization of acceptor doping level in CZTS absorber by varying its stoichometric composition ratio is important for solar cell application. Carrier concentration of the films determines the strength of built in electric field with in the space charge region of the solar cell [103]. However, higher carrier concentration is responsible for increase in carrier recombination and also the semiconductor become degenerate in terms of Mott-transition behaviour [104]. Hence the study of the electrical properties of CZTS absorber film is important. For the present work, Hall Measurement System (Ecopia HMS 3000)

was used with a magnetic field 0.54Tesla to study the electrical properties.

2.2.9 Solar cell characteristics

After fabricating solar cell in the present work, its performance was analysed by measuring I-V characteristics. The major solar cell parameters are open circuit voltage (V_{oc}), short circuit current (I_{sc}), short circuit current density (J_{sc}), maximum power point (P_{max}), fill factor (FF), efficiency (□), shunt resistance and series resistance. Solar cells are basically *p-n* junction diodes under illumination. Hence the solar cells are modelled by standard diode equations. Equivalent circuit of solar cell with series resistance and shunt resistance are shown in Fig. 2.15.

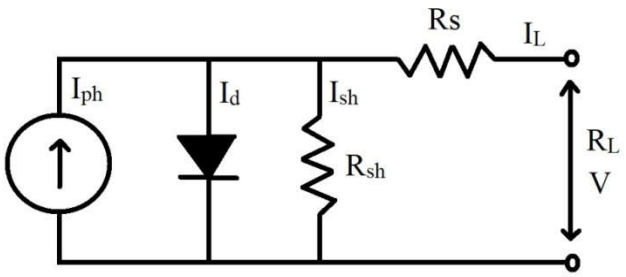

Fig. 2.15 Solar cell equivalent circuit with R_s and R_{sh}

This equivalent model consists of current due to optical generation, diode current, series resistance and shunt resistance.

Diode current,

$$I_d = I_0(e^{\left(\frac{qV_d}{VkT}\right)} - 1) \quad \text{----- (2.28)}$$

$$I_{ph} - I_d - I_{sh} = I_L \quad \text{----- (2.29)}$$

$$I_{p\square} - I_0\left(e^{\left(\frac{qV_d}{VkT}\right)} - 1\right) - \left(\frac{V_L + I_L R_S}{R_{sh}}\right) = I_L \quad \text{----- (2.30)}$$

Solving it by Newton Rapson method [105], the I-V relation dependent to the load can be obtained (Figure 2.16). The performance of solar cells can be measured on the basis of following parameters,

Open circuit voltage (V_{oc}) is the maximum voltage occurs when there is no current passing through the solar cell (with zero loads). $V=V_{oc}$ when $I_L=0$; for an ideal solar cell Voc is independent to the illumination intensity. Short circuit current (I_{sc}) is the maximum current flows through the circuit when the impedance is low (maximum load), $I_L=I_{sc}$ when $V_L=0$. Current density (J_{sc}) is the current per unit area in a solar cell. For an ideal device, current density equal to photon current density ($J_{sc}=J_{ph}$). V_{max} and I_{max} are the maximum current and voltage delivered to the load.

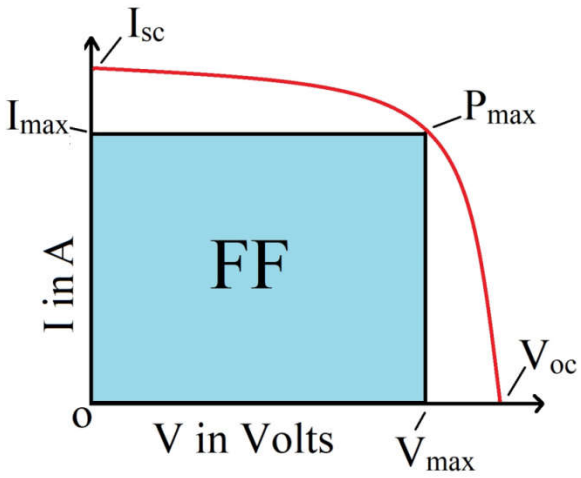

Fig. 2.16 Schematic diagram of I-V characteristics of a solar cell

Fill factor is another important parameter in a solar cell that defines the quality of solar cell [106]. It is the ratio of the maximum power (P_{max}) to the theoretical power (P_T).

$$FF = \frac{P_{MAX}}{P_T} \qquad \text{----- (2.31)}$$

$$FF = \frac{V_{MAX} \times I_{MAX}}{V_{OC} \times I_{SC}} \qquad \text{----- (2.32)}$$

The efficiency of a solar cell is the ratio of electrical power output (P_{OUT}) compared to the solar cell power input (P_{IN})

$$\square = \frac{P_{MAX}}{P_{IN}} = \frac{V_{MAX} \times I_{MAX}}{P_{IN}} = \frac{I_{SC} \times V_{OC} \times FF}{P_{IN}} \qquad \text{----- (2.33)}$$

Standard laboratory conditions are used for the efficiency measurements in the present work. Photon input power is set to 1000W/m^2 under AM 1.5 condition and the temperature of the solar

cell while measurement is set to 25°C. Fig. 2.17 shows the efficiency measurement setup (Newport Oriel Sol AAA solar simulator, USA) used for the evaluation of solar cell performance. It uses a calibrated xenon light source (450W) and computer controlled electrometer (Keithley, USA) for the efficiency measurements.

Fig. 2.17 Solar simulator set up used for efficiency measurements

Series resistance and shunt resistance are the limiting factors for the ideal characteristics of a solar cell [107-110]. Shunt resistance in a device bypass the electric current from one point to another by creating a low resistance path. For an ideal device, this has to be infinity; however, usually shunt resistance path exists due to manufacturing defects [109-112]. Series resistance in a device will also reduce efficiency of the device. Series resistance in devices arises from its metal contacts in the front surface of the cell, impurity concentration and junction depth [113,114]. It reduces short circuit current and maximum power output of the cell. Series resistance in a device should be minimum; it can be reduced by proper device

engineering in the interface of layers [115-117]. Series resistance and shunt resistance can be calculated by analysing the slope of the I-V characteristics, or it can be measured by using two I-V curves with different irradiation at same temperature and same spectrum [105,106].

$$\text{Series resistance, } R_S = \frac{V_{oc2} - V_{oc1}}{I_{sc1} - I_{sc2}} \qquad \text{----- (2.34)}$$

Where V_{oc1}, I_{sc1} and V_{oc2}, I_{sc2} are the open circuit voltage and short circuit current of two I-V characteristic curves. In this work, series and shunt resistances were calculated by analyzing the slope of the I-V characteristic curve.

2.3. Summary

Major experimental techniques used for coating of kesterite thin films are described along with the details of fabrication of other layers such as top TCO and buffer films. Basic principles, major components along with schematic diagram were included. In addition to this, the major characterization equipments and techniques used for studying structural, surface morphological, optical and electrical properties of the CZTS thin films prepared by various routes, and the details of photovoltaic measurements of the solar cells fabricated were described in detail.

2.4. References

1) Ramasamy K, Malik M A, O'Brien P, Routes to copper zinc tin sulfide Cu_2ZnSnS_4 a potential material for solar cells, Chem. Commun.48 (2012) 5703.

2) Abermann S, Non-vacuum processed next generation thin film photovoltaics: towards marketable efficiency and production of CZTS based solar cell, Sol. Energy. 94 (2013) 37.

3) Vanalakar S A, Agawane G L, Shin S W, Suryawanshi M P, Gurav K V, Jeon K S, Patil P S, Jeong C W, Kim J Y, Kim J H, A review on pulsed laser deposited CZTS thin films for solar cell applications, J. Alloys Compd. 619 (2015) 109.

4) Zhuk S, Kushwaha A, Wong T K, Masudy-Panah S, Smirnov A, Dalapati G K, Critical review on sputter-deposited Cu_2ZnSnS_4 (CZTS) based thin film photovoltaic technology focusing on device architecture and absorber quality on the solar cells performance, Sol. Energy Mater. Sol. Cells. 171 (2017) 239.

5) Parida B, Iniyan S, Goic R, A review of solar photovoltaic technologies, Renewable Sustainable Energy Rev. 15 (2011) 1625.

6) Branker K, Pathak M J, Pearce J M, A review of solar photovoltaic levelized cost of electricity, Renewable Sustainable Energy Rev.15 (2011) 4470.

7) Song X, Ji X, Li M, Lin W, Luo X, Zhang H, A review on development prospect of CZTS based thin film solar cells, Int. J. Photoenergy. 2014 (2014) 613173.

8) Kahraman S, Çetinkaya S, Podlogar M, Bernik S, Çetinkara H A, Güder H S, Effects of the sulfurization temperature on sol gel-processed Cu_2ZnSnS_4 thin films, Ceram. Int. 39 (2013) 9285.

9) Suryawanshi M P , Agawane G L, Bhosale S M, Shin S W, Patil P S, Kim J H, Moholkar A V, CZTS based thin film solar cells: a status review, Mater Technol. 28 (2013) 98.

10) Lee T D, Ebong A U, A review of thin film solar cell technologies and challenges, Renewable Sustainable Energy Rev. 70 (2017) 1286.

11) Ramanujam J, Singh U P, Copper indium gallium selenide based solar cells–a review, Energy Environ. Sci.10 (2017) 1306.

12) Sigmund P, Theory of sputtering. I. Sputtering yield of amorphous and polycrystalline target, Phys. Rev. 184 (1969) 383.

13) Matsunami N, Yamamura Y, Itikawa Y, Itoh N, Kazumata Y, Miyagawa S, Morita K, Shimizu R, Tawara H, Energy dependence of the ion-induced sputtering yields of monatomic solids, At. Data Nucl. Data Tables. 31 (1984) 1.

14) Sivaram S, Thin Film Phenomena. Chemical Vapor Deposition. Springer, Boston, MA. 1995

15) Chopra, Kasturi L, Thin film phenomena, McGraw-Hill, New York, NY 1969.

16) Smith, Donald Leonard. Thin-film deposition: principles and practice. New York etc: McGraw-hill, 108, 1995.

17) Chiou W T, Wu W Y, Ting J M, Growth of single crystal ZnO nanowires using sputter deposition, Diamond Relat. Mater. 12 (2003) 1841.

18) Braun M, Magnetron Sputtering Technique. Handbook of Manufacturing Engineering and Technology, Springer, 2013

19) Swann S, Magnetron sputtering, Phys. Technol. 19 (1988) 67.

20) Berg S, Nyberg T, Fundamental understanding and modelling of reactive sputtering processes, Thin solid films. 476 (2005) 215.

21) Cuomo, Jerome J., Stephen M. Rossnagel, Harold R. Kaufman, Handbook of ion beam processing technology, Elsevier 1989.

22) Liu F, Li Y, Zhang K, Wang B, Yan C, Lai Y, Zhang Z, Li J, Liu Y, In situ growth of Cu_2ZnSnS_4 thin films by reactive magnetron co-sputtering, Sol. Energy Mater. Sol. Cells. 94 (2010) 2431.

23) Katagiri H, Jimbo K, Maw WS, Oishi K, Yamazaki M, Araki H, Takeuchi A, Development of CZTS-based thin film solar cells, Thin Solid Films. 517 (2009) 2455.

24) Suryawanshi M P, Ghorpade U V, Shin S W, Pawar S A, Kim I Y, Hong C W, Wu M, Patil P S, Moholkar A V, Kim J H, A simple aqueous precursor solution processing of earth-abundant Cu_2SnS_3 absorbers for thin-film solar cells, ACS Appl. Mater. Interfaces. 8 (2016) 11603.

25) Tumbul A, Goktas A, Zarbali M Z, Aslan F, Structural, morphological and optical properties of the vacuum-free processed CZTS thin film absorbers, Mater. Res. Express. 5 (2018) 1591.

26) Shin B, Gunawan O, Zhu Y, Bojarczuk N A, Chey S J, Guha S, Thin film solar cell with 8.4% power conversion efficiency using an earth-abundant Cu_2ZnSnS_4 absorber, Prog. Photovolt. Res. Appl. 21 (2011) 72.

27) Wang W, Winkler M T, Gunawan O, Gokmen T, Todorov T K, Zhu Y, Mitzi D B, Device characteristics of CZTSSe thin film solar cells with 12.6% efficiency, Adv. Energy Mater. 4 (2014) 1301465.

28) Yang R, Mazalan E, Chaudhary K T, Haider Z, Ali J, Non-vacuum deposition methods for thin film solar cell, AIP Conference Proceedings, AIP Publishing, 1824 (2017) 030018.

29) Geffcken W and Berger E, Method of amending the Reflective optical glasses, Patent DE736411 (C) 1939.

30) Lu Y, Ganguli R, Drewien C A, Anderson M T, Brinker C J, Gong W, Guo Y, Soyez H, Dunn B, Huang M H, Zink J I, Continuous formation of supported cubic and hexagonal mesoporous films by sol–gel dip-coating, Nature. 389 (1997) 364.

31) Brinker C J, Frye G C, Hurd A J, Ashley C S, Fundamentals of sol-gel dip coating, Thin solid films. 201 (1991) 97.

32) Scriven L E, Physics and applications of dip coating and spin coating, MRS Online Proc. Libr. 121 (1988) 717.

33) Kemell M, Ritala M, Leskelä M, Thin film deposition methods for $CuInSe_2$ solar cells, Crit. Rev. Solid State Mater. Sci. 30 (2005) 1.

34) Tanaka K, Moritake N, Oonuki M, Uchiki H, Pre-annealing of precursors of Cu_2ZnSnS_4 thin films prepared by sol–gel sulfurizing method, Jpn. J. Appl. Phys. 47 (2008) 598.

35) Bornside D E, Macosko C W, Scriven L E, Modeling of spin coating, J. Imaging Technol. 13 (1987) 122.

36) Lawrence C J, The mechanics of spin coating of polymer films, Phys. Fluids. 31 (1988) 2786.

37) Brabec C J, Durrant J R, Solution-processed organic solar cells, MRS Bull. 33 (2008) 670.

38) Girotto C, Rand B P, Genoe J, Heremans P, Exploring spray coating as a deposition technique for the fabrication of solution-processed solar cells, Sol. Energy Mater. Sol. Cells. 93 (2009) 454.

39) Chen C H, Kelder E M, Shoonman J, Effects of additives in electrospraying for materials preparation, J. Eur. Ceram. Soc. 18 (1998) 1439.

40) Caillaud F, Smith A, Baumard J F, Effect of pH of the solution on the deposition of zinc oxide films by spray pyrolysis, J. Am. Ceram. Soc. 76 (1993) 998.

41) Rajeshmon V G, Kartha C S, Vijayakumar K P, Sanjeeviraja C, Abe T, Kashiwaba Y, Role of precursor solution in controlling the opto-electronic properties of spray pyrolysed Cu_2ZnSnS_4 thin films, Sol. Energy. 85 (2011) 249.

42) Balkenende A R, Bogaerts A A, Scholtz J J, Tijburg R R, Willems H X, Thin MgO layers for effective hopping transport of electrons, Philips J. Res. 50 (1996) 365.

43) Arya S P, Hintermann H E, Growth of Y-Ba-Cu-O superconducting thin films by ultrasonic spray pyrolysis, Thin Solid Films. 193 (1990) 841.

44) Chunhua Chen, Erik M Kelder, Paul J J, M, van der Put and Joop Schoonman, Morphology control of thin $LiCoO_2$ films fabricated using the electrostatic spray deposition (ESD) technique, J. Mater. Chem. 6 (1996) 765.

45) Espindola-Rodriguez M, Placidi M, Vigil-Galán O, Izquierdo-Roca V, Fontané X, Fairbrother A, Sylla D, Saucedo E, Pérez-Rodríguez A. Compositional optimization of photovoltaic grade Cu_2ZnSnS_4 films grown by pneumatic spray pyrolysis. Thin Solid Films. 535 (2013) 67.

46) Nair P K, Nair M T, Garcıa V M, Arenas O L, Pena Y, Castillo A, Ayala I T, Gomezdaza O, Sanchez A, Campos J, Hu H, Semiconductor thin films by chemical bath deposition for solar energy related applications, Sol. Energy Mater. Sol. Cells. 52 (1998) 313.

47) Kale S S, Lokhande C D, Thickness-dependent properties of chemically deposited CdSe thin films, Mater. Chem. Phys. 62 (2000) 103.

48) Arenas O L, Nair M T, Nair P K. Chemical bath deposition of ZnS thin films and modification by air annealing, Semicond. Sci. Technol. 12 (1997) 1323.

49) Pawar S H, Deshmukh L P, Studies on electrochemical photovoltaic cells formed with as-deposited In-doped CdS films, Mater. Chem. Phys. 10 (1984) 83.

50) O'Brien P, McAleese J, Developing an understanding of the processes controlling the chemical bath deposition of ZnS and CdS, J. Mater. Chem. 8 (1998) 2309.

51) Dhawale D S, More A M, Latthe S S, Rajpure K Y, Lokhande C D, Room temperature synthesis and characterization of CdO nanowires by chemical bath deposition (CBD) method, Appl. Surf. Sci. 254 (2008) 3269.

52) Shahanie C, Sutrave D S, Deshmukh L P, Chemical deposition of CdSe thin films: photoelectrochemical applications, Indian J. Pure Appl. Phys. 34 (1996) 153.

53) Cullity B D, Stock S R, Elements of X-ray diffraction, Third Edn, Prentise Hall, New Jersey, 2001

54) Levine D, Steinhardt P J, Quasicrystals: a new class of ordered structures, Phys. Rev. Lett. 53 (1984) 2477.

55) Smith R, Wright K L, Ashton L, Raman spectroscopy: an evolving technique for live cell studies, Analyst.141 (2016) 3590.

56) Mote V D, Purushotham Y, Dole B N, Williamson-Hall analysis in estimation of lattice strain in nanometer-sized ZnO particles, J. Theor. Appl. Phys. 6 (2012) 6.

57) Venkateswarlu K, Bose AC, Rameshbabu N, X-ray peak broadening studies of nanocrystalline hydroxyapatite by Williamson–Hall analysis, Physica B: Condens. Matter. 405 (2010) 4256.

58) Prabhu T, Rao K V, Sai Kumar V S, Siva Kumari B, X-Ray Analysis by Williamson Hall and Size-Strain Plot Methods of ZnO Nanoparticles with Fuel Variation, World J. Nano Sci. Eng. ,4 (2014) 21

59) Larson A C, Von Dreele R B, General Structure Analysis System (GSAS), Los Alamos National Laboratory Report LAUR 86 (1994) 748.

60) Toby B H, EXPGUI, a graphical user interface for GSAS, J. Appl. Crystallogr. 34 (2001) 210.

61) Fischereder A, Rath T, Haas W, Amenitsch H, Albering J, Meischler D, Larissegger S, Edler M, Saf R, Hofer F, Trimmel G, Investigation of Cu_2ZnSnS_4 formation from metal salts and thioacetamide, Chem. Mater. 22 (2010) 3399.

62) Vogel S C, a GSAS script language for automated Rietveld refinements of diffraction data. J. Appl. Crystallogr, 44 (2011) 873.

63) Young R A, The Rietveld Method, Oxford University Press, Oxford, 1995.

64) Izumi F, Saisho H, Gohshi Y, Applications of Synchrotron Radiation to Materials Analysis, Elsevier, Amsterdam 1996.

65) Hugo Rietveld, The Rietveld Method-The Early Days: a Retrospective View, Oxford: University Press. 1993.

66) Taylor J C, Rietveld made easy: a practical guide to the understanding of the method and successful phase quantifications, Canberra: Sietronics Pty Ltd. 2001.

67) Rodriguez-Carvajal J, FullProf.98 and WinPLOTR: New Windows 95/NT Applications for Diffraction Commission For Powder Diffraction, Physica B. 192 (1993) 55

68) Izumi F, A Rietveld-analysis program RIETAN-98 and its applications to zeolites, Mater. Sci. Forum 321 (2000) 198.

69) Bruker A X, Topas V4.2: General profile and structure analysis software for powder diffraction data, Bruker AXS, Karlsruhe, Germany. 2009.

70) Dušek M, Petříček V, Wunschel M, Dinnebier R E, Van Smaalen S, Refinement of modulated structures against Xray powder diffraction data with JANA2000, J. Appl. crystallogr. 34 (2001) 398.

71) Quaas M, Eggs C, Wulff H, Structural studies of ITO thin films with the Rietveld method, Thin Solid Films. 332 (1998) 277.

72) Fernandes P A, Salomé P M, Da Cunha A F, A study of ternary Cu_2SnS_3 and Cu_3SnS_4 thin films prepared by sulfurizing stacked metal precursors, J. Phys. D: Appl. Phys. 43 (2010) 215403.

73) Dumcenco D, Huang Y S, The vibrational properties study of kesterite Cu_2ZnSnS_4 single crystals by using polarization dependent Raman spectroscopy, Opt. Mater. 35 (2013) 419.

74) Fontané X, Calvo-Barrio L, Izquierdo-Roca V, Saucedo E, Pérez-Rodriguez A, Morante J R, Berg D M, Dale P J, Siebentritt S, In-depth resolved Raman scattering analysis for the identification of secondary phases: characterization of Cu_2ZnSnS_4 layers for solar cell applications, Appl. Phys. Lett. 98 (2011) 181905.

75) Fernandes P A, Salomé P M, Da Cunha A F, Study of polycrystalline Cu_2ZnSnS_4 films by Raman scattering, J.Alloys Compd. 509 (2011) 7600.

76) Gurieva G, Guc M, Bruk L I, Izquierdo Roca V, Pérez Rodríguez A, Schorr S, Arushanov E, Cu_2ZnSnS_4 thin films grown by spray pyrolysis: characterization by Raman spectroscopy and Xray diffraction, Phys. Status Solidi C. 10 (2013) 1082.

77) Long, Derek Albert, Long D A, Raman spectroscopy. New York: McGraw-Hill, 276, 1977.

78) Colthup N, Introduction to infrared and Raman spectroscopy, Elsevier; 2012.

79) Drago, Russell S. Physical methods in inorganic chemistry, New York, Reinhold Pub. Corp. 1965

80) Dimitrievska M, Fairbrother A, Fontané X, Jawhari T, Izquierdo-Roca V, Saucedo E, Pérez-Rodríguez A, Multiwavelength excitation Raman scattering study of polycrystalline kesterite Cu_2ZnSnS_4 thin films, Appl. Phys. Lett., 104 (2014) 021901.

81) Hiroi H, Sakai N, Sugimoto H, Cd-free 5×5cm 2-sized Cu_2ZnSnS_4 submodules, 37th IEEE Photovoltaic Specialists Conference (PVSC), 37 (2011) 002719.

82) Li J B, Chawla V, Clemens B M, Investigating the role of grain boundaries in CZTS and CZTSSe thin film solar cells with scanning probe microscopy, Adv. Mater. 24 (2012) 720.

83) Goldstein, J, Scanning electron microscopy and x-ray microanalysis, Kluwer Adacemic/Plenum Pulbishers, 2003

84) Goldstein J I, Newbury D E, Michael J R, Ritchie N W, Scott J H, Joy D C, Scanning electron microscopy and X-ray microanalysis, Springer; 2017.

85) Reimer L. Scanning electron microscopy: physics of image formation and microanalysis, Springer, 1998

86) Egerton, R F, Physical principles of electron microscopy: an introduction to TEM, SEM, and AEM, Springer, 202, 2005.

87) Chen S, Gong X G, Walsh A, Wei S H, Defect physics of the kesterite thin-film solar cell absorber Cu_2ZnSnS_4, Appl. Phys. Lett. 96 (2010) 021902.

88) Das S, Mandal K C, Low-cost Cu_2ZnSnS_4 thin films for large-area high-efficiency heterojunction solar cells, 38th IEEE Photovoltaic Specialists Conference (PVSC), 38 (2012) 002668.

89) Redinger A, Berg D M, Dale P J, Valle N, Siebentritt S, Route towards high efficiency single phase $Cu_2ZnSn(S,Se)_4$ thin film solar cells: Model experiments and literature review, 37th Photovoltaic Specialists Conference (PVSC), IEEE 37 (2011) 000025.

90) Shin B, Zhu Y, Bojarczuk N A, Chey S J, Guha S, High efficiency $Cu_2ZnSnSe_4$ solar cells with a TiN diffusion barrier on the molybdenum bottom contact, 38th IEEE Photovoltaic Specialists Conference (PVSC), 38 (2012) 000671.

91) Gunawan O, Gokmen T, Shin B S, Guha S, Device characteristics of high performance Cu_2ZnSnS_4 solar cell, 38th IEEE Photovoltaic Specialists Conference (PVSC), 38 (2012) 003001.

92) Bell D C, Garratt-Reed A J, Energy dispersive X-ray analysis in the electron microscope, Garland Sci. 2003

93) Long B, Cheng S, Lai Y, Zhou H, Yu J, Zheng Q, Effects of sulfurization temperature on phases and opto-electrical properties of Cu_2ZnSnS_4 films prepared by sol–gel deposition, Thin Solid Films. 573 (2014) 117.

94) Skujins, S, Handbook for ICP-AES (Varian-Vista). A short guide to vista series ICP-AES operation, Varian Int. AG, Zug, 1 (1998) 235.

95) Chopra K L, Paulson P D, Dutta V, Thin film solar cells: an overview. Prog. Photovoltaics Res. Appl. 12 (2004) 69.

96) Pawar B S, Pawar S M, Gurav K V, Shin S W, Lee J, Kolekar S S, Kim J H, Effect of annealing atmosphere on the properties of

electrochemically deposited Cu_2ZnSnS_4 (CZTS) thin films, ISRN Renew. Energ. 2011 (2011) 934575.

97) Tanaka K, Oonuki M, Moritake N, Uchiki H, Cu_2ZnSnS_4 thin film solar cells prepared by non-vacuum processing, Sol. Energy Mater. Sol. Cells. 93 (2009) 583.

98) Haschke J, Amkreutz D, Korte L, Ruske F, Rech B, Towards wafer quality crystalline silicon thin-film solar cells on glass, Sol. Energy Mater. Sol. Cells. 128 (2014) 190.

99) Van Puyvelde L, Lauwaert J, Tempez A, Devulder W, Nishiwaki S, Pianezzi F, Detavernier C, Tiwari AN, Vrielinck H, Electronic defect study on low temperature processed $Cu(In,Ga)Se_2$ thin-film solar cells and the influence of an Sb layer, J. Phys. D: Appl. Phys. 48 (2015) 175104.

100) Van der Pauw l J. A method of measuring specific resistivity and Hall effect of discs of arbitrary shape. Philips Res. Rep. 13 (1958):1.

101) Ellmer K, Hall effect and conductivity measurements in semiconductor crystals and thin films, Charact. Mater. (2012) 1.

102) van der Pauw L J, A method of measuring the resistivity and hall coefficient on lamellae of arbitrary shape, Philips Tech. Rev. 20 (1958) 220.

103) Patel M, Ray A, Enhancement of output performance of Cu_2ZnSnS_4 thin film solar cells - A numerical simulation approach and comparison to experiments, Physica B: Condens. Matter. 407 (2012) 4391.

104) Mott N F, Metal-insulator transition, Rev. Mod. Phys. 40 (1968) 677.

105) Abou-Ras D, Kirchartz T, Rau U, Advanced characterization techniques for thin film solar cells, John Wiley & Sons; 2016.

106) Poortmans J, Arkhipov V, Thin film solar cells: fabrication, characterization and applications, John Wiley & Sons; 2006.

107) Shin B, Gunawan O, Zhu Y, Bojarczuk N A, Chey S J, Guha S, Thin film solar cell with 8.4% power conversion efficiency using an earth abundant Cu_2ZnSnS_4 absorber, Prog. Photovoltaics Res. Appl. 21 (2013) 72.

108) Sun K, Yan C, Liu F, Huang J, Zhou F, Stride J A, Green M, Hao X, Over 9% efficient kesterite Cu_2ZnSnS_4 solar cell fabricated by using $Zn_{1-x}Cd_xS$ buffer layer, Adv. Energy Mater. 6 (2016) 1600046.

109) Tiwari D, Chaudhuri T K, Shripathi T, Deshpande U, Rawat R, Non-toxic, earth-abundant 2% efficient Cu_2SnS_3 solar cell based on tetragonal films direct-coated from single metal-organic precursor solution, Sol. Energy Mater. Sol. Cells. 113 (2013) 165.

110) De Blas M A, Torres J L, Prieto E, Garcıa A, Selecting a suitable model for characterizing photovoltaic devices, Renewable energy. 25 (2002) 371.

111) Katagiri H, Jimbo K, Yamada S, Kamimura T, Maw W S, Fukano T, Ito T, Motohiro T, Enhanced conversion efficiencies of Cu_2ZnSnS_4-based thin film solar cells by using preferential etching technique, Appl. Phys. Express. 1 (2008) 041201.

112) Zhang J, Lexi S H, Yujun F U, Erqing XI, Cu_2ZnSnS_4 thin films prepared by sulfurization of ion beam sputtered precursor and their electrical and optical properties, Rare Met. 25 (2006) 315.

113) Tanaka T, Nagatomo T, Kawasaki D, Nishio M, Guo Q, Wakahara A, Yoshida A, Ogawa H, Preparation of Cu_2ZnSnS_4 thin films by hybrid sputtering, J. Phys. Chem. Solids. 66 (2005) 1978.

114) Dale P J, Hoenes K, Scragg J, Siebentritt S, A review of the challenges facing kesterite based thin film solar cells, 34th IEEE Photovoltaic Specialists Conference (PVSC), 34 (2009) 002080.

115) Zeng F, Sun K, Gong L, Jiang L, Liu F, Lai Y, Li J, Back contact–absorber interface modification by inserting carbon intermediate layer and conversion efficiency improvement in $Cu_2ZnSn(S,Se)_4$ solar cell, Phys. Status Solidi. 9 (2015) 687.

116) Schnabel T, Ahlswede E, On the interface between kesterite absorber and Mo back contact and its impact on solution-processed thin-film solar cells, Sol. Energy Mater. Sol. Cells. 159 (2017) 290.

117) Crovetto A, Palsgaard M L, Gunst T, Markussen T, Stokbro K, Brandbyge M, Hansen O, Interface band gap narrowing behind open circuit voltage losses in Cu_2ZnSnS_4 solar cells, Appl. Phys. Lett. 110 (2017) 083903.

Chapter 3

Preparation of Cu_2ZnSnS_4 films by dip coating technique and study of their structural, morphological, optical and electrical properties

This chapter discusses the fabrication of CZTS precursor thin films by dip coating technique and the effect of sulphurization temperature on various properties of kesterite thin films. Two types of stable precursor solutions with and without sulphur were prepared for dip coating. The precursor films coated from the two types of solutions are hereafter referred to as CZTS and CZT for samples prepared from solutions with and without sulphur, respectively. The effects of sulphurizing or annealing temperature on the formation of phase pure kesterite thin films from these two precursor films were studied systematically. Phase purity of the films was studied by X-ray diffraction and Raman spectroscopy after sulphurizing or annealing precursor films at different temperatures. Structural refinement was carried out by Rietveld analysis using the data collected from high resolution grazing incidence X-ray diffraction data. Surface morphology of the film was examined by both scanning electron microscopy and field emission scanning electron microscopy. Film thickness was estimated by FESEM cross sectional analysis. Elemental compositions were determined by EDXS coupled to the SEM and also by inductively coupled plasma - atomic emission spectroscopy, ICP-AES. UV-visible spectroscopy was used to calculate the optical band

gap. Electrical properties for the films were studied using Hall measurement technique.

3.1 Cu_2ZnSnS_4 film from CZT precursor and subsequent sulphurization

3.1.1 Preparation of stable Precursor solutions for dip coating

In solution based routes, elements are mixed at the molecular level enabling precise control of stoichometry due to molecular level homogeneity [1]. This control provides homogeneity in the CZTS films, which leads to improved solar cell performance [1]. Solution processed thin films undergoes solvent evaporation, precursor decomposition and crystallization upon subsequent thermal treatment. These events affect the density and orientation of the film [2,3].

Two types of precursor solutions were prepared, one without sulphur and the other with thiourea as sulphur source. Precursor solution without sulphur was prepared from copper (II) acetate monohydrate [$(CH_3COO)_2Cu.H_2O$, Merck Emsure, 99-102%], zinc (II) acetate dihydrate [$(CH_3COO)_2Zn.2H_2O$, Merck Emsure, 99.5-101%], tin (II) chloride dehydrate [($SnCl_2.2H_2O$, Merck, Emsure, 98-103%], 2-methoxy ethanol [Ethylene glycol monomethyl ether, $CH_3OCH_2CH_2OH$, Merck Emparta, 99.3%] and monoethanolamine (MEA, C_7H_7NO, Merck Emparta 99%). The chemicals were used without further purification. 2-methoxyethanol and MEA were used as solvent and stabilizer, respectively. In the solution preparation, acetates and chlorides were used as precursors, because these compounds are cheap and readily available from commercial suppliers. Metal acetates have low sensitivity to moisture [4]. Organic solvents were used to

increase solubility [5]. The solvent 2-methoxy ethanol used has optimum viscosity and boiling point (125°C) and also able to solubilize a variety of different precursors. The stabilizer MEA is inexpensive and non-toxic and easily dissociates by forming carbon dioxide during annealing with less carbon residue [1,5].

The reagents in stoichiometric molar ratio of 2:1:1 were dissolved in 2-methoxyethanol and MEA, and the resultant solution was stirred at 45°C for 1 hour to get clear and homogenous solution. When MEA is added to the solution, the $-NH_2$ group of MEA coordinates with metal ions resulting in metal-amine complex solution [1]. The formation of metal-amine complex was confirmed by the change in colour of the solution [6]. In the solution, Cu^{2+} reacts with Sn^{2+} to form Cu^{+} and Sn^{4+}. These are formed due to the redox reaction between Cu^{2+} and Sn^{2+} ions, where Cu^{2+} is reduced to Cu^{+} and Sn^{2+} is oxidized to Sn^{4+}[6].

3.1.2 Substrate cleaning

To obtain uniform defect free coating of films, substrate cleaning is important. Substrate has be free of dust and other particles, free from organic residues. It has to wet uniformly the precursor solution over the substrates. 0.5inch × 3inch glass substrates were used for dip coating. The glass substrates were cleaned ultrasonically with mild soap water, distilled water, acetone, ethanol and distilled water successively for 15 min each, and finally dried with free flow of nitrogen.

3.1.3. Precursor film fabrication by dip coating

Glass substrates with dimension mentioned above were used for dip coating CZTS precursor films. The films were coated on to the pre-cleaned glass substrates with dipping/withdrawal speed of 30mm/minute. The dip coated films were dried in air in tubular furnace at 300°C for 10 minutes. The process was repeated for 10 times to increase the film thickness. Flow chart for the coating process adopted is shown in Fig. 3.1.

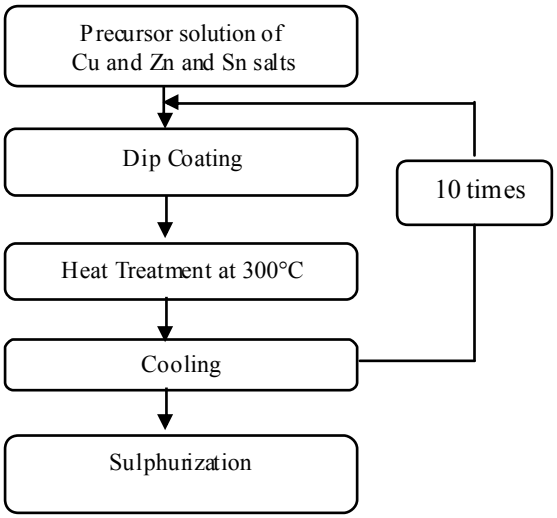

Fig. 3.1 Flow chart of the coating of CZTS thin films by dip coating

3.1. 4. Sulphurization process

The dip coated CZT precursor films were converted to Cu_2ZnSnS_4 by sulphurizing in an environment of N_2(95%)+H_2S(5%) gas mixture. The films were sulphurized at different temperature from 400°C to 600°C for 30minutes to optimize the sulphurization temperature. The gas mixture with certificate of purity was purchased from M/s Bhuruka

Gases Limited Bengaluru. The experimental set up shown in Fig. 3.2 was used for the sulphurization process and sulphurization profile is shown in Fig. 3.2 (b). Structural, optical, surface morphological and electrical properties of the films were investigated after sulphurizing CZT thin films at different temperatures.

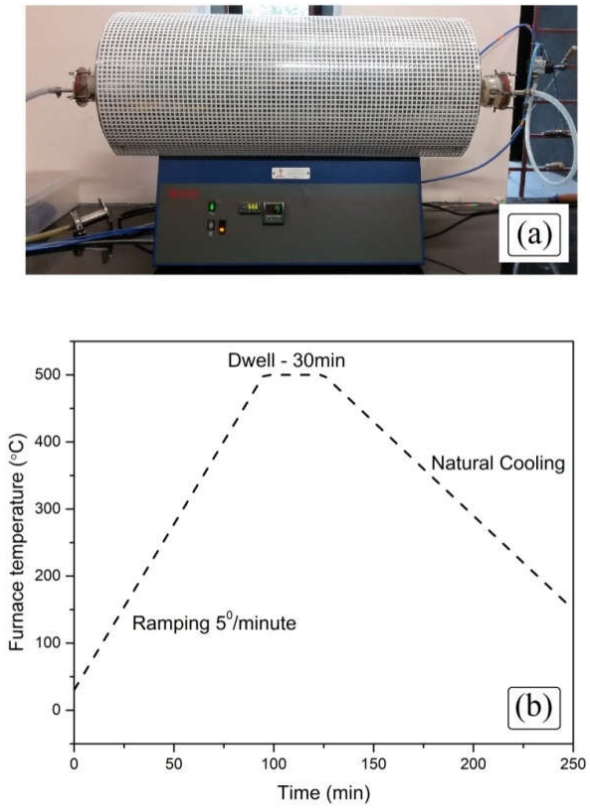

Fig. 3.2 (a) Setup used for the sulphurization of CZTS precursor films b) Sulphurization profile used for the study

3.1.5 Structural studies of dip coated CZTS thin films

3.1.5.1 X-Ray Diffraction studies

Fig. 3.3 shows the X-ray diffraction patterns of the dip coated Cu_2ZnSnS_4 films sulphurized at different temperatures ranging from 400 to 600°C. The peaks were indexed with the help of ICDD file 26-0575; all the films exhibited the characteristic peaks (1 0 1), (1 1 2), (2 0 0), (2 2 0) and (3 1 2) of tetragonal Cu_2ZnSnS_4. Films sulphurized at 400°C and 450°C show additional peak at 31.6°, which corresponds to $Cu_{2-x}S$ phase (ICDD PDF 32-0348).

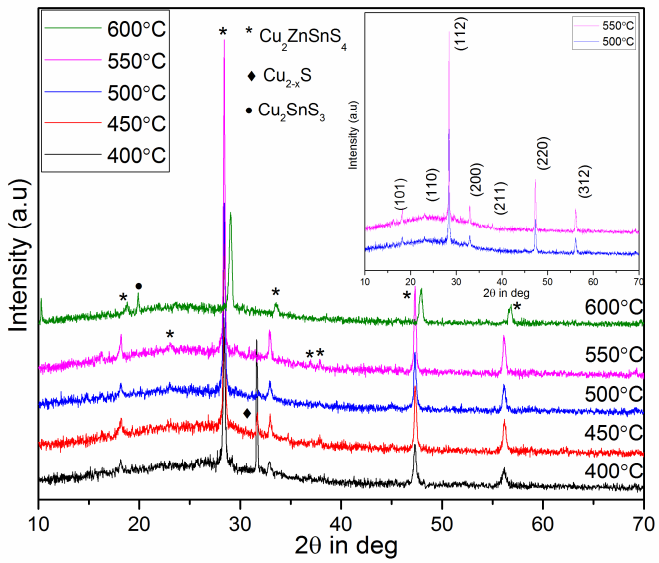

Fig. 3.3 XRD patterns of the films sulphurized at different temperatures

The intensity of $Cu_{2-x}S$ peak is found to decrease with sulphurizing temperature and this peak disappears at 500°C. According to Long et al. [7], the $Cu_{2-x}S$ phase is formed due to low

bond energy and this phase will migrate into the surface and subsequently will disappear at higher sulphurization temperature [8]. No extra peaks were observed at the sulphurization temperatures 500 and 550°C (inset of Fig. 3.3). The peak intensity was found to change when the sulphurizing temperature was changed from 500°C to 550°C. The increased peak intensity indicates the improved crystallinity of the film. Lattice constants for tetragonal CZTS crystal structure were estimated for the films sulphurized at various temperatures and are shown in Table 4.1. The values obtained for 500°C and 550°C were found to match with those of the standard ICDD file 26-0575 (a=b=5.42700Å, c=10.84800Å). The XRD of the film sulphurized at 600°C shows an additional peak at 19.9° (2θ), which corresponds to Cu_2SnS_3 phase. In this case, the CZTS peaks are shifted to lower 2 theta angles. Sulphurization at 600°C caused significant change in lattice parameter values.

The average crystallite size was calculated using the Scherrer's formula [9] as discussed in chapter 2 section 2.1.1. The average size calculated for the films sulphurized at 500°C, 550°C and 600°C using the (112) and (220) planes are listed in Table 3.1.

Table 3.1 Lattice parameters and average crystallite size of the CZTS thin films

Sulphurization temperature	Lattice parameter (Å)		Average crystallite size (nm)	Micro strain
	a=b	c		
500°C	5.430	10.892	47	7.45×10^{-4}
550°C	5.430	10.899	58	5.96×10^{-4}
600°C	5.382	10.444	25	1.22×10^{-3}

As seen in the table, the size increases with increase in sulphurizing temperature, upto 550°C. The microstrain (s) of the films were estimated by using the formula S=βcosθ/4 [9]. The film sulphurized at 600°C contains secondary phases, but reveals relatively smaller crystallites of CZTS. The microstrain at this temperature was found to be very high (Table 3.1).

3.1.5.2 Raman spectra

XRD peaks of CZTS overlap with those of secondary binary or ternary sulphides, such as, ZnS, Cu_2SnS_3, etc [7]. Hence, Raman spectroscopy was used further to analyze phase purity of the dip coated films. The films were scanned in the 200 to 600cm^{-1} region using a high resolution grating system and 532nm laser irradiation, as described in section 2.2.3 of this thesis.

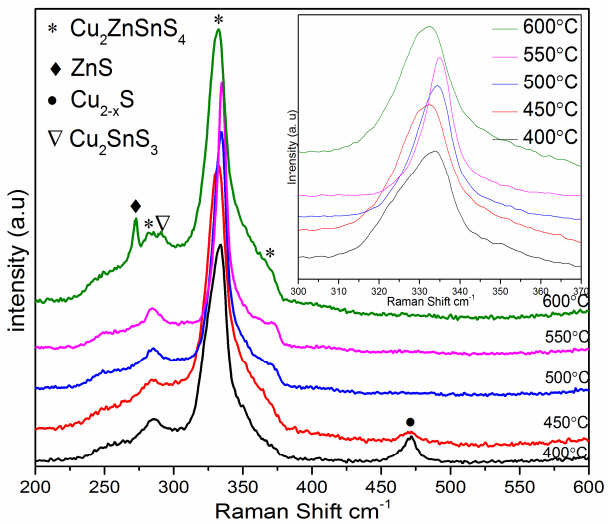

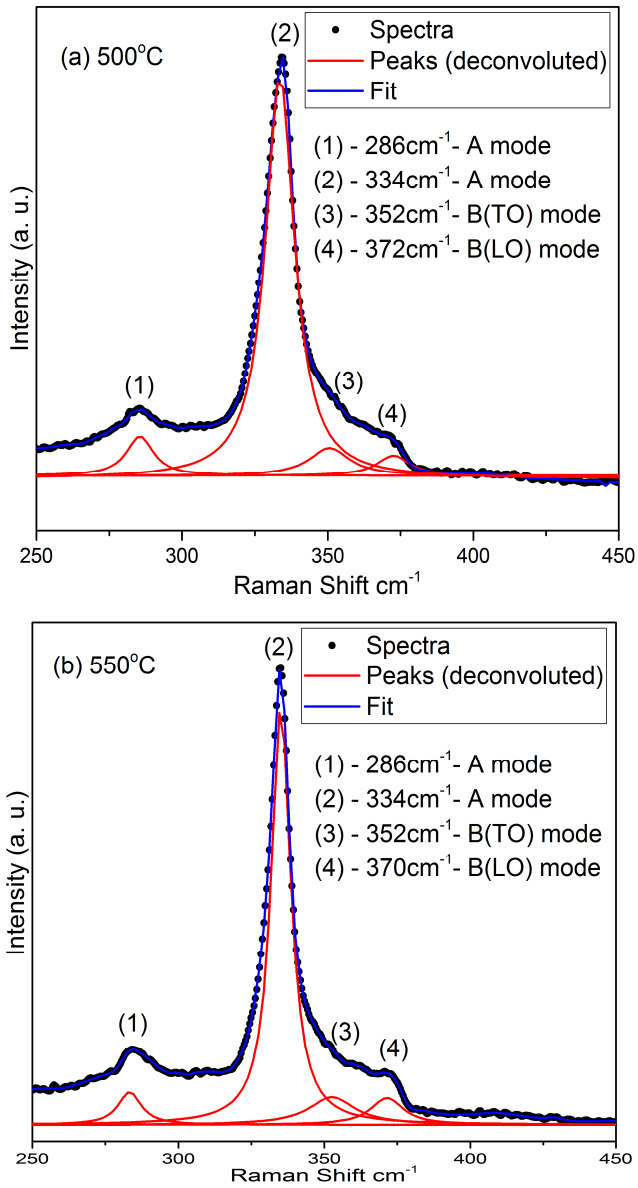

Fig. 3.4 (a) Raman Spectra of films sulphurized at different temperatures; (b) deconvoluted Raman spectra of films sulphurized at 500°C and 550°C

Fig. 3.4(a) shows the Raman spectra of films sulphurized at various temperatures. All the films exhibited characteristic peaks of CZTS, at 286cm^{-1} and 334cm^{-1}/332cm^{-1}, which corresponds to the A vibrational mode of CZTS [10]. Films sulphurized at 400°C and 450°C show additional peaks at 471cm^{-1}, which corresponds to $Cu_{2-x}S$ phase; this was observed in the XRD analysis also. Films sulphurized at 500°C and 550°C show three major peaks of CZTS at 286cm^{-1}, 334cm^{-1} and 370cm^{-1}, and no secondary or ternary phases were observed in these sulphurization temperatures. The 286cm^{-1} and 332cm^{-1}/334cm^{-1} peaks corresponds to the A vibrational mode and 370cm^{-1}/372cm^{-1} peak corresponds to the B(LO) vibrational mode of CZTS [10]. Fig. 3.4(b) shows the deconvoluted Raman spectra of films sulphurized at 500°C and 550°C fitted with Lorentzian function. The CZTS peak at 352cm^{-1} which corresponds to the B(TO) vibrational mode [10] of CZTS was clearly resolved in the deconvoluted spectra. No other impurity peaks were found after deconvolution. When sulphurization temperature was increased to 600°C, two additional peaks at 272cm^{-1} and 291cm^{-1} corresponding to ZnS and Cu_2SnS_3 [11-14] were observed along with shift in the positions of the major CZTS peaks. As seen in the inset of Fig. 3.4(a), the FWHM of the Raman peaks were found to decrease with increase in sulphurization temperature, indicating the increased crystallinity of the films [13]. The film sulphurized at 600°C exhibited a shift for the peak at 334cm^{-1} to lower wave number. However, in the XRD analysis, the peaks were found to shift to higher 2θ angle. Similar observations were made by Yoo and Kim [12] in spray pyrolysed CZTS films when Cu content was changed from 2.4 to 1.6.

3.1.5.3 Rietveld refinement

Structure refinement was carried out by Rietveld method using the diffraction data collected at room temperature from high resolution grazing angle XRD. The data was recorded with a step size of 0.02^o and a collection time of 3 sec per step, at 1^o grazing angle. Fig. 3.5(a) shows the high resolution grazing incidence x-ray diffraction pattern of the dip coated CZTS film sulphurized at 550°C. All the peaks corresponding to kesterite phase are resolved well in the GIXRD pattern and are indexed with the ICDD file 26-0575. Tetragonal kesterite type model (a=b=5.427Å, c=10.871Å, α=β=γ=90°) with S.G *I* 4□ (S.G No: 82) was used as starting model in the GSAS software [15]. In kesterite model, copper occupies 2a (0 0 0) position, zinc is at 2d (0 ½ ¾) position, Zinc + copper at 2c (0 ½ ¼) position, tin is at 2b (0 ½ ½) and sulphur is at 8g (x y z) position [16,17]. Fig. 3.5(b) shows the Rietveld refinement pattern of the film sulphurized at 550°C. Black curve shows the recorded pattern and red curve shows the calculated one; magenta vertical lines are the Braggs reflection corresponding to kesterite phase and blue curve is the difference between recorded and calculated patterns. Refinement parameters obtained are Goodness of fit ($\chi 2$) = 1.102, W_{rp} = 0.2081 and $R(F^2)$ =0.1026. Refined lattice parameter for kesterite structure is a=b=5.4290Å, c=10.8312Å and c/2a=0.998. Lattice parameter obtained from refinement are in good agreement with the reported lattice parameter values [16]. Schorr et.al [18] observed variations in the lattice parameter values when CZTS stannite phase was changed to kesterite. In the present work, the refined lattice parameter of the CZTS films perfectly matches with those of the kesterite phase.

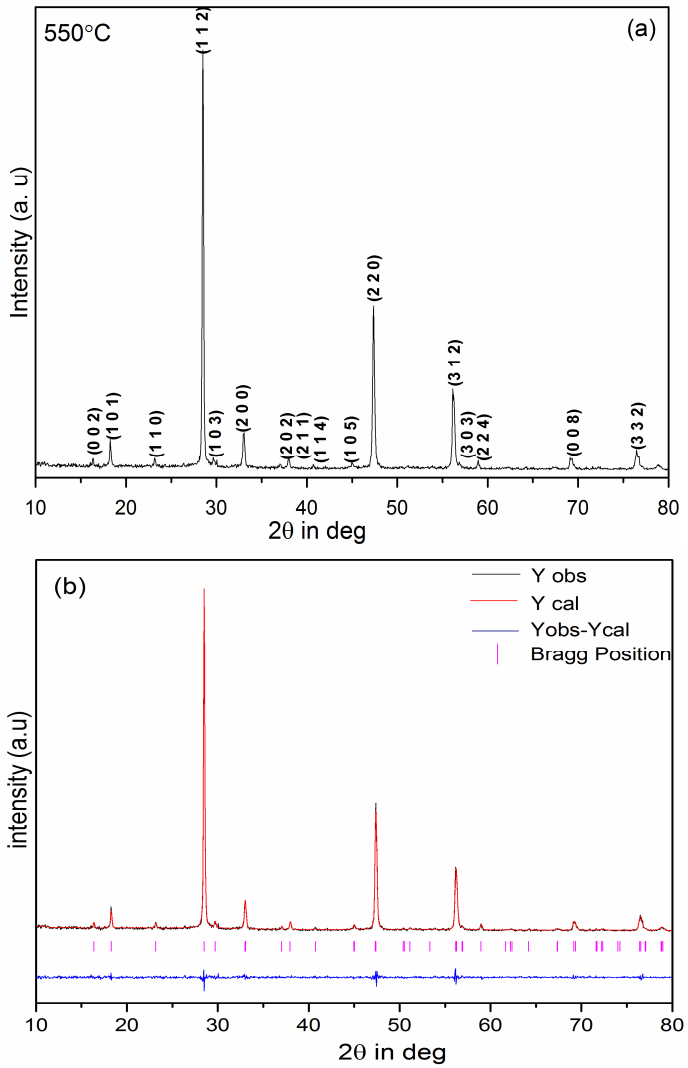

Fig. 3.5 High Resolution Grazing incidence XRD pattern of the film sulphurized at 550°C (a) and Rietveld refined plot (b)

3.1.6 Defect Physics

P type conductivity in CZTS absorber is mainly due to its intrinsic point defects. These defects play very important role to yield highly efficient solar cells by influencing generation, separation and

recombination of electron hole pair [19-22]. 13 different point defects were reported for CZTS and are mainly classified as vacancies (V_{Cu}^{-}, V_{Zn}^{2-}, V_{Sn}^{4-}, V_S^{2+}), antisites (Cu_{Zn}^{-}, Zn_{Cu}^{+}, Cu_{Sn}^{3-}, Sn_{Cu}^{3+}, Zn_{Sn}^{2+}, Sn_{Zn}^{2-}) and interstitial defects (Cu_i, Zn_i, Sn_i). Defect complexes are also possible in CZTS system; they are [V_{Cu}+Zn_{Cu}], [V_{Zn}+Sn_{Zn}], [Zn_{Sn}+2Zn_{Cu}], [2Cu_{Zn}+Sn_{Sn}], [Cu_{Zn}+Zn_{Cu}], [Cu_{Sn}+Sn_{Cu}] and [Zn_{Sn}+Sn_{Zn}] [19]. These defects and defect-complexes form shallow accepter/donor levels, deep trap states and mid gap states within the band gap of CZTS [19]. A few studies were reported describing the defect physics of CZTS [19-24]. The theoretical studies were based on DFT calculations.

Cu_2ZnSnS_4 has three different cation species with similar radii giving rise to various possible antisite defects. [19,22]. Among the cations, Cu and Zn have small size and valence difference, and hence the antisite Cu_{Zn} can have low formation energy since the difference between Cu and Zn is smaller than Cu and vacancy. Thus exchange of Cu and Zn atoms in the Cu_{Zn} layer costs very little energy [24]. However, this is different from $CuInSe_2$, where Cu vacancy dominates, and the transition energy level of this antisite is relatively deeper than V_{Cu}. There is large difference between the cations Cu and In, and hence the antisite Cu_{In} is expected to have higher formation energy than V_{Cu}. The intrinsic p-type conductivity in CZTS is attributed to the Cu_{Zn} antisite, which has an acceptor level deeper than the Cu vacancy [21]. The low formation energy of acceptor defects makes n-type doping difficult in Cu_2ZnSnS_4 [19].

The possible secondary and ternary phases, which have to be avoided during the phase formation of CZTS, are CuS, Cu_2S, ZnS, SnS, SnS_2, and Cu_2SnS_3, and also other compounds such as $Cu_4Sn_7S_{16}$ or $Cu_9Zn_3Sn_4S_{16}$ formed under certain conditions [21]. In order to get phase pure CZTS, Chen et al constructed a polyhedron of chemical potential region where CZTS is stable, based on the fact that the chemical potential of the constituent elements of the concerned impurity phase must be less than its formation enthalpy. The three dimensional chemical potential thus obtained was very small. The group found that the chemical potential of Zn is much lower than that of Cu, and hence concluded that Cu-rich and Zn-poor conditions are necessary for the growth of phase pure CZTS.

However, most of the experimental results already reported point out Cu-poor and Zn-rich conditions for achieving higher efficiency in CZTS cells [5,25-27]. And the relatively deep acceptor level of Cu_{Zn} may not be ideal for solar cell application [21]. This has led to the concept of passivation of active point defects through the formation of the above mentioned defect complexes. It has been pointed out that the antisite defect pair $[Cu_{Zn}^{-} + Zn_{Cu}^{+}]^0$ is easier to form in CZTS, but will not lead to strong carrier separation [21]. The other antisite pair Zn_{Sn} and Cu_{Sn} is less favorable because of large chemical and size disparity. The formation energy of the $[V_{Cu}^{-}+Zn_{Cu}^{+}]^0$ is 0.65 eV in the calculated polyhedron of the chemical potential region, where the intrinsic defects have positive formation energies [21]. Formation of this pair is said to be beneficial for maximizing

solar cell performance. The formation energy decreases rapidly when Cu becomes poorer and Zn becomes richer. But in this case, the formation of ZnS has to be avoided [21,28].

Since CZTS forms in a very small window, it is very important to control the deposition conditions. The films have to be grown under Cu-poor and Zn-rich conditions, which will yield required defects V_{Cu} and Zn_{Cu} in the system. However, the formation of secondary phases has to be avoided during fabrication of the films. Most researchers have been investigating to explore novel deposition methods for CZTS thin films to control defect engineering without forming secondary phases. Studies on elemental composition ratios of CZTS films give brief information about the Cu poor and Zn rich nature of the films.

3.1.7 Elemental composition analysis

Elemental analyses of films sulphurized at different temperatures were examined by EDXS and ICP-AES (Inductively Coupled Plasma-Atomic Emission Spectroscopy). Table 3.2 shows the elemental composition results. In CZTS, the ideal stoichiometry corresponds to Cu/(Zn+Sn) and Zn/Sn ratios of unity. As seen in Table 3.2, these ratios for the films sulphurised at 400°C and 450°C are very low. The ratios Cu/(Zn+Sn) and Zn/Sn for the films sulphurized at 500°C were 0.80 and 1.03, and the corresponding values at 550°C were 0.84 and 0.98, respectively. To further establish the elemental composition of the film sulphurized at 550°C, the films were examined by ICP-AES and the Cu/(Zn+Sn) and Zn/Sn ratios obtained from this study were 0.93 and 1.09, respectively. The results obtained in the EDXS analysis

for Cu/(Zn+Sn) and Zn/Sn ratios were 0.84 and 0.98, respectively. ICP-AES results of the film sulphurised at 550°C confirmed the formation of Cu poor Zn rich films.

Table 3.2 EDXS and ICP-AES results of the CZTS thin films

Temperature	Cu (at%)	Zn (at%)	Sn (at%)	S (at%)	Cu/ (Zn+Sn)	Zn/Sn
EDXS						
400°C	15.21(±3)	8.29(±1)	12.17(±2)	64.33(±3)	0.74	0.68
450°C	15.71(±2)	8.82(±4)	11.25(±4)	64.22(±6)	0.78	0.78
500°C	17.17(±3)	10.86(±3)	10.53(±3)	61.44(±3)	0.80	1.03
550°C	18.07(±1)	10.61(±2)	10.79(±3)	60.53(±4)	0.84	0.98
600°C	16.8(±2)	9.14(±1)	11.22(±2)	62.84(±4)	0.83	0.81
ICP AES						
550°C	19.05(±0.01)	10.68(±0.01)	9.83(±0.1)	59.99(±0.1)	0.93	1.09

3.1.8 Surface morphology

Fig. 3.6 shows the SEM images of the dip coated CZT precursor films sulphurized at different temperatures. As seen in the images, the grain size is increased to micrometer range with increase in sulphurization temperature. Film sulphurized at 550°C consists of large grains with size ranging from 300 to 700nm. Films morphology becomes worse due to secondary phase formation when the sulphurization temperature reaches 600°C.

For better understanding of grain size and grain morphology, the films sulphurized at 500°C and 550°C were further analyzed by Field Emission SEM (FESEM). FESEM gives high resolution images and better focus compared to conversional SEM as discussed in chapter 2 section 2.2.4. Fig. 3.7 shows the higher resolution field

emission SEM images of the films sulphurized at 500°C and 550°C. It can be seen from Fig. 3.7 (a and b) that the grain size of the film sulphurized at 550°C is very large compared to that of the film sulphurized at 500°C. The grain and grain boundaries are clearly visible at this temperature. Fig. 3.7(c) shows the cross section of the film sulphurized at 550°C. Thickness of the film was found to be ~700nm. .

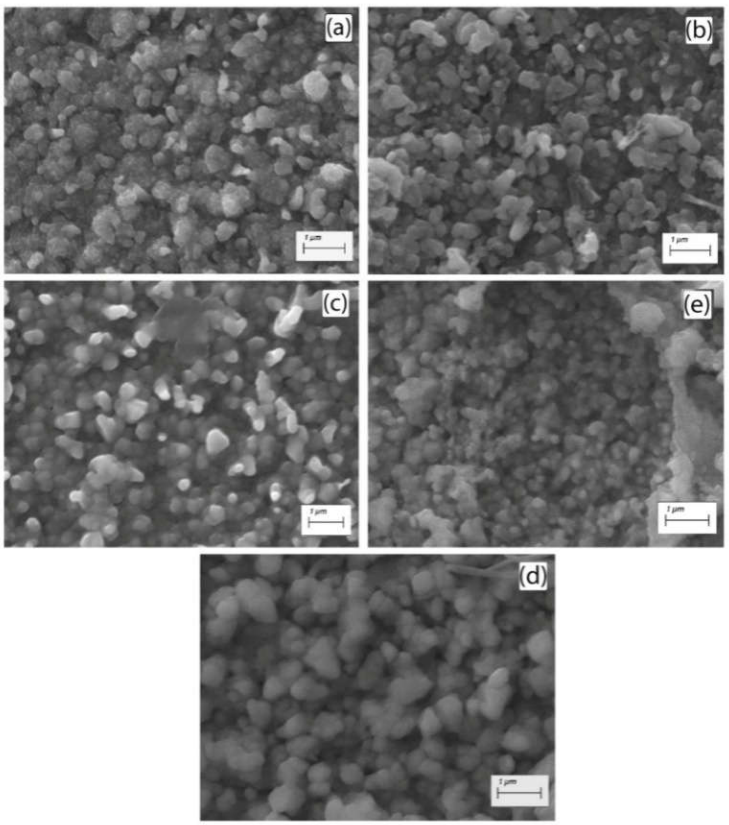

Fig. 3.6 SEM images of dip coated CZT precursor films sulphurized at (a) 400°C (b) 450°C (c)500°C (d) 550°C (e) 600°C

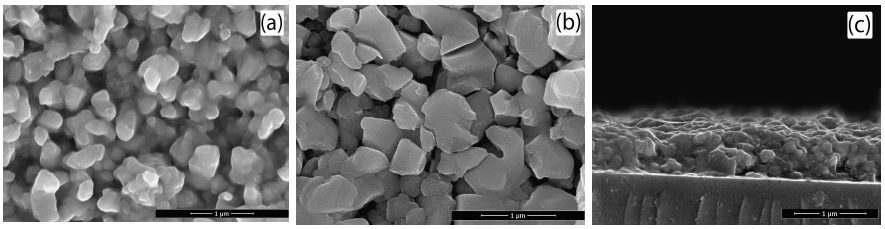

Fig. 3.7 FESEM images of CZT precursor films sulphurized at (a) 500°C, (b) 550°C and (c) cross section of 550°C sulphurized film

3.1.9 Optical Properties

The direct band gap energy of CZTS thin film was calculated using the Tauc relation [29,30], as described in chapter 2 section 2.2.7. Fig. 3.8 (a) shows the $(\alpha h\nu)^2$ versus hν curve of the films sulphurized at different temperatures and (b) shows the absorption coefficient vs wavelength plot of CZT precursor film sulphurized at 500°C and 550°C. Band gap was estimated by extrapolating the linear portion of the plot of $(\alpha h\nu)^2$ versus hν to the x intercepting point at y=0 (inset of Fig. 3.8(a)). As seen in the Figure, the band gap is changed from 1.47eV to 1.65eV with increase in the sulphurization temperature. The observed change in the band gap may be due to the difference in the crystallinity and the presence of secondary phases [27,29,30], as observed in the XRD and Raman studies. Films annealed at 500°C and 550°C exhibited band gaps of 1.47eV and 1.48eV; these values are close to the optimum value of 1.5eV required for ideal photovoltaic application [7,29]. Fig. 3.8(b) shows the absorption coefficient versus

wavelength plot of CZT precursor film sulphurized at 500°C and 550°C. From the Fig. 3.8(b) the absorption coefficient of the films was calculated and found to be ~ 10^4 cm^{-1} in the visible region; this value indicates that the dip coated CZT precursor film sulphurized at 500°C and 550°C can absorb most of the incident radiation with minimum film thickness.

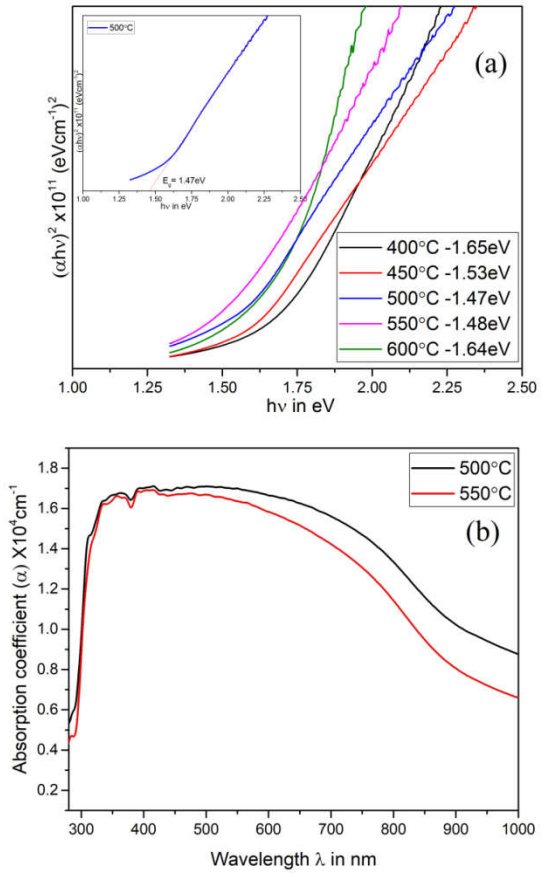

Fig. 3.8 (a) $(\alpha h\nu)^2$ versus photon energy (hν) of dip coated CZT precursor films sulphurized at different temperatures and (b) shows the absorption coefficient versus wavelength plot of CZT precursor film sulphurized at 500°C and 550°C.

3.1.10 Electrical Properties

To confirm the p type nature of the films and to measure the electrical properties, Hall measurements were carried out in van der pauw configuration with a constant magnetic field of 0.54Tesla (chapter 2 section 2.2.8). Carrier density, mobility and resistivity of the films were measured and are given in Table 3.3. *P* type nature of the films was confirmed from the positive sign of the Hall coefficient and carrier concentration. As seen in the Table 3.3, the carrier concentration increases by one order at 500°C, the mobility shows a reverse trend. However, the resistivity decreases slightly at this temperature. The decrease in mobility may be due to the decrease of $Cu_{2-x}S$ phase as observed in XRD and Raman. $Cu_{2-x}S$ phase shows conducting nature in CZTS thin films [19,31].

Table 3.3 Electrical properties of CZTS films sulphurized at different temperature

Sulphurizing temperature	Carrier concentration ($/cm^3$)	Mobility (cm^2/Vs)	Resistivity (Ωcm)
400°C	1.823×10^{17}	46.960	0.729
450°C	3.814×10^{17}	10.680	1.533
500°C	1.629×10^{18}	2.711	1.414
550°C	1.434×10^{18}	5.257	0.828
600°C	3.159×10^{17}	0.291	68.020

When the sulphurization temperature is increased from 500°C to 550°C, the carrier concentration decreases from $1.692\times10^{18}cm^{-3}$ to $1.434\times10^{18}cm^{-3}$. The mobility increases from $2.711cm^2/Vs$ to $5.257cm^2/Vs$, in this sulphurization temperature. The improved mobility of the films at 550°C may be attributed to the better structural quality of the film at this temperature [7] As described in the XRD results (Fig. 3.3 and Table 3.1), the crystallite size of the film increases from 47nm to 58nm with the increase in sulphurization temperature from 500°C to 550°C. Long et al [7] reported the electrical properties of spin coated CZTS films and found a decrease in the carrier concentration with increase in sulphurization temperature. The film resistivity reported in this article is very high compared to the results of this study. However, carrier concentration, mobility and resistivity of the films of this study are similar to the values reported by several other groups. The carrier concentration, mobility and resistivity reported by Tanaka et al. for their CZTS films fabricated via hybrid sputtering technique [32] were $8\times10^{18}/cm^3$, $6cm^2/Vs$ and $0.13\Omega cm$, respectively. The corresponding values reported by Zhang et al. [33] for the films prepared by sulphurizing ion beam sputtered precursor films were $8.2\times10^{18}/cm^3$, $6.3cm^2/Vs$ and $0.16\Omega cm$ respectively. In another article, Zhou et al. [34] reported the electrical properties of screen printed CZTS films. The carrier concentration, mobility and resistivity of these films were $3.8\times10^{18}/cm^3$, $12cm^2/Vs$ and $0.649\Omega cm$, respectively. In the present study, the carrier concentration and the mobility decreased considerably to $3.159\times10^{17}/cm^3$ and $0.219cm^2/Vs$ when the sulphurization temperature was increased to 600°C. The

increased resistivity (68 Ωcm) at 600°C may be due the undesired ZnS phase, which was observed in Raman and XRD studies.

3.2 Cu_2ZnSnS_4 film from CZTS precursor and subsequent sulphurization

Precursor solution for dip coating containing sulphur was prepared by dissolving copper (II) acetate monohydrate [$(CH_3COO)_2Cu.H_2O$, Merck Emsure, 99-102%], zinc (II) acetate dihydrate [$(CH_3COO)_2Zn.2H_2O$, Merck Emsure, 99.5-101%], tin (II) chloride dehydrate [$(SnCl_2.2H_2O$, Merck Emsure, 98-103%] and thiourea [$(H_2NCSNH_2$, Merck Emparta, 99%] in to 2-methoxy ethanol [ethylene glycol monomethyl ether, $CH_3OCH_2CH_2OH$, Merck Emparta, 99.3%] and monoethanolamine (MEA, C_7H_7NO,99%). Thiourea was used as sulphur source in the precursor solution. As described earlier, 2-methoxyethanol and MEA were used as solvent and stabilizer, respectively. copper (II) acetate monohydrate, zinc (II) acetate dihydrate, tin (II) chloride and thiourea were dissolved in the solution containing 2-methoxyethanol and MEA. The resultant solution was stirred at 45°C for 1 hour to dissolve the metal complexes and thiourea completely to obtain a clear and homogeneous solution.

3.2.1 CZTS film fabrication by dip coating

As described in the previous section, the glass substrates were cleaned with standard cleaning procedure. The films were coated on to the pre-cleaned glass substrates with dipping/withdrawal speed of 30mm/minute. The dip coated films were dried in air in tubular furnace

at 300°C for 10 minutes. The process was repeated for 10 times to increase the film thickness. Flow chart for the coating process adopted is shown in Fig. 3.9.

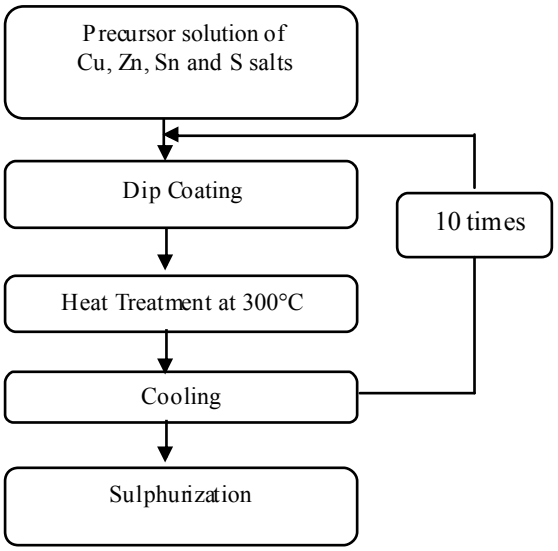

Fig. 3.9 Flow chart of the coating of CZTS thin films by dip coating

Precursor films with sulphur were further annealed in reactive atmosphere [N_2(95%)+H_2S(5%)] to compensate possible sulphur loss, which may occur during annealing process [7]. The effects of sulphurization temperature on structural, optical, surface morphological and electrical properties of the films were studied in detail.

3.2.2 *Structural studies*

3.2.2.1 *X-Ray Diffraction studies*

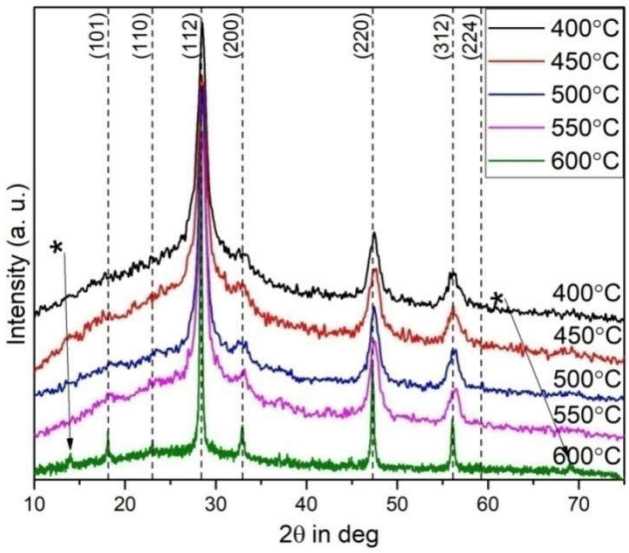

Fig. 3.10 XRD patterns of films annealed at 400°C, 450°C, 500°C, 550°C and 600°C

XRD patterns of the CZTS precursor films sulphurized at different temperatures are shown in Fig.3.10. Crystal structure and phase purity of the films were confirmed by comparing the observed *d* values with those in the ICDD powder diffraction file 26-0575. The films showed characteristic peaks of CZTS at 2θ angles 28.5°, 32.9°, 47.4° and 56.3°. However, the film sulphurized at 600°C exhibited two additional peaks at 2 theta 14° and 69°, which are identified as due to SnS_2 secondary phase, with the help of ICDD file 89-2028. This higher annealing temperature might have resulted in melting and evaporation

of film, which may be the reason for the formation of secondary phases [14] at this temperature.

Table 3.4 Lattice parameters and average crystallite size of the films annealed at different temperatures

Sulphurization temperature (°C)	Lattice parameter (nm)		Crystallite size (nm)
	a	*c*	
400	0.5409	1.0825	6
450	0.5387	1.0963	8
500	0.5387	1.0970	11
550	0.5424	1.0758	14
600	0.5435	1.0981	19
ICDD 26-0575	*0.5427*	*1.0848*	--

Lattice constants of the films annealed at different temperatures were estimated and are shown in Table 3.4. The values are in good agreement with those of the standard ICDD data of kesterite structure (a=b=0.5427 nm and c=1.0848nm). As seen, the diffraction peaks become narrow with increase in sulphurization temperature indicating increased crystallite size for the films. Change in average crystallite size with annealing temperature was analyzed using Scherrer's formula [9] and results are summarized in Table 3.4. As given in the table, the film sulphurized at 400°C has average crystallite size of 6 nm, whereas the size of the film sulphurized at 600°C is 19 nm.

As explained in the previous section, it is difficult to confirm the formation of exact Cu_2ZnSnS_4 phase from X-ray diffraction studies

alone because of the similar crystal structure possessed by other secondary phases such as ZnS and Cu_2SnS_3 [11,12]. To confirm formation of phase pure CZTS, the films were further investigated by Raman spectroscopy.

3.2.2.*2 Raman spectroscopic studies*

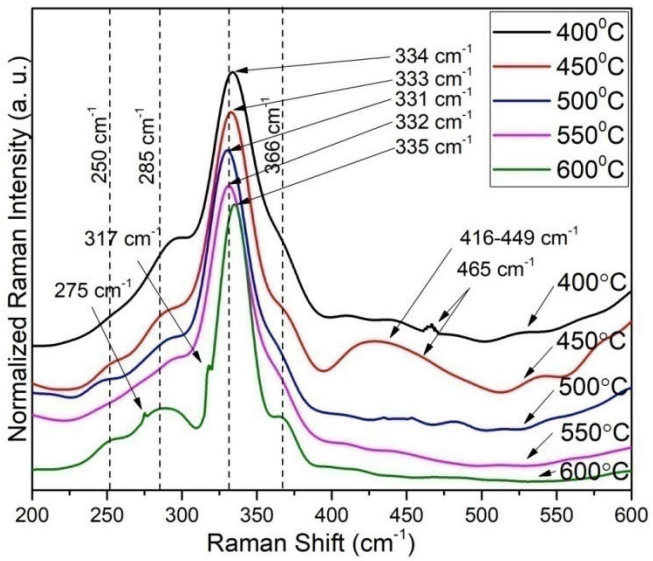

Fig. 3.11 Raman spectra of films sulphurized at 400°C, 450°C, 500°C, 550°C and 600°C

Raman spectra of the CZTS films sulphurized at various temperatures are shown in Fig. 3.11. The films showed characteristic CZTS peaks at 332cm^{-1} and 289 cm^{-1}, which arises from A symmetry mode of kesterite phase [10]. Film sulphurized at 400°C showed a peak at 366cm^{-1},which is due to the B(LO) symmetry mode of CZTS and another one at 465cm^{-1} corresponding to the vibrational mode of $Cu_{2-x}S$ [34,35]. When sulphurization temperature was increased from

400°C to 450°C, a broad peak was observed at 429cm^{-1} and another peak at 465cm^{-1}. The broad Raman mode observed at 429cm^{-1} could not be identified, but the peak at 465cm^{-1} corresponds to the vibrational mode of $Cu_{2-x}S$ phase [35].

At sulphurization temperatures 500°C and 550°C, two peaks at 280cm^{-1} and 366 cm^{-1} were observed, which were identified as the E(TO) and B(LO) symmetry modes of CZTS, respectively [10,36,37]. Film sulphurized at 600°C consists of four Raman modes, at 250cm^{-1}, 285cm^{-1}, 335cm^{-1} and 366cm^{-1} of CZTS, along with one mode of ZnS at 275cm^{-1} and one of SnS_2 at 315cm^{-1} [14,35,38]. Presence of SnS_2 secondary phase in the film sulphurized at 600°C has been observed in the XRD analysis. It is also observed that the major Raman peak corresponding to CZTS at 332cm^{-1} is shifted its position to higher wavelength side for the films sulphurized at 400°C, 450°C and 600°C. The observed shift may be due to the presence of secondary phases in CZTS [14] at these temperatures. Raman studies confirmed formation of phase pure CZTS at the sulphurization temperatures 500°C and 550°C.

3.2.3 Elemental composition analysis

Elemental compositions of as-coated and films sulphurized at various temperatures were studied by EDXS equipped with SEM. Table 3.5 shows the summary of the EDXS results. As-deposited film showed traces of oxygen, chlorine and silicon. All films sulphurized at different temperatures show presence of Si, which might be from the SLG substrate. The other impurities were removed after high

temperature annealing in sulphur atmosphere. Si peaks were subtracted from the experimental data to estimate the exact elemental ratios. Wang et al. [26] reported composition ratios of 1.2 for Zn/Sn and 1.85 for Cu/Sn in their 6.8% efficient CZTS solar cell. In the present study, the corresponding ratios were 1.19, 1.62 and 1.14, 1.75 respectively for the films sulphurized at 500°C and 550°C. As seen in the table, better composition ratios were obtained for the films sulphurized at 500°C and 550°C; both films show Cu poor and Zn rich composition. As described in section 3.1.6, films with Cu poor Zn rich condition is required for high performance CZTS solar cell fabrication.

Table 3.5 Elemental composition ratios of films sulphurized at various temperatures

Sulphurizing temperature	EDXS results						
	Cu (at.%)	**Zn** (at.%)	**Sn** (at.%)	**S** (at. %)	**Cu/ (Zn+Sn)**	**Zn/Sn**	Other elements
As coated	12.06(±3)	05.86(±2)	06.10(±4)	50.45(±5)	1.00	0.96	O(5.32at%), Si(10.61at%), Cl(9.61at%)
400 °C	15.38 (±4)	15.38 (±3)	5.76 (±3)	62.20 (±4)	0.79	2.67	----
450 °C	21.82 (±7)	9.75 (±5)	7.83 (±4)	60.60 (±8)	1.24	1.25	----
500 °C	20.86 (±5)	15.30 (±6)	12.88 (±4)	50.96 (±7)	0.74	1.19	----
550 °C	23.29 (±5)	15.23 (±8)	13.32 (±5)	48.16 (±6)	0.82	1.14	----
600 °C	28.38 (±3)	11.31 (±6)	11.05 (±6)	49.26 (±8)	1.27	1.02	----

Note. Silicon is observed in all films; this was subtracted, as mentioned in section 3.2.3)

To further analyze depth-dependent changes in elemental composition, EDXS spot analysis at different depths were carried out on cross-sections. Fig. 3.12 shows the SEM cross-sectional image of film sulphurized at 550°C along with the different spots selected for elemental analysis. Summary of the EDXS results obtained from different spots are given in Table 3.6. Similar results obtained from the elemental analysis at various spots confirmed uniform elemental composition of the film.

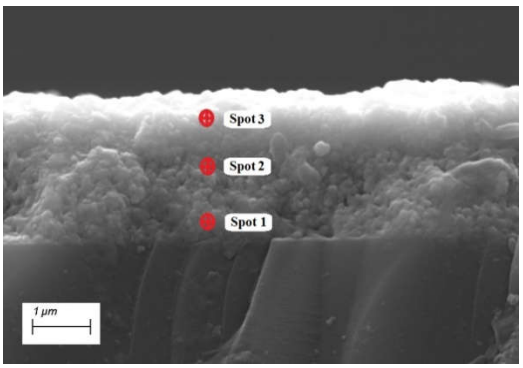

Fig. 3.12 SEM cross sectional image used for studying depth dependent changes

Table 3.6 Summary of EDXS results at different depths

Positions	EDXS results			
	Cu (at. %)	Zn (at. %)	Sn (at. %)	S (at. %)
Spot 1	23.31(±2)	15.30(±3)	13.38(±1)	48.01(±2)
Spot 2	23.28(±4)	15.28(±2)	13.35(±1)	48.09(±4)
Spot 3	23.35(±3)	15.31(±4)	13.32(±2)	48.02(±4)

3.2.4 Surface morphology

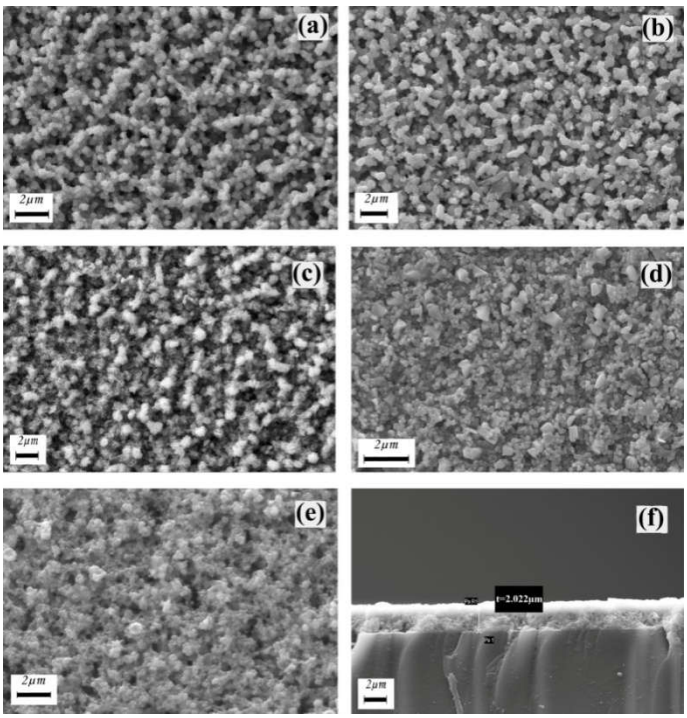

Fig. 3.13 SEM images of films sulphurized at (a) 400°C, (b) 450°C, (c) 500°C, (d) 550°C, (e) 600°C and (f) cross section of the film sulphurized at 550°C

Surface morphologies of dip coated CZTS films sulphurized at different temperatures studied by scanning electron microscope are shown in Fig.3.13. As seen in the images, the films consist of particles with uniform distribution and no cracks were observed in the films. The grain sizes of the films were found to increase when the sulphurization temperature is increased from 400°C to 500°C. The morphology was found to change from porous to dense nature at 500°C sulphurization temperature. As seen, sulphurization at 550°C leads to completely different surface morphology, where one can see

comparatively lower grain size. However, XRD and Raman studies revealed improved crystallinity at this temperature. Though the grain structures of the films sulphurized at 550°C and 600°C are different from those of the films sulphurized at lower temperatures, the cross sectional SEM confirms dense nature of the films. Similar surface morphology was reported for CZTS films prepared by dip coating using methanol based precursor solution [39]. Fig. 3.13(f) shows the cross sectional image of film sulphurized at 550°C and the thickness was found to be ~2μm.

3.2.5 Optical properties

Energy band gaps were calculated by extrapolating the linear portion of $(\alpha h\nu)^2$ versus hν plots (Tauc plot) to the x axis (Fig. 3.14). The optical band gaps of the films estimated are given in Table 3.7. The band gap was found to increase from 1.23eV to 1.46eV, when the sulphurization temperature was increased from 400°C to 600°C. Raman spectra revealed presence of $Cu_{2-x}S$, which has relatively narrow bandgap [27], in the films sulphurized at 400°C and 450°C and this may be the reason for the lower band gap observed at lower sulphurization temperatures [27,40]. The band gap calculated for the film sulphurized at 500°C was 1.39eV, which is slightly lower than the values reported earlier [33,34,36]. However, the film sulphurized at 550°C exhibited band gap of 1.43eV, which is close to the required band gap for CZTS absorber film. Higher band gap was observed for the film sulphurized at 600°C (1.46eV); however, XRD and Raman studies revealed the presence of secondary phases in this film.

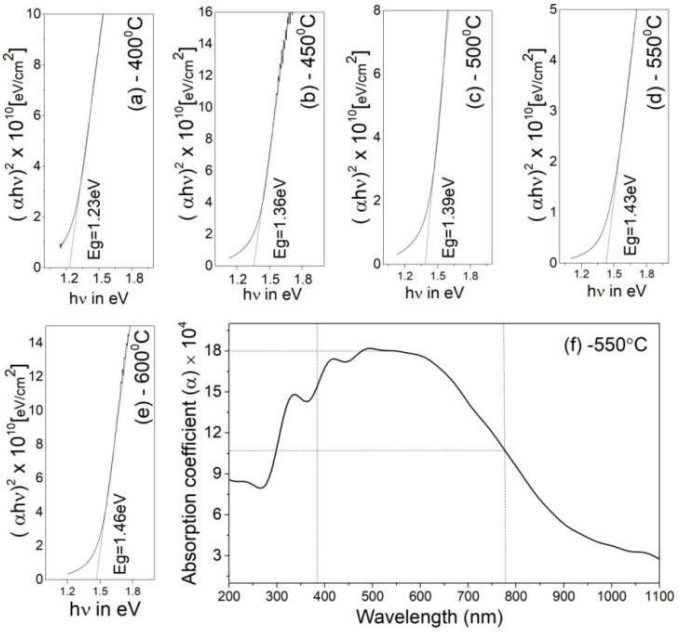

Fig. 3.14 (*a-e*) $(\alpha h\upsilon)^2$ versus hυ plots of dip coated CZTS films sulphurized at various temperatures, (*f*) optical absorption coefficient versus wavelength plot of the film sulphurized at 550°C.

Fig. 3.14(f) shows the absorption coefficient versus wavelength plot of the film sulphurized at 550°C. As seen in the plot, the absorption coefficient is almost constant in the visible region and decreases thereafter at higher wavelengths. Efficient solar cell absorber should have an absorption coefficient above $10^4 cm^{-1}$. Film sulphurized at 550°C exhibited an average absorption coefficient of $\sim 1.4 \times 10^5 cm^{-1}$ in the visible region (380nm to 780nm) indicating that film can absorb most of the incident radiations with minimum film thickness.

Table 3.7 Optical band gap of films sulphurized at different temperatures

Sulphurizing temperature	Band gap (eV)
400°C	1.23
450°C	1.36
500°C	1.39
550°C	1.43
600°C	1.46

3.2.6 Electrical properties

Electrical properties of the dip coated Cu_2ZnSnS_4 films sulphurized at different temperatures were studied using Hall Effect measurements with magnetic field intensity 0.54T, as described in the chapter 2 section 2.2.8 of this thesis. The summary of the Hall analysis are given in Table 3.8. Positive sign of the carrier concentration indicated *p* type nature of the films. As seen in the table, carrier concentrations of the films decrease from 1.4×10^{19} to $1.4\times10^{16}cm^{-3}$ with increase in sulphurization temperature, from 400°C to 600°C. Maximum carrier concentration was obtained at 400°C, while the mobility was low at this temperature. With further increase in temperature, the carrier concentration decreased (1.4×10^{19} to 1.4×10^{16} cm^{-3}) and mobility increased (0.2 to 21.8cm^2/Vs). Increased mobility may be due to the improved crystalline size of the film, as observed in the XRD; better crystallinity will improve carrier mobility by weakening grain boundary scattering [41]. The carrier concentrations of the films were found to decrease with increase in sulphurization

temperature. The observed increase in Cu/(Sn+Zn) ratio with sulphurization temperature (Table 3.5) indicates decrease in Cu vacancies which are the main source of holes in CZTS film [42]. However, as seen in the Table, higher Cu/(Zn+Sn) ratio is also observed for the film sulphurized at 450°C; which also exhibited better carrier concentration and this may due to the presence of secondary phases observed in the film after sulphurization [43].

Table 3.8 Electrical properties of the films sulphurized at different temperatures

Temperature (°C)	Carrier concentration (/cm^3)	Mobility (cm^2/Vs)	Resistivity (Ωcm)
400	1.413×10^{19}	0.2753	1.605
450	1.019×10^{18}	0.3642	16.83
500	6.617×10^{17}	0.6225	15.15
550	3.157×10^{17}	2.577	7.672
600	1.412×10^{16}	21.79	22.90

In the present study, minimum electrical resistivity (1.6Ωcm) was observed for the film sulphurized at 400°C and maximum resistivity (22.9Ωcm) for the film sulphurized at 600°C. Higher resistivity observed at 600°C may be due to the observed ZnS phase at this sulphurization temperature [42, 44]. The decrease in resistivity with increase in sulphurization temperature from 500°C to 550°C may be because of increased mobility, this may be due to the improved crystallinity of the film or its changed surface morphology at this temperature [42,43]. The carrier concentration, mobility and resistivity

obtained for the film sulphurized at 550°C were 3.157×10^{17} cm^{-1}, 2.577cm^2/Vs and 7.672Ωcm respectively; the values match with the results of the previous reports [45,46].

3.3 Comparison of properties of dip coated CZTS thin films prepared by two routes

Important properties obtained for the CZTS films coated by two routes are listed in Table 3.9. Of the two routes studied, the CZTS precursor film further sulphurized exhibited entirely different properties. While comparing both routes, each route has specific advantages and disadvantages. Optimized temperature was found to be 550°C for both routes. With same number of coatings, higher thickness was observed for the CZTS film sulphurized at 550°C. However, higher crystallite size, optimum band gap and good electrical properties were observed for CZT precursor films annealed in sulphur atmosphere. But highest absorption coefficient and comparatively better composition ratios (Cu poor and Zn rich) were observed for CZTS precursor film further annealed in sulphur atmosphere. Certain optimum properties were obtained in first route, while the second route exhibited some other excellent properties. For large scale production by dip coating, the second route, CZTS precursor film annealed in sulphur atmosphere, appears good.

Table 3.9 Comparison table of dip coated CZTS thin films by two routes

Properties	CZT precursor films annealed in sulphur atmosphere	CZTS precursor film annealed in sulphur atmosphere
Optimized sulphurization temperature	550°C	550°C
Lattice parameters	a=b=5.430Å & c=10.899Å	a=b=5.524Å & c=10.758Å
Crystallite size	58nm	14nm
Elemental ratios	Cu/(Zn+Sn)=0.93 and Zn/Sn=1.09	Cu/(Zn+Sn)=0.82 and Zn/Sn=1.14
Film thickness	~700nm	~2μm
Absorption coefficient	$\sim 10^4 cm^{-1}$	$\sim 10^5 cm^{-1}$
Band gap	1.48eV	1.43eV
Conductivity type	*p* type	*p* type
Carrier concentration	$1.434\times10^{18} cm^{-3}$	$3.157\times10^{17} cm^{-3}$
Mobility	$5.257 cm^2/Vs$	$2.577 cm^2/Vs$
Resistivity	0.828 Ωcm	7.672Ωcm

3.4. Summary

Cu_2ZnSnS_4 absorber thin films were successfully fabricated through a simple dip coating technique. Two types of stable precursor solutions with and without sulphur were prepared for dip coating. The precursor films prepared from the solution without sulphur were sulphurized at different temperatures to optimize the sulphurization temperature. XRD analysis revealed the formation of kesterite phase at a sulphuizing temperature of 500°C. However, the crystallinity of the film was found to increase when the temperature was increased to 550°C. Raman spectra of the films did not indicate any secondary

phases in the films annealed at 500°C and 550°C. The study indicated that the film annealed at 550°C possesses proper phase and crystallinity. Rietveld refinement technique was used to extract the structural properties using the GSAS software and the study confirmed the formation of phase pure kesterite. The absorption co-efficient calculated from the UV-visible spectra was found to be ~10^4 cm^{-1} in the visible region and the optical band gap estimated was 1.48 eV, for the films annealed at 550°C. SEM and FESEM studies show a thickness of ~700nm and good surface morphology with large grains for the film sulphurized at 550°C. Hall measurements revealed *p* type nature for all the films. Carrier concentration, mobility and resistivity of the films annealed at 550°C were found to be 1.434×10^{18} cm^{-3}, 5.2 cm^2/Vs and 0.82Ωcm respectively.

In the second route, CZTS precursor films dip coated from solution containing sulphur were annealed at various temperatures to study the effect of sulphurization on the structural, optical and electrical properties of CZTS thin films. XRD and Raman studies indicated the presence of secondary phases, such as, $Cu_{2-x}S$, ZnS, and SnS_2 in the films sulphurized at 400°C, 450°C and 600°C. However, the studies confirmed the formation of phase pure Cu_2ZnSnS_4 in the films sulphurized at 500°C and 550°C. The lattice parameter calculated for the films sulphurized at 500°C and 550°C were $a=b$=0.5387nm, c=1.0970nm and $a=b$=0.5427nm, c=1.0758nm, respectively. The average crystallite size was found to be 11nm for the film sulphurized at 500°C and 14nm for the one sulphurized at 550°C.

EDXS results indicated Cu poor and Zn rich composition for the films sulphurized at 500°C and 550°C. Surface morphological studies revealed a dense and improved grain structure for the films sulphurized at 550°C. The band gap of the film sulphurized at 500°C was comparatively low (1.39eV). However, band gap of 1.43 eV and absorption coefficient of ~10^5 cm^{-1} in the visible region were obtained for the film sulphurized at 550°C. Hall Effect measurements indicated *p* type nature for the films. The film sulphurized at 550°C exhibited a carrier concentration of $3.157\times10^{17}cm^{-3}$, mobility of $2.6cm^2/Vs$ and resistivity of 7.7Ωcm. The structural, optical and electrical investigations indicated optimum material properties required for thin film solar absorber materials in the dip coated film annealed in sulphur atmosphere (N_2+ H_2S) at 550°C.

4.5 References

1) Suryawanshi M P, Ghorpade U V, Shin S W, Pawar S A, Kim I Y, Hong C W, Wu M, Patil P S, Moholkar A V, Kim J H, A simple aqueous precursor solution processing of earth-abundant Cu_2SnS_3 absorbers for thin-film solar cells, ACS Appl. Mater. Interfac. 8 (2016) 11603.

2) Schwartz R W, Schneller T, Waser R, Chemical solution deposition of electronic oxide films, C. R. Chim. 7 (2004) 433.

3) Wang G, Zhao W, Cui Y, Tian Q, Gao S, Huang L, Pan D, Fabrication of a $Cu_2ZnSn(S, Se)_4$ photovoltaic device by a low-toxicity ethanol solution process, ACS Appl. Mater. Interfaces. 5 (2013) 10042.

4) Oral A Y, Menşur E, Aslan M H, Başaran E, The preparation of copper (II) oxide thin films and the study of their microstructures and optical properties, Mater. Chem. Phys. 83 (2004) 140.

5) Ahn S, Son T H, Cho A, Gwak J, Yun J H, Shin K, Ahn S K, Park SH, Yoon K, CuInSe$_2$ Thin Film Solar Cells with 7.72% Efficiency Prepared via Direct Coating of a Metal Salts/Alcohol Based Precursor Solution, Chem. Sus. Chem. 5 (2012) 1773.

6) Sun Y, Zhang Y, Wang H, Xie M, Zong K, Zheng H, Shu Y, Liu J, Yan H, Zhu M, Lau W, Novel non-hydrazine solution processing of earth-abundant $Cu_2ZnSn(S,Se)_4$ absorbers for thin-film solar cells, J. Mater. Chem. A. 1 (2013) 6880.

7) Long B, Cheng S, Lai Y, Zhou H, Yu J, Zheng Q, Effects of sulfurization temperature on phases and opto-electrical properties of Cu_2ZnSnS_4 films prepared by sol–gel deposition, Thin Solid Films. 573 (2014) 117.

8) Watjen J T, Scragg J J, Edoff M, Rubino S, Platzer-Bjorkman C, Cu out-diffusion in kesterites - A transmission electron microscopy specimen preparation artifact, Appl. Phys. Lett. 102 (2013) 051902.

9) Cullity B D, Stock S R , Elements of X-ray diffraction , Third Edn, Prentice Hall, New Jersey, (2001)

10) Dumcenco D, Huang Y S, The vibrational properties study of kesterite Cu_2ZnSnS_4 single crystals by using polarization dependent Raman spectroscopy, Opt. Mater. 35 (2013) 419.

11) Yazici S, Olgar MA, Akca FG, Cantas A, Kurt M, Aygun G, Tarhan E, Yanmaz E, Ozyuzer L, Growth of Cu_2ZnSnS_4 absorber layer on flexible metallic substrates for thin film solar cell applications, Thin Solid Films. 589 (2015) 563.

12) Yoo H, Kim J, Comparative study of Cu_2ZnSnS_4 film growth, Sol. Energy Mater. Sol. Cells. 95 (2011) 239.

13) Ge J, Wu Y, Zhang C, Zuo S, Jiang J, Ma J, Yang P, Chu J, Comparative study of the influence of two distinct sulfurization ramping rates on the properties of Cu_2ZnSnS_4 thin films, Appl. Surf. Sci. 258 (2012) 7250.

14) Hyesun Yoo, JunHo Kim, Comparative study of Cu_2ZnSnS_4 films growth, Sol. Energy Mater. Sol. Cells, 95 (2011) 239.

15) Larson A C, Von Dreele R B, General Structure Analysis System (GSAS), Los Alamos National Laboratory Report LAUR 86 (1994) 748.

16) Gurieva G, Guc M, Bruk L I, Izquierdo Roca V, Pérez Rodríguez A, Schorr S, Arushanov E, Cu_2ZnSnS_4 thin films grown by spray pyrolysis: characterization by Raman spectroscopy and Xray diffraction, Phys. Status Solidi c, 10 (2013) 1082.

17) Nozaki H, Fukano T, Ohta S, Seno Y, Katagiri H, Jimbo K, Crystal structure determination of solar cell materials: Cu_2ZnSnS_4 thin films using X-ray anomalous dispersion, J. Alloys Compd. 524 (2012) 22.

18) Schorr S, Hoebler H J, Tovar M, A neutron diffraction study of the stannite-kesterite solid solution series, Eur. J. Mineral. 19 (2007) 65.

19) Kumar M, Dubey A, Adhikari N, Venkatesan S, Qiao Q, Strategic review of secondary phases, defects and defect-complexes in kesterite CZTS–Se solar cells, Energy Environ. Sci. 8 (2015) 3134.

20) Chen S, Wang L W, Walsh A, Gong X G, Wei S H, Abundance of $Cu_{Zn}+Sn_{Zn}$ and $2Cu_{Zn}+Sn_{Zn}$ defect clusters in kesterite solar cells, Appl. Phys. Lett. 101 (2012) 223901.

21) Chen S, Gong X G, Walsh A, Wei S H, Defect physics of the kesterite thin-film solar cell absorber Cu_2ZnSnS_4, Appl. Phys, Lett. 96 (2010) 021902.

22) Chen S, Yang J H, Gong X G, Walsh A, Wei S H, Intrinsic point defects and complexes in the quaternary kesterite semiconductor Cu_2ZnSnS_4, Phys. Rev. B. 81 (2010) 245204.

23) Wang H, Progress in thin film solar cells based on, Int. J. Photoenergy. 2011 (2011).

24) Paris M, Choubrac L, Lafond A, Guillot-Deudon C, Jobic S, Solid-State NMR and Raman spectroscopy to address the local structure of defects and the tricky issue of the Cu/Zn disorder in Cu-poor, Zn-rich CZTS materials, Inorg. Chem. 53 (2014) 8646.

25) Tanaka K, Moritake N, Oonuki M, Uchiki H, Pre-annealing of precursors of Cu_2ZnSnS_4 thin films prepared by sol–gel sulfurizing method, Jpn. J. Appl. Phys. 47 (2008) 598.

26) Wang K, Gunawan O, Todorov T, Shin B, Chey S J, Bojarczuk N A, Mitzi D, Guha S, Thermally evaporated Cu_2ZnSnS_4 solar cells, Appl. Phys. Lett. 97 (2010) 143508.

27) Guan H, Shen H, Gao C, He X, Sulfurization time effects on the growth of Cu_2ZnSnS_4 thin films by solution method, J. Mater. Sci.: Mater. Electron. 24 (2013) 2667.

28) Walsh A, Chen S, Gong X G, Wei S H, Crystal structure and defect reactions in the kesterite solar cell absorber Cu_2ZnSnS_4 (CZTS): theoretical insights, AIP Conf. Proc. 1399 (2011) 63.

29) Chaudhuri T K, Tiwari D, Earth-abundant non-toxic Cu_2ZnSnS_4 thin films by direct liquid coating from metal–thiourea precursor solution, Sol. Energy Mater. Sol. Cells. 101 (2012) 46.

30) Kahraman S, Cetinkaya S, Podlogar M, Bernik S, Cetinkara H A, Güder H S, Effects of the sulfurization temperature on sol gel-processed Cu_2ZnSnS_4 thin films, Ceram. Int. 39 (2013) 9285.

31) Kim G Y, Kim J R, Jo W, Lee K D, Kim J Y, Nguyen T T, Yoon S, Effects of $Cu_{2-x}S$ phase removal on surface potential of Cu_2ZnSnS_4 thin-films grown by electroplating, Curr. Appl. Phys. 14 (2014) 1665.

32) Tanaka T, Nagatomo T, Kawasaki D, Nishio M, Guo Q, Wakahara A, Yoshida A, Ogawa H, Preparation of Cu_2ZnSnS_4 thin films by hybrid sputtering, J. Phys. Chem. Solids. 66 (2005) 1978.

33) Zhang J, Lexi S H, Yujun F U, Erqing X I, Cu_2ZnSnS_4 thin films prepared by sulfurization of ion beam sputtered precursor and their electrical and optical properties, Rare Metals. 25 (2006) 315.

34) Zhou Z, Wang Y, Xu D, Zhang Y, Fabrication of Cu_2ZnSnS_4 screen printed layers for solar cells, Sol. Energy Mater. Sol. Cells. 94 (2010) 2042.

35) Fernandes P A, Salomé P M, Da Cunha A F, Study of polycrystalline Cu_2ZnSnS_4 films by Raman scattering, J. Alloys Compd. 509 (2011) 7600.

36) Yoo H, Kim J, Comparative study of Cu_2ZnSnS_4 film growth, Sol. Energy Mater. Sol. Cells, 95 (2011) 239.

37) Khare A, Himmetoglu B, Johnson M, Norris D J, Cococcioni M, Aydil E S, Calculation of the lattice dynamics and Raman spectra of copper zinc tin chalcogenides and comparison to experiments, J. Appl. Phys. 111 (2012) 083707.

38) Nilsen W G, Raman spectrum of cubic ZnS, Phys. Rev. 182 (1969) 838.

39) Rakhshani A E, Thomas S, Cu_2ZnSnS_4 films grown on flexible substrates by dip coating using a methanol-based solution: electronic properties and devices, J. Electron. Mater. 44 (2015) 4760.

40) Siebentritt S, Why are kesterite solar cells not 20% efficient?, Thin Solid Films. 535 (2013) 1.

41) Dhanasekar M, Bhat S V, Facile synthesis of Cu_2ZnSnS_4 absorber layer for thin film solar cells using a highly stable precursor solution, Appl. Surf. Sci. 418 (2016) 194.

42) Long B, Cheng S, Zheng Q, Yu J, Jia H, Effects of sulfurization time and H_2S concentration on electrical properties of Cu_2ZnSnS_4 films prepared by sol–gel method, Mater. Res. Bull. 73 (2016) 140.

43) Patil R M, Nagapure D R, Mary G S, Chandra G H, Sunil M A, Subbaiah Y V, Prathap P, Gupta M, Rao R P, Low temperature

crystallization of $Cu_2ZnSnSe_4$ thin films using binary selenide precursors, J. Mater. Sci. Mater. Electron. 28 (2017) 18244.

44) Kevin P, Malik M A, O'Brien P, The controlled deposition of $Cu_2(Zn_vFe_{1-v})$ SnS_4, $Cu_2(Zn_vFe_{1-v})SnSe_4$ and $Cu_2(Zn_vFe_{1-v})$ $Sn(S_xSe_{1-x})_4$ thin films by AACVD: potential solar cell materials based on earth abundant elements, J. Mater. Chem. C. 3 (2015) 5733.

45) Silvena G G, John B, Christinal R A, Kumar M S, Chakravarty S, Rajesh A L, Solution Processed p-Type Cu_2ZnSnS_4 Thin Films for Absorber Layer, J. Inorg. Organomet. Polym. Mater. 27 (2017) 1556.

46) Aslan F, Goktaş A, Tumbul A, Influence of pH on structural, optical and electrical properties of solution processed Cu_2ZnSnS_4 thin film absorbers, Mater. Sci. Semicond. Process. 43 (2016) 139.

Chapter 4

Preparation of Cu_2ZnSnS_4 films by spin coating and study of their structural, morphological, optical and electrical properties

This chapter describes the fabrication of Cu_2ZnSnS_4 thin films by spin coating and the studies carried out to investigate their structural, morphological, optical and electrical properties. Two different solution based approaches were adopted to prepare precursor films by spin coating. The precursor films were converted to phase pure CZTS absorber films by various annealing/sulphurization techniques. Table 4.1 shows the various routes selected for fabricating phase pure CZTS thin films by spin coating and subsequent temperature treatment. Detailed studies on the structural and photovoltaic properties of films have been carried out after annealing/sulphurizing precursor films at different temperatures. Phase purity of the films was studied by XRD and Raman spectroscopy. Surface morphology of the films was examined by scanning electron microscope. Film thicknesses were determined from the cross-sectional FESEM images. Elemental compositions were studied by EDXS coupled to the SEM. UV-visible spectroscopy was used to calculate optical band gap and absorption coefficient of the films. Electrical properties of the films were studied using Hall measurements.

Table 4.1 Various routes adopted for fabricating phase pure CZTS thin films by spin coating and subsequent temperature treatment

Sl No.	Sample Code/details	Annealing/sulphurizing treatment
01	CZT *(Precursor solution without sulphur)*	Annealed at different temperatures in sulphur environment
02	CZTS *(Precursor solution with sulphur)*	Annealed at different temperatures in sulphur environment
03		Annealed at different temperatures in inert atmosphere (nitrogen)

4.1 Cu_2ZnSnS_4 films from CZT precursor and subsequent sulphurization

4.1.1 Preparation of stable precursor solutions for spin coating

Stable precursor solution without sulphur was prepared for spin coating using copper (II) acetate monohydrate (0.6 M), zinc (II) acetate dihydrate (0.3M), tin (II) chloride (0.3 M), 2-methoxyethanol and mono-ethanolamine (MEA). 2-methoxy ethanol and MEA were used as solvent and stabilizer respectively, as described in section 3.1.1 of this thesis. In spin coating technique, solution preparation and substrate cleaning procedure are similar to dip coating technique.

4.1.2 Fabrication of CZTS thin film by spin coating

For spin coating on to pre-cleaned glass substrates, 75µl of the precursor solution was used each time during the deposition process. The spin coating was performed at a speed of 3000 rpm for 20s. The films were dried after coating process at 300°C in a tubular furnace for

10 min to evaporate the solvent completely. The procedure was repeated for 10 times to achieve films with desired thickness. After the spin coating, precursor films without sulphur (CZT) were converted to Cu_2ZnSnS_4 by sulphurizing in an environment of sulphur [N_2(95%)+H_2S(5%) gas mixture], as described for dip coated films in the section 3.1.1 of this thesis. However, after sulphurization, the films except the ones sulphurized at 500°C and 550°C were peeled off from the glass substrates. Since the films prepared at 400°C and 450°C did not yield good quality films, further studies have been carried out with the films obtained at sulphurization temperatures 500°C and 550°C. After the sulphurization process, structural, optical, surface morphological and electrical properties of the films were studied.

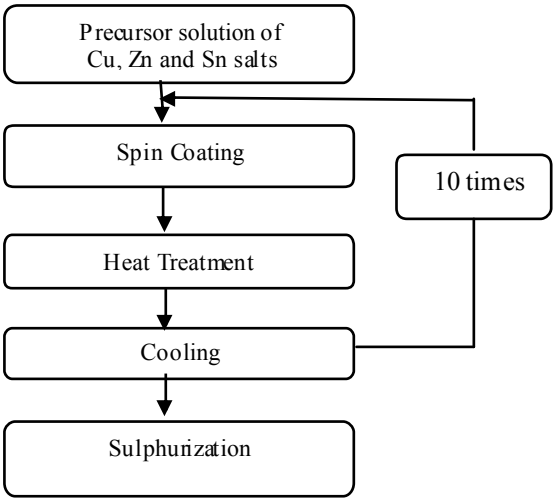

Fig. 4.1 Flow chart of the deposition of CZTS thin films by spin coating

4.1.3 Structural studies

4.1.3.1 X-ray Diffraction Studies

Fig. 4.2 shows the x-ray diffraction pattern of Cu_2ZnSnS_4 film prepared by spin coating followed by sulphurization in N_2+H_2S atmosphere at 500°C and 550°C. The XRD pattern shows peaks corresponding to kesterite Cu_2ZnSnS_4 structure. The peaks were indexed as (101), (112), (200), (220) and (303) planes of kesterite structure, with the help of the ICDD file 026-0575. There are no peaks corresponding to other secondary phases in the pattern of films sulphurized at 500°C. However, an additional peak at 31.7° was observed for the film sulphurized at 550°C. This peak was identified as due to $Cu_{2-x}S$ phase, with the help of ICDD powder diffraction file 32-0348. Thus the XRD analysis revealed secondary phase in the film sulphurized at 550°C.

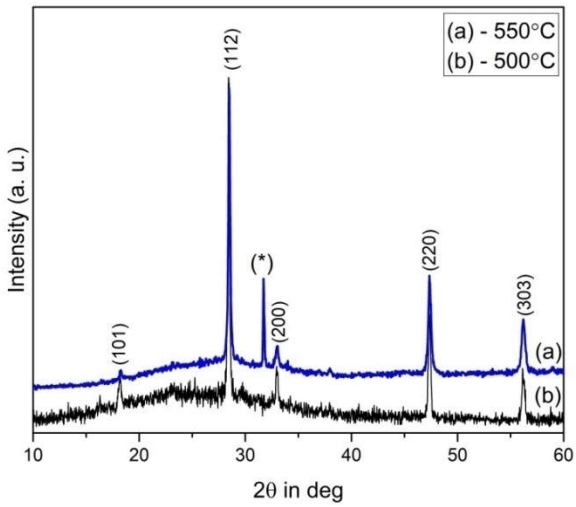

Fig. 4.2 XRD pattern of Cu_2ZnSnS_4 film sulphurized at 500ºC and 550ºC

Lattice constants based on CZTS tetragonal crystal structure estimated for the films sulphurized at 500°C and 550°C are shown in Table 4.2. The values obtained were found to match with those of the standard ICDD file 26-0575 ($a=b$=5.42700Å, c=10.84800Å), as seen in the table. The average crystallite size was calculated using the Scherrer's formula and W-H relation as described in section 2.2.1. The average size calculated for the films sulphurized are given in Table 4.2. The average size increases with increase in sulphurizing temperature. However, as discussed, secondary phase $Cu_{2-x}S$ was observed for the film sulphurized at 550°C.

Table 4.2 Lattice parameters and crystallite size for films sulphurized at 500°C and 550°C

Sulphurization temperature	Lattice parameter (Å)		Average crystalline size (nm)	W-H relation	
	$a=b$	c		Crystallite size (nm)	Strain
500°C	5.428(2)	10.851(1)	39	40	0.0026
550°C	5.435(2)	10.866(2)	44	51	0.0314

4.1.3.2 Raman spectroscopic Analysis

To further confirm the formation of phase pure Cu_2ZnSnS_4 film at 500°C in this approach, the samples were investigated by Raman spectroscopy. Fig. 4.3 shows the Raman spectra of CZTS thin films sulphurized at 500°C and 550°C. As seen, one major peak at 332cm^{-1} and a shoulder peak at 286cm^{-1} were observed, which are of Raman modes of CZTS and are in agreement with the Raman peaks reported

for kesterite in literature [1,2]. These peaks do not match with those of secondary phases β-ZnS and $Cu_{2-x}S$ [3]. For the film sulphurized at 550°C, one major peak at 334cm^{-1} and minor peaks at 248cm^{-1}, 284cm^{-1}, 372cm^{-1} and 474cm^{-1} were observed. Peaks at 334cm^{-1}, 248cm^{-1} 284cm^{-1} and 372cm^{-1} correspond to the A, B(TO), A and B (LO) vibrational modes of CZTS, respectively [1,4]. Peak at 474cm^{-1} may be due to the $Cu_{2-x}S$ phase [3,4] With the increase in sulphurization temperature from 500°C to 550°C major CZTS peak shift to higher wavelength (332cm^{-1} to 334cm^{-1}) and this may be due to the presence of secondary phase ($Cu_{2-x}S$), as observed in XRD and Raman analyses at this temperature.

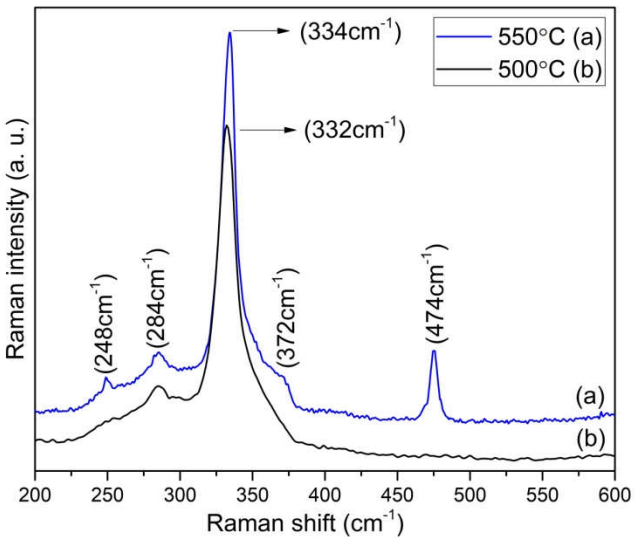

Fig. 4.3 Raman spectra of Cu_2ZnSnS_4 film sulphurized at 500ºC and 550°C

4.1.4 Elemental composition

The elemental analysis in the films was estimated by EDXS carried out along with the SEM study. Table 4.3 shows the summary of the elemental composition of the CZTS thin films prepared by sulphurizing spin coated CZT precursor films. As seen, the films sulphurized at 500°C are Sn poor and Zn rich, and the Cu/(Zn+Sn) ratio is unity. However, as described in section 3.1.6 of this thesis, Cu poor Zn rich condition is more preferable in the case of CZTS thin films. Films sulphurized at 550°C exhibited Cu rich and Zn poor nature, which is also not favorable for efficient CZTS solar cell [5-7]. The films were sulphur poor at 500°C and 550°C, and this may be due to the slow reaction of the CZT precursor film with H_2S gas mixture during sulphurization [8].

Table 4.3 Elemental compositions of films sulphurized at 500°C and 550°C

Sulphurizing temperature	EDXS results					
	Cu (at.%)	Zn (at.%)	Sn (at.%)	S (at %)	Cu/ (Zn+Sn)	Zn/Sn
500 ℃	25.79 (±4)	13.93(±4)	11.96(±3)	48.39(±7)	1.00	1.16
550 ℃	27.89 (±3)	11.63(±3)	11.61(±4)	48.87(±4)	1.20	1.00

4.1.5 Surface morphology

Fig. 4.4 shows the SEM image along with the cross sectional image of CZTS thin films sulphurized at 500°C. Grains were distributed uniformly on the surface with average grain size of ~200nm. Thickness of the film measured from the cross-sectional SEM images was found to be ~1.5µm

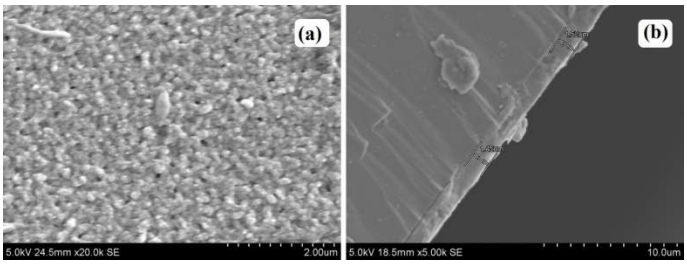

Fig. 4.4 SEM image (a) and its cross sectional image (b) of the films sulphurized at 500°C

4.1.6 Optical properties

Fig.4.5 (a) shows the absorption spectra of Cu_2ZnSnS_4 films sulphurized at 500°C in this route. Optical absorption coefficient (α) of the films calculated from the spectra was found to be ~$10^5 cm^{-1}$ in the visible region. This large value of α indicates that a layer thickness of a few micrometers is sufficient to absorb ~90% of the incident photons [4,9].

The energy band gap for direct band gap materials can be estimated using the well known Tauc's relation, as discussed in chapter

2 section 2.2.7. Band gap energy was deduced by extrapolating linear portion of $(\alpha h\nu)^2$ versus $h\nu$ plot to the x-axis.

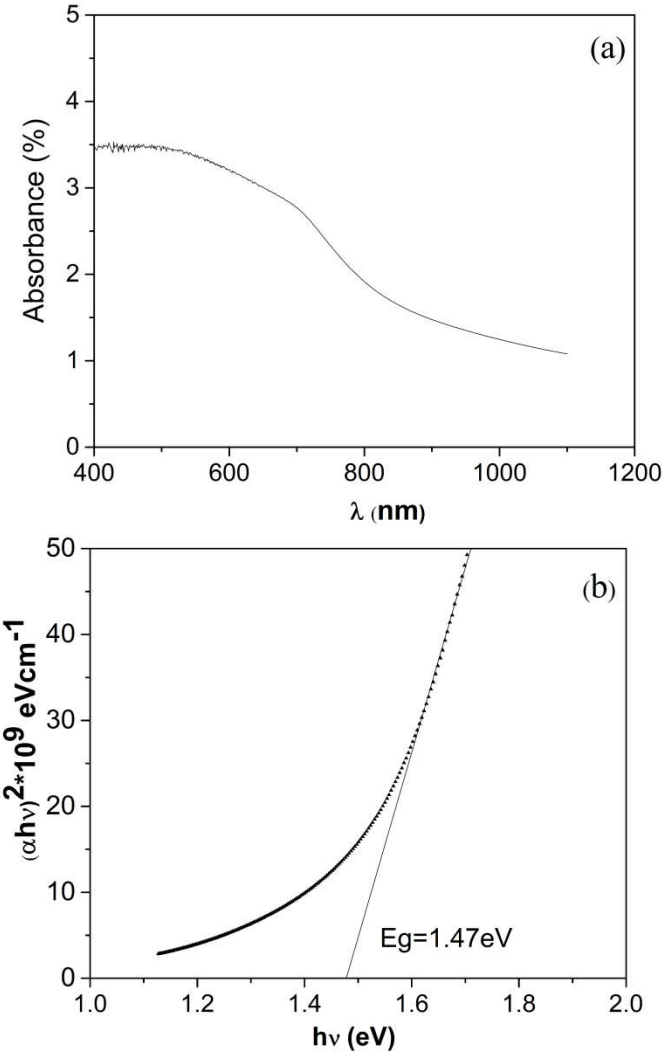

Fig. 4.5 (a) Absorption spectra of Cu_2ZnSnS_4 film sulphurized at 500°C, and (b) $(\alpha h\nu)^2$ versus $h\nu$ plot used for determining band gap

Fig.4.5 (b) shows the tauc's plot of the thin films sulphurized at 500°C. The band gap estimated for the film was 1.47eV. This is close to the optimum value for thin film solar cells, and in consistent with earlier report by Tanaka et al [8]. This group prepared CZTS thin films by spin coating followed by sulphurizing method and studied the effects of pre-annealing of precursor of Cu_2ZnSnS_4 thin films. They observed a variation in band gap from 1.20 to 1.53eV, in their study. Band gap of 1.47eV was observed for CZTS films pre-annealed at 560°C in air, followed by further sulphurization in N_2+H_2S atmosphere at 500°C for 1 hr. However, the same band gap was obtained in the present study without pre-annealing. Band gap of the film prepared by the present route indicates that the Cu_2ZnSnS_4 film can be used as an absorber layer in thin film solar cells.

4.1.7 Electrical properties

Electrical properties of the films were studied by Hall Effect measurement system. *p* type nature of the film was confirmed from Hall measurement studies. Carrier concentration, mobility and resistivity of the CZTS films sulphurized at 500°C were 1.71×10^{1} □ cm^{-3}, 48.20cm^2/Vs and 0.812 Ωcm, respectively. This is the highest mobility for CZTS films of all samples studied for the present thesis work. The electrical resistivity of the films was also found to be small (0.812 Ωcm). To the best of the author's knowledge, the highest mobility of 65cm^2/Vs was reported for CZTS films prepared by co-sputtering using metal targets and sulphurization in H_2S atmosphere [10]. As seen in section 4.1.4, the EDXS results revealed Cu rich, Zn

rich, and Sn poor compositions for the film sulphurized at 500°C. Muhunthan et. al. [10] reported similar composition for higher mobility for the film prepared by co-sputtering of metal targets. Metal rich (Cu,Zn) composition of films may be the reason for higher mobility of CZTS films [11,12].

4.2 Cu_2ZnSnS_4 films from CZTS precursor and subsequent sulphurization

4.2.1 Preparation of stable *precursor solutions for spin coating*

In this route, precursor solution for spin coating was prepared by incorporating thiourea as sulphur source. Copper (II) acetate monohydrate, zinc (II) acetate dihydrate, tin (II) chloride, thiourea, 2-methoxyethanol and mono-ethanolamine (MEA) were used for preparing stable precursor solution, as described in section 3.2.1 of this thesis.

4.2.2 Fabrication of CZTS thin film by spin coating

75µl of precursor solution was used each time during the deposition process. The spin coating was performed at a speed of 3000 rpm for 20s on pre-cleaned glass substrates. The films were dried after coating process at 300°C in a tubular furnace for 10 min to evaporate the solvent completely. The procedure was repeated for 10 times to achieve films with desired thickness. After spin coating, precursor films with sulphur (referred to as CZTS) were further sulphurized in an environment of N_2(95%)+H_2S(5%) gas mixture, as described in section 3.1.4 of this thesis. Films were sulphurized at different temperature to

study the effects of sulphurization temperature on the structural, optical and electrical properties of the CZTS thin films. After the sulphurization, structural, optical, surface morphological and electrical properties of the films were systematically studied.

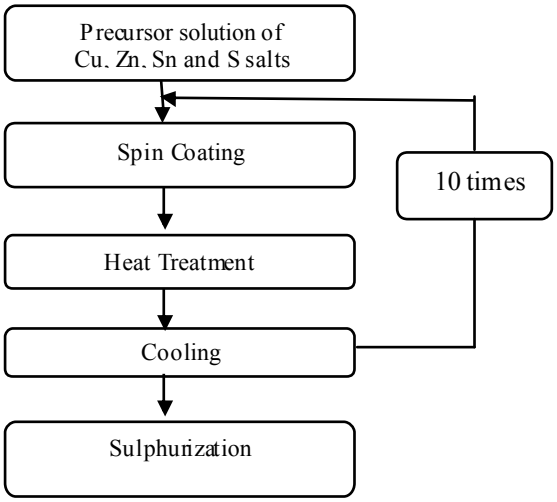

Fig. 4.6 Flow chart of the deposition of CZTS thin films by spin coating

4.2.3 Structural studies

4.2.3.1 X-ray Diffraction Studies

In this study, CZTS precursor thin films were prepared by spin coating technique using sulphur containing solution and the films were sulphurized subsequently at different temperatures (400°C, 450°C, 500°C, 550°C and 600°C) to investigate the effect of sulphurization temperature on phase formation. As described in the previous section, phase purity of the films was investigated initially by X-ray diffraction. Fig. 5.5 shows the XRD pattern of CZTS films sulphurized at different temperatures.

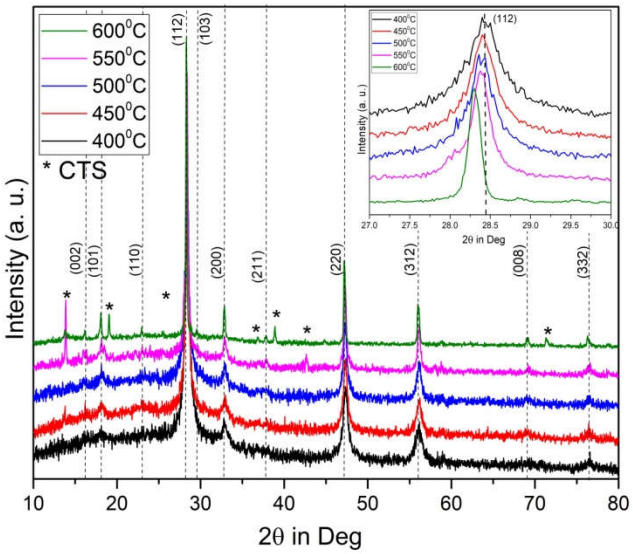

Fig. 4.7 XRD patterns of the films sulphurized at different temperatures

From the XRD patterns, all films were observed to be grown well with good crystallinity. For all annealing temperatures, film showed peaks corresponding to (101), (112), (200), (220), (312), (008) and (332) planes of kesterite phase, which are the characteristic peaks of CZTS. In addition to these peaks, CZTS films sulphurized at 450°C, 550°C and 600°C exhibited a few additional peaks, which were identified as due to Cu_2SnS_3 phase. Inset of Fig. 4.7 shows the magnified image of (112) plane of kesterite phase. As seen, the full width at half maximum (FWHM) of the peaks are found to decrease when sulphurizing temperature is increased from 400°C to 600°C. The film shows a shift in the position of (112) peak at 600°C sulphurization temperature. The shift in 2θ angle may be due to the presence of ternary phases [4,13]. The decrease of the FWHM of peaks with increase in sulphurization temperature may due to the improved

crystallinity of the CZTS films. Lattice constants of the films sulphurized at different temperature were estimated based on tetragonal symmetry. Table 4.4 shows the summary of the values of lattice constants estimated. These values are good agreement with the standard data, a = 0.5427nm and c = 1.0848nm (ICDD-PDF No.26-0575).

Table 4.4 Lattice parameters estimated for the films annealed at different temperatures

Sulphurization Temp. (°C)	Lattice Parameter (nm)		Scherrer Equation (nm)	W-H relation	
	$a = b$	c	Crystallite Size	Crystallite Size (nm)	Strain
400	0.5430	1.0901	15	34	0.0048
450	0.5427	1.0919	22	36	0.0034
500	0.5440	1.0861	31	38	0.0009
550	0.5430	1.0956	33	48	0.0017
600	0.5442	1.0988	40	63	0.0011
ICDD 26-0575	0.5427	1.0848	-----	-----	-----

Variation in crystallite size with sulphurization temperature was studied using Scherrer formula and Williamson-Hall (W-H) method. The W-H relation accounts the contribution from strain broadening as well. The results obtained from W-H relation and Scherrer method are given in Table 5.2. It can be seen that the values calculated for crystallite size using Scherrer formula is less than those obtained by W-H method. The differences in values of crystallite size by two methods are due to the strain observed (Table 4.4) in the CZTS films [14]. It reveals that importance of strain calculation in estimating

average crystallite size. As given in Table 4.4, the average crystallite size of the films increases with the increase in sulphurization temperature. Higher crystallite size was observed for films sulphurized at 600°C.

Crystal structure and phase purity of CZTS film cannot be distinguished clearly by X-ray diffractometry alone because of the identical crystal structure possessed by secondary phases such as ZnS, Cu_2SnS_3. The films were further investigated by Raman spectroscopy to confirm the phase formation.

4.2.3.2 Raman spectroscopic Analysis

Raman spectra of spin coated CZTS films sulphurized at different temperatures are shown in Fig.4.8. As shown in the Figure, the spectra are characterized by the presence of two main peaks at about 286cm^{-1} and 332cm^{-1}. These peaks were identified as the main vibrational A1 symmetry modes from CZTS [1-3]. The films sulphurized at 400ºC and 450ºC show one peak at 275cm^{-1}, which can be assigned to the characteristic peaks of ZnS phase [3]. In addition to the aforementioned peaks of CZTS, the films sulphurized at 500^{o}C, 550ºC and 600ºC exhibits peaks at 352cm^{-1} and 371cm^{-1}, which can be assigned to the B(TO) and B(LO) vibrational modes of CZTS, respectively [1,15]. Two other distinct peaks were observed clearly in the films sulphurized at higher temperatures (550°C and 600°C). The film treated at 550ºC and 600ºC shows peaks at 317cm^{-1} and 362cm^{-1}; the 317cm^{-1} peak can be assigned to the characteristic peaks of

Cu_3SnS_4 phase [16]. The origin of the other peak at 362cm^{-1} is still unclear. A few reports show a mode at 366cm^{-1}, which is also a vibration mode of CZTS phase [15,17], and another mode at 360cm^{-1}, which is the characteristic peak of Cu_2SnS_3 [16,18]. A mode at 296cm^{-1} due to Cu_2SnS_3 [19,20] was also observed for the films sulphurized at 550^{o}C.

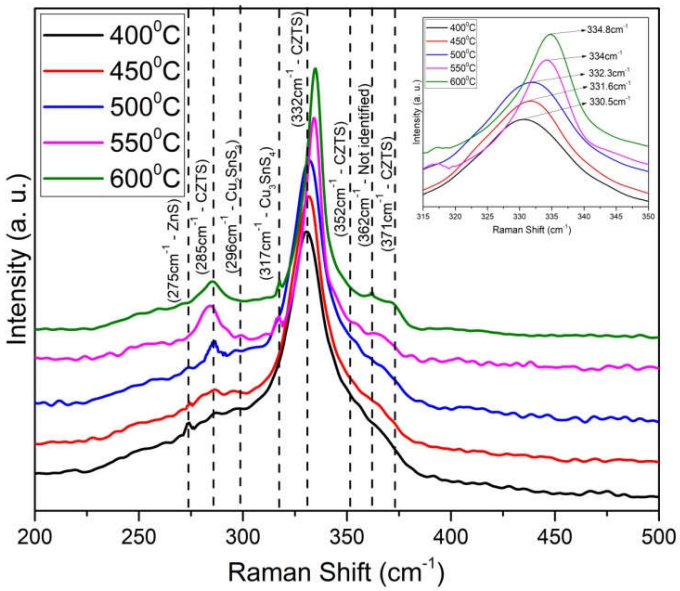

Fig. 4.8 Raman spectra of spin coated CZTS films sulphurized at different temperatures

Inset of Fig. 4.8 shows magnified image of the 332cm^{-1} peak of CZTS films sulphurized at different temperatures. The modes are found to shift to higher wavelength, with increase in sulphurization temperatures. Several factors could contribute red shit in Raman peaks, mainly phonon confinement, strain, non-homogeneity in size

distribution [21], non-stoichometry in films and defects in the crystal lattice [22,23]. Variation in crystallite size was observed with increase in sulphurization temperature, in the XRD analysis. From XRD and Raman spectroscopy, except the film sulphurized at 500ºC, all films irrespective of annealing temperature were found to contain secondary (ZnS) or ternary phases (Cu_2SnS_3, Cu_3SnS_4).

4.2.3.3 Rietveld refinement

Rietveld refinement analysis was carried out to further study the structural parameter of the spin coated films prepared in this route. The studies were conducted using GSAS software described earlier in section 3.1.5.3, with the high resolution data collected from the grazing incidence x-ray diffraction analysis (GIXRD) of the film sulphurized at 500ºC. Fig. 4.9 shows the rietveld plot of CZTS film sulphurized at 500°C. Black curve is the observed XRD pattern for the film, red curve is the calculated pattern, vertical magenta lines are the Bragg reflections and blue line gives the difference curve between observed and calculated patterns.

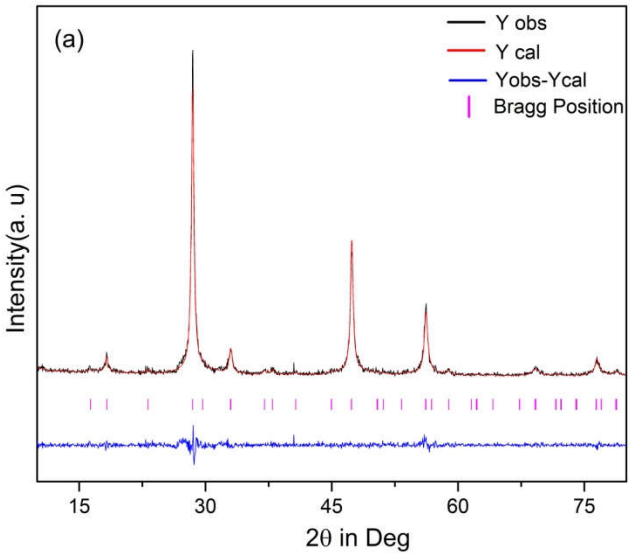

Fig. 4.9 Rietveld refinement plot of CZTS thin films sulphurized at 500°C (black curve is the observed XRD pattern, red curve is the calculated pattern, vertical magenta lines are the Bragg reflections and blue line gives the difference curve between observed and calculated patterns)

Lattice constants were extracted from the refined data. Lattice parameter after refinement for the CZTS thin film on glass substrates were $a=b=5.4213(3)$Å, $c=10.8391(5)$Å and $c/2a=0.9996(4)$, Refined lattice parameters matches with the standard kesterite lattice parameters obtained from mineral data [14]. The rietveld refinement results confirm formation of phase pure kesterite phase. Detailed analysis of the rietveld results is presented in the section 3.1.5.3 of this thesis.

4.2.4 *Elemental composition analysis*

Elemental compositions of the spin coated CZTS films sulphurized at different temperatures were investigated by Energy dispersive X-ray spectroscopy (EDXS) equipped with SEM. Table 4.5 shows the summary of the EDXS results of CZTS films sulphurized at different temperatures. It can be seen from Table 4.5 that the Cu/(Zn+Sn) ratio of the film decreases with increase in sulphurization temperature. Films were Cu rich and Zn poor at 400°C sulphurization temperature; Cu ratio is found to decrease with increase in temperature. The films sulphurized at 500°C were Cu poor and Zn rich, such a condition will enhance the solar cell efficiency in CZTS device [24-27], as detailed in section 3.1.6 of this thesis. In the present study, considering the Zn/Sn ratios, films sulphurized at 400°C and 500°C were Zn rich, whereas other CZTS films were Sn rich. Taking into consideration of the optimum case of Cu poor and Zn rich conditions, the film sulphurized at 500°C in the present study exhibited composition ratios similar to those observed in high performance CZTS devices [28-31].

Table 4.5 EDXS results of CZTS films sulphurized at different temperatures

Sulphurizing temperature	EDXS results						
	Cu (at%)	Zn(at%)	Sn(at%)	S(at%)	Cu/ (Zn+Sn)	Zn/Sn	S/ (Cu+Zn+Sn)
400 °C	25.80(±5)	10.16(±1)	9.20(±7)	54.84(±8)	1.33	1.10	1.21
450 °C	24.73(±2)	11.14(±3)	11.43(±4)	52.70(±7)	1.10	0.97	1.11
500°C	23.82(±3)	12.95(±4)	11.3(±6)	51.90(±5)	0.98	1.14	1.08
550 °C	23.12(±6)	11.12(±4)	12.65(±5)	53.11(±8)	0.97	0.88	1.13
600 °C	20.01(±4)	10.23(±6)	10.98(±5)	58.78(±7)	0.94	0.93	1.43

4.2.5 Surface morphology

Surface morphology of the films were analysed by scanning electron microscope, as described earlier (chapter 2 section 2.2.4). Fig. 4.10 (a-e) show the SEM images of the spin coated CZTS films on glass substrates sulphurized at 400°C to 600°C.

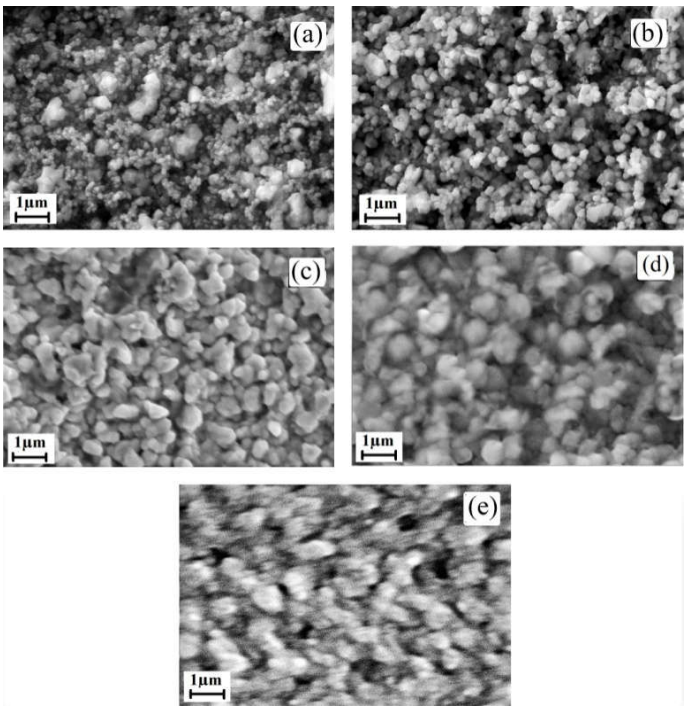

Fig. 4.10 SEM image of CZTS thin films sulphurized at (a) 400°C, (b) 450°C, (c) 500°C, (d) 550°C and (e) 600°C.

As seen in the images, the grain sizes of the films increase with increase in sulphurization temperature. Different morphologies are observed for the films sulphurized at 400°C and 450°C. This may be due to the incomplete grain growth of the film [32]. The film becomes dense and grains are uniformly distributed at 500°C sulphurization

temperature. Average grain size was found to be ~400nm for the film sulphurized at this temperature. Higher sulphurization temperatures (550°C and 600°C) improved grain size; however, detected Cu_2SnS_3 and Cu_3SnS_4 secondary phases at these temperatures, as seen in XRD and Raman studies. A few voids were observed for film sulphurized at 600°C. In the present work, best film morphology was obtained for the film sulphurized at 500°C.

4.2.6 Optical properties

Optical properties of the spin coated and sulphurized CZTS films were studied using UV-visible spectroscopy.

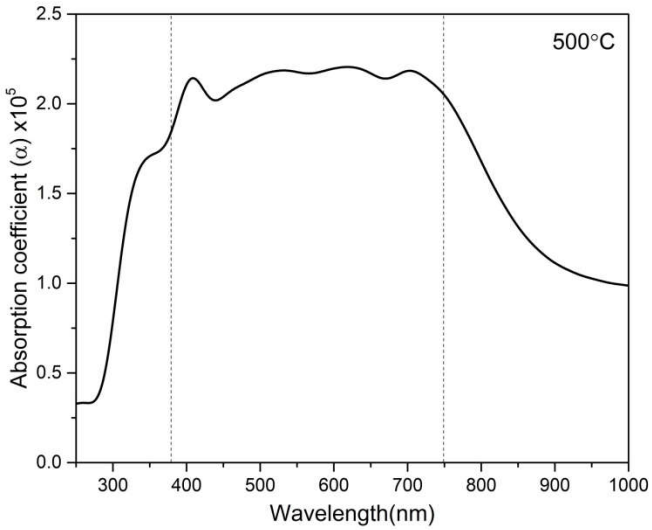

Fig. 4.11 Absorption coefficient versus wavelength plot for the film sulphurized at 500°C

The absorption spectra of film sulphurized at 500°C is shown in Fig. 4.11. Absorption coefficient of the film was calculated in the 380nm-750nm wavelength region. As shown in the Fig. 4.11, the film has absorption coefficient of ~2×10^5 cm^{-1} in the visible region. Higher absorption coefficient of the film indicates that it can absorb most of the incident photons with minimum thickness.

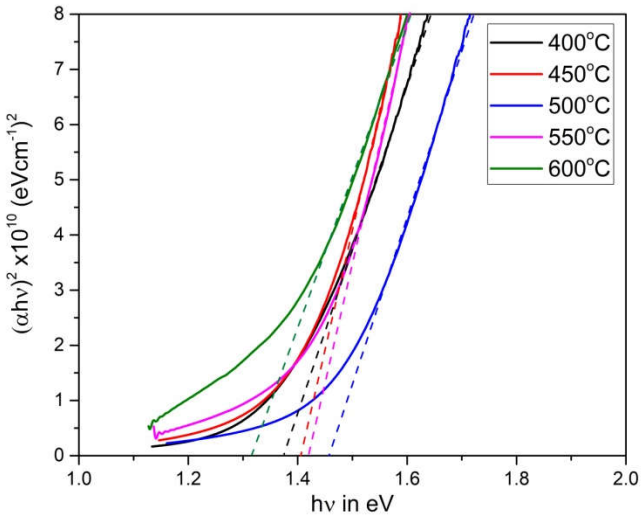

Fig. 4.12 $(\alpha h\upsilon)^2$ versus hυ plots of spin coated CZTS films sulphurized at different temperatures

The energy band gap for the direct band gap materials can be estimated using the well known Tauc's relation as described in section 2.2.7 of this thesis. The bandgap energy was estimated by extrapolating the linear portion of $(\alpha h\upsilon)^2$ versus energy plot to the x-axis (Fig. 4.12). The change in band gap energy with sulphurizing temperature is summarised in Table 4.6

Table 4.6 Optical band gap of spin coated CZTS films sulphurized at different temperatures

Sulphurizing Temp. (°C)	Band Gap eV
400	1.37
450	1.41
500	1.45
550	1.43
600	1.31

Optical band gap is found to increase up to the sulphurization temperature 500°C and thereafter reduces with further increase in sulphurization temperature (Table 4.6). Increase in bandgap with increase in sulphurization temperature may due to the improved crystallinity of the films. Sulphurization at lower temperatures (400°C and 450°C) revealed impurity phases and this could be a reason for the observed lower band gaps at these temperatures. The band gap value observed at 500°C sulphurization temperature was 1.45eV, and this value is close to the optimum band gap energy required for thin film photovoltaic cell. With further increase in sulphurization temperature >500°C, the band gap of the film decreases from 1.45eV to 1.31 eV, this drastic decrease may be due to formation of ternary phases Cu_2SnS_3 and Cu_3SnS_4. These phases were detected in the XRD and

Raman studies. These ternary phases are *n* type semiconductors and possess lower band gap [21,33,34].

4.2.7 Electrical properties

Hall measurement was performed in a magnetic field intensity of 0.54T. Hall measurement with van der Pauw configuration showed positive sign for the Hall coefficient and carrier concentration, indicating *p* type conduction for the film. Summary of the data obtained from the Hall measurement analysis of the spin coated CZTS films sulphurized at different temperatures are given in Table 4.7.

As seen in Table 4.7, carrier concentration of the film decreases and mobility increases with the increase in sulphurization temperature. Increase in mobility may be due to the improved crystallinity of the films, as observed in XRD patterns [35]. Resistivity of the CZTS films significantly increased at the sulphurization temperature 600°C; this may due to the presence of ternary phases [11,12], as observed in XRD and Raman studies. The carrier concentration, mobility and resistivity of the film sulphurized at 500°C were found to be $1.022\times10^{19}cm^{-3}$, $0.2295cm^2V^{-1}s^{-1}$ and $2.662\Omega cm$ respectively. Rajeshmon et. al. [36] reported the the values as $1.03\times10^{19}cm^{-3}$, $0.2295cm^2V^{-1}s^{-1}$ and $2.662\Omega cm$ respectively for spray coated CZTS thin films. This is close to the values observed for CZTS films sulphurized at 500°C. The Hall measurement studies revealed favourable electrical properties in the film sulphurized at 500°C.

Table 4.7 Electrical properties of CZTS films sulphurized at different temperatures

Sulphurizing Temp. (°C)	Carrier concentration (cm^{-3})	Mobility (cm^2/Vs)	Resistivity (Ωcm)
400	5.92×10^{18}	0.1669	6.946
450	6.34×10^{18}	0.1914	6.513
500	1.02×10^{19}	0.2295	2.662
550	5.58×10^{18}	1.089	1.026
600	2.62×10^{15}	24.22	98.26

4.3 Cu_2ZnSnS_4 films from spin coated CZTS precursor samples and post-deposition annealing in inert atmosphere

4.3.1 Fabrication of CZTS thin film by spin coating and further annealing in inert atmosphere

In this route, CZTS precursor films were spin coated as described in the section 4.2.1 of this chapter; the films were further annealed in inert (nitrogen) atmosphere to complete phase formation. Annealing at different temperatures help to study the effect of inert atmosphere on the structural, optical and electrical properties of CZTS films. These films were treated at different temperatures ranging from 400°C to 550°C for 30 minutes in nitrogen atmosphere. Fig.4.13 depicts the experimental set up used for annealing films. This process was carried out in tubular furnace (Lenton, USA Make) with a gas flow rate of 5SCCM using controlled gas purging set up. Heating rate was set to 5°per min up to the annealing temperature (350°C, 400°C,

450°C, 500°C, 550°C) and the dwell time given was 30min. After dwell time, heater was switched off and the furnace was cooled down to room temperature. Gas purging was kept in the same flow rate in the entire annealing process. The flow rate was controlled by a standard gas flow meter attached with cylinder regulator. After annealing, the structural, optical and electrical properties of the films were studied in detail.

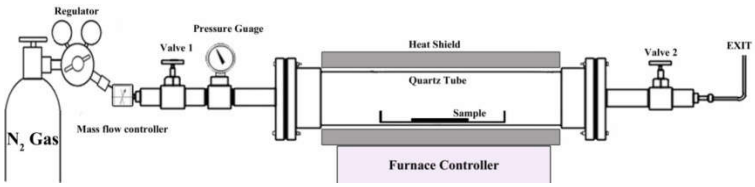

Fig.4.13 Experimental set up used for annealing films in nitrogen atmosphere

4.3.2 Structural studies

4.3.2.1. X-ray Diffraction Studies

Structural properties of the films were studied by x-ray diffraction. Fig. 4.14 shows the XRD patterns of as-deposited film along with those of the films annealed in nitrogen atmosphere at various temperatures between 350°C and 550°C. As seen in the XRD patterns, the as-deposited film exhibits predominantly amorphous phase, while the nitrogen annealing was found to improve the crystallinity of the films. Peaks at $2\theta=28.5°$ and $2\theta=47.3°$ are clearly visible in all the patterns. The peaks were identified as (112) and (220) planes of Cu_2ZnSnS_4 with the help of ICDD powder diffraction file 026-0575. The XRD peak of the film annealed at 500°C and 550°C

become sharp and strong compared to other patterns. Lattice parameters of the annealed films were calculated based on tetragonal system [37,38]. The values obtained are given in Table 4.8 are in good agreement with those in the ICDD file 26-0575 (a=b=0.5427nm, c=1.0848nm).

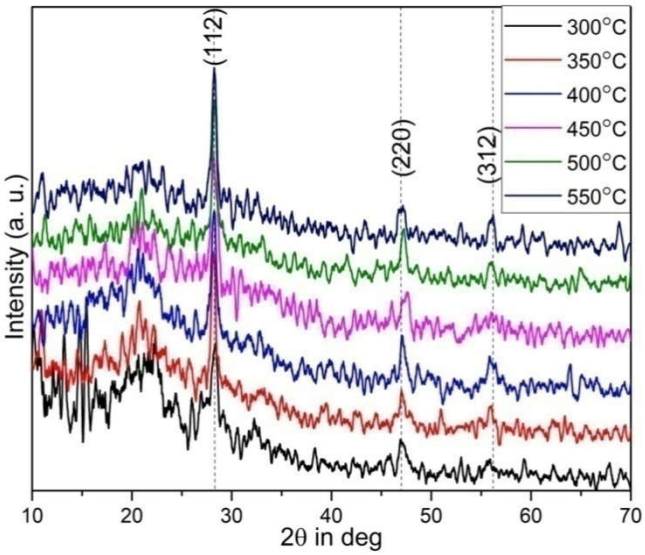

Fig. 4.14 XRD pattern of spin coated CZTS thin films annealed at different temperatures

The average crystallite size of the CZTS was calculated using the Scherrer's formula and W–H relation. The full width at half maximum (FWHM) of diffraction peaks and average crystalline size calculated for the films annealed at different temperatures using the (112) plane. As seen in the table (Table 4.8), the average crystallite size is found to increase with increase in annealing temperature. The improvement in crystallite size with temperature is lower compared to the other route attempted for the present study (section 4.1.3.1 and

4.2.3.1). The highest crystallite size in the present study was observed for the films prepared by this route. The XRD analysis did not indicate any secondary or ternary phases at this temperature.

Table 4.8 Lattice constants and average crystallite size of the as-deposited and films annealed at different temperatures

N_2 annealing temperature (°C)	Lattice parameters		Crystalline size *d* (nm)	W-H relation	
	a = *b* (Å)	*c* (Å)		Crystallite size (nm)	Strain
As-deposited	5.4611	10.8319	15.8	16	0.1480
350	5.4738	10.8213	17.1	19	0.0892
400	5.4722	10.8611	20.7	20	0.0061
450	5.4068	10.8208	21.0	22	0.2801
500	5.4315	10.8260	22.2	24	0.6210
550	5.4427	10.8320	22.9	31	0.0154

4.3.2.2 Raman spectroscopy

In kesterite, two dominant peaks normally observed are at 286cm^{-1} and 332cm^{-1}, when irradiated with 532nm laser beam [39-41]. Here, as seen in Fig.4.15, all films show one major peak at 332cm^{-1}, which corresponds to the A vibration mode of kesterite structure [1,42]. The as-deposited film revealed predominantly amorphous phase in the XRD, which may due to unreacted complexes of Sn and S [4,40]. Films annealed in nitrogen environment at 350°C shows two additional peaks, one at 286cm^{-1} corresponding to CZTS [1,2] and another peak at 360cm^{-1}, which may be due to the presence of ZnS phase; identification of this mode with ZnS phase is difficult because of the lack of ZnS major peak at 348cm^{-1}[42]. Films annealed at 400°C, 450°C and 500°C exhibited two more peaks of kesterite at 286cm^{-1} and 356cm^{-1}/368cm^{-1} , which indicate improved crystallinity

of the film [43]. No other impurity peaks corresponding to β ZnS, $Cu_{2-x}S$, Cu_2SnS_3, SnS_2, etc., were observed in the Raman spectra of these films [43]. Raman spectra of the film annealed at 550°C shows two kesterite peaks at 283cm^{-1} and 368cm^{-1} along with peaks corresponding to other impurity phases, at 303cm^{-1} and 433cm^{-1} [44,45]. The low intensity peak at 303cm^{-1} corresponds to Cu_2SnS_3 phase [44]. The presence of this phase was not detected in XRD, which may be due to the low concentration of this phase in the film. The other impurity peak at 433cm^{-1} in the Raman spectra of film annealed at 550°C could not be identified. XRD and Raman confirm the formation of phase pure CZTS at 500°C.

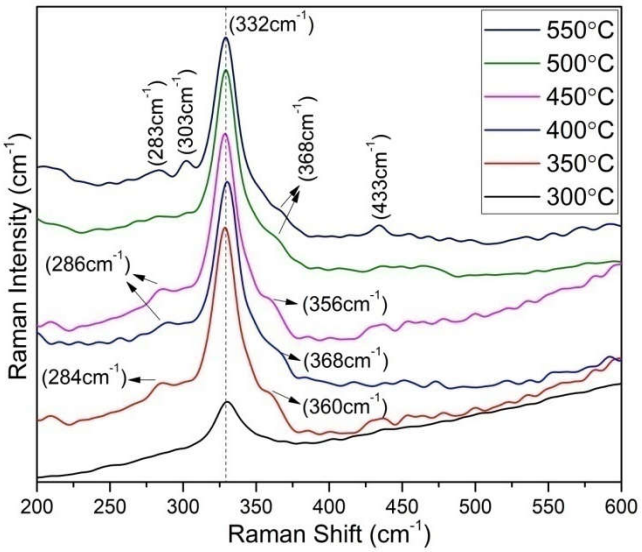

Fig. 4.15 Raman spectra of CZTS thin films annealed in inert atmosphere at different temperatures

4.3.3 Elemental composition analysis

Table 4.9 shows the results of the elemental composition analysis of CZTS thin films annealed in inert atmosphere at different temperatures. It can be seen that the elemental composition of Cu, Zn and Sn increases and sulphur decreases with increase in annealing temperature. As deposited film showed higher sulphur content; however, the sulphur concentration decreases with increase in annealing temperature. This may be due to the evaporation of sulphur at higher temperatures [6,8]. The film annealed at 500°C is found to be Cu poor and Zn rich, this condition is favourable for high performance CZTS solar cells [24,26,30]. The SEM analysis indicated a few voids or pores in the film annealed at 550°C. The elemental analysis revealed very low sulphur at higher temperatures (550°C); the porous nature of films may be due to the evaporation of sulphur at higher (550°C) temperature.

Table 4.9 Summary of elemental composition study of CZTS thin films annealed at various temperatures

Sulphurizing temperature	EDXS results					
	Cu (at. %)	Zn (at. %)	Sn (at. %)	S (at. %)	Cu/ (Zn+Sn)	Zn/Sn
As deposited	10.74 (±3)	11.38 (±2)	8.65 (±2)	69.23 (±3)	0.54	1.32
350°C	18.76(±5)	11.22 (±2)	9.58 (±4)	60.44 (±5)	0.90	1.17
400°C	20.51 (±3)	11.89 (±4)	11.37 (±3)	56.23 (±3)	0.88	1.05
450°C	22.34 (±2)	12.96 (±4)	11.94 (±3)	53.66 (±3)	0.93	1.01
500°C	23.74 (±4)	13.03 (±4)	11.96 (±3)	51.27 (±5)	0.95	1.09
550°C	27.39 (±2)	14.43 (±3)	14.41 (±3)	43.77 (±4)	0.95	1.00

4.3.4 *Surface morphology*

Fig. 4.16 (a) shows the FESEM images of as-deposited and annealed films. As seen, the surface image of as deposited CZTS film shows a different feature on the surface, which may be due to the unreacted complexes of Sn and S, as explained earlier [44].

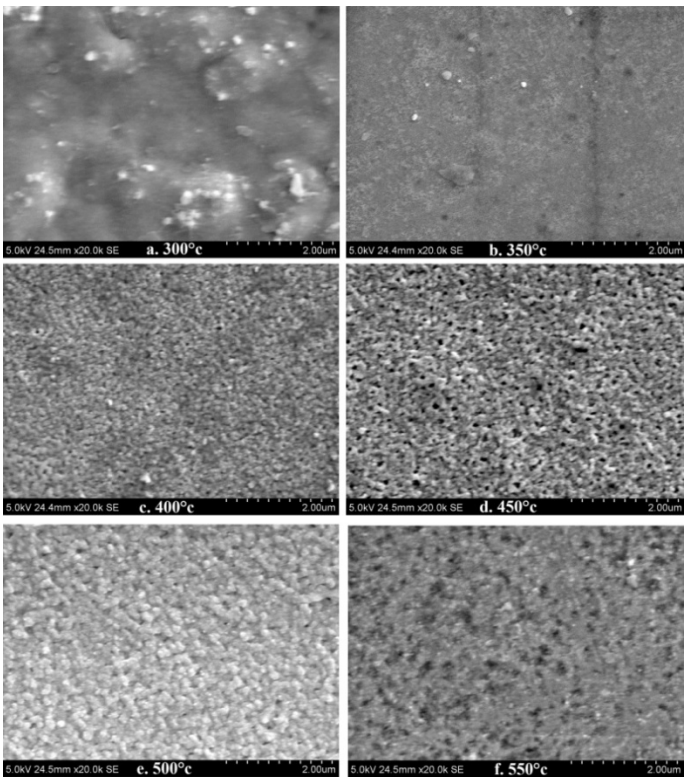

Fig. 4.16 FESEM images of the films (a) as deposited and (b) annealed at 350°C, c) 400°C, d) 450°C, e) 500°C and f) 550°C in nitrogen atmosphere

As seen in the FESEM image, no grains are visible when the film is annealed at 350°C. With increase in annealing temperature, the particle size is found to increase, which can be clearly seen in the images. The improved grain size is reported to enhance the photovoltaic properties by reducing the carrier recombination [46]. Many voids are appeared when the film is annealed at 550°C; these large voids in absorber layer will result in lower conversion efficiency [46]. In the present study, best film morphology was obtained for the film annealed at 500°C, which has uniformly distributed grains with size ~100nm.

4.3.5. Optical properties

Fig. 4.17 (a) shows the absorption coefficient versus wavelength plot in the range 300nm-1100nm of the as-prepared and nitrogen annealed films. It can be seen from the absorption spectra that the photon absorption properties are mainly in the visible light region. Band gap was estimated using the Tauc's relation, [47] by extrapolating the linear portion of the plot of $(\alpha h\nu)^2$ versus $h\nu$ to the x intercepting point at y=0 (inset of Fig. 4.17(b)). As seen in the Fig. 4.17(b), the band gap is found to vary from 1.46eV to 1.56eV when the annealing temperature was increased from 300°C to 550°C. Lower band gap at lower temperatures (300°C, 350°C) may due to the secondary phases or the organic precursor materials existing on the system [39]. The band gap was found to change from 1.56 to 1.49 when annealed from 400°C to 500°C, which can be attributed to the increased crystallinity of the film [48]. The band gap was further

increased when the temperature reached 550°C, this may be due to the loss of sulphur [49].

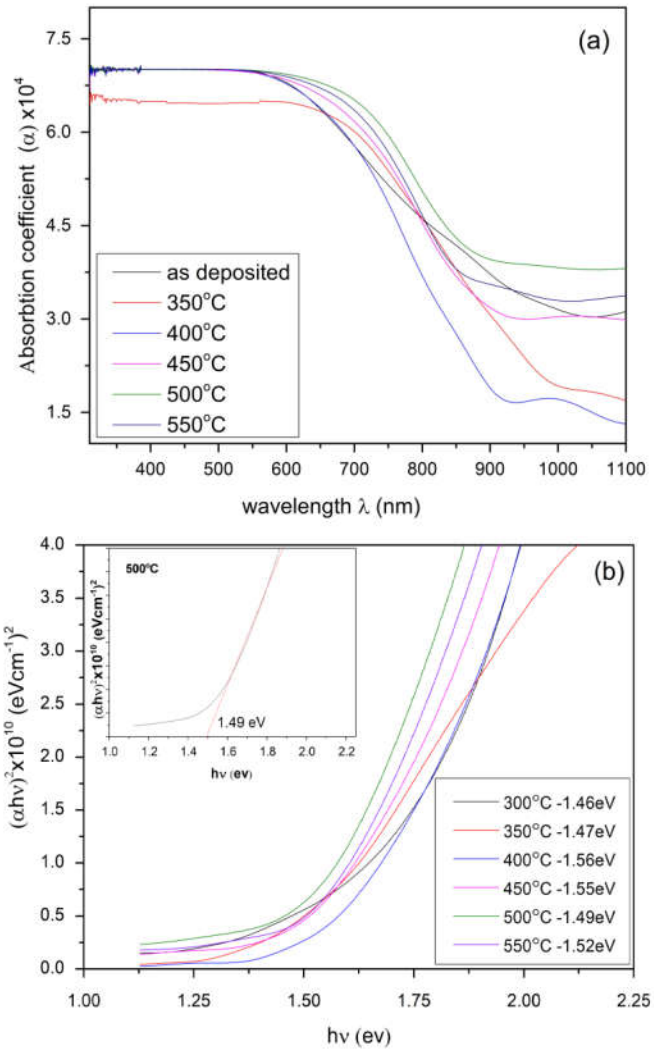

Fig. 4.17 (a) Absorption coefficient versus wavelength plot of thin films annealed at 300°C-550°C, (b) $(\alpha h\nu)^2$ versus $(h\nu)$ plots for estimating band gap.

The band gap obtained at 500°C (1.49eV) is close to the optimum band gap for thin film absorbers [50-53]. Absorption coefficient of the CZTS was calculated to be ~ 10^4 cm^{-1} in the visible region, from 400nm (3.1eV) to 700nm (1.77eV). This shows that the spin coated film can absorb most of the incident radiation with minimum film thickness. Kahraman et al. [39] reported optical band gap values between 1.32 to 2.27eV for their CZTS films depending on sulphurization temperature and the absorption coefficient obtained was $10^4 cm^{-1}$. Fischereder et al [54] reported the preparation of CZTS thin films using thio-acetamide as sulphur source and studied the influence of vacuum annealing. In their work, all films exhibited optical absorption coefficient of the order of $10^4 cm^{-1}$ and the films had optical band gap between 1.41eV and 1.81eV with respect to annealing temperature.

4.3.6 Electrical properties

Hall measurements were performed with a constant magnetic field 0.54T at room temperature and resistivity measurements were carried out using van der Pauw configuration equipped with Hall measurement system. *p* type nature of the films was confirmed from the positive signs of Hall coefficient and carrier concentration. Carrier concentration, mobility and resistivity of the films measured are given in Table 4.10. Lower resistivity of the as-deposited film and the film annealed at 350°C may be due to the presence of the carbon contents and the amorphous nature of the films [54,55]. According to Patel et al, high mobility may also be due to enrich of Zn and S content [56].

When annealing temperature was increased from 400°C to 500°C, the carrier concentration increased and mobility decreased, which may be due to the decrease of ZnS phase on the surface [57]. However, presence of ZnS was not detected in the present study; the ZnS on the surface may not be detectable in Raman spectra with a 532nm laser excitation because of its deeper penetration, as reported by Zakaria et al and Long et al. [58,59]. Higher value for carrier concentration (2.16×10^{19} cm^{-3}) was obtained for the film annealed at 500°C. Hall mobility and resistivity at this temperature was 41.41 cm^2/Vs and 0.0880 Ωcm, respectively. Previous reports indicate wide variation the resistivity, from 10^{-2} to 10^4 Ωcm [4,33,36]. The low resistivity of the films in the present study may be due to the enhanced crystallinity of the CZTS [60,61]. Resistivity of the material mainly depends on the Cu/(Zn+Sn) and Zn/Sn ratios of the sample [52,60]. On further increasing the temperature to 550°C, the carrier concentration and mobility decrease to lower values, which increases the resistivity of the film. This may be due to the formation of secondary phases and this was evident in the Raman analysis [56]. The structural, optical and electrical investigations revealed that the film annealed in nitrogen at 500°C possesses excellent absorber material properties required for thin film solar cells.

Table 4.10 Electrical properties of CZTS thin films annealed at different temperatures

Annealing temperature	Carrier concentration (cm^{-3})	Mobility (cm^2/Vs)	Resistivity (Ωcm)
as deposited	2.280×10^{18}	71.92	0.0381
350°C	8.075×10^{17}	53.53	0.1444
400°C	1.877×10^{17}	45.51	0.7309
450°C	1.198×10^{18}	39.47	0.1320
500°C	2.164×10^{19}	41.40	0.0880
550°C	3.024×10^{18}	17.32	0.1192

4.4 Comparison of properties of spin coated CZTS thin films prepared by three routes

Formation of phase pure CZTS was confirmed at lower sulphurization temperature (500°C) by spin coating compared to the case of dip coated films described in the previous chapter, where the proper phase was formed at sulphurization temperature of 550°C. Similar to the dip coated film, higher crystallinity is observed for the CZT precursor film annealed in sulphur atmosphere. The spin coated films prepared by all the three routes show optimum band gap, the highest value obtained was 1.49eV for the CZTS precursor film annealed in nitrogen atmosphere. The CZTS precursor film further annealed in sulphur (second route) atmosphere exhibited the highest optical absorption coefficient ($10^5 cm^{-1}$) in the visible region. The elemental composition ratios of the CZTS precursor film annealed in sulphur environment were found to be Cu poor and Zn rich, while the films annealed in inert atmosphere showed Cu poor nature and but stoichiometric ratios for Zn and Sn. The CZT film annealed in sulphur

atmosphere (first route) showed Cu/(Zn+Sn) ratio equal to unity and Zn/Sn ratio to 1.16; this shows the Zn rich nature of the films. High carrier concentration of the films fabricated by the second and third routes may be due to the Cu poor nature of the films. Carrier motilities of the films prepared by the first and third routes were very high compared to the CZTS film annealed in sulphur atmosphere (second route). Similar trends were observed in the case of dip coated films, discussed in the previous chapter. With same number of coatings, the CZTS precursor film annealed in sulphur atmosphere (second route) gave higher film thickness; hence this route would be favorable for large scale fabrication. Among the three routes, the films fabricated by the second route had better properties in terms of Cu poor Zn rich nature, absorption coefficient, carrier concentration and film thickness. The summary of the properties obtained for the films of the three spin coating routes are given in Table 4.1

Table 4. 11 Summary of the properties of the CZTS thin films fabricated by three different spin coating routes.

Properties	*CZT* precursor films annealed in reactive (sulphur) atmosphere	*CZTS* precursor films annealed in reactive (sulphur) atmosphere	*CZTS* precursor films annealed in inert atmosphere
Optimized temperature	500°C	500°C	500°C
Film Area	1×1 inch	1×1 inch	1×1 inch
Crystallite size	39nm	31nm	22nm
Cu/(Zn+Sn) ratio	1.00	0.98	0.95
Zn/Sn ratio	1.16	1.14	1.01
Energy Band Gap	1.47eV	1.45eV	1.49eV
Absorption Coefficient	$>10^4$ cm^{-1}	$>10^5$ cm^{-1}	$\sim10^4 cm^{-1}$
Carrier Type	p type	p type	p type
Carrier Concentration	$1.7\times10^{18} cm^{-3}$	1.02×10^{19} cm^{-3}	2.17×10^{19} cm^{-3}
Resistivity	0.8 Ωcm	2.66 Ωcm	0.09 Ωcm
Mobility	$48.20 cm^2/Vs$	$0.2295 cm^2/Vs$	$41.40 cm^2/Vs$
Film Thickness	~1.5μm	~2.2μm	~1.2μm

4.5 Summary

CZTS thin films were coated successfully by spin coating technique followed by annealing/ sulphurization. Two different precursor solutions with and without sulphur were prepared for spin coating. Films were sulphurized or annealed in three different routes.

For the fabrication of CZTS thin films by the first method, precursor films without sulphur coated on pre-cleaned glass substrates were converted to Cu_2ZnSnS_4 by annealing in sulphur environment at various temperatures. Phase purity of the films was confirmed by x-ray diffraction and Raman spectroscopic studies. No impurity phases were

detected for the precursor film sulphurized at 500°C. For the film sulphurized at 550°C showed peak corresponding to $Cu_{2-x}S$ secondary phase. Elemental composition ratios of both films were calculated and the Cu/(Zn+Sn) and Zn/Sn ratios of films sulphurized at 500°C were 1.00 and 1.16 respectively. This composition ratios are not favourable for efficient CZTS solar cell fabrication. Surface morphology and grain size were examined by SEM. Film thickness obtained from SEM cross section was ~1.5μm for the films sulphurised at 500°C. Optical absorption coefficient of the films calculated from the UV-Vis absorption spectra was ~ $10^4 cm^{-1}$ in the visible region. Optical band gap estimated was ~1.47eV, which is quite close to the optimum band gap energy for thin film photovoltaic cells. The carrier concentration, mobility and resistivity of the films sulphurized at 500°C were $1.7\times10^{18} cm^{-3}$, $48.20 cm^2/Vs$ and 0.8 Ωcm, respectively. Highest mobility of 48.20 cm^2/Vs was observed in this route.

In the second route, precursor films with sulphur spin coated on pre-cleaned glass substrates were annealed further in sulphur atmosphere at various temperatures. Formation of Cu_2ZnSnS_4 phase was confirmed from XRD and Raman studies. The crystallinity of the films was found to increase with sulphurization temperature. Films sulphurized at 500°C were found to be phase pure from the XRD and Raman studies. Surface morphology of spin coated films sulphurized at 500ºC exhibits dense, uniform and improved crystallite structure. The films sulphurized at 500ºC exhibited optical bandgap of 1.45eV and absorption coefficient of $>10^5 cm^{-1}$. Hall measurement indicated *p*

type conduction for all films. The electrical properties such as resistivity, carrier concentration and mobility of the films sulphurized at 500ºC were 2.662Ωcm, $1.022\times10^{19}/cm^3$, $0.23 cm^2/Vs$, respectively. Thus, the CZTS thin films fabricated by spin coating technique exhibited required photovoltaic properties.

In the third route, Cu_2ZnSnS_4 precursor films fabricated through spin coating route using sulphur containing solution were annealed in inert (nitrogen) atmosphere and studied the effect of annealing temperature in the range 350-550°C on the structural, optical and electrical properties. XRD results revealed the formation of kesterite phase at all annealing temperatures, while the Raman studies indicated Cu_2SnS_2 impurity phase in the film annealed at 550°C. The band gap of the films annealed in nitrogen varies from 1.46eV to 1.56eV, depending on the annealing temperature. Good crystallinity, dense structure, ideal band gap (1.49eV) and good absorption coefficient (10^4 cm^{-1}) were obtained for the film annealed at 500°C for 30 minutes in nitrogen. Thus the film annealed at 500°C in inert atmosphere possesses the optimum properties required for thin film absorber.

4.6 References

1) Dumcenco D, Huang Y S, The vibrational properties study of kesterite Cu_2ZnSnS_4 single crystals by using polarization dependent Raman spectroscopy, Opt. Mater. 35 (2013) 419.

2) Dimitrievska M, Xie H, Fairbrother A, Fontané X, Gurieva G, Saucedo E, Pérez-Rodríguez A, Schorr S, Izquierdo-Roca V. Multiwavelength excitation Raman scattering of $Cu_2ZnSn(S_xSe_{1-x})_4$ ($0 \leq x \leq 1$) polycrystalline thin films: vibrational properties of sulfoselenide solid solutions, Appl. Phys. Lett. 105 (2014) 031913.

3) Fernandes P A, Salomé P M, Da Cunha A F, Study of polycrystalline Cu_2ZnSnS_4 films by Raman scattering, J. Alloys Compd. 509 (2011) 7600.

4) Ge J, Chu J, Jiang J, Yan Y, Yang P, Characteristics of In-Substituted CZTS Thin Film and Bifacial Solar Cell, ACS Appl. Mater. Interfaces. 6 (2014) 21118.

5) Scragg J J, Dale P J, Peter L M, Towards sustainable materials for solar energy conversion: Preparation and photoelectrochemical characterization of Cu_2ZnSnS_4, Electrochem. Commun. 10 (2008) 639.

6) Catlow C R, Guo Z X, Miskufova M, Shevlin S A, Smith A G, Sokol A A, Walsh A, Wilson D J, Woodley S M, Advances in computational studies of energy materials, Philos. Trans. R. Soc., A. 368 (2010) 3379.

7) Chen S, Walsh A, Yang J H, Gong X G, Sun L, Yang P X, Chu J H, Wei S H, Compositional dependence of structural and electronic properties of $Cu_2ZnSn(S,Se)_4$ alloys for thin film solar cells, Phys. Rev. B. 83(2011) 125201.

8) Tanaka K, Moritake N, Oonuki M, Uchiki H, Pre-annealing of precursors of Cu_2ZnSnS_4 thin films prepared by sol–gel sulfurizing method, Jpn. J. Appl. Phys. 47 (2008) 598.

9) Guan H, Shen H, Gao C, He X, Sulfurization time effects on the growth of Cu_2ZnSnS_4 thin films by solution method, J. Mater. Sci.: Mater. Electron. 24 (2013) 2667.

10) Muhunthan N, Singh O P, Singh S, Singh V N, Growth of CZTS thin films by co-sputtering of metal targets and sulfurization in H_2S, Int. J. Photoenergy. 2013 (2013) 7.

11) Long B, Cheng S, Zheng Q, Yu J, Jia H, Effects of sulfurization time and H_2S concentration on electrical properties of Cu_2ZnSnS_4 films prepared by sol–gel method, Mater. Res. Bull. 73 (2016) 140.

12) Long B, Cheng S, Lai Y, Zhou H, Yu J, Zheng Q, Effects of sulfurization temperature on phases and opto-electrical properties of Cu_2ZnSnS_4 films prepared by sol–gel deposition, Thin Solid Films. 573 (2014) 117.

13) Ge J, Wu Y, Zhang C, Zuo S, Jiang J, Ma J, Yang P, Chu J, Comparative study of the influence of two distinct sulfurization ramping rates on the properties of Cu_2ZnSnS_4 thin films, Appl. Surf. Sci. 258 (2012) 7250.

14) Zak A K, Majid W A, Abrishami M E, Yousefi R, X-ray analysis of ZnO nanoparticles by Williamson–Hall and size–strain plot methods, Solid State Sci. 13 (2011) 251.

15) Gürel T, Sevik C, Çağın T, Characterization of vibrational and mechanical properties of quaternary compounds Cu_2ZnSnS_4 and $Cu_2ZnSnSe_4$ in kesterite and stannite structures, Phys. Rev. B. 84 (2011) 205201.

16) Fontané X, Calvo-Barrio L, Izquierdo-Roca V, Saucedo E, Pérez-Rodriguez A, Morante J R, Berg D M, Dale P J, Siebentritt S, In-depth resolved Raman scattering analysis for the identification of secondary phases: characterization of Cu_2ZnSnS_4 layers for solar cell applications, Appl. Phys. Lett. 98 (2011) 181905.

17) Khare A, Himmetoglu B, Johnson M, Norris D J, Cococcioni M, Aydil E S, Calculation of the lattice dynamics and Raman spectra of copper zinc tin chalcogenides and comparison to experiments, J. Appl. Phys. 111 (2012) 083707.

18) Gurieva G, Guc M, Bruk LI, Izquierdo Roca V, Pérez Rodríguez A, Schorr S, Arushanov E, Cu_2ZnSnS_4 thin films grown by spray pyrolysis: characterization by Raman spectroscopy and Xray diffraction, Phys. Status Solidi C. 10 (2013) 1082.

19) Fernandes P A, Salomé P M, Da Cunha A F, Cu_xSnS_{x+1} ($x=2,3$) thin films grown by sulfurization of metallic precursors deposited by dc magnetron sputtering, Phys. Status Solidi C. 7 (2010) 901.

20) Fernandes P A, Salomé P M, Da Cunha A F, A study of ternary Cu_2SnS_3 and Cu_3SnS_4 thin films prepared by sulfurizing stacked metal precursors, J. Phys. D: Appl. Phys. 43 (2010) 215403.

21) Ge J, Wu Y, Zhang C, Zuo S, Jiang J, Ma J, Yang P, Chu J, Comparative study of the influence of two distinct sulfurization

ramping rates on the properties of Cu_2ZnSnS_4 thin films, Appl. Surf. Sci. 258 (2012) 7250.

22) Kermadi S, Sali S, Ameur FA, Zougar L, Boumaour M, Toumiat A, Melnik N N, Hewak D W, Duta A, Effect of copper content and sulfurization process on optical, structural and electrical properties of ultrasonic spray pyrolysed Cu_2ZnSnS_4 thin films, Mater. Chem. Phys. 169 (2016) 96.

23) Šćepanović M J, Grujić-Brojčin M, Dohčević-Mitrović Z D, Popović Z V, Characterization of anatase TiO_2 nanopowder by variable-temperature Raman spectroscopy, Sci. Sintering. 41 (2009) 67.

24) Mitzi D B, Gunawan O, Todorov T K, Wang K, Guha S, The path towards a high-performance solution-processed kesterite solar cell, Sol. Energy Mater. Sol. Cells. 95 (2011) 1421.

25) Shin B, Gunawan O, Zhu Y, Bojarczuk N A, Chey S J, Guha S, Thin film solar cell with 8.4% power conversion efficiency using an earth abundant Cu_2ZnSnS_4 absorber, Prog. Photovoltaics Res. Appl. 21 (2013) 72.

26) Chen S, Gong X G, Walsh A, Wei S H, Defect physics of the kesterite thin-film solar cell absorber Cu_2ZnSnS_4, Appl. Phys. Lett. 96 (2010) 021902.

27) Samji S K, Mannam R, Rao M R, Do defects get ordered in Cu_2ZnSnS_4?, Scr. Mater. 117 (2016) 11.

28) Das S, Mandal K C, Low-cost Cu_2ZnSnS_4 thin films for large-area high-efficiency heterojunction solar cells, 38th IEEE Photovoltaic Specialists Conference (PVSC), 38 (2012) 002668.

29) Redinger A, Berg D M, Dale P J, Valle N, Siebentritt S, Route towards high efficiency single phase $Cu_2ZnSn(S,Se)_4$ thin film solar cells: Model experiments and literature review, 37th IEEE Photovoltaic Specialists Conference (PVSC), 37 (2011) 000025.

30) Shin B, Zhu Y, Bojarczuk N A, Chey S J, Guha S, High efficiency $Cu_2ZnSnSe_4$ solar cells with a TiN diffusion barrier on the molybdenum bottom contact, 38th IEEE Photovoltaic Specialists Conference (PVSC), 38 (2012) 000671.

31) Gunawan O, Gokmen T, Shin BS, Guha S, Device characteristics of high performance Cu_2ZnSnS_4 solar cell, 38th IEEE Photovoltaic Specialists Conference (PVSC), 38 (2012) 003001.

32) Zoppi G, Forbes I, Miles R W, Dale P J, Scragg J J, Peter L M, $Cu_2ZnSnSe_4$ thin film solar cells produced by selenisation of

magnetron sputtered precursors, Prog. Photovoltaics Res. Appl. 17 (2009) 315.

33) Akkari A, Guasch C, Kamoun Turki N, Chemically deposited tin sulphide, J. Alloys Compd. 490 (2010) 180.

34) Jemetio J P, Zhou P, Kleinke H, Crystal structure, electronic structure and thermoelectric properties of $Cu_4Sn_7S_{16}$, J. Alloys Compd. 417 (2006) 55.

35) Dhanasekar M, Bhat S V, Facile synthesis of Cu_2ZnSnS_4 absorber layer for thin film solar cells using a highly stable precursor solution, Appl. Surf. Sci. 418 (2017) 194.

36) Rajeshmon V G, Kartha C S, Vijayakumar K P, Sanjeeviraja C, Abe T, Kashiwaba Y, Role of precursor solution in controlling the opto-electronic properties of spray pyrolysed Cu_2ZnSnS_4 thin films, Sol. Energy. 85 (2011) 249.

37) Romanyuk Y E, Fella C M, Uhl A R, Werner M, Tiwari A N, Schnabel T, Ahlswede E, Recent trends in direct solution coating of kesterite absorber layers in solar cells, Sol. Energy Mater. Sol. Cells. 119 (2013) 181.

38) Tanaka T, Yoshida A, Saiki D, Saito K, Guo Q, Nishio M, Yamaguchi T, Influence of composition ratio on properties of Cu_2ZnSnS_4 thin films fabricated by co-evaporation, Thin Solid Films. 518 (2010) 29.

39) Kahraman S, Cetinkaya S, Podlogar M, Bernik S, Cetinkara H A, Güder H S, Effects of the sulfurization temperature on sol gel-processed Cu_2ZnSnS_4 thin films, Ceram. Int. 39 (2013) 9285.

40) Tanju Gurel, Cem Sevik, Tahir Cagın, Characterization of vibrational and mechanical properties of quaternary compounds Cu_2ZnSnS_4 and $Cu_2ZnSnSe_4$ in kesterite and stannite structures, Phys. Rev. B 84 (2011) 205201.

41) Su Z, Yan C, Sun K, Han Z, Liu F, Liu J, Lai Y, Li J, Liu Y, Preparation of Cu_2ZnSnS_4 thin films by sulfurizing stacked precursor thin films via successive ionic layer adsorption and reaction method, Appl. Surf. Sci. 258 (2012) 7678.

42) Fernandes P A, Salomé PMP, Cunha da A F, Growth and Raman scattering characterization of Cu_2ZnSnS_4 thin films, Thin Solid Films 517 (2009) 2519.

43) Fontane X, Calvo-Barrio L, Izquierdo-Roca V, Saucedo E, Perez-Rodriguez, Morante J R, Berg D M, Dale P J, Siebentritt S, In-depth

resolved Raman scattering analysis for the identification of secondary phases: Characterization of Cu_2ZnSnS_4 layers for solar cell applications, Appl. Phys. Lett. 98 (2011) 181905.

44) Fernandes P A, Salom´e1 PMP, Cunha A F da, A study of ternary Cu_2SnS_3 and Cu_3SnS_4 thin films prepared by sulfurizing stacked metal precursors, J. Phys. D. Appl. Phys. 43 (2010) 215403.

45) Serrano J, Cantarero A, Cardona M, Garro N, Lauck R, Tallman R E, Ritter T M, Weinstein BA, Raman scattering in β-ZnS, Phys. Rev. B. 69 (2004) 014301.

46) Kunihiko Tanaka, Noriko Moritake, Masatoshi Oonuki, Hisao Uchiki, Pre-Annealing of Precursors of Cu_2ZnSnS_4 Thin Films Prepared by Sol–Gel Sulfurizing Method, Jpn. J. Appl. Phys. 47 (2008) 598.

47) Pawar B S, Pawar S M, Gurav K V, Shin S W, Lee J Y, Kolekar S S, Kim J H, Effect of annealing atmosphere on the properties of electrochemically deposited Cu_2ZnSnS_4 (CZTS) thin films, ISRN Renewable Energy. 2011 (2011) 934575.

48) Bodnar I V, Telesh E V, Gurieva G, Schorr S, Transmittance Spectra of Cu_2ZnSnS_4, Thin Films, J. Electron. Mater. 44 (2015) 3283.

49) Suna Y M, Yaoa B, Mengc X C, Wangc D, Longc D, Huac Z, Effect of Annealing Temperature and Ambient on Formation, Composition and Bandgap of Cu_2ZnSnS_4 Thin Films, ACTA PHYS. POL. A. 126 (2014) 751.

50) Tapas Kumar Chaudhuri N, Devendra Tiwari, Earth-abundant non-toxic Cu_2ZnSnS_4 thin films by direct liquid coating from metal–thiourea precursor solution, Sol. Energy Mater. Sol. Cells 101 (2012) 46.

51) Nitsche R, Sargent D F, Wild P, Crystal Growth of Quaternary I(2)II-IV-VI(4) Chalcogenides by Iodine Vapor Transport, J. Cryst. Growth 1 (1967) 52.

52) Hironori Katagiri, Nobuyuki Sasaguchi, Shima Hando, Suguru Hoshino, Jiro Ohashi, Takaharu Yokota, Preparation films by and evaluation of Cu_2ZnSnS_4 thin sulfurization of E-B evaporated precursors, Sol. Energy Mater. Sol. Cells 49 (1997) 407.

53) Kamoun N, Bouzouita H, Rezig B, Fabrication and characterization of Cu_2ZnSnS_4 thin films deposited by spray pyrolysis technique, Thin Solid Films. 515 (2007) 5949.

54) Fischereder A, Rath T, Haas W, Amenitsch H, Albering J, Meischler D, Larissegger S, Edler M, Saf R, Hofer F, Trimmel G, Investigation of Cu_2ZnSnS_4 formation from metal salts and thioacetamide, Chem. Mater. 22 (2010) 399.

55) Liu R, Tan M, Zhang X, Chen J, Song S, Zhang W, Impact of sol–gel precursor treatment with preheating temperature on properties of Cu_2ZnSnS_4 thin film and its photovoltaic solar cell, J. .Alloys. Compd. 655 (2016) 124.

56) Patel M, Mukhopadhyay I, Ray A, Structural, optical and electrical properties of spray-deposited CZTS thin films under a non-equilibrium growth condition, J. Phys. D. Appl. Phys. 45 (2012) 445103.

57) Zhenghua Su, Chang Yan, Kaiwen Sun, Zili Han, Fangyang Liu, Jin Liu, Yanqing Lai, Jie Li, Yexiang Liu, Preparation of Cu_2ZnSnS_4 thin films by sulfurizing stacked precursor thin films via successive ionic layer adsorption and reaction method, Appl. Surf. Sci. 258 (2012) 7678.

58) Zakaria Z, Chelvanathan P, Rashid M J, Akhtaruzzaman M, Alam M M, Al-Othman Z A, Alamoud A, Sopian K, Amin N, Effects of sulfurization temperature on Cu_2ZnSnS_4 thin film deposited by single source thermal evaporation method, Jpn. J. Appl. Phys. 54 (2015) 08KC18.

59) Long B, Cheng S, Lai Y, Zhou H, Yu J, Zheng Q, Effects of sulfurization temperature on phases and opto-electrical properties of Cu_2ZnSnS_4 films prepared by sol–gel deposition, Thin Solid Films. 573 (2014) 117.

60) Patel M, Mukhopadhyay I, Ray A, Structural, optical and electrical properties of spray-deposited CZTS thin films under a non-equilibrium growth condition, J. Phys. D. Appl. Phys. 45 (2012) 445103.

61) David Mitzi B, Oki Gunawan, Teodor Todorov K, Kejia Wang, Supratik Guha, The path towards a high-performance solution-processed kesterite solar cell, Sol. Energy. Mater. Sol. Cells 95 (2011) 1421.

Chapter 5

Preparation of Cu_2ZnSnS_4 films by spray coating and study of their structural, morphological, optical and electrical properties

This chapter describes the fabrication of CZTS thin films by simple spray coating technique. As in the case of spin coating, two different solution based approaches were adopted to prepare precursor films by spray coating. Three different temperature treatments as given in Table 5.1 were adopted to prepare phase pure CZTS films.

The precursor films were annealed or sulphurized at different temperatures and carried out detailed studies on their structural, surface morphological, optical and electrical properties. Phase purity of the films was studied by X-ray diffraction and Raman spectroscopy. Surface morphology of the films was examined by both scanning electron microscopy and field emission scanning electron microscopy. Film thickness was estimated by FESEM cross sectional analysis. Elemental composition analysis was carried out by EDXS coupled to the SEM. UV-visible spectroscopy was used to study the optical properties. Hall measurement technique was used to measure the electrical properties for the spray coated films.

Table 5.1 Various routes adopted for fabricating phase pure CZTS thin films by spray coating and subsequent temperature treatment

Sl. No.	Sample Code/details	Annealing/sulphurizing treatment
01	CZT *(Precursor solution without sulphur)*	Annealed at different temperatures in sulphur environment
02	CZTS *(Precursor solution with sulphur)*	Annealed at different temperatures in sulphur environment
03		Annealed at different temperatures in inert atmosphere (nitrogen)

5.1 Cu_2ZnSnS_4 films from spray coated CZT precursor and subsequent sulphurization

5.1.1 Precursor solution for spray coating

Several groups investigated various different parameters of spray coating to improve phase purity of CZTS thin films [1-3]. Kumar et al. studied the effect of concentration of Cu and S [2], while Rajeshmon et al. studied the role of precursor solution in controlling optoelectronic properties of CZTS thin films [3]. Water is used as solvent in spray coating process in most of the already published reports. Dependence of solvent type on the final properties of CZTS films is also reported. [4]. In several studies, 2-methoxy ethanol is used as solvent, as mentioned in chapter 3 section 3.1.1 of this thesis. In view of this, the use of organic solvent was explored in this study for fabricating CZTS thin films by spray coating.

Stable precursor solution without sulphur source was prepared for spray coating in a similar manner described in section 4.1.1 with

same chemicals, but with different concentrations. 0.02M copper (II) acetate monohydrate, 0.01M zinc (II) acetate dehydrate, 0.01M tin (II) chloride and 100ml 2-methoxyethanol were used for preparing precursor solution.

5.1.2. Fabrication of CZTS thin films by spray coating

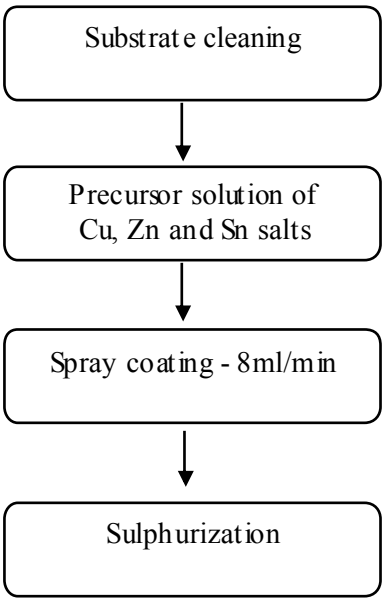

Fig. 5.1 Flow chart of the deposition of CZTS thin films by spray coating

Cleaning of glass substrates were carried out as per the standard cleaning procedure described in section 3.1.2. CZT precursor films were coated by spraying precursor solution on to the pre-cleaned glass substrates at the rate of 8ml/minute, through locally fabricated spray set up. Substrate temperature was kept at 300°C throughout the process. Air blast atomizer contains pure nitrogen gas with flow rate 4l/minute was used for coating. The distance between spray nozzle and

substrate kept was 10cm. After coating, the film was allowed to cool to room temperature. Fig. 5.1 shows the flow chart indicating the spray coating procedure used in this study. The CZT precursor thin films were sulphurized in N_2+H_2S atmosphere to complete the Cu_2ZnSnS_4 phase formation by incorporating sulphur into the crystal lattice. The sulphurizations were carried out at different temperatures (450°C-600°C) to study the effect of sulphurization temperature on the structural, optical and electrical properties of the CZTS thin films. The sulphurization setup was described in the section 4.13 of this thesis. The structural, morphological, optical and electrical properties of the spray coated films were studied in detail.

5.1.3 Structural studies

5.1.3.1 X-ray Diffraction Studies

Structural properties of the films were investigated by High Resolution grazing incidence XRD (GIXRD), as described in chapter 2 section 2.2.1 of this thesis. Fig. 5.2 shows the GIXRD pattern of CZTS films sulphurized at different temperature. All films showed characteristic peaks of CZTS phase and the peaks were marked with the help of ICDD file 26-0575. Films sulphurized at 450°C exhibited a few peaks other than CZTS planes. These peaks were identified as SnS_2, with the help of its ICDD file, 89-2028. Similarly, additional peaks were observed in the film sulphurized at 500°C, and were identified as that of Cu_2SnS_3 phase, with the help of its ICDD file 27-0198.

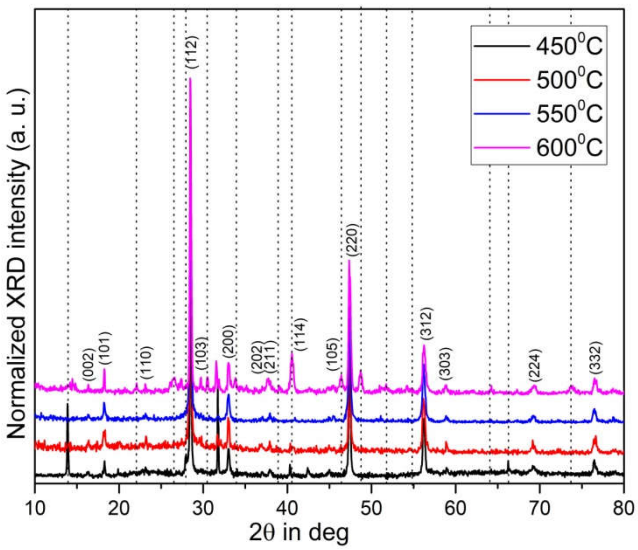

Fig. 5.2 GIXRD pattern of precursor films after sulphurizing at different temperature

In addition, the films sulphurized at 600°C exhibited extra peaks, and these were identified as those of secondary phases, SnS_2 and Cu_4SnS_4 (ICDD file for Cu_4SnS_4 used was 27-0196). As seen in the XRD patterns, the film sulphurized at 550°C is phase pure. Lattice constants for the films were calculated based on tetragonal system. Table 5.2 lists the calculated values of lattice constants for films sulphurized at various temperatures. The values of lattice constants were found to match with those in the kesterite mineral data [5]. The lattice parameter calculated for the films sulphurized at 550°C parameters were $a=b=5.424$Å and $c=10.821$Å. The corresponding values of kesterite mineral are $a=b=5.428$Å and $c=10.864$Å [5].

Average crystalline size of the films was calculated using Scherer's formula and Williamson-Hall (W-H) relation. The W-H analysis was described in section 2.2.1 of chapter 2 in this thesis. Table

5.2 shows the calculated average crystallite size and strain of films sulphurized at different temperatures. It can be seen that the values calculated for crystallite size using Scherrer formula is less than those obtained by the W-H method. As seen in table, the average crystallite size increases with increase in sulphurization temperature. Higher crystallite size was observed for the films sulphurized at 600°C; however, X-ray analysis revealed the presence of secondary/ ternary phases along with CZTS. The average size of the crystallites in film sulphurized at 550°C was 52nm by Scherrer analysis, whereas the same by W-H relation was 56nm.

Table 5.2 Lattice parameters and crystallite size of films sulphurized at different temperatures

Sulphurization temperature	Lattice parameter		Crystallite size *(nm)*	W-H relation	
	a=b (*Å*)	*c* (*Å*)		Crystallite size (nm)	strain
450°C	5.423	10.817	42	43	0.0007
500°C	5.440	10.823	46	50	0.0043
550°C	5.424	10.821	52	56	0.0012
600°C	5.433	10.785	56	62	0.0342
ICDD 26-0575	5.4270	10.8480	--------	--------	--------

5.1.3.2 Raman spectroscopic Analysis

ZnS, Cu_2ZnS_3, Cu_4ZnSnS_4 are the major secondary/ternary phases commonly observed in the preparation of CZTS phases [6]. X-ray diffraction peaks of these phases coincide with the CZTS peaks, and hence it is difficult to confirm the exact CZTS phase formation from XRD alone. Raman spectroscopy was further used to investigate phase purity of the films. Fig. 5.3 shows the Raman spectra of CZTS thin films sulphurized at various temperatures.

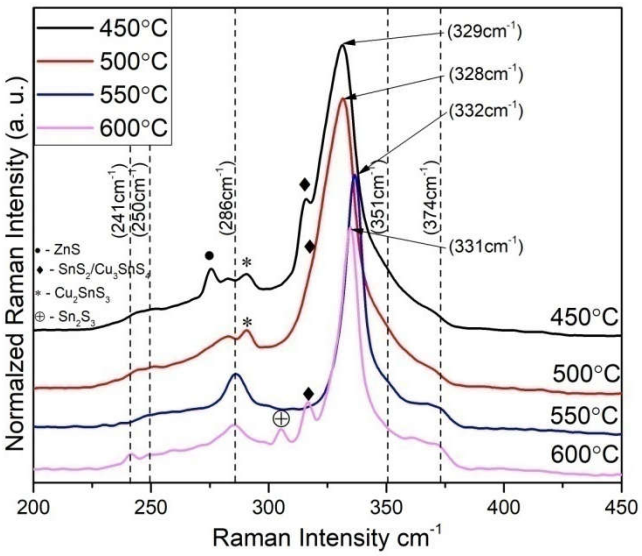

Fig. 5.3 Raman spectra of CZTS films sulphurized at different temperatures

The films sulphurized at different temperatures showed characteristic vibrational modes of CZTS at 250cm^{-1}, 328-332cm^{-1}, 286cm^{-1}, 351cm^{-1} and 374cm^{-1}. Peaks at 250cm^{-1}, 328-332cm^{-1}, 286cm^{-1}, 351cm^{-1} and 374cm^{-1} correspond to the B(LO), A, A, B(TO) and B(LO) vibrational modes of kesterite phase, respectively [3,6,7].

Raman spectra of film sulphurized at 450°C consist of a few additional peaks due to Cu_2SnSn_3, ZnS and SnS_2/Cu_3SnS_4, in addition to the kesterite vibrational modes. These peaks observed at 275cm^{-1}, 291cm^{-1} and 316cm^{-1} are identified as the vibrational modes of ZnS [6,8], Cu_2SnS_3 [6], SnS_2/Cu_3SnS_4 respectively [8-11]. Origin of the mode at 317cm^{-1} is not clear since this is coinciding with the major modes of SnS_2 and Cu_3SnS_4 [8,12]. XRD analysis revealed the presence of SnS_2 phase in the film sulphurized at 450°C. Raman spectra of films sulphurized at 500°C exhibited vibrational modes at 291cm^{-1} and 316cm^{-1} corresponding to impurity phases Cu_2SnS_3 and SnS_2/Cu_3SnS_4 respectively [9,11]. The film sulphurized at 600°C showed peaks at 304cm^{-1} and 316cm^{-1} corresponding to secondary phases Sn_2S_3 and SnS_2/Cu_3SnS_4, respectively [9-12]. Raman studies confirmed phase purity in the film sulphurized at 550°C. However, the broad peak observed in this case may include peaks from other secondary phases also. To further confirm the phase purity of the CZTS films prepared in this route undoubtedly, the Raman spectra of films sulphurized at 500°C and 550°C were deconvoluted with Lorentzian peak fitting function [13].

Fig. 5.4 shows the deconvoluted Raman spectra of films sulphurized at 500°C and 550°C. Eight peaks were deconvoluted from the broader peaks for the films sulphured at 500°C. Major Peak of CZTS at 332cm^{-1} was found to be shifted to lower angle, may be due to the presence of secondary phase. The deconvolution revealed that

the peak at 328cm^{-1} composed of two peaks; and corresponds to CZTS and SnS_2 [7,12].

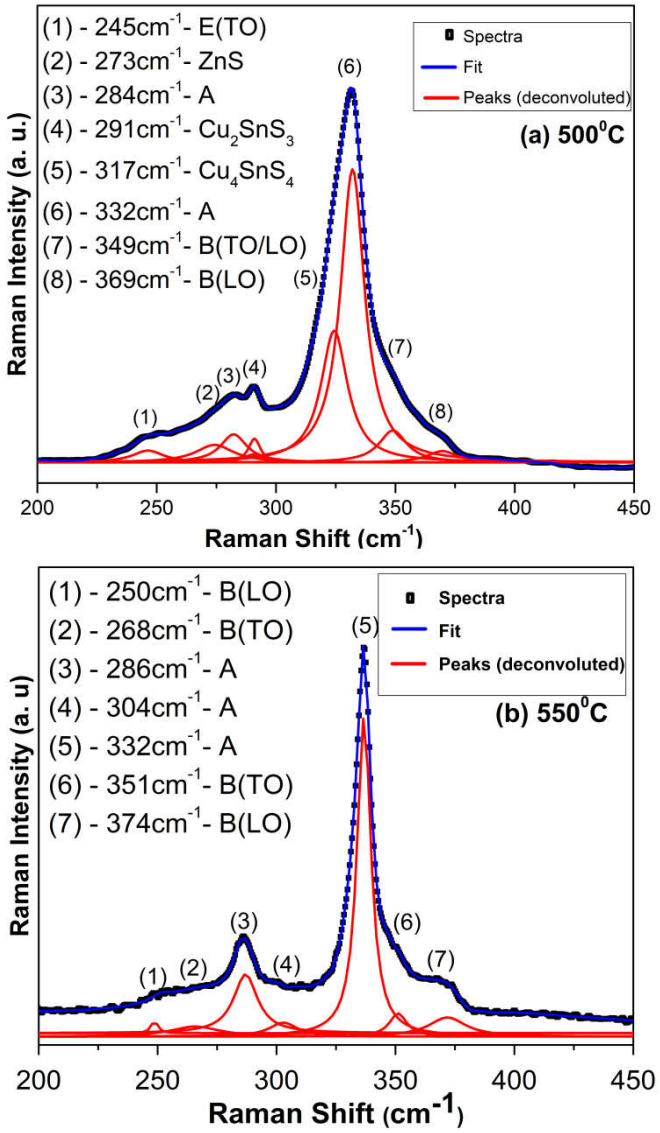

Fig. 5.4 Deconvoluted Raman spectra of films sulphurized at (a) 500 and (b) 550°C

Shift in Raman peaks was observed for CZTS due to the presence of secondary phases as discussed in the section 3.1.5.2 of chapter 3. Deconvoluted Raman spectra of films sulphurized at 550°C composed of seven peaks at 250cm^{-1}, 268cm^{-1}, 286cm^{-1}, 304cm^{-1}, 332cm^{-1}, 351cm^{-1}and 374cm^{-1}, and these peaks were assigned to the B(LO), B(TO), A, A, A, B(LO) and B(LO) vibrational modes of CZTS respectively [6-11]. Thus, the XRD and Raman studies confirmed the formation of phase pure CZTS when the spray coated precursor films were sulphurized at 550°C.

5.1.3.3 Rietveld refinement studies

Structural properties of the films were further investigated by rietveld refinement technique. Refinements were carried out using GSAS software, as described in section 4.2.3.3 of this thesis. Tetragonal kesterite type model (a=b=5.427Å, c=10.871Å, α=β=γ=90°) in the S.G I4□ (S.G No: 82) was used as the starting model [5]. Fig. 5.5 shows the rietveld refined plot of films sulphurized at 550°C. Black dots represent experimental data, red line is the calculated fit, pink vertical lines are the positions of refined phase reflections and blue line is the difference line between the experimental and fitted data. The agreement factors of the fit are Wrp=0.2030, Rf^2=0.1448 and χ^2=1.287.

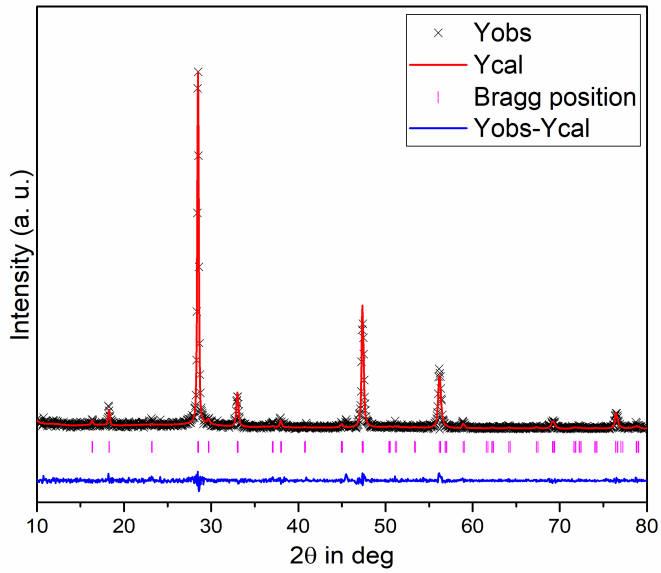

Fig. 5.5 Rietveld refinement results of spray coated CZT thin film sulphurized at 550°C. Black dots represent experimental data, red line is the calculated fit, pink vertical lines are the positions of refined phase reflections and blue line is the difference line between experimental and fitted data

The lattice parameters $a=b$ and c of films sulphurized at 550°C were extracted from the refined data. Refined lattice parameters were $a=b$=5.4309465Å, c=10.858355Å and $c/2a$=0.9993, which is close to the reported values of lattice constants for kesterite mineral data (a=b=5.428(2)Å, c=10.864(4) Å and c/2a = 0.9854(5)) [5,14,15]. In the case of kesterite type crystals, tetrahedral distortion can be expressed in terms on cation-anion-cation bond angles. Ideally, the bond angle in tetrahedral symmetry is 109.47°. However, in kesterite crystal structure, the Cu-S-Sn and Zn-S-Sn angles are smaller and Cu-S-Zn and Cu-S-Cu angles are larger than this ideal value. In this study, for the spray coated CZT precursor film sulphurized at 550°C, the

bond angles obtained were 107.317(6)°, for Cu-S-Sn, 108.21(10)°, for Zn-S-Sn, 111.321(11)° for Cu-S-Zn and 110.510(9)° for Cu-S-Cu. The bond angle values calculated are in agreement with the reported values for kesterite structure [5,15].

5.1.4 Elemental composition analysis

Elemental compositions of the films were investigated by EDXS equipped with SEM. EDXS results of films sulphurized at different temperatures are shown in Table 5.3. In the stoichometric conditions, the Cu/(Zn+Sn) and Zn/Sn ratios are unity [16-18]. As seen in the table, the stoichometry is considerably deviated for the film sulphurized at 450°C. This indicates that CZTS phase may not be formed completely when sulphurized at 450°C [11]. The sulphur concentration decreases with increase in sulphurization temperature to 550°C. According to Katagiri et al [19], non-stoichometric composition ratios (Cu poor and Zn rich) were obtained for high performance CZTS cells. In this work, these composition ratios of the spray coated films were Cu/(Zn+Sn)=0.91 and Zn/Sn=0.92 for the film sulphurized at 550°C; this condition is not favourable as explained in section 3.1.6 of this thesis. Similar results were published by Araki et al [20], observed Cu poor with Sn and Zn rich composition at this temperature. The composition ratios of CZTS film sulphurized at 600°C, which contain secondary phases, were Cu/(Zn+Sn)=1.05 and Zn/Sn=1.22.

Table 5.3 Summary of EDXS results of the films sulphurized at different temperatures

Sulphurizing temperature	EDXS results					
	Cu (at%)	Zn (at%)	Sn (at%)	S (at%)	Cu/(Zn+Sn)	Zn/Sn
450 °C	14.49(±4)	9.01 (±5)	17.17 (±2)	59.33 (±4)	0.55	0.52
500 °C	20.88 (±5)	10.83(±3)	10.79 (±4)	57.55 (±6)	0.97	1.00
550 °C	23.64 (±4)	12.38(±5)	13.39 (±2)	50.59 (±5)	0.91	0.92
600 °C	23.29 (±4)	12.23(±5)	10.05 (±4)	54.43 (±5)	1.05	1.22

5.1.5 Surface morphology

Surface morphologies of the films were analysed by SEM and FESEM. Fig. 5.6 (a-d) show the SEM images of films sulphurized at a) 450°C, b) 500°C, c) 550°C and d) 600°C. As seen, cracks were observed in the film sulphurized at 450°C. Dense surface morphology with large grains was observed for the films sulphurized at 500°C and 550°C. However, grains with different sizes and shapes were observed when sulphurized at 600°C. The XRD and Raman studies revealed secondary and ternary phases in the films sulphurized at 600°C. Higher temperature sulphurization may lead to decomposition of CZTS and form secondary or ternary phases [21]. However, XRD and Raman investigations confirmed the phase pure nature of the film sulphurized at 550°C. Fig. 5.6 (e) shows the FESEM image of the film sulphurized at 550°C. Grain and grain boundaries are clearly visible at this temperature. The cross-sectional image of the film sulphurized at 550°C is shown in Fig. 5.6 (f). Thickness of the film was found to be ~ 1.9μm from this image.

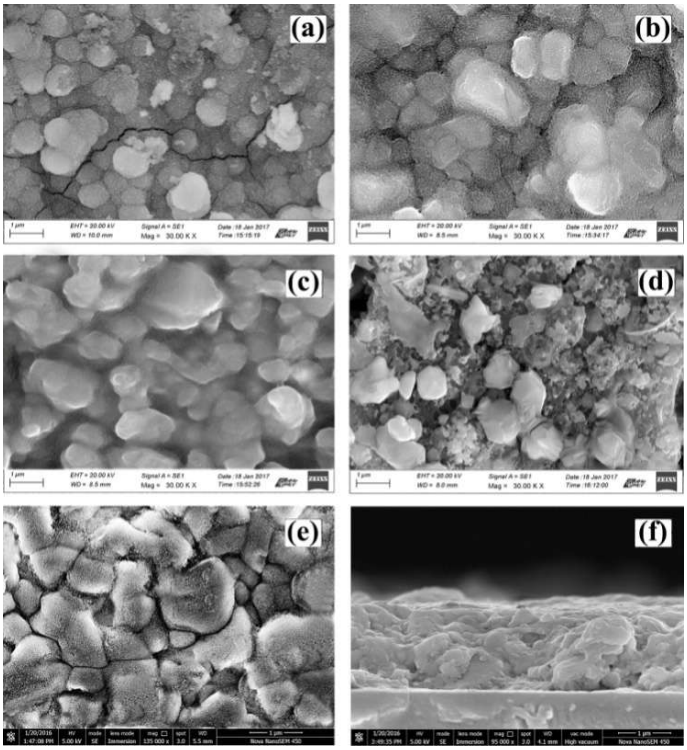

Fig. 5.6 SEM images of films sulphurized at a) 450°C, b) 500°C, c) 550°C and d) 600°C, e) FESEM images of films sulphurized at 550°C and f) cross section of the films sulphurized at 550°C.

5.1.6. Optical properties

Fig. 5.7 shows the optical properties of the films sulphurized at various temperatures. As described in the previous chapters, the optical band gap of the films were estimated by extrapolating the linear portion of the Tauc plot, $(\alpha h\upsilon)^2$ vs $h\upsilon$, to the x axis. Calculated band gaps for the films sulphurized at different temperatures are listed in Table 5.4. Band gap of the films were found to decrease from 1.53eV to 1.33eV with increase in sulphurization temperature. The observed change in band gap may due to the increase in crystalline size and the

presence of secondary phases [16,22,23]. The higher band gap of films sulphurized at 450°C may due to the presence of ZnS (Eg=3.7eV) [22]. The band gap was found to be 1.47eV for the film sulphurized at 550°C.

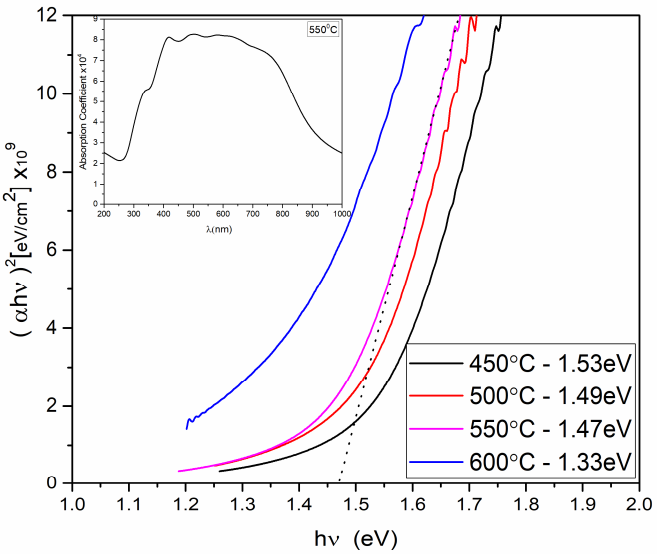

Fig. 5.7 $(\alpha h\upsilon)^2$ versus $h\upsilon$ plot of the films sulphurized at different temperature; (inset) absorption coefficient versus wavelength plot of films sulphurized at 550°C

Inset of Fig. 5.7 shows the absorption coefficient versus wavelength plot for the films sulphurized at 550°C. As shown, the film exhibits an average absorption coefficient of ~8×10^4 cm^{-1} in the visible region. The higher absorption coefficient indicates that a thin film with thickness ~ 1.9μm fabricated in this study can absorb most of the incident photons.

Table 5.4 Optical band gap of films sulphurized at various temperatures

Sulphurizing temperature	Band gap
450 °C	1.53eV
500 °C	1.49eV
550 °C	1.47eV
600 °C	1.33eV

5.1.7. Electrical properties

Hall measurements were performed with constant magnetic filed 0.54T at room temperature, as described in section 2.2.8 of chapter 2 of this thesis. *p* type nature of the films were confirmed from the positive sign of the carrier concentration. Carrier concentration, mobility and resistivity of the film sulphurized at 550°C obtained were $1.544\times10^{19}cm^{-1}$, $0.87cm^2V^{-1}S^{-1}$ and 0.46Ωcm, respectively. Similar results were published by Rajeshmon et al. [3] for CZTS films coated by spray coating using chloride precursor solution and water as solvent. According to Long et al, the optimum values for resistivity, mobility and carrier concentration for CZTS films are 10 to 10^3Ωcm, 10^{16} to $10^{18}cm^{-3}$ and 1 to 10 cm^2/Vs, respectively [24]. However, several articles were published later with different electrical properties for CZTS films, fabricated by various techniques. Most of these articles reported lower resistivity, higher mobility and moderate carrier concentration for CZTS films [25-32].

5.2. Cu_2ZnSnS_4 films from spray coated CZTS precursor and subsequent sulphurization

5.2.1 Preparation of stable precursor solution for spray coating

In this route, the precursor solution for spray coating was prepared with sulphur source (referred to as CZTS precursor solution) was prepared by dissolving copper (II) acetate monohydrate (0.02M), zinc (II) acetate dehydrate (0.01M), tin (II) chloride (0.01M) and thiourea (0.16M) into 100ml 2-methoxyethanol. All chemicals were purchased from Merck and were used without further purification. Thiourea was used as the sulphur source. The resultant solution was stirred at 45°C for 1 hour to dissolve precursor salts completely, as in the case of the previous case described in section 5.1.1 of this thesis.

5.2.2 Fabrication of CZTS thin film by spray coating

CZTS precursor films were coated by spraying the precursor solution on to a pre-cleaned substrate. Glass substrates were cleaned by a standard cleaning procedure described in section 3.1.2. Substrate temperature and spray coating conditions were described in section 5.1.2 of this chapter. The CZTS precursor films were sulphurized at different temperatures to study the effect of sulphurization temperature on the phase formation and the structural, optical and electrical properties. The experimental setup used for sulphurizing CZTS thin films were described in section 3.1.4. After the sulphurization structural, optical and electrical properties of the films were studied.

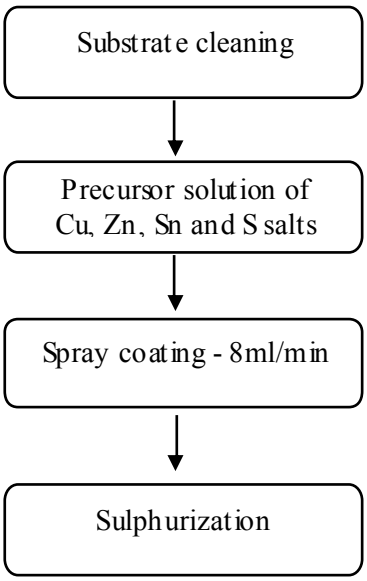

Fig. 5.8 Flow chart of the deposition of CZTS thin films by spray coating

5.2.3 Structural studies

5.2.3.1 X-ray Diffraction Studies

Fig. 5.9 shows the x-ray diffraction patterns of spray coated CZTS films sulphurized at different temperatures. Crystal structures of the films were identified by comparing the *d* values with those in the ICDD-PDF 26-0575. The film sulphurized at 400°C showed four peaks corresponding to (112), (220), (312) and (332) planes of CZTS. Almost all peaks of kesterite phase were observed when sulphurization temperature was increased. As seen in the XRD patterns, number of peaks and peak intensity increases with sulphurizing temperature. Thus the crystallinity of the film is found to increase when sulphurization temperature was increased from 400°C to 600°C. All CZTS peaks were present even at lower sulphurizing temperature (400°C). XRD

studies did not reveal any secondary phases in the films irrespective of the sulphurization temperature. The film did not show any phases other than CZTS even at higher sulphurizing temperatures (550°C and 600°C).

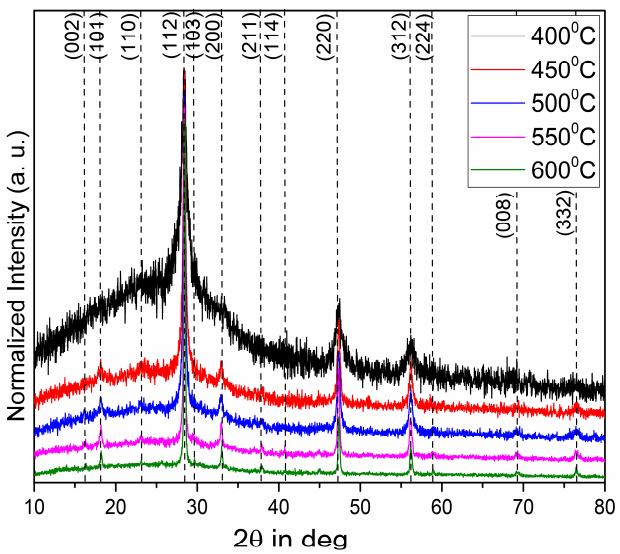

Fig. 5.9 XRD pattern of CZTS thin films sulphurized at different temperatures

Lattice constants were estimated from the XRD patterns. Cu_2ZnSnS_4 possesses tetragonal structure and the lattice constants were calculated based on the tetragonal symmetry. Table 5.5 shows the lattice constants calculated for the CZTS films sulphurized at different temperatures. These values are in good agreement with the single crystal data, a = 0.5427nm and c = 1.0848nm (ICDD-PDF No.26-0575). Change in crystalline size with sulphurizing temperatures was studied using Scherrer's formula and W-H relation and the results are given in Table 5.5. Average crystalline size of the CZTS thin films was

found to increase with sulphurizing temperature. Higher crystalline size was observed for the films sulphurized at 600°C.

Table 5.5 Lattice constants of CZTS films sulphurized at different temperatures

Sulphurization Temp	Lattice parameter (nm)		Crystallite size (nm)	W-H relation	
	$a = b$	c		Crystallite size (nm)	Strain
400°C	0.5434	1.0805	20	31	0.0651
450°C	0.5427	1.0887	38	39	0.0087
500°C	0.5426	1.0911	47	51	0.0023
550°C	0.5428	1.0882	59	60	0.0008
600°C	0.5424	1.0744	70	69	0.0021
ICDD 26-0575	0.5427	1.0848	----	----	----

5.2.3.2. Raman spectroscopic Analysis

As discussed in the previous chapters, it is difficult to confirm the exact formation of kesterite phase from XRD measurements due to similar crystal structure possessed by other impurity phases, such as ZnS and Cu_2SnS_3. Hence the films were investigated by Raman spectroscopy to further confirm phase formation. Raman spectra of films sulphurized at different temperatures are shown in Fig. 5.10

As shown in Fig. 5.10, all films possess characteristic Raman peaks of CZTS at 249cm^{-1}, 334cm^{-1} and 366 cm^{-1}, irrespective of the sulphurization temperature. Films sulphurized at 400°C and 450ºC showed another peak at 274cm^{-1}, which is due to ZnS phase [6,7]. This secondary phase was not observed in the XRD analysis. In addition to the peaks at 249cm^{-1}, 334cm^{-1} and 366 cm^{-1}, Raman spectra

of the films sulphurized at 500°C and 550°C showed peaks at 284cm^{-1} and 352cm^{-1}. Among the peaks, those at 284cm^{-1} and 334cm^{-1} correspond to the A vibrational mode, whereas peaks at 249cm^{-1}, 352cm^{-1} and 366 cm^{-1} correspond to the B(TO LO) vibrational mode of CZTS [7].

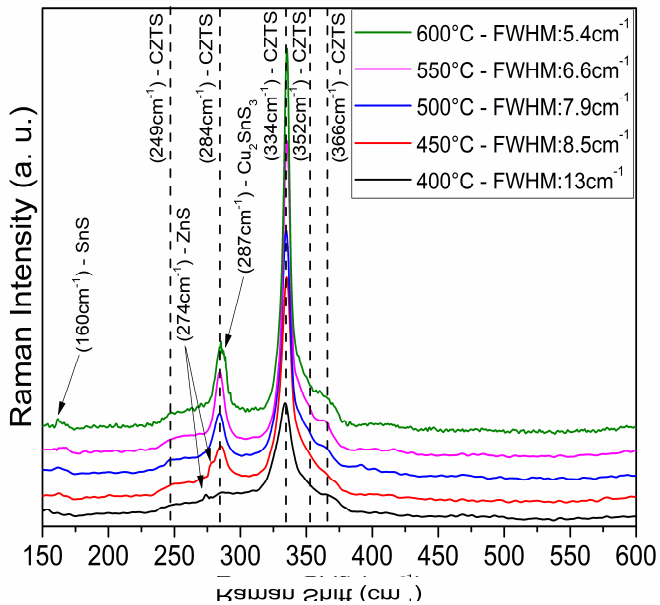

Fig. 5.10 Raman spectra of CZTS thin films sulphurized at different temperatures.

When sulphurization temperature was increased to 600°C, peak at 160 cm^{-1}of SnS and another peak at 287cm^{-1} of Cu_2SnS_3 were observed along with the peaks of CZTS [6]. Thus, Raman studies confirmed the formation of phase pure CZTS when the films were sulphurized at 500ºC and 550ºC. FWHM of intense Raman peaks were calculated and shown in Fig. 6.8. As seen, FWHM of intense peak (334cm^{-1}) decreases with increase in sulphurization temperature. This

may be due to the improved crystallinity of the films [33]. For photovoltaic devices, crystallinity of the film is also important [16,34]. Here, the film sulphurized at 600°C exhibited higher crystallinity, but contains secondary phases. Hence the film sulphurized at 550°C possesses phase purity and better crystallinity.

5.2.3.3. Rietveld refinement

In addition to the phase formation and identification, investigations such as lattice and bond angle distortion are also important in the structural characterization of CZTS thin films prepared in this study. In order to carry out structural refinement by Rietveld analysis, high quality data were obtained from high resolution grazing incidence x-ray diffraction. Fig. 5.11 shows the high resolution GI-XRD patterns of film sulphurized at 550°C and its Rietveld refined pattern. For refinement, high resolution data was recorded with a step size of 0.02° and collection time of 3s per step, at 1° grazing angle. EXPGUI, the graphical interface of GSAS (General structural analysis system) software, is used for the refinement process [35]. All peaks observed in the GI-XRD pattern were indexed with the help of ICDD file 26-0575. No peaks from secondary phases were observed in this GI-XRD study. For refinement, the kesterite type model was used as starting model and the details were discussed in the section 5.1.3.3 of this thesis.

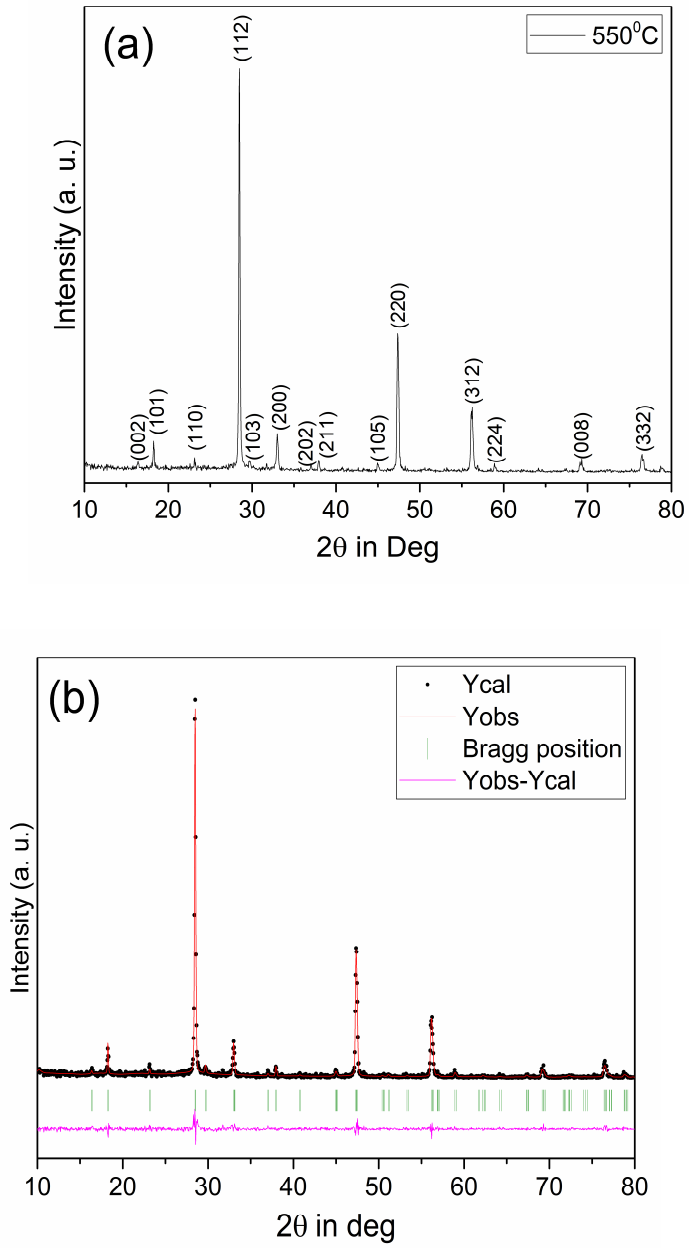

Fig. 5.11 (a) High resolution GI-XRD pattern of CZTS film sulphurized at 550°C and (b) its Rietveld refined pattern

Observed refinement parameters are goodness of fit (χ^2)=1.260 Wrp= 0.2789and R_f^2=0.2592. Lattice constants obtained after refinement are a=b=5.4307, c=10.8294 and $c/2a$=0.9971. These values are in good agreement with those obtained earlier for the kesterite type structure [5,34].

As discussed in the previous section, tetrahedral distortion in kesterite type crystal can be expressed in terms on cation-anion-cation bond angles. Ideally, the bond angle in tetrahedral structure is 109.47°. However, in kesterite crystal structure, the Cu-S-Sn and Zn-S-Sn angles are smaller and Cu-S-Zn and Cu-S-Cu angles are larger than this ideal value. In this study, for the CZTS film sulphurized at 550°C, the bond angles obtained are 108.528(14)° for Cu-S-Sn, 109.33(7)° for Zn-S-Sn, 112.257(7)° for Cu-S-Zn and 109.612(7)° for Cu-S-Cu. The bond angle values calculated are in agreement with the reported values for kesterite structure [15].

5.2.4. Elemental composition analysis

Elemental compositions of the spray coated CZTS films sulphurized at various temperatures were analysed by EDXS . Table 5.6 shows summary of elemental compositions of the films. For CZTS, ideal stoichiometry is when Cu/(Zn+Sn) and Zn/Sn ratios are unity. However, it has been reported that non-stoichometry in CZTS is favourable for obtaining higher efficiency [36-38]. The results shown in Table 5.6 indicate non-stoichometry in the films sulphurized at all temperatures. Similar stoichometric variations were also reported by

Huang et al. for spray coated CZTS films with ultrasonic spray pyrolysis setup [37]. Higher variations in stoichiometry were observed for the film sulphurized at 400°C. The ratios Cu/(Zn+Sn) and Zn/Sn of films sulphurized at 550°C were 0.97 and 0.99 respectively. Cu/(Zn+Sn) ratios of CZTS films varies with sulphurization temperature. Cu poor Zn rich conditions are preferred in CZTS solar cells as discussed in chapter 3 section 3.1.6 [2,3,24]. In the present study, as seen in the table, copper concentration increases, while the Zn concentration decreases with increases in sulphurization temperature. The Zn/Sn ratio is found to decrease with increase in sulphurization temperature. Thus, in this route, Cu poor and Sn rich films were obtained for films sulphurized at 550°C; this condition may not be preferable for high performance CZTS solar cells [19].

Table 5.6 EDXS results of CZTS films sulphurized at different temperatures

Sulphurizing temperature	EDXS results					
	Cu	Zn	Sn	S	Cu/(Zn+Sn)	Zn/Sn
400 °C	21.66(±3)	16.38(±1)	5.65(±2)	56.31(±5)	0.98	2.90
450 °C	22.87(±6)	11.75(±3)	10.83(±3)	54.55(±6)	1.01	1.08
500 °C	23.0 (±4)	11.7 (±4)	11.8 (±3)	53.5 (±4)	0.98	0.99
550 °C	22.78(±4)	11.67(±5)	11.8 (±4)	53.75(±3)	0.97	0.99
600 °C	26.39(±2)	11.31(±4)	13.05(±2)	49.25(±8)	1.08	0.87

5.2.5 Surface morphology

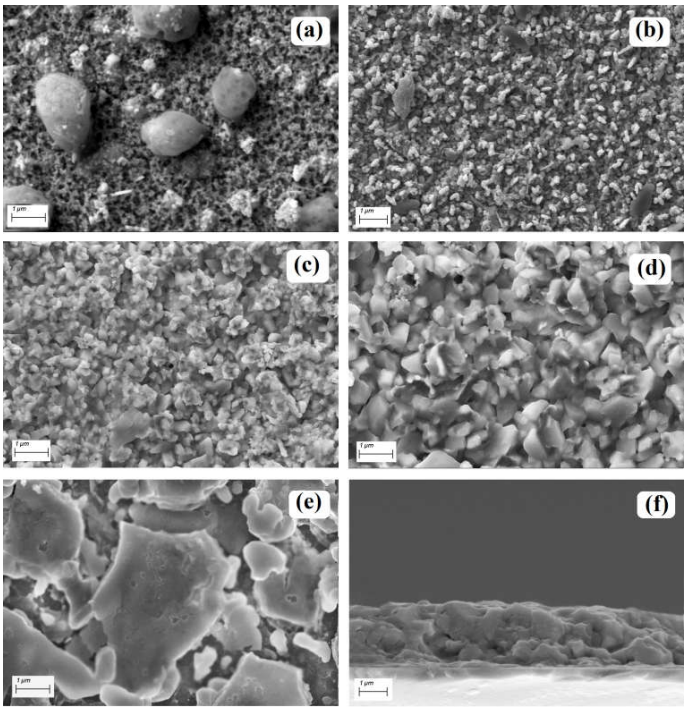

Fig. 5.12 SEM images of films sulphurized at a) 400°C, b) 450°C, c) 500°C, d) 550°C, e) 600°C, and f) cross-sectional view of the film sulphurized at 550°C

Surface morphology and film thickness of spray coated CZTS films sulphurized at different temperatures were analysed by scanning electron microscope. Fig. 5.12 shows the SEM images of films sulphurized at various temperatures. Features with large size were observed in the SEM images of the films sulphurized at 400°C and 450°C; these large grains may be of the secondary phases and are confirmed using EDXS analysis. Secondary phases were also detected in the XRD and Raman studies. Grains and grain boundaries are clearly visible for the films sulphurized above 450°C. As seen in the

figures, the grain sizes increase with sulphurization temperature. The grain size is very small at lower sulphurization temperatures, 400°C and 450°C. The films became dense when sulphurized at 500°C and 550°C and large grains were observed at these temperatures. This may be due to Ostwald ripening of grains at higher temperatures [39,40]. Thus, a dense CZTS film with good microstructure was formed at 500°C and 550°C sulphurizing temperature. Average grain size of the films sulphurized at 550°C was found to be ~600nm. However, voids and cracks were observed when the temperature was increased to 600°C (Fig. 5.12e). The cross-section of the film sulphurized at 550°C film is shown in Fig. 5.12 (f). The thickness of the film was estimated to be 2.02μm from the SEM image.

5.2.6. Optical properties

Fig. 5.13 (a-f) show the $(\alpha h\upsilon)^2$ versus $h\upsilon$ plots of the CZTS films sulphurized at various temperatures and a typical curve indicating the absorption coefficient versus energy curve obtained for the film sulphurized at 550°C. The optical absorption coefficient α, of the film sulphurized at 550°C was found to be $10^5 cm^{-1}$ in the visible region, as seen in Fig. 5.13 (f). Optical band gap for direct band gap materials are estimated using the well known Tauc's relation [16,34,39]. Band gaps were deduced from the $(\alpha h\upsilon)^2$ versus $h\upsilon$ plots by extrapolating the linear portion of plot to the x-axis. Table 5.7 gives the band gaps of the films sulphurized at different temperatures.

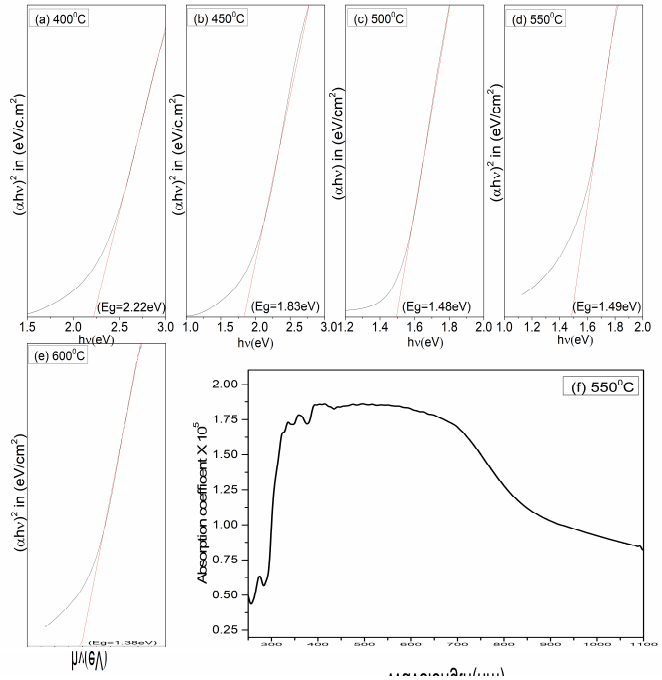

Fig. 5.13 $(\alpha h\upsilon)^2$ versus $h\upsilon$ plot of the films sulphurized at different temperature (a-e) and absorption coefficient versus wavelength plot of the film sulphurized at 550°C (f)

Table 5.7 Band gaps obtained for the CZTS films sulphurized at different temperatures

Sulphurizing temperature	Band gap
400 °C	2.22eV
450 °C	1.83eV
500 °C	1.48eV
550 °C	1.49eV
600 °C	1.38eV

As seen in the table, band gaps of the films were found to decrease with increase in sulphurization temperature. The band gap was found to be very high at the sulphurization temperature 400°C. This may be due to the presence of secondary phase ZnS, which was identified in Raman analysis [33]. The band gap decreased to 1.83 eV after sulphurizing at 450°C, the difference in band gap with sulphurization temperature may due to the difference in crystallinity and the decrease in ZnS phase at higher temperature [16,34]. When sulphurization temperature is increased, ZnS react with other metallic sulphides and form CZTS phase [33]. In the Raman spectra, intensity of the ZnS peak was found to decrease when sulphurizing temperature was increased from 400°C to 450°C. However, optical band gaps became 1.48eV for the film sulphurized at 500°C and ~1.49eV for the fil sulphurized at 550°C. These values are close to the ideal value required for single junction solar cells. The band gap was found to decrease with further increase in sulphurization temperature (600°C). This is may be due to the presence of secondary and ternary phases (SnS, Cu_2SnS_3) observed at this higher temperature [16,34]. The n type semiconductors SnS has much lower bang gap energy [33].

5.2.7. Electrical properties

Electrical properties using Hall set up were investigated with 0.54T magnetic field intensity, as described in the previous chapters. The Hall measurement revealed positive sign for the hall coefficient and the carrier density, indicating *p* type conduction for the films. Table 5.8 lists the summary of the results of electrical studies carried

out on the films sulphurized at various temperatures. As seen, the carrier concentration of the films increases with increase in sulphurization temperature (from 400°C to 500°C), while the mobility decreases; this trend may be due to the decrease in ZnS phase, as observed in the Raman spectra [34]. Patel et al [1] reported that decrease in Zn and S contents will lower the carrier mobility in CZTS film. Further increase in sulphurization temperature increases in mobility, which can be attributed to the improved crystallinity of the film, as observed in the XRD analysis.

Table 5.8 Electrical properties of CZTS films sulphurized at different temperatures

Sulphurization Temperature (°C)	Carrier Concentration (cm^{-3})	Mobility ($cm^2V^{-1}s^{-1}$)	Resistivity (Ω cm)
400	1.93×10^{18}	0.87	4.01
450	1.56×10^{19}	0.81	0.47
500	4.12×10^{19}	0.15	1.01
550	3.67×10^{19}	0.33	0.52
600	5.26×10^{17}	2.33	5.11

Higher resistivity and lower carrier concentration were observed at 600°C, which may be due to the secondary phases observed in the film at this sulphurization temperature [22]. At this sulphurization temperature, SnS phase was observed, which is n type and is unfavourable to device performance. Larger voids observed in the SEM image of the film sulphurized at 600°C may increase the

resistivity of the CZTS films [41]. As given in Table 5.8, the films sulphurized at 500°C and 550°C possesses higher carrier concentration and lower resistivity. Optimum electrical properties required for CZTS absorber material were discussed in the previous section of this chapter. The carrier concentration, mobility and resistivity of the film sulphurized at 550°C were $3.67\times10^{19}cm^{-3}$, $0.33cm^2V^{-1}s^{-1}$and 0.52Ωcm, respectively. In this work, better structural and optical properties were obtained for the film fabricated by spray coating followed by sulphurization at 550°C. The film possessed higher carrier concentration, but the hole mobility was very low.

5.3. Cu_2ZnSnS_4 film from ***spray*** coated CZTS precursor and subsequent ***annealing in inert atmosphere***

In this third route, CZTS precursor films were spray coated on to pre-cleaned glass substrates, as described in the section 5.2.1 of this chapter. The films were further annealed in inert (nitrogen) atmosphere to complete phase formation. Substrate cleaning and precursor solution preparation were carried out in a similar manner described in the previous route (section 5.2.1). The spray coated films were heat treated at different temperatures 400°C, 450°C, 500°C and 550°C for 30 minutes in nitrogen atmosphere. Experimental setup used for annealing CZTS thin films was described in section 4.3.1. The structural, optical and electrical properties of the films were investigated.

5.3.1. Structural studies

5.3.1.1. X-ray Diffraction Studies

CZTS precursor films were fabricated by spray coating technique and the films were further annealed in nitrogen atmosphere to study the effect of annealing temperature on the phase formation. Fig. 5.14 shows the XRD patterns of as-deposited and nitrogen annealed CZTS thin films. The as-deposited film did not show any peaks in the XRD analysis indicating the amorphous nature of the film. Two peaks were observed in the XRD pattern of films annealed at 400°C, corresponds to (112) and (220) planes of kesterite phase. As seen in the XRD pattern, the film annealed at 450°C exhibited three peaks corresponding to (112), (220) and (224) planes of CZTS (ICDD-PDF 26-0575). This indicates the formation of kesterite phase at 450°C. The film annealed at 500°C had relatively high intense peaks corresponding to (112), (200), (220), and (312) planes of kesterite. At 550°C, a peak corresponding to the secondary phase $Cu_{2-x}S_x$ was observed, in addition to the (112), (200), (220) and (224) planes of CZTS [42]. Annealing at high temperature may have resulted in melting and subsequent evaporation [43] of the film and this may be the reason for the appearance of secondary phase.

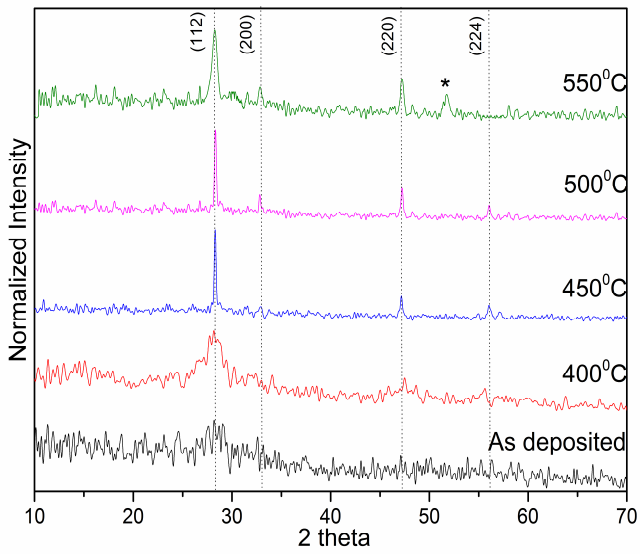

Fig. 5.14 XRD patterns of CZTS films annealed at different temperatures

Lattice constants and crystalline size were estimated from the XRD patterns. Average crystalline size was calculated using Scherrer's formula and W-H relation [44]. Table 5.9 shows the values of lattice constants and average size of the CZTS films annealed at 450°C and 500°C. These values are in good agreement with the single crystal data, a = 0.5427nm and c = 1.0848nm (ICDD PDF No.26-0575). The crystal structure and size of CZTS thin films were found to vary with annealing temperature. Also, the peak width is narrowed with temperature. As seen in the figure, the peak intensity is found to increase with the increase in annealing temperature. Thus, the average particle size and the crystallinity of the particles were found to increase with the annealing temperature. It has been reported that the improvement in crystallinity of the absorber layer enhances the

efficiency of solar cells [45]. In this study, the kesterite phase was formed at 450°C and the crystallinity was found to increase when the annealing temperature was increased to 500°C. Lattice strain of the CZTS film was calculated using W-H relation and found to increase with sulphurization temperature.

Table 5.9 Lattice parameters and average crystallite size of the films annealed at 450°C and 500°C

Annealing temperature	Lattice parameter (nm)		Crystalline size (nm)	W-H relation	
	a=b	c		Crystallite size (nm)	Strain
500°C	0.543	1.08	44	48	0.0034
450°C	0.544	1.09	42	44	0.0022

5.3.1.2 Raman spectroscopic Analysis

To confirm the formation of single phase Cu_2ZnSnS_4, the films were further investigated by Raman spectroscopy. Cu_2ZnSnS_4 has a space group of I4, primarily consists of two alternating cation layers each containing Cu and Zn atoms [15]. CZTS contains 8 atoms per primitive cell and there are 24 vibrational modes, in which 15 Raman active modes exist for kesterite structure [46] and 14 for stannite structure [47, 48]. It includes A, B and E modes. A mode arises from the symmetric vibration of anions, B mode arise from the movement of cations along the z-direction and E mode from the motion of cation in

the X-Y plane. Among these modes, B and E may lead to TO/LO splitting due to their (cation) polar character [46].

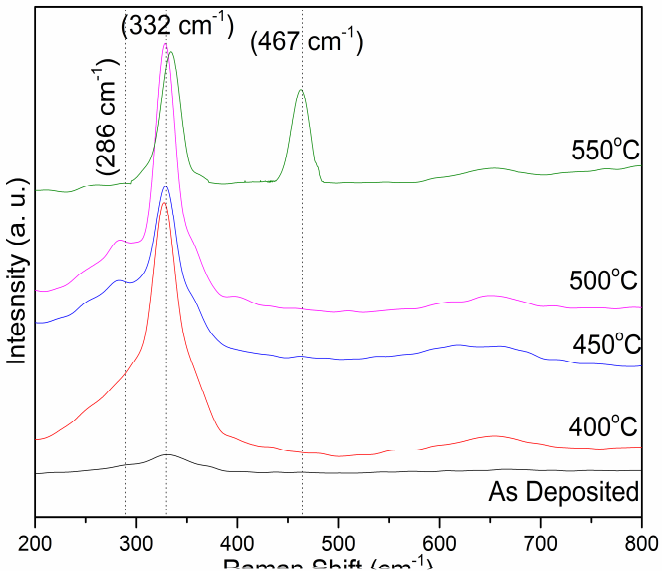

Fig. 5.15 Raman spectra of films annealed at different temperatures

Raman spectra of the films annealed at different temperatures are shown in Fig. 5.15. The films annealed at 350°C and 400°C exhibited major peak of CZTS at 332cm^{-1}. The film annealed at 450°C and 500°C showed peaks at 332cm^{-1}and 286cm^{-1}, which arises from the vibration of A mode [49]. No other peaks from any binary or ternary secondary phases were observed. This indicates phase pure nature of the films annealed at 450°C and 500°C. One major peak at 465cm^{-1} was observed in the spectra of the film annealed at 550°C, which may be due to $Cu_{2-x}S$ [42], and a shoulder peak at 331cm^{-1} belongs to Cu_2ZnSnS_4, but with shift in the peak position. XRD and

Raman studies confirmed formation of single phase kesterite in the films annealed in inert atmosphere at 450°C and 500°C.

5.3.2. Elemental composition analysis

Elemental compositions of the films were analysed by EDXS equipped with SEM. The EDXS results of the CZTS films annealed at different temperatures are given in Table 5.10. As seen in the table, the sulphur content decreases with annealing temperature and this may be due to the evaporation of sulphur with increase in temperature. It is found that the Copper concentration increases with increase in annealing temperature. However, Sn and Zn concentrations do not show systematic variations in the temperature range studied. Lowest Cu/(Zn+Sn) and highest Zn/Sn ratios were observed for films annealed at 400°C. As described in the previous sections, Cu poor and Zn rich conditions are favourable for high efficient CZTS solar cell [36]. In the present route, the CZTS films sulphurized at 450°C and 500°C were phase pure. Cu poor and Zn rich condition were not observed in these films.

Table 5.10 EDXS results of CZTS films annealed at different temperatures

Annealing temperature	EDXS results					
	Cu (at. %)	Zn (at. %)	Sn (at. %)	S (at. %)	Cu/(Zn+Sn)	Zn/Sn
400 ºC	21.65(±2)	11.65(±2)	14.77(±3)	53.23(±4)	0.94	1.02
450 ºC	23.74(±4)	11.06(±3)	13.54(±2)	51.66(±3)	0.97	0.82
500 ºC	24.67(±3)	12.12(±2)	12.11(±3)	51.01(±4)	1.02	1.00
550 ºC	26.39(±4)	14.33(±4)	14.51(±2)	44.77(±4)	0.92	0.99

5.3.3. Surface morphology

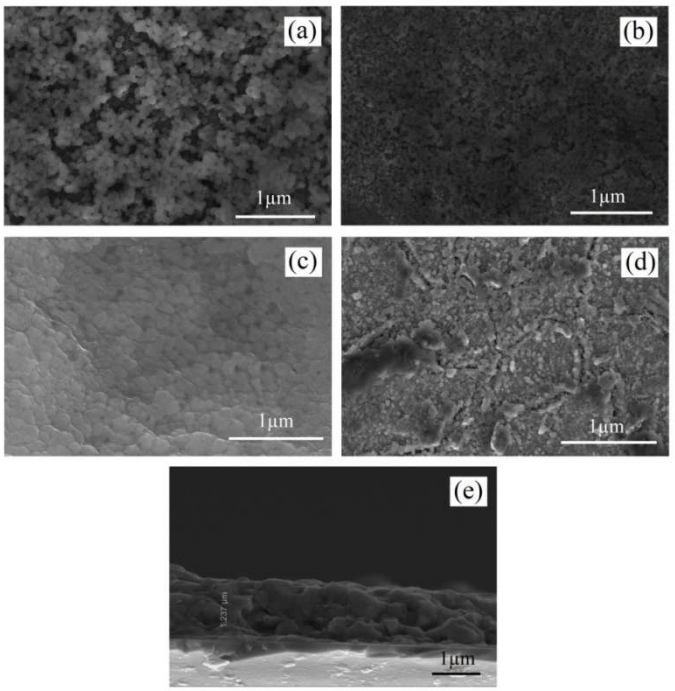

Fig. 5.16 FESEM images of the CZTS films annealed at (a) 400°C, (b) 450°C, (c) 500°C, (d) 550°C and (e) cross-sectional image of CZTS film annealed at 500°C

Fig. 5.16 (a-d) shows FESEM micrographs of CZTS films annealed at different temperatures from 400°C to 550°C in inert atmosphere. As seen in the images, surface morphology of the films is significantly affected by post-annealing treatment in inert atmosphere. Grain size is found to be very small when annealed at 450°C. However, the film annealed at 500°C showed densely packed grains with large grain size. Thus, a dense CZTS film with improved microstructure was formed at an annealing temperature of 500°C. Fig.

5.16 (e) shows the cross section of film annealed at 500°C and the thickness of the film measured from the cross section was ~1.2μm.

5.3.4. Optical properties

Optical absorption coefficient α, of the film was calculated from the transmittance spectra. Energy bandgap was estimated by extrapolating the linear portion of the $(\alpha h\nu)^2$ versus hν plot to the x intercepting point at y=0 (inset of Fig. 5.17). Band gaps of the films obtained were in the range 1.51-1.87eV at room temperature, depending on the annealing temperature. The band gap was found to decrease with increase in annealing temperature. The decrease in bandgap from 1.81eV to1.51eV may be due to the improved crystallinity of the film [50]. The bandgap is found to increase at higher temperatures, above 500°C, and this may be due to the formation of secondary phases in the films. Secondary phase was observed in the XRD and Raman studies carried out in the films annealed at this temperature. The band gap was found to be ~1.51 eV for the film annealed at 500°C in nitrogen atmosphere. This value is close to the optimum band gap energy needed for thin film photovoltaic cell. The absorption coefficient (α) was found to be ~10^5 cm^{-1} in the visible region; the higher value indicates that it can absorb most of the incident photons with minimum thickness. As discussed in the previous sections in this chapter, band gap energies of the spray coated thin films were 1.47eV and 1.49eV for CZT precursor film sulphurized at 550°C and CZTS precursor film sulphurized at 550°C, respectively. Thus, the spray coated films fabricated through the three

routes exhibited band gaps close to 1.5eV, which is considered as the ideal value for solar cells.

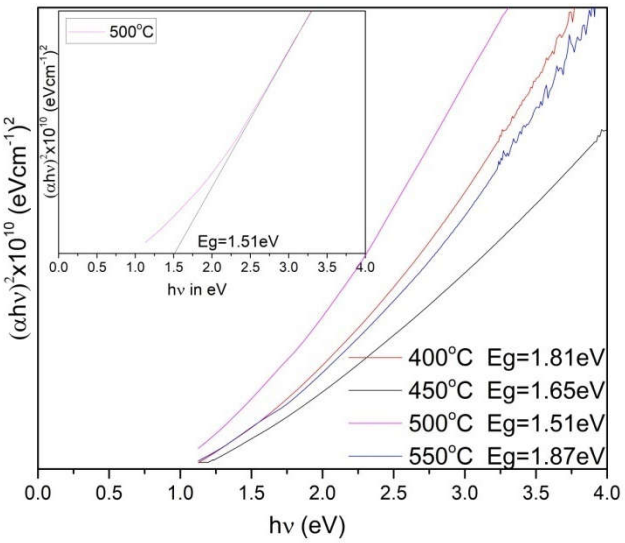

Fig. 5.17 $(\alpha h\nu)^2$ versus $h\nu$ plot for the CZTS films annealed at different temperatures in inert atmosphere

5.3.5. Electrical properties

Hall measurements were carried out in magnetic field intensity of 0.54T. The measurements in van der Pauw configuration revealed positive Hall coefficient, indicating *p* type nature of the films. Electrical properties of the films annealed at different temperature are summarized in Table 5.11. As seen, the carrier concentration is found to increase with annealing temperature, while the mobility and resistivity are found to decrease up to 500°C. This may be due to the improved crystallinity of the films at higher temperatures [34,42]. Carrier concentration, mobility and resistivity of the films annealed at

500°C were observed to be $2.37\times10^{18}cm^{-3}$, 12 $cm^2V^{-1}s^{-1}$ and 0.22Ωcm, respectively. Similar results have been reported by Swami et al and Rajeshmon et al. for spray pyrolysed film [18, 42] Zhang et al. and Tanaka et al. for sputtered and sulphurized film (in N_2/Ar+S atmosphere) and Zhou et al for screen printed and argon annealed film [51-53]. The study conducted reveals that the non-vacuum and non-toxic process described in this section is suitable for deposition of phase pure CZTS thin films for photovoltaic applications.

Table 5.11 Summary of the Hall Measurement studies of CZTS thin films annealed at different temperatures

Annealing temperature (°C)	Carrier concentration (cm^{-3})	Mobility cm^2/Vs	Resistivity Ωcm
350	4.299×10^{15}	47.04	30.86
400	2.128×10^{16}	40.24	18.07
450	5.147×10^{17}	33.94	0.36
500	2.368×10^{18}	12.03	0.22
550	8.448×10^{15}	100.4	73.62

5.4. Comparison of properties of spray coated CZTS thin films prepared by three different routes

Two different solutions, with and without sulphur source, were used to prepare precursor films by spray coating. Three different temperature treatments have been adopted to prepare phase pure CZTS films. In the first and second routes, that is, CZTS films from solutions without and with sulphur respectively, the optimized phase formation temperature was 550°C. However, the processing temperature could be brought down in the third route, where the sulphur incorporated

precursor films were annealed in inert (nitrogen) atmosphere. The properties of the spray coated CZTS films were entirely different from those of the films processed through spin and dip coating techniques. Higher crystallite size was observed for the precursor film with sulphur further annealed in sulphur atmosphere. Cu poor condition was observed in the films prepared by first and second routes, but obtained Cu rich condition for the films fabricated by third route. In all three routes, Zn rich condition was not observed. Hence the favorable Cu poor and Zn rich conditions were not observed in any of the three spray coating routes. The spray coated films exhibited optimum band gap; the highest value obtained was 1.51eV for the film prepared by the third route. Similar values were observed for the spin coated CZTS films (section 4.1.6 of this thesis). The CZTS precursor films annealed in sulphur (second route) and inert (third route) atmospheres exhibited higher optical absorption coefficients ($10^5 cm^{-1}$) in the visible region. Hall measurements indicated *p* type conductivity for all films. Carrier mobility was low in the CZTS films sulphurized from the precursors without and with sulphur (first and second routes); however, higher mobility was observed when the precursor film containing sulphur was annealed further in inert atmosphere (third route). The resistivities of films obtained were almost similar. With same parameters of spray coating, maximum film thickness was obtained when the precursor film with sulphur was annealed further in sulphur atmosphere (second route). This route appears favorable for large scale fabrication. Spin and dip coating routes, discussed in the previous chapters, also yielded films with higher thickness when the precursor films with sulphur were

further annealed in sulphur atmosphere. Though Cu poor and Zn rich condition was not obtained in the CZTS films prepared from the second route, these films exhibited better properties for band gap, absorption coefficient, carrier concentration and film thickness. The summary of the properties obtained for the films of the three spray coating routes are given in Table 5.12.

Table 5.12 Summary of the properties of the CZTS thin films fabricated by three different spray coating routes.

Properties	***CZT* precursor films annealed in reactive (sulphur) atmosphere** *(First Route)*	***CZTS* precursor films annealed in reactive (sulphur) atmosphere** *(Second Route)*	***CZTS* precursor films annealed in inert atmosphere** *(Third Route)*
Optimized temperature	550°C	550°C	500°C
Film Area	1×1 inch	1×1 inch	1×1 inch
Crystallite size	52nm	59nm	44nm
Cu/(Zn+Sn) ratio	0.91	0.97	1.02
Zn/Sn ratio	0.92	0.99	1.00
Band Gap Energy	1.47eV	1.49eV	1.51eV
Absorption Coefficient	$>10^4 cm^{-1}$	$>10^5 cm^{-1}$	$\sim 10^5 cm^{-1}$
Carrier Type	p type	p type	p type
Carrier Concentration	$1.6\times10^{19} cm^{-3}$	3.67×10^{19} cm^{-3}	2.37×10^{18} cm^{-3}
Mobility	$0.87 cm^2V^{-1}s^{-1}$	0.33 $cm^2V^{-1}s^{-1}$	12.03 $cm^2V^{-1}s^{-1}$
Resistivity	0.46 Ωcm	0.52 Ωcm	0.22 Ωcm
Film Thickness	~1.9μm	~2.02 μm	~1.2μm

5.5. Summary

Two different precursor solutions, with and without sulphur, were prepared for coating precursor films by spray coating. These precursor films were converted to phase pure CZTS through three different temperature treatments. The precursor films were coated on pre-cleaned glass substrates using a custom made spray coater.

In the first approach, CZTS thin films were prepared by spray coating of precursor solution without sulpur (CZT precursor solution) followed by sulphurization in N_2+H_2S atmosphere. The films were sulphurized at 450°C, 500°C, 550°C and 600°C to study the effect of sulphurization temperature on their structural and various other optoelectronic properties. Structural properties and phase purity of the films were investigated by XRD and Raman spectroscopy. Raman and XRD studies indicated phase pure nature of the film sulphurized at 550°C. Sulphurizations at lower or higher temperature were resulted in the formation of secondary or ternary phases. Structural properties of the 550°C sulphurized films were further investigated by rietveld refinement technique. Refined lattice parameters are a=b=5.4309465Å, c=10.858355Å and c/2a=0.9993, which is close to the reported lattice parameter for kesterite mineral. The changes in the bond angle were also studied and the refined bond angles were found to match with the reported values. Elemental compositions of the films were studied by EDXS equipped with SEM. Cu/(Zn+Sn) and Zn/Sn ratios of the film sulphurized at 550°C were 0.91 and 0.92, respectively. SEM and FESEM studies show a thickness of ~1.9µm and good surface

morphology with large grains for films sulphurized at 550°C. Band gap and absorption coefficient of the 550°C sulphurized films were 1.47eV and $8\times10^4 cm^{-1}$ respectively. Carrier concentration, mobility and resistivity of the films sulphurized at 550°C were found to be $1.544\times10^{19} cm^{-3}$, $0.87 cm^2V^{-1}s^{-1}$ and 0.46Ωcm respectively.

In the second approach, CZTS precursor films were prepared by spray coating and sulphurization in 95% N_2+5% H_2S atmosphere at various temperatures ranging from 400°C to 600°C. Formation of Cu_2ZnSnS_4 phase was confirmed from XRD and Raman studies. XRD and Raman studies revealed phase pure kesterite phase at 500°C and 550°C. The lattice parameter calculated for the films sulphurized at 550°C were $a = b = 0.5431$nm, $c = 1.083$nm, and $c/2a = 0.9971$ and are closely matching with the ICDD data. The study indicated that the film sulphurized at 500°C and 550°C exhibited proper phase and crystallinity. However, better crystallinity was observed for the film sulphurized at 550°C. Further structural studies were carried out with rietveld refinement technique and cation-anion-cation bond angles obtained for the CZTS film sulphurized at 550°C were 108.528(14)° for Cu-S-Sn, 109.33(7)° for Zn-S-Sn, 112.257(7)° for Cu-S-Zn and 109.612(7)° for Cu-S-Cu. SEM image exhibited dense grain structure for the film sulphurized at 550°C. The thickness of the film was found to be ~2μm from the cross-sectional image. Elemental composition of the film studied by EDXS were found to be Cu/(Zn+Sn)=0.97 and Sn/Zn=0.99 for the film sulphurized at 550°C. The absorption coefficient estimated from UV-visible spectra was $\sim10^5 cm^{-1}$ in the

visible region and the optical band gap calculated was 1.49eV for the film sulphurized at 550°C. Carrier concentration, mobility and resistivity of the film sulphurized at 550°C were $3.67\times10^{19}cm^{-3}$, $0.33cm^2V^{-1}s^{-1}$ and 0.52Ωcm, respectively.

In the third approach, CZTS precursor films fabricated by spray coating were further annealed in inert (nitrogen) atmosphere. X-ray diffraction, Raman spectroscopy, FESEM, UV-visible spectroscopy and Hall Effect measurements were carried out to characterize the spray coated films. Formation of phase pure Cu_2ZnSnS_4 was confirmed from the XRD patterns and Raman spectra. XRD analysis indicated the formation of kesterite phase at an annealing temperature of 450°C. However, crystallinity was found to increase when the annealing temperature was increased to 500°C. Raman spectra of the films did not indicate any secondary phases in the films annealed at 450°C and 500°C. The study indicated that the film annealed at 500°C possesses proper phase and crystallinity. The absorption co-efficient calculated from the UV-visible spectra was found to be $\sim10^5cm^{-1}$ in the visible region and the optical band gap estimated was 1.51 eV for the films annealed at 500°C. Microstructure of the film annealed at 500°C exhibited dense and improved grain structure. Hall measurements indicated *p* type nature for all the films. Hole concentration and resistivity of the films were found to be $2.37\times10^{18}cm^{-3}$and 0.22Ωcm respectively. Thus, the Cu_2ZnSnS_4 absorber film fabricated through spray coating technique possesses required photovoltaic properties.

5.6 References

1) Patel M, Mukhopadhyay I, Ray A, Structural, optical and electrical properties of spray-deposited CZTS thin films under a non-equilibrium growth condition, J. Phys. D: Appl. Phys. 45 (2012) 445103.

2) Kumar Y B, Bhaskar P U, Babu G S, Raja V S, Effect of copper salt and thiourea concentrations on the formation of Cu_2ZnSnS_4, Thin films by spray pyrolysis, phys. status solidi (a), 207 (2010) 149.

3) Rajeshmon V G, Kartha C S, Vijayakumar K P, Sanjeeviraja C, Abe T, Kashiwaba Y, Role of precursor solution in controlling the opto-electronic properties of spray pyrolysed Cu_2ZnSnS_4 thin films, Sol. Energy, 85 (2011) 249.

4) Nakayama N, Ito K, Sprayed films of stannite Cu_2ZnSnS_4, Appl. Surf. Sci. 92 (1996) 171.

5) Schorr S, Hoebler H J, Tovar M, A neutron diffraction study of the stannite-kesterite solid solution series, Eur. J. Mineral. 19 (2007) 65.

6) Fernandes P A, Salomé P M, Da Cunha A F. Study of polycrystalline Cu_2ZnSnS_4 films by Raman scattering, J. Alloys Compd. 509 (2011) 7600.

7) Dumcenco D, Huang Y S, The vibrational properties study of kesterite Cu_2ZnSnS_4 single crystals by using polarization dependent Raman spectroscopy, Opt. Mater. 35 (2013) 419.

8) Fontané X, Calvo-Barrio L, Izquierdo-Roca V, Saucedo E, Pérez-Rodriguez A, Morante J R, Berg D M, Dale P J, Siebentritt S, In-depth resolved Raman scattering analysis for the identification of secondary phases: characterization of Cu_2ZnSnS_4 layers for solar cell applications, Appl. Phys. Lett. 98 (2011) 181905.

9) Fernandes P A, Salomé P M, Da Cunha A F, Growth and Raman scattering characterization of Cu_2ZnSnS_4 thin films, Thin solid films. 517 (2009) 2519.

10) Gurieva G, Guc M, Bruk L I, Izquierdo Roca V, Pérez Rodríguez A, Schorr S, Arushanov E, Cu_2ZnSnS_4 thin films grown by spray pyrolysis: characterization by Raman spectroscopy and Xray diffraction, Phys. Status Solidi C. 10 (2013) 1082.

11) Tanaka K, Moritake N, Oonuki M, Uchiki H, Pre-annealing of precursors of Cu_2ZnSnS_4 thin films prepared by sol–gel sulfurizing method, Jpn. J. Appl. Phys. 47 (2008) 598.

12) Nilsen W G, Raman spectrum of cubic ZnS, Phys. Rev. 182 (1969) 838.

13) Von Meerwall E, A least-squares spectral curve fitting routine for strongly overlapping Lorentzians or Gaussians, Comput. Phys. Commun. 9 (1975) 117.

14) Nozaki H, Fukano T, Ohta S, Seno Y, Katagiri H, Jimbo K, Crystal structure determination of solar cell materials: Cu_2ZnSnS_4 thin films using X-ray anomalous dispersion, J. Alloys Compd. 524 (2012) 22.

15) Schorr S, The crystal structure of kesterite type compounds: A neutron and X-ray diffraction study, Sol. Energy Mater. Sol. Cells. 95 (2011) 1482.

16) Patel K, Kheraj V, Shah D V, Panchal C J, Dhere N G, Cu_2ZnSnS_4 thin-films grown by dip-coating: Effects of annealing, J. Alloys. Compd. 663 (2016) 842.

17) Lloyd M A, Bishop D, Gunawan O, McCandless B, Fabrication and performance limitations in single crystal $Cu_2ZnSnSe_4$ solar cells, 44th IEEE Photovoltaic Specialist Conference (PVSC), 44 (2017) 1.

18) Kişnişci Z, Özel F, Yüksel ÖF, Tuğluoğlu N, Optical characterization of Cu_2ZnSnS_4 nanocrystals thin film, J. Mater. Sci.: Mater. Electron. 27 (2016) 10128.

19) Katagiri H, Jimbo K, Yamada S, Kamimura T, Maw W S, Fukano T, Ito T, Motohiro T, Enhanced conversion efficiencies of Cu_2ZnSnS_4-based thin film solar cells by using preferential etching technique, Appl. Phys. Express. 1 (2008) 041201.

20) Araki H, Kubo Y, Mikaduki A, Jimbo K, Maw W S, Katagiri H, Yamazaki M, Oishi K, Takeuchi A, Preparation of Cu_2ZnSnS_4 thin films by sulfurizing electroplated precursors, Sol. Energy Mater. Sol. Cells. 93 (2009) 996.

21) Lokhande A C, Chalapathy R B, He M, Jo E, Gang M, Pawar S A, Lokhande C D, Kim JH, Development of Cu_2SnS_3 (CTS) thin film solar cells by physical techniques: A status review, Sol. Energy Mater. Sol. Cells. 153 (2016) 84.

22) Siebentritt S, Why are kesterite solar cells not 20% efficient?, Thin Solid Films. 535 (2013) 1.

23) Guan H, Shen H, Gao C, He X, Sulfurization time effects on the growth of Cu_2ZnSnS_4 thin films by solution method, J. Mater. Sci.: Mater. Electron. 24 (2013) 2667.

24) Long B, Cheng S, Lai Y, Zhou H, Yu J, Zheng Q, Effects of sulfurization temperature on phases and opto-electrical properties of Cu_2ZnSnS_4 films prepared by sol–gel deposition, Thin Solid Films. 573 (2014) 117.

25) Scragg J J, Dale P J, Peter L M, Zoppi G, Forbes I, New routes to sustainable photovoltaics: evaluation of Cu_2ZnSnS_4 as an alternative absorber material, Phys. Status Solidi B. 245 (2008) 1772.

26) Fernandes P A, Salomé P M, Da Cunha A F, Schubert B A. Cu_2ZnSnS_4 solar cells prepared with sulphurized dc-sputtered stacked metallic precursors. Thin Solid Films. 519 (2011) 7382.

27) Liu F, Zhang K, Lai Y, Li J, Zhang Z, Liu Y, Growth and characterization of Cu_2ZnSnS_4 thin films by dc reactive magnetron sputtering for photovoltaic applications, Electrochem. Solid-State Lett. 13 (2010) H379.

28) Ito K, Nakazawa T, Electrical and optical properties of stannite-type quaternary semiconductor thin films, Japanese J. Appl. Phys. 27 (1988) 2094.

29) Tanaka T, Nagatomo T, Kawasaki D, Nishio M, Guo Q, Wakahara A, Yoshida A, Ogawa H, Preparation of Cu_2ZnSnS_4 thin films by hybrid sputtering, J. Phys. Chem. Solids. 66 (2005) 1978.

30) Liu F, Li Y, Zhang K, Wang B, Yan C, Lai Y, Zhang Z, Li J, Liu Y, In situ growth of Cu_2ZnSnS_4 thin films by reactive magnetron co-sputtering, Sol. Energy Mater. Sol. Cells. 94 (2010) 2431.

31) Chan C P, Lam H, Surya C, Preparation of Cu_2ZnSnS_4 films by electrodeposition using ionic liquids, Sol. Energy Mater. Sol. Cells. 94 (2010) 207.

32) Zhang H X, Hong R J, CIGS absorbing layers prepared by RF magnetron sputtering from a single quaternary target, Ceramics International. 42 (2016) 14543.

33) Ge J, Wu Y, Zhang C, Zuo S, Jiang J, Ma J, Yang P, Chu J, Comparative study of the influence of two distinct sulfurization

ramping rates on the properties of Cu_2ZnSnS_4 thin films, Appl. Surf. Sci. 258 (2012) 7250.

34) Ge J, Chu J, Jiang J, Yan Y, Yang P, Characteristics of In-Substituted CZTS Thin Film and Bifacial Solar Cell, ACS Appl. Mater. Interfaces. 6 (2014) 21118.

35) Toby B H, EXPGUI, a graphical user interface for GSAS, J. Appl. Cryst. 34 (2001) 210-213.

36) Todorov T K, Reuter K B, Mitzi D B, High efficiency solar cell with earth abundant liquid processed absorber, Adv. Mater. 22 (2010) E156

37) Huang S, Luo W, Zou Z, Band positions and photoelectrochemical properties of Cu_2ZnSnS_4 thin films by the ultrasonic spray pyrolysis method, J. Phys. D: Appl. Phys., 46 (2013) 235108

38) Redinger A, Berg D M, Dale P J, Siebentritt S, The consequences of kesterite equilibria for efficient solar cells, J. Am. Chem. Soc. 133 (2011) 3320.

39) Tiong V T, Bell J, Wang H, One-step synthesis of high quality kesterite Cu_2ZnSnS_4 nanocrystals–a hydrothermal approach, Beilstein J. Nanotechnol. 5 (2014) 438.

40) Schneider C A, Rasband W S, Eliceiri K W, NIH Image to ImageJ: 25 years of image analysis, Nat. Methods. 9 (2012) 671.

41) Liu X, Cui H, Li W, Song N, Liu F, Conibeer G, Hao X, Improving Cu_2ZnSnS_4 (CZTS) solar cell performance by an ultrathin ZnO intermediate layer between CZTS absorber and Mo back contact, Phys. Status Solidi RRL. 8 (2014) 966.

42) Swami S K, Chaturvedi N, Kumar A, Dutta V, Effect of deposition temperature on the structural and electrical properties of spray deposited kesterite (Cu_2ZnSnS_4) films, Sol. Energy. 122 (2015) 508.

43) Redinger A, Berg D M, Dale P J, Siebentritt S, The consequences of kesterite equilibria for efficient solar cells, J. Am. Chem. Soc. 133 (2011) 3320.

44) Cullity B D, Stock S R, Elements of X-Ray Diffraction, 3rd Ed., Prentice-Hall ,2001.

45) Tanaka K, Kato M, Goto K, Nakano Y, Uchiki H, Face-to-face annealing process of Cu_2ZnSnS_4 thin films deposited by spray pyrolysis method, Jpn. J. Appl. Phys. 51 (2012) 10NC26.

46) Dimitrievska M, Fairbrother A, Fontané X, Jawhari T, Izquierdo-Roca V, Saucedo E, Pérez-Rodríguez A, Multiwavelength excitation Raman scattering study of polycrystalline kesterite Cu_2ZnSnS_4 thin films, Appl. Phys. Lett. 104 (2014) 021901.

47) Gürel T, Sevik C, Çağın T, Characterization of vibrational and mechanical properties of quaternary compounds Cu_2ZnSnS_4 and $Cu_2ZnSnSe_4$ in kesterite and stannite structures, Phys. Rev. B. 84 (2011) 205201.

48) Khare A, Himmetoglu B, Johnson M, Norris D J, Cococcioni M, Aydil E S, Calculation of the lattice dynamics and Raman spectra of copper zinc tin chalcogenides and comparison to experiments, J. Appl. Phys. 111 (2012) 083707.

49) Kahraman S, Çetinkaya S, Podlogar M, Bernik S, Çetinkara H A, Güder H S, Effects of the sulfurization temperature on sol gel-processed Cu_2ZnSnS_4 thin films, Ceram. Int. 39 (2013) 9285.

50) Bodnar I V, Telesh E V, Gurieva G, Schorr S, Transmittance spectra of Cu_2ZnSnS_4 thin films, J. Electron. Mater. 44 (2015) 3283.

51) Zhang J, Lexi S H, Yujun F U, Erqing X I, Cu_2ZnSnS_4 thin films prepared by sulphurization of ion beam sputtered precursor and their electrical and optical properties, Rare met. 25 (2006) 315.

52) Tanaka T, Nagatomo T, Kawasaki D, Nishio M, Guo Q, Wakahara A, Yoshida A, Ogawa H. Preparation of Cu_2ZnSnS_4 thin films by hybrid sputtering, J. Phys. Chem. Solids. 66 (2005) 1978.

53) Zhou Z, Wang Y, Xu D, Zhang Y, Fabrication of Cu_2ZnSnS_4 screen printed layers for solar cells, Sol. Energy Mater. Sol. Cells. 94 (2010) 2042.

Chapter 6

Prototype CZTS Solar cell fabrication and further study for conversion efficiency improvement

Coating of phase pure CZTS thin films on glass substrates by spin, dip and spray coating routes has been discussed in the previous chapters. In this chapter, a method to fabricate a prototype CZTS solar cell is demonstrated. For efficiency measurement studies, absorber films have been prepared with various thicknesses. After this study, analysis of the interface of various layers has been done to throw new light on improving the conversion efficiency. The chapter is divided in to two subsections. The first section described efficiency measurements carried out using absorber layers with different thickness and the second section discusses the difference in the structural properties of CZTS film on glass substrates and device quality CZTS film on molybdenum coated soda lime glass substrates. The study reveals important features on the structure of CZTS, when deposited on Mo coated glass using the same process methodology optimized for coating CZTS on glass substrates.

6.1 Fabrication of Cu_2ZnSnS_4 solar cell using ZnS as buffer layer

The highest efficiency CZTSSe thin film solar cells reported was fabricated by hydrazine based solution technique and using cadmium sulphide as buffer layer. Hence, preparation of CZTS films using non-toxic solvent is important. For CZTS/CdS junction devices, solar cell efficiency drop at shorter wavelength due to optical

absorption losses from the cadmium sulphide buffer layer [1-3]. Replacing CdS buffer layer also helps to avoid toxic Cd from the solar cells; this will lead to the fabrication of eco-friendly thin film solar cells [4]. Selection of wide band gap material as buffer layer is important; the selected material should be able to form good *p-n* junction with absorber layer and also should be a good hetero junction partner in terms of band alignment and lattice matching [4-6]. An *n* type semiconductor with wide bandgap ensures maximum transmission of photons to the absorber layer [6].

Many alternatives to cadmium sulphide buffer layer is currently available. Commonly used buffer layer materials are ZnS, ZnO, In_2S_3 and zinc tin oxide [6]. Only a few reports have investigated the effect of alternate buffer layers in CZTS solar cells [4,5]. Among the available buffer layer materials, ZnS is a promising earth abundant eco-friendly wide band gap (3.6eV) material. This is widely used for as an alternative to CdS in CIGS solar cells [7,8]. For CZTS solar cell, the highest efficiency of 5.83% with an active area of 0.54cm^2 was reported by Sakai et al. [9] with ZnS buffer layer. They have prepared CZTS thin films by evaporation technique and ZnS buffer layer by chemical vapour deposition. In the Zn based buffer cell, they also observed different behaviour with respect to the Zn/Sn ratio of absorber, compared to Cd based buffer layer cells [9]. In 2014, Kim et al [10] prepared CZTS thin film by sequential sputtering and ZnS by RF sputtering. The group reported a conversion efficiency of 2.11% with an active area of 0.44 cm^2.

Chemical bath deposition is the widely accepted method for buffer layer coating. CdS thin film with good surface coverage can be

obtained by chemical bath deposition technique. However, coating of ZnS thin film by chemical bath deposition is a difficult task due to complex reaction mechanism and the formation of secondary phases [5]. Hence it is challenging to coat ZnS thin film by chemical bath deposition onto CZTS absorber layer. Park et al. [5] and Nguyen et al. [11] deposited ZnS thin film by chemical bath deposition on to CZTSSe absorber layer and the cell exhibited an efficiency of 3.8% and 4.5% respectively. As far as the author knows, no reports are available for cells with solution processed CZTS absorber and chemical bath deposited ZnS buffer layer. In the present work, the effect of absorber layer thickness on the photovoltaic properties of solar cell with solution processed CZTS and chemical bath deposited ZnS buffer layer is studied. Fig. 6.1 shows the schematic diagram of the CZTS solar cell fabricated in the study.

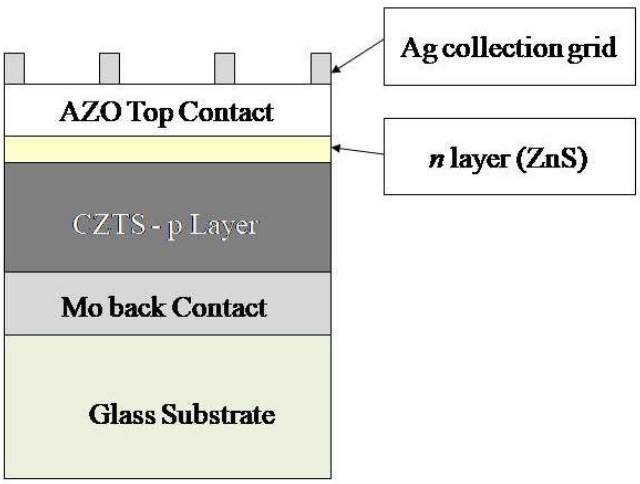

Fig. 6.1 Schematic diagram of CZTS solar cell

6.1.1 Fabrication of Cu_2ZnSnS_4 absorber layer by spin coating

For fabricating prototype CZTS solar cell, CZTS thin films were prepared by spin coating and post-sulphurization in sulphur (N_2+H_2S) atmosphere at 500°C, as described in the section 4.2.2 of this thesis. The optimised technology was used for fabricating CZTS films on Mo coated soda lime glass (SLG) substrate, for device fabrication. Films with different thicknesses were prepared by controlling the number of coating cycles to 8, 10 and12 times, and studied the effect of film thickness on the photovoltaic properties of the cell. The thicknesses of the films were estimated from the SEM cross-sections.

Fig. 6.2 shows the cross-sectional SEM images of the CZTS films coated with different numbers of spin coating cycles (8,10 and 12 times). Thicknesses for the films were found to be 1.8µm, 2.2µm and 2.7µm, respectively. The boundaries between glass (SLG), Mo and CZTS films are clearly visible in the SEM images.

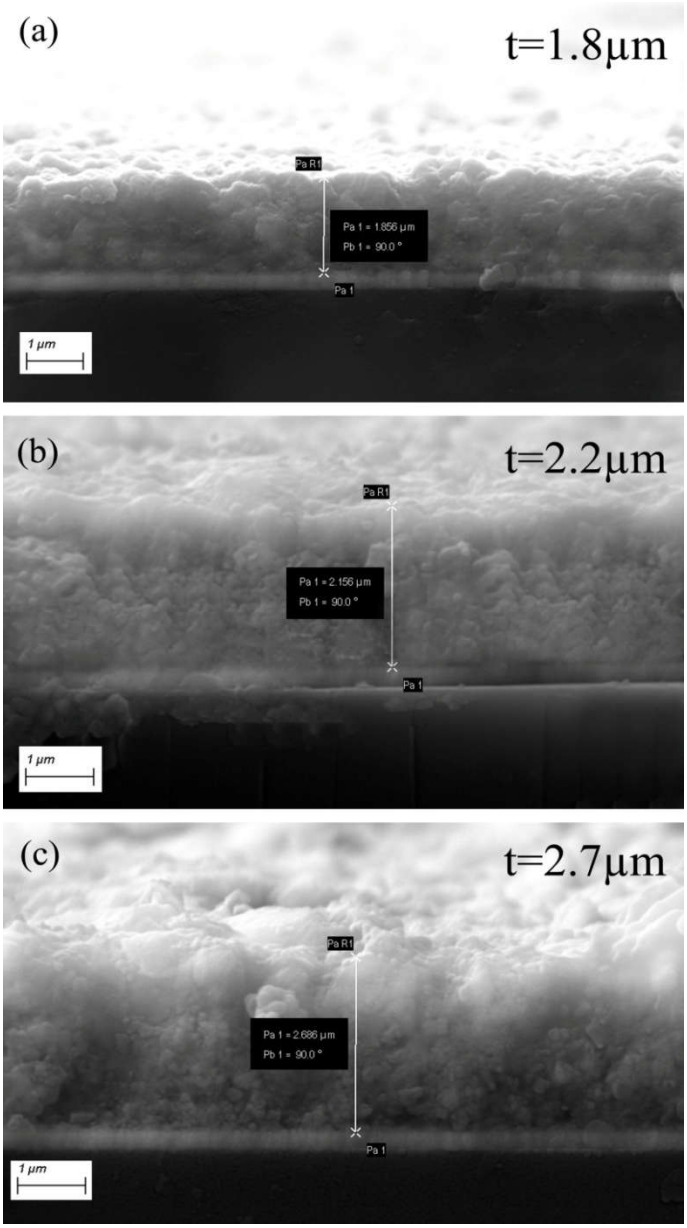

Fig. 6.2 SEM images of CZTS films with different thicknesses indicating various cross-sections

6.1.2 Fabrication of ZnS buffer layer

ZnS buffer layer was coated on to the already prepared CZTS film by chemical bath deposition (CBD). For this, 0.5M NH_4OH (complexing agent) solution was stirred with 50ml of distilled water and 0.44M tri-sodium citrate (complementary complexing agent) was added to this, followed by 0.03M $ZnSO_4$ (zinc source). 0.05M thiourea (sulphur source) was added to the resulting solution, as sulphur source. The substrates were mounted near vertically in this solution and heated for two hours at 80°C. Details of chemical bath deposition carried out were described in section 2.1.2.4 of this thesis. After deposition, the films were washed with distilled water and finally dried at 100°C for 10 minutes. Thickness of the ZnS film was found to be 60nm by ellipsometric technique. Before coating ZnS buffer layer on to the SLG/Mo/CZTS device structure, its structural, surface morphological and optical properties were studied by coating on glass substrates.

6.1.2.1 Structural characterization

Fig. 6.3 shows the X-ray diffraction pattern of ZnS thin film coated by CBD. The pattern shows low intense peaks at 28.5°, 33.1°, 47.6° and 56.3° corresponding to the (111), (200), (220) and (311) peaks of cubic ZnS, respectively. The observed peaks were identified with the help of ICDD powder diffraction file 05-0566. The XRD pattern observed in this study is in good agreement with those in the previous reports [4,5]. The low intense of XRD peak observed may be due to the small thickness of the thin film.

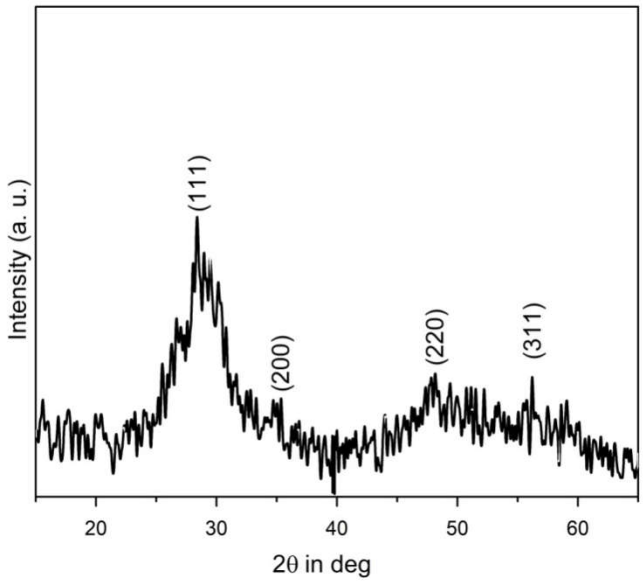

Fig. 6.3 XRD pattern of ZnS film coated by CBD

6.1.2.2 Surface morphological studies

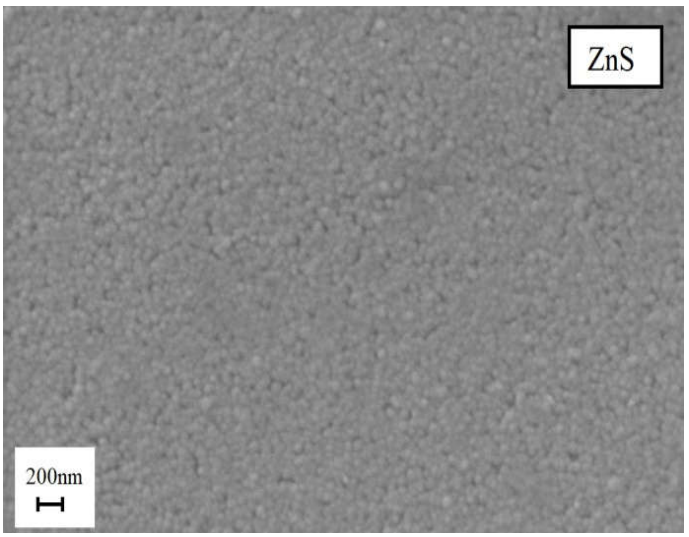

Fig. 6.4 SEM image of ZnS film coated by CBD

Surface morphology of the films was studied by scanning electron microscopy. Fig. 6.4 shows the SEM image of ZnS film coated by chemical bath deposition. Film possesses uniform distribution with comparatively good grain structure. No voids or cracks were observed in the ZnS film.

6.1.2.3 Optical properties

The optical absorption coefficient α, of the film was calculated from the UV-visible transmittance data. The band gap energy for the direct band gap materials was calculated using the well known Tauc's relation as described in chapter 2 section 2.2.7.

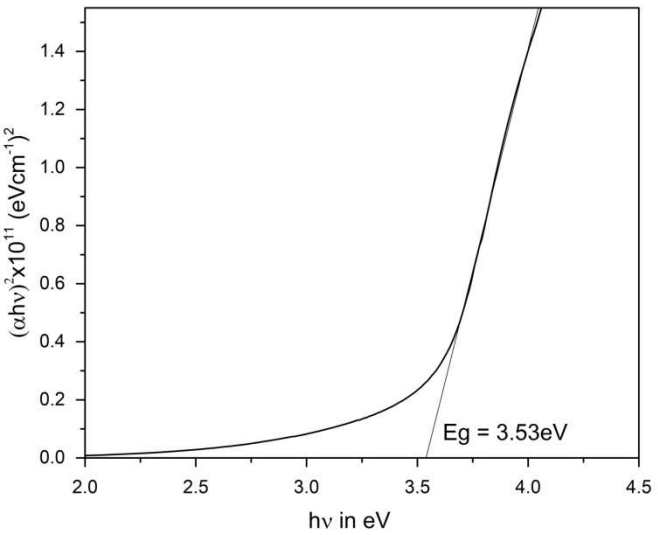

Fig. 6.5 Tauc plot of ZnS film coated by CBD to determine band gap

Fig. 6.5 shows the Tauc plots of ZnS films prepared by chemical bath deposition. Band gap of the ZnS films were calculated was found to be 3.53eV. The wider band gap of ZnS film ensures the

maximum transmittance of light in to the pn junction. Park et al [5] fabricated CZTSSe solar cell with ZnS as buffer layer; the ZnS film had a thickness of 53nm with band gap 3.53eV.

6.1.3 Fabrication of Al doped ZnO top electrode by RF sputtering

The top electrode, aluminium doped zinc oxde (AZO) was deposited over the SLG/Mo/CZTS/ZnS device structure by RF sputtering. ZnO sputter target doped with 2wt% Al was used for the sputtering. Sputtering conditions were optimized initially on SLG substrate. Prior to sputter deposition, a base pressure of ~1.9×10^{-6}mbar was achieved using a diffusion pump. Sputter depositions were carried out at a working pressure of 3.8×10^{-3} mbar with argon and a flow rate of 80sccm was maintained. Substrate to target distance was set to 7cm and RF power used was 100W throughout the deposition. Before coating AZO onto the device structure to fabricate CZTS solar cell, its structural, surface morphological, optical and electrical properties were studied by coating on glass substrate.

6.1.3.1 Structural characterization

Fig. 6.6 shows the XRD patterns of AZO film coated on glass substrates. The XRD patterns were compared with the standard ICDD pattern (ICDD PDF 36-1451). The patterns exhibited 2θ peaks at 31.7° and 34.4° corresponding to the (100) and (002) crystal planes of hexagonal wurtzite type ZnO, respectively. The XRD pattern indicated the polycrystalline nature of the films. The high intense (002) peak

observed indicates the orientation of the film along the c-axis. No other secondary phases were observed in the XRD analysis.

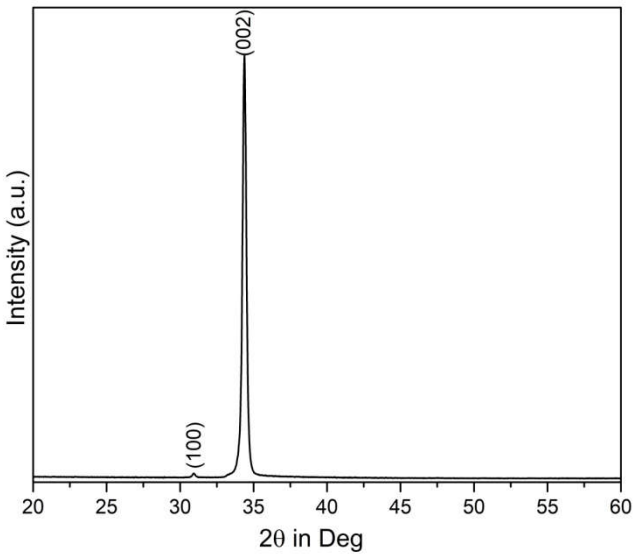

Fig. 6.6 XRD pattern of AZO thin film coated by RF sputtering

6.1.3.2 Surface morphology and film thickness

Surface morphology of the films was studied by SEM. Fig. 6.7 shows the SEM image of Al doped ZnO thin films coated by RF sputtering. Grains and grain boundaries were not observed in the SEM image. Inset of Fig. 6.7 shows the cross-sectional SEM image and the thickness of the films estimated from this was found to be ~700nm. Densely packed nature of the films can be observed in the cross sectional SEM image.

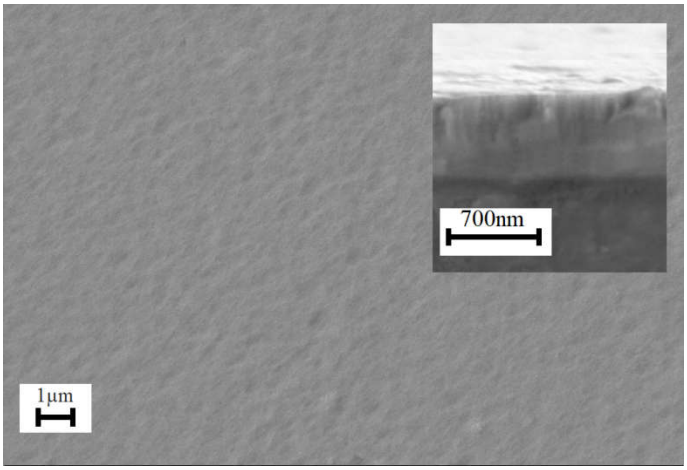

Fig. 6.7 Surface and cross-sectional (inset) SEM images of AZO films

6.1.3.3 Optical properties of AZO film

Optical properties of the AZO films were studied by UV-Vis spectroscopy. Fig. 6.8 shows the transmittance and Tauc plots of AZO film coated on glass substrate. Film shows an average transmittance (~70%) in the visible wavelength region. Optical band gap of the films were estimated to be 3.59eV. The wider band of AZO films ensures the maximum transmittance of light in to the pn junction through AZO coating.

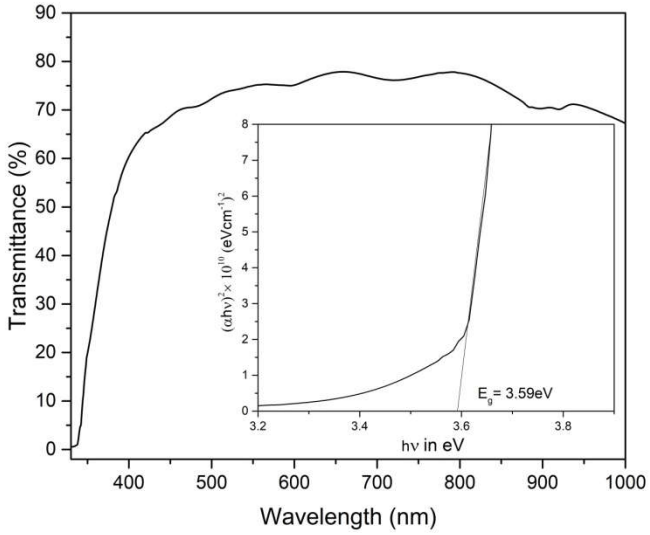

Fig. 6.8 Transmittance curve and Tauc plot of AZO film deposited by RF sputtering

6.1.3.4 Electrical properties of AZO film

Electrical properties of Al doped ZnO thin films were studied by Hall Effect measurement system. *n* type conductivity of the films were confirmed from the negative signs of the Hall coefficient and the carrier concentration. Carrier concentration, mobility and resistivity of the films were $3.69\times10^{20}cm^{-3}$, $20.9cm^2/Vs$ and $6.31\times10^{-4}\Omega cm$ respectively. Electrical studies revealed the excellent electrical conductivity of the AZO film deposited by RF sputtering.

6.1.4 Development of prototype non-toxic solar cell

In order to complete the cell fabrication, collection grid was coated manually using room temperature curable silver paste (Alfa Aesar, sheet resistance: <0.025ohm/square at 0.001inch thick).

Prototype cell with structure SLG/Mo/CZTS/ZnS/AZO/Ag has been fabricated for photovoltaic efficiency measurement. Efficiency measurements were carried out in a standard test condition, as described in section 2.2.9 of this thesis, with an active area of 0.21cm^2. Fig. 6.9 shows the illuminated J-V characteristics of the prototype CZTS solar cell fabricated with non-toxic ZnS buffer layer and manually coated collection grid. The summary of the studies are given in Table 6.1. The values V_{oc}, J_{sc}, I_{max}, V_{max}, FF, □, R_s R_{sh} are open circuit voltage, short circuit current density, maximum current, maximum voltage, fill factor, efficiency, series resistance and shunt resistance, respectively. The parameters were directly obtained from the J-V measurement setup used for the experiment.

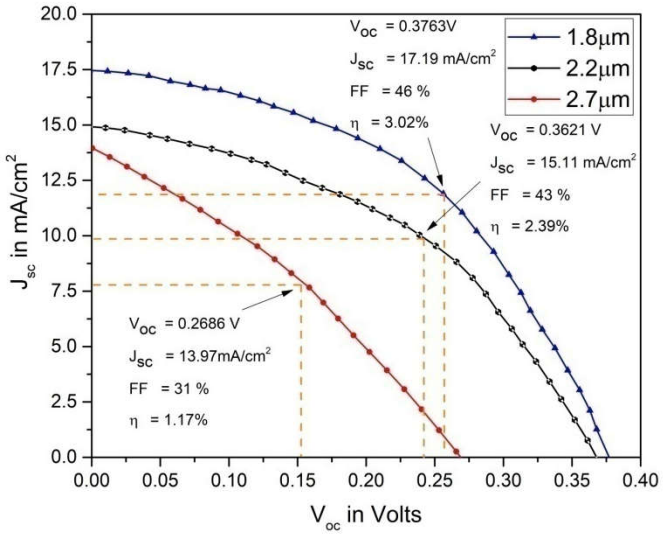

Fig. 6.9 J-V characteristics of CZTS solar cell with different absorber layer thickness

Table 6.1 J-V characteristics of CZTS solar cells with different absorber layer thickness

CZTS layer thickness	V_{oc} (V)	J_{sc} (mA/cm^2)	I_{max} (mA)	V_{max} (V)	FF (%)	Efficiency %	Rs Ωcm^2	Rsh Ωcm^2
1.8μm	0.3763	17.19	2.50	0.2538	46	3.02	24	224
2.2μm	0.3621	15.11	2.05	0.2452	43	2.39	35	81
2.7μm	0.2686	13.97	1.64	0.1494	31	1.17	59	154

As seen in Table 6.1, J_{sc} and Voc of the CZTS cells fabricated decrease with increase in absorber layer thickness. The cell with absorber layer thickness 1.8μm exhibited open-circuit voltage (Voc) of 0.38V and short circuit current density (J_{sc}) of 17mA/cm^2. When thickness of the absorber layer is increased from 2.2μm to 2.7μm, Voc is found to drop by 100mV; this may due to the increase in absorber film thickness as observed from cross-sectional SEM analysis.

Nguyen et al. [11] reported Voc of 0.596V, Jsc of 15.4 and power conversion efficiency of 4.5% for CZTSSe solar cell with ZnS absorber layer. Park et al. [5] reported a conversion efficiency of 3.84% with V_{oc}= 0.309V and J_{sc}=23.5mA/cm^2 for sputter deposited CZTS absorber with ZnS buffer layer. The short circuit current density obtained in this work is low compared to that of other reported cells [5, 12,13]; this may be explained on the basis of low mobility (0.2295cm^2/Vs) of the CZTS absorber film, though possessed commendable carrier concentration (1.02×10^{19}cm^{-3}) [13-15]

For an ideal PV device, shunt resistance should be very high (>500Ωcm^2) and series resistance should be very low (<90Ωcm^2)

[16,17]. For the best cell in this work, shunt resistance and series resistance were 224Ωcm^2 and 24Ωcm^2, respectively. Fill factor of the device was found to decrease with increase in absorber layer thickness. The high efficiency sputter deposited CZTS cell reported so far has values for R_s = 4.25Ωcm^2 and R_{sh}=370Ωcm^2 [18,19]. National Renewable Energy Laboratory (NREL) reported typical values of R_s and R_{sh} for CIGS devices; these values are R_s=0.22Ωcm^2 and R_{sh}=5.9kΩcm^2 with fill factor >78% [19,20]. High series resistance and low shunt resistance arise mainly from the poor transport in absorber layer and buffer layer, from interfaces, and also due to bad contact of electrode to the cell [21,22].

In the present study, the highest efficiency, 3.02%, was observed for the CZTS film with lower thickness (1.8μm). As far the author knows, the efficiency obtained in this work is the highest value reported so far for cadmium free cell with solution processed CZTS absorber. The efficiency may be improved by reducing the absorber thickness further [23-26]. It has been reported that recombination rate increases with higher thickness, which can reduce the performance of the device [5,27]. According to Lee et al. [25], the thickness of the solar cell has to be less than the diffusion length of the induced carriers. Hence, further study is required to fix optimum thickness for CZTS absorber layer. In the present case, the cell was fabricated without intrinsic ZnO (i-ZnO) layer and anti-reflection coating. The main use of i-ZnO layer in solar cell is to provide a barrier for shunting path between ZnS and AZO layer and this layer also make a protection for CBD deposited ZnS layer. Chemically deposited ZnS layer can be very easily damaged during AZO sputtering deposition [28,29]. Most

of the incident photos are reflected back at the surface of solar cell and this can be reduced by providing antireflection coating on the top of solar cell. MgF_2 film is generally coated as antireflection layer [30,31]. Hence, efficiency of the cell can be improved by incorporating these layers. Theoretical studies predict that ZnS is not a suitable buffer layer for CZTS system due to a high spike in the band alignment and this will act as a barrier for electron transport across the interface [5,11]. However, ZnS absorber layer is a suitable candidate for the CZTSSe system [5, 32]. ZnS is considered to be the suitable choice due to the lattice match, strain and inter-diffusion of particles between ZnS and CZTSSe absorber layer [32]. However, ZnS deposited by chemical bath deposition in this system contains defects, which are liable to diffuse into the absorber layer. This can be avoided by using different methods for fabrication of ZnS buffer layer [32].

6.2. Further structural study by Rietveld refinement on device point of view

In most cases, processing conditions of CZTS films are optimized on normal soda lime glass substrates and then transfer the process to Mo coated SLG substrates for device fabrication. This is due to the difficulty in analyzing some of the properties of CZTS films coated on opaque metallic film substrate. As far as the authors know, there are no reports on the effect of substrate type on the properties of solution processed CZTS film. Structural parameters of thin films were found to vary with the type of substrates in many cases [33]. In the present study, CZTS films were fabricated on glass substrate and Mo coated SLG substrates using similar spin coating and sulphurization conditions. Rietveld refinement technique has been used in this study

for detailed structural analysis. Kesterite structure was used as the starting model for the refinement, in which Cu occupies on 2a as well as 2c positions and Zn, Sn and S are in the 2d, 2b, 8g positions, respectively [34].

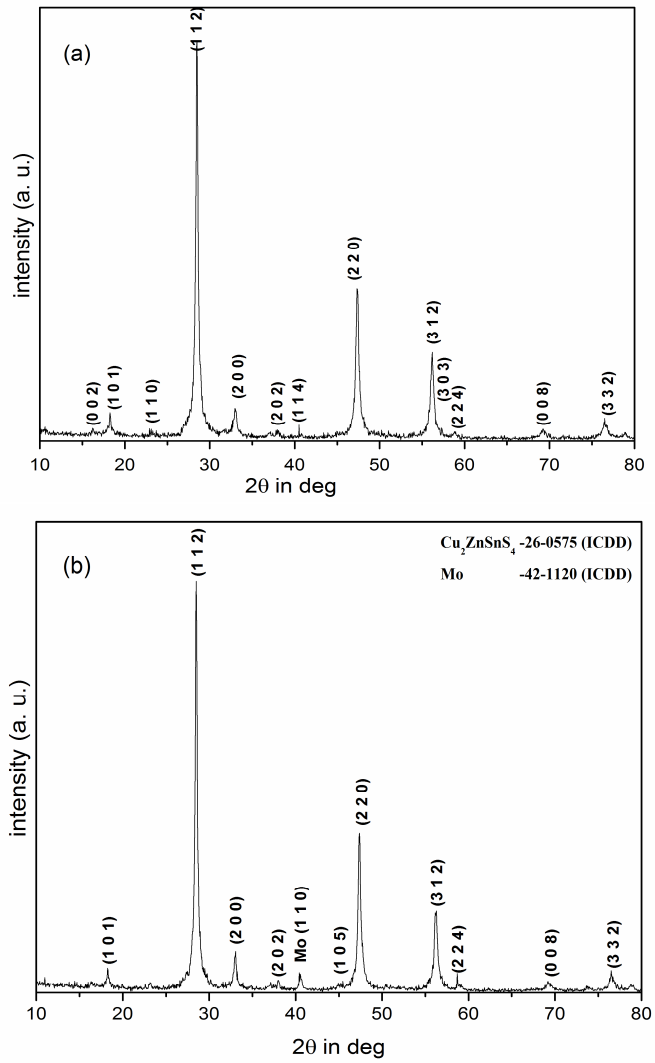

Fig. 6.10 High resolution grazing incidence x-ray diffraction (GIXRD) patterns of CZTS films on (a) glass and (b) Mo coated SLG substrates.

Fig. 6.10 shows the GIXRD patterns of the CZTS thin films coated on glass and Mo coated substrates. As seen, the X-ray diffraction peaks are closely match with that of the ICDD data of CZTS (PDF No: 00-26-0575, tetragonal, a=b=5.427nm, c=10848nm). Both patterns exhibited almost all the characteristic peaks of CZTS. A low intense peak of Mo was observed in the GIXRD pattern of the film on Mo coated substrate. Average crystallite sizes of the films were calculated from Scherrer's formula and Williamson Hall method. Williamson-Hall method is more effective method to calculate crystallite size by considering the effect of strain broadening [35].

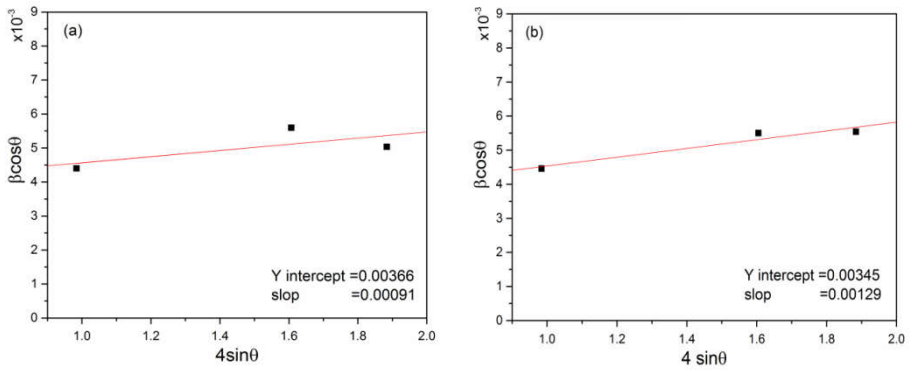

Fig. 6.11 W-H plots (4sinθ versus βcosθ) for the CZTS films deposited on (a) SLG and (b) Mo coated SLG substrates; strain is extracted from the slope, and the crystallite size is extracted from the y-intercept of the fit.

Fig. 6.11 shows the W-H plot, i.e., 4sinθ versus βcosθ for the films deposited on glass and Mo coated SLG substrates. Strain can be extracted from the slope and the crystallite size from the y-intercept of the fit. The average crystallite sizes estimated using these methods are given in Table 6.2. The strain is found to be 0.91×10^{-3} for films on

glass substrate and 1.29×10^{-3} for films on Mo coated substrate. Average crystallite size estimated from Scherrer equation is ~31nm for both films; while with W-H relation, it is ~38nm for the film on glass substrate and ~40nm for the film on Mo coated SLG substrate. As seen in the table 6.2, there is difference in the strain on CZTS films coated on glass and Mo coated substrates, which may due to the difference in the expansion coefficient of the substrates [33].

Table 6.2 Average crystallite size and strain of the films on glass substrate and Mo coated SLG substrates

Substrate	Average crystallite size (nm)		Strain calculated from W-H plot
	Scherrer's	W-H	
Glass	31	38	0.00091
Mo coated SLG	31	40	0.00129

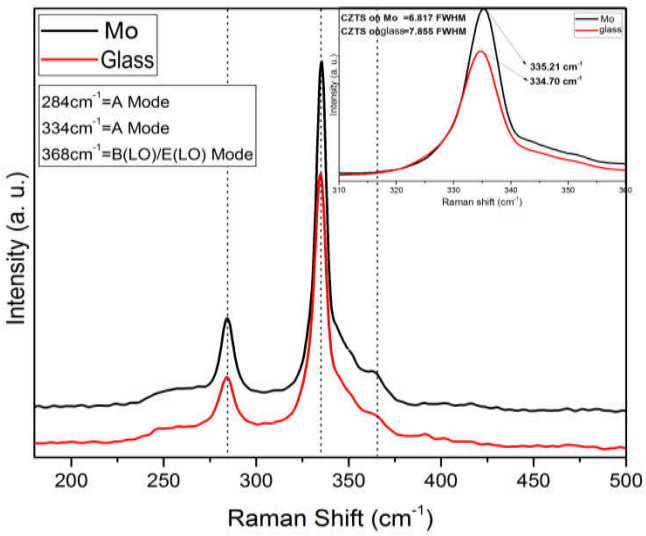

Fig. 6.12 Raman spectra of the CZTS films coated on glass and Mo coated SLG substrates

Fig. 6.12 shows the Raman spectra of films deposited on glass and Mo coated SLG substrates. Both films show Raman peaks at 284cm^{-1}, 334cm^{-1} and 368cm^{-1}, which corresponds to the A and B vibrational modes of CZTS. The peaks at 284cm^{-1} and 334cm^{-1} belongs to the A vibrational modes and 368cm^{-1} corresponds to the B (LO) vibrational modes of CZTS [36-38]. Dumitru et al [36] show that the peak corresponds to 284cm^{-1} is due to the vibration mode of kesterite structure. Inset of Fig. 6.12 shows the FWHM of the characteristic peak of CZTS at 334cm^{-1}. A small shift of ~1cm^{-1} in the major peak of CZTS can be seen for the film on Mo coated SLG substrate. In addition, the FWHM of the CZTS peak was found to decrease when substrate changes from glass to Mo coated SLG; the reduction in FWHM may be due to the increased crystallite size of the film [39-41]. The observed shift in Raman peaks of CZTS on Mo coated SLG may also be due to the increased crystallinity of the film [40,41]. As discussed in the chapter 3 section 3.1.5.2, we observed a shift in Raman peak to higher wave number, which was interpreted on the basis of improved crystallinity of the film. The improvement in the crystallinity of the absorber film improves the solar cell efficiency [35].

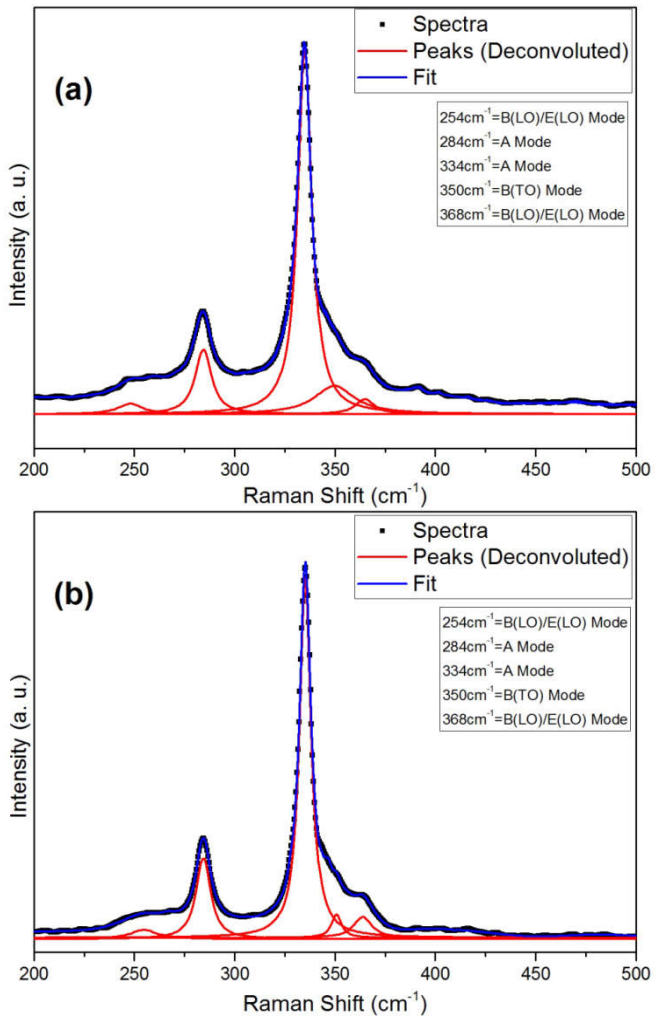

Fig. 6.13 Deconvoluted Raman spectra of the CZTS films coated on (a) glass and (b) Mo coated SLG substrates.

To further analyse the Raman spectra of the films, the peaks were deconvoluted with Lorentzian peak fitting function [40]. Fig. 6.13 shows the deconvoluted Raman spectra of CZTS thin film coated on the two substrates. Two more peaks of CZTS phases were resolved

in the Lorentzian peak fitting, at 254cm^{-1} and 368cm^{-1}. These peaks correspond to the B(LO)/E(LO) vibrational modes of CZTS [36,40]. No peaks corresponding to any other secondary phases were observed in the deconvoluted spectra.

Rietveld refinement of the GIXRD data was carried out with GSAS (General Structure Analysis System) package. Tetragonal kesterite type model (a=b=5.427Å, c=10.871Å, α=β=γ=90°) in the S.G I4□ (S.G No: 82) was used as the starting model. [3] The structural parameters used for refinement are listed in Table 6.3.

Table 6.3 Structural parameters used for refinement

Element	Z	W_{yck}	X	Y	Z	SOF
Cu	29	2a	0	0	0	1
Cu	29	2c	0	½	¼	0.5
Zn	30	2d	½	0	¼	0.5
Sn	50	2b	½	½	0	1
S	16	8g	0.7560	0.7566	0.8722	1

In the refinement procedure, all the structural parameters, such as, atomic positions, scale factor, lattice parameters, occupancy, preferred orientation correction, isotropic atomic displacement parameters, peak width and shape functions were refined until the goodness of fit (χ^2) becomes an acceptable value (ideally, 1) or a good fit between the observed and the calculated pattern is observed. In this refinement, pseudo-Voigt profile shape was assumed [42],

$$\chi^2 = \sum \frac{(\sigma_{ip}^2 - \sigma_{ib}^2)^{-1} \times (y_{io} - y_{ic})^2}{(N-P)} \qquad (6.1)$$

Where, χ^2 is the goodness of fit, σ_{ip} is the standard deviation associated with the peak, σ_{ib} is the standard deviation associated with background intensity, y_{io} is the observed intensity, y_{ib} is the background intensity, y_{ic} is the calculated intensity, N is the total number of observations, P is the number of variables in least square refinement. y_{ic} can be calculated using the equation,

$$y_{ic} = S \sum_j M_j PL_j |F_j|^2 G(\Delta\theta_{ij}) + y_{ib} \qquad (6.2)$$

Where, M_j is the multiplicity factor, PL_j is the Lorentz polarization factor, F_j is the structure factor, S is the scale factor, G is the reflection factor and $\Delta\theta_{ij}$ is the calculated position of Bragg peak.

All parameters were refined for the films on both substrates. The Rietveld refinement results are presented in Fig. 6.14. Black curve is the experimental pattern, red curve is the Rietveld fit, the magenta ticks (vertical lines) are the positions of phase reflection and the blue curve is the difference between observed and calculated intensities.

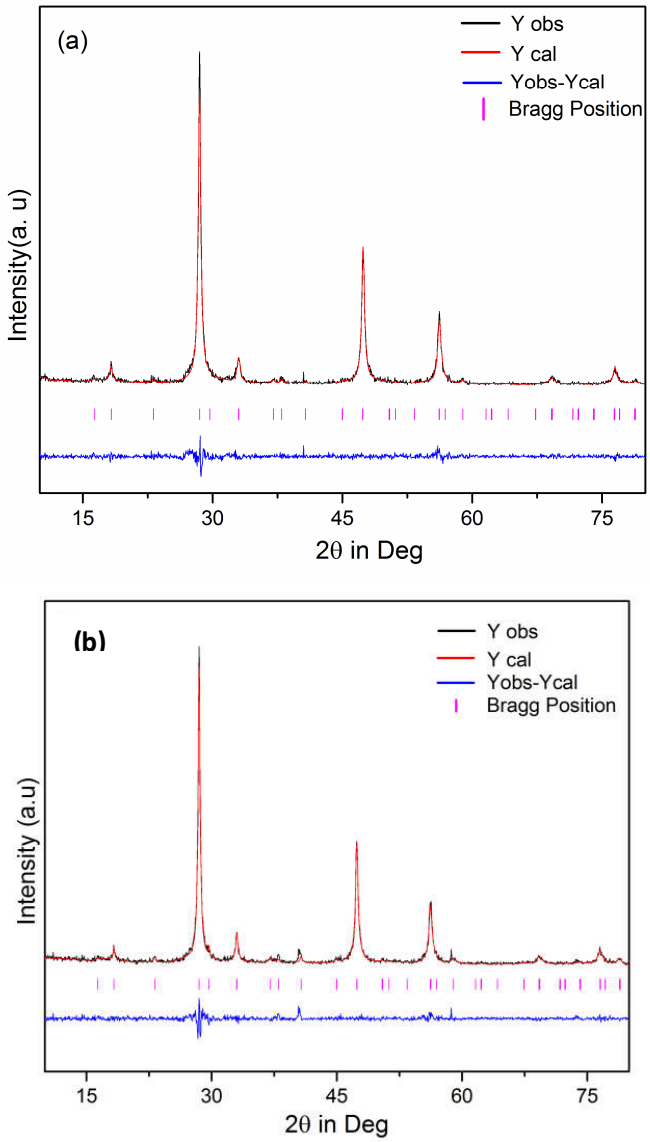

Fig. 6.14 Result of the rietveld refinement for CZTS film on (a) glass substrate (b) on Mo coated SLG Substrate

As seen in Fig.6.14, all background parameters (global profile refinement parameters, such as scale factor, peak shape function {U,V,

W}, etc) are well refined. The refinement results and unit cell parameters for the films on both substrates are given in Table 6.4. According to Susan et al [43], crystal structure is same for kesterite and stannite phases, but there are differences in the lattice constants. Lattice parameter for kesterite structure is a = b = 5.428(2)Å, c =10.864(4)Å and c/2a = 0.9854(5) and a = b = 5.444(2)Å, c = 10.729(4)Å and c/2a = 1.0008(5) for stannite structure. These values reported by Susan et al. are similar to the mineral data for kesterite and stannite phases [34]. In the present study, the unit cell parameters estimated from the refinement match with those of the kesterite phase.

Table 6.4 Rietveld refinement results for the films on glass and Mo coated SLG substrates

Parameter		On glass substrate	On Mo coated SLG substrate
Refinement results	χ^2	1.294	1.256
	R_F^2	0.0896	0.0774
	Rwp	0.2049	0.2069
	Rp	0.1518	0.1481
Lattice parameter	A	5.4213(3)Å	5.4371(3)Å
	C	10.8391(5)Å	10.8475(5)Å
	c/2a	0.9996(4)	0.9975(4)
Bond angles	Cu-S-Sn	107.867(24)	105.88(4)
	Zn-S-Sn	108.180(11)	110.072(21)
	Cu-S-Cu	111.177(11)	108.147(21)
	Cu-S-Zn	110.915(11)	115.170(20)

Table 6.4 shows slightly different lattice constants for the films on glass and Mo coated SLG substrates. The X-ray diffraction studies revealed higher lattice strain for the film on Mo coated SLG substrate (table 7.2). The changes observed in the lattice strain and lattice constants with respect to substrates may be due to the difference in the coefficient of thermal expansion (CTE) of substrates [44,45]. The CTE of glass and SLG substrates are 4.5×10^{-6} K^{-1} and 8.6×10^{-6} K^{-1}, respectively [44]. Sarswat et al. [46] and Singh et al. [47] reported the CTE of CZTS as 1.8×10^{-6} K^{-1}, which is close to that of the glass substrate.

According to Susan et al., tetrahedral distortion can be expressed in terms of cation-anion-cation bond angles [48]. Structural parameters were extracted from the refined data to obtain bond angle and bond length. Ideal cation-anion-cation bond angle for a tetrahedral system is 109.47°. In the case of kesterite tetragonal crystal system, bond angles differ substantially from 109.47° [48]. Cu-S-Sn=108.172° and Zn-S-Sn=108.206° angles are smaller than 109.47, while Cu-S-Cu=110.788° and Cu-S-Zn=110.712° angles are larger than this ideal value. In the present investigation, as seen in Table 6.4, the cation-anion-cation bond angles in the film on Mo coated substrate are disordered in contrast to the earlier report [48]. However, the cation-anion-cation bond angles calculated for the film on glass substrate is close to the reported value [48]. The shifts observed in the bond angles can be related to the induced strain on the film (Table 6.2) [44]. The higher strain in the film may affect photovoltaic properties [44]. The

present study indicates that a different strategy has to be adopted for coating film on Mo coated glass substrate, instead of following the same processing conditions used for coating CZTS on glass substrate.

6.3 Summary

CZTS solar cell was fabricated with ZnS buffer layer and Al doped ZnO transparent conducting layer. Prior to fabrication, the structural, optical and electrical properties of the ZnS and AZO layers were studied. Prototype CZTS solar cells with device structure SLG/Mo/CZTS/ZnS/AZO/Ag were fabricated with different absorber layer thicknesses (1.8µm, 2.2µm and 2.7µm). Highest efficiency of 3.02% was observed for film with lower thickness (1.8µm). Efficiency of the cell was found to decrease with increasing absorber layer thickness.

Further structural studies on device point of view were carried out by Rietveld refinement technique. For this, CZTS thin films were coated on glass substrates and Mo coated SLG substrates by spin coating followed by sulphurization at 500°C for 30 min. Phase purity of the films was analyzed and confirmed by GIXRD and Raman spectroscopy. The crystallite sizes were found to be 38nm for the film on glass substrate and 40nm for the film on Mo coated SLG substrate, using the W-H relation. The films on both substrates showed Raman peaks at 284cm^{-1}, 334cm^{-1} and 368cm^{-1}, corresponding to the A and B vibrational modes of CZTS phase. Further structural studies were carried out with Rietveld refinement technique using GSAS package. For refinement, kesterite model with space group I4 (SG No:82) was

chosen as starting model. All background parameters, such as, scale factor, peak shape function {U, V, W}, etc) are well refined. The difference between observed and calculated refined pattern for the films on both substrates is negligible. χ^2 for films on glass substrate is 1.294 and on Mo coated SLG is 1.256. The calculated lattice constants after the refinement for the film on glass substrates were a = b = 5.4213(3)Å, c = 10.8391(5) Å and c/2a = 0.9996(4) and for the film on Mo coated SLG substrates were a = b = 5.4371(3)Å, c = 10.8475(5)Å and c/2a = 0.9975(4). Refined lattice constants match with those of the standard kesterite structure obtained from the mineral data. Analysis of calculated and actual bond angles in the film on Mo coated SLG substrate showed a mismatch, while these were close enough in the film on glass substrate. The reported coefficient of thermal expansion (CTE) of CZTS is close to that of the glass than the SLG substrate. The difference in the CTE may be the reason for lattice strain and different bond angles in the film on Mo coated SLG substrate. The observed small deviation in the lattice constants of the film on Mo coated SLG substrate may be due to the lattice strain in the film. The study indicates that it is important to adopt a different strategy for coating CZTS film on Mo coated SLG substrate, instead of adopting the same processing conditions used for coating the film on glass substrate.

6.4 References

1) Inamdar A I, Lee S, Jeon K Y, Lee C H, Pawar S M, Kalubarme R S, Park CJ, Im H, Jung W, Kim H, Optimized fabrication of sputter deposited Cu_2ZnSnS_4 (CZTS) thin films, Sol. Energy. 91 (2013) 196.

2) Li L, Zhang B L, Cao M, Sun Y, Jiang J C, Hu P F, Shen Y, Wang LJ. Facile synthesis of Cu_2ZnSnS_4 nanocrystals and its use for dye-sensitized solar cells applications, J. Alloys Compd. 551 (2013) 24.

3) Katagiri H, Cu_2ZnSnS_4 thin film solar cells., Thin Solid Films. 480 (2005) 426.

4) Nakada T, Mizutani M, 18% efficiency Cd-free $Cu(In,Ga)Se_2$ thin-film solar cells fabricated using chemical bath deposition (CBD)-ZnS buffer layers, Jpn. J. Appl. Phys. 41 (2002) L165.

5) Park J Y, Chalapathy R B, Lokhande A C, Hong C W, Kim J H, Fabrication of earth abundant $Cu_2ZnSnSSe_4$ (CZTSSe) thin film solar cells with cadmium free zinc sulfide (ZnS) buffer layers, J. Alloys Compd. 695 (2017) 2652.

6) Abermann S, Non-vacuum processed next generation thin film photovoltaics: towards marketable efficiency and production of CZTS based solar cells, Sol. Energy. 94 (2013) 37.

7) Hariskos D, Menner R, Jackson P, Paetel S, Witte W, Wischmann W, Powalla M, Bürkert L, Kolb T, Oertel M, Dimmler B, New reaction kinetics for a high rate chemical bath deposition of the Zn(S,O) buffer layer for $Cu(In,Ga)Se_2$ based solar cells, Prog. Photovoltaics Res. Appl. 20 (2012) 534.

8) Haque F, Khan N A, Rahman K S, Islam M A, Alam M M, Sopian K, Amin N, Prospects of zinc sulphide as an alternative buffer layer for CZTS solar cells from numerical analysis, International

Conference on Electrical and Computer Engineering (ICECE) (2014) 504.

9) Sakai N, Hiroi H, Sugimoto H, Development of Cd-free buffer layer for Cu_2ZnSnS_4 thin-film solar cells, 37th IEEE Photovoltaic Specialists Conference (PVSC), 37 (2011) 003654.

10) Kim J, Park C, Pawar S M, Inamdar A I, Jo Y, Han J, Hong J, Park Y S, Kim D Y, Jung W, Kim H, Optimization of sputtered ZnS buffer for Cu_2ZnSnS_4 thin film solar cells, Thin Solid Films. 566 (2014) 88.

11) Nguyen M, Ernits K, Tai K F, Ng C F, Pramana S S, Sasangka W A, Batabyal S K, Holopainen T, Meissner D, Neisser A, Wong L H, ZnS buffer layer for $Cu_2ZnSn(SSe)_4$ monograin layer solar cell, Sol. Energy. 111 (2015) 344.

12) Wang W, Winkler M T, Gunawan O, Gokmen T, Todorov T K, Zhu Y, Mitzi D B, Device characteristics of CZTSSe thin film solar cells with 12.6% efficiency, Adv. Energy Mater. 4 (2014) 1301465.

13) Rajeshmon V G, Kartha C S, Vijayakumar K P, Sanjeeviraja C, Abe T, Kashiwaba Y, Role of precursor solution in controlling the opto-electronic properties of spray pyrolysed Cu_2ZnSnS_4 thin films, Sol. Energy. 85 (2011) 249.

14) Zhang J, Lexi S H, Yujun F U, Erqing X I, Cu_2ZnSnS_4 thin films prepared by sulfurization of ion beam sputtered precursor and their electrical and optical properties, Rare met. 25 (2006) 315.

15) Tanaka T, Nagatomo T, Kawasaki D, Nishio M, Guo Q, Wakahara A, Yoshida A, Ogawa H, Preparation of Cu_2ZnSnS_4 thin films by hybrid sputtering, J. Phys. Chem. Solids. 66 (2005) 1978.

16) Tiwari D, Chaudhuri T K, Shripathi T, Deshpande U, Rawat R, Non-toxic, earth-abundant 2% efficient Cu_2SnS_3 solar cell based on

tetragonal films direct-coated from single metal-organic precursor solution, Sol. Energy Mater. Sol. Cells. 113 (2013) 165.

17) De Blas M A, Torres J L, Prieto E, Garcıa A, Selecting a suitable model for characterizing photovoltaic devices. Renewable energy, 25 (2002) 371.

18) Katagiri H, Jimbo K, Yamada S, Kamimura T, Maw W S, Fukano T, Ito T, Motohiro T, Enhanced conversion efficiencies of Cu_2ZnSnS_4-based thin film solar cells by using preferential etching technique, Appl. Phys. Express. 1 (2008) 041201.

19) Contreras M A, Ramanathan K, AbuShama J, Hasoon F, Young D L, Egaas B, Noufi R, Diode characteristics in state of the art ZnO/CdS/$Cu(In_{1-x}Ga_x)Se_2$ solar cells, Prog. Photovoltaics Res. Appl. 13 (2005) 209.

20) Contreras M A, Repins I, Metzger W K, Romero M, Abou Ras D, Se activity and its effect on $Cu(In,Ga)Se_2$ photovoltaic thin films, Phys. Status Solidi A. 206 (2009) 1042.

21) Dale P J, Hoenes K, Scragg J, Siebentritt S, A review of the challenges facing kesterite based thin film solar cells, 34th IEEE Photovoltaic Specialists Conference (PVSC), 34 (2009) 002080.

22) Katagiri H, Jimbo K, Maw W S, Oishi K, Yamazaki M, Araki H, Takeuchi A, Development of CZTS-based thin film solar cells, Thin Solid Films. 517 (2009) 2455.

23) Ferry V E, Sweatlock L A, Pacifici D, Atwater H A, Plasmonic nanostructure design for efficient light coupling into solar cells. Nano Lett. 8 (2008) 4391.

24) Shin B, Gunawan O, Zhu Y, Bojarczuk N A, Chey S J, Guha S, Thin film solar cell with 8.4% power conversion efficiency using an

earth□abundant Cu_2ZnSnS_4 absorber, Prog. Photovoltaics Res. Appl. 21 (2013) 72.

25) Lee Y S, Gershon T, Gunawan O, Todorov T K, Gokmen T, Virgus Y, Guha S. $Cu_2ZnSnSe_4$ thin film solar cells by thermal co evaporation with 11.6% efficiency and improved minority carrier diffusion length, Adv. Energy Mater. 5 (2015) 1401372.

26) Wang K, Gunawan O, Todorov T, Shin B, Chey SJ, Bojarczuk N A, Mitzi D, Guha S, Thermally evaporated Cu_2ZnSnS_4 solar cells, Appl. Phys. Lett. 97 (2010) 143508.

27) Sun K, Yan C, Liu F, Huang J, Zhou F, Stride J A, Green M, Hao X, Over 9% efficient kesterite Cu_2ZnSnS_4 solar cell fabricated by using $Zn_{1-x}Cd_xS$ buffer layer, Adv. Energy Mater. 6 (2016) 1600046.

28) Ishizuka S, Sakurai K, Yamada A, Matsubara K, Fons P, Iwata K, Nakamura S, Kimura Y, Baba T, Nakanishi H, Kojima T, Fabrication of wide-gap $Cu(In_{1-x}Ga_x)Se_2$ thin film solar cells: a study on the correlation of cell performance with highly resistive i-ZnO layer thickness, Sol. Energy mater. Sol. Cells. 87 (2005) 541.

29) Lee J C, Kang K H, Kim S K, Yoon K H, Park I J, Song J, RF sputter deposition of the high-quality intrinsic and n-type ZnO window layers for $Cu(In,Ga)Se_2$-based solar cell applications, Sol. Energy mater. Sol. Cells. 64 (2000) 185.

30) Zhao J, Green M A, Optimized antireflection coatings for high-efficiency silicon solar cells, IEEE Trans. Electron Devices. 38 (1991) 1925.

31) Contreras M A, Egaas B, Ramanathan K, Hiltner J, Swartzlander A, Hasoon F, Noufi R, Progress toward 20% efficiency in $Cu(In,Ga)Se_2$ polycrystalline thin film solar cells, Prog. Photovoltaics Res. Appl. 7 (1999) 311.

32) Arbouz H, Aissat A, Vilcot J P, Modeling and Optimization of a Superstrate solar cell based on $Cu_2ZnSn(S_xSe_{1-x})_4$/ZnS Structure, Int. J. Energy Syst.1 (2017) 56.

33) Ghosh R, Basak D, Fujihara S, Effect of substrate-induced strain on the structural, electrical, and optical properties of polycrystalline ZnO thin films, J. Appl. Phys. 96 (2004) 2689.

34) Hall S R, Szymański J T, Stewart J M, Kesterite, ($Cu_2(Zn,Fe)SnS_4$), and stannite, ($Cu_2(Fe, Zn)SnS_4$), structurally similar but distinct minerals Can. Mineral. 16 (1978) 131.

35) Siebentritt S, Why are kesterite solar cells not 20% efficient?, Thin Solid Films. 535 (2013) 1.

36) Dumcenco D, Huang Y S, The vibrational properties study of kesterite Cu_2ZnSnS_4 single crystals by using polarization dependent Raman spectroscopy, Opt. Mater. 35 (2013) 419.

37) Gürel T, Sevik C, Çağın T, Characterization of vibrational and mechanical properties of quaternary compounds Cu_2ZnSnS_4 and $Cu_2ZnSnSe_4$ in kesterite and stannite structures, Phys. Rev. B. 84 (2011) 205201.

38) Khare A, Himmetoglu B, Johnson M, Norris D J, Cococcioni M, Aydil E S, Calculation of the lattice dynamics and Raman spectra of copper zinc tin chalcogenides and comparison to experiments, J. Appl. Phys. 111 (2012) 083707.

39) Nozaki H, Fukano T, Ohta S, Seno Y, Katagiri H, Jimbo K, Crystal structure determination of solar cell materials: Cu_2ZnSnS_4 thin films using X-ray anomalous dispersion, J. Alloys Compd. 524 (2012) 22.

40) Hyesun Yoo, JunHo Kim, Comparative study of Cu_2ZnSnS_4 films growth, Sol. Energy Mater. Sol. Cells, 95 (2011) 239.

41) Ge J, Wu Y, Zhang C, Zuo S, Jiang J, Ma J, Yang P, Chu J, Comparative study of the influence of two distinct sulfurization ramping rates on the properties of Cu_2ZnSnS_4 thin films, Appl. Surf. Sci. 258 (2012) 7250.

42) Quaas M, Eggs C, Wulff H, Structural studies of ITO thin films with the Rietveld method, Thin Solid Films. 332 (1998) 277.

43) Schorr S, Hoebler H J, Tovar M, A neutron diffraction study of the stannite-kesterite solid solution series, Eur. J. Mineral. 19 (2007) 65.

44) Ishizuka S, Yamada A, Fons P, Niki S, Flexible $Cu(In,Ga)Se_2$ solar cells fabricated using alkali-silicate glass thin layers as an alkali source material, J. Renewable Sustainable Energy. 1 (2009) 013102.

45) Li C, Furuta M, Matsuda T, Hiramatsu T, Furuta H, Hirao T, Effects of substrate on the structural, electrical and optical properties of Al-doped ZnO films prepared by radio frequency magnetron sputtering, Thin Solid Films. 517 (2009) 3265.

46) Sarswat P K, Free M L, Tiwari A, Temperature dependent study of the Raman A mode of Cu_2ZnSnS_4 thin films, Phys. Status Solidi B. 248 (2011) 2170.

47) Singh O P, Muhunthan N, Singh V N, Samanta K, Dilawar N, Effect of temperature on thermal expansion and anharmonicity in Cu_2ZnSnS_4 thin films grown by co-sputtering and sulfurization, Mater. Chem. Phys. 146 (2014) 452.

48) Schorr S, The crystal structure of kesterite type compounds: A neutron and X-ray diffraction study, Sol. Energy Mater. Sol. Cells. 95 (2011) 1482.

Chapter 7
Brief summary of thesis and scope for future work

7.1 Summary of thesis

The studies presented in this thesis were mainly focussed on the fabrication of phase pure kesterite Cu_2ZnSnS_4 films by dip, spin and spray coating routes and their characterization. The thesis completely covers the proposed objectives. The study addressed the Cu poor and Zn rich nature of the films, which will yield required defects in the material, by investigating the elemental composition ratios of CZTS films. Phase pure films were fabricated by eight different routes and investigated their photovoltaic properties. Separate procedures for thin film coating and optimizing annealing temperature were adopted for each route. Structural properties and phase purities of the films were investigated by XRD, Raman spectroscopy and Rietveld refinement technique. Elemental compositions of the films were calculated by EDXS equipped with SEM. The important photovoltaic properties such as band gap and absorption coefficient were calculated from the UV-visible absorption spectra. Hall Effect measurements were employed to study the electrical properties of the films. Prototype CZTS solar cells with non-toxic ZnS buffer layer were fabricated and efficiency measurements were conducted under standard test condition.

The major results obtained from this work are,

1) Phase pure CZTS thin films were fabricated in two different methods by dip coating. For this, precursor films were coated from solutions without sulphur (CZT) and with sulphur (CZTS), and sulphurized at different temperature to optimise the preparation conditions. The CZT films sulphurized at 550°C formed phase pure Cu_2ZnSnS_4, whereas the second route yielded phase pure films at 500°C and 550°C. However, higher absorption coefficient ($10^5 cm^{-1}$), with comparatively lower band gap (1.43eV) was observed for the film sulphurized at 550°C. The band gap and absorption coefficient of the films optimized through the first route were 1.48eV and $10^4 cm^{-1}$ in the visible region, respectively. The average crystallite sizes of the films from the first and second routes were 25nm and 14nm respectively. Comparing both techniques, the lowest electrical resistivity of 0.828Ωcm and the highest carrier concentration of $1.43\times10^{18} cm^{-3}$ were observed for the CZT films sulphurized at 550°C. Cu_2ZnSnS_4 films fabricated by both approaches exhibited Cu poor and Zn rich compositions required for solar cell application.

2) Three different approaches were used for preparing Cu_2ZnSnS_4 films by spin coating. Two different precursor solutions with and without sulphur were prepared for coating precursor films. The precursor films were converted Cu_2ZnSnS_4 films by annealing in sulphur or nitrogen atmospheres. The annealing/sulphurization conditions were optimized for all the

three routes; the optimized temperature for phase pure films was 500°C for all approaches. Of the three routes, the highest absorption coefficient of $10^5 cm^{-1}$ was observed for the Cu_2ZnSnS_4 film fabricated by annealing sulphur containing precursor film (CZTS) in sulphur atmosphere. However, the film prepared by annealing sulphur containing precursor film in nitrogen atmosphere exhibited better properties, except absorption coefficient; the band gap obtained was close to the ideal band gap (1.49eV) and higher carrier concentration ($2.17\times10^{17} cm^{-3}$) with lower resistivity (0.09Ωcm). The highest average crystallite size (38nm) was observed for the CZTS precursor film annealed in nitrogen atmosphere. The precursor films without sulphur were peeled off from the substrate when sulphurized at certain temperatures. The phase pure Cu_2ZnSnS_4 films prepared by annealing precursor films with sulphur in nitrogen and sulphur environments exhibited the required Cu poor and Zn rich compositions.

3) Similar to the spin coating process, three different routes were adopted for fabricating Cu_2ZnSnS_4 films by spray coating. For this, precursor films were prepared from solutions without sulphur (CZT) and with sulphur (CZTS) by spray coating and these films were sulphurized or annealed at various temperatures to optimise the conditions. The CZT precursor films were converted to phase pure kesterite by sulphurizing at 550°C. However, the optimised temperatures in the case of

CZTS precursor films were 550°C and 500°C when annealed in sulphur and nitrogen atmospheres, respectively. Among the three routes, the best optical properties (band gap of 1.49eV and absorption coefficient of $10^5 cm^{-1}$) were exhibited by the film sulphurized at 550°C. The carrier concentration and resistivity of these films were $3.67 \times 10^{19} cm^{-3}$ and 0.52Ωcm, respectively. However, copper poor and zinc rich compositions were not observed in the phase pure films prepared by this route. Higher crystallite size of 59nm was observed for the CZTS thin film sulphurized at 550°C. Compared with other coating techniques, the spray coating technology can be easily up-scaled to any size. In this study, the coating procedure was optimized up to a substrate size of 2 inch by 2 inch.

4) After optimizing the sulphurization temperature, prototype CZTS solar cells were fabricated with different absorber layer thickness (1.8µm, 2.2µm and 2.7µm). Non-toxic zinc sulphide film was used as buffer layer instead of the commonly used CdS. The solar cell was fabricated with device structure Mo/CZTS/ZnS/AZO/Ag on soda lime glass (SLG) substrates and efficiency measurements were carried out under standard test condition. Highest efficiency of 3.02% is observed for film with lower thickness (1.8µm). Efficiency of the CZTS cell was found to decrease with increasing absorber layer thickness. As far the author knows, the efficiency obtained in this work may

be the highest value reported so far for cadmium free cell with solution processed CZTS absorber.

5) The study was extended further with Rietveld refinement technique to find out the possible reasons for the observed low efficiency of solar cells. For this, Cu_2ZnSnS_4 films were prepared on glass substrates and Mo coated SLG substrates by spin coating followed by sulphurization at 500°C for 30 min. The calculated lattice constants after the refinement for the films on glass substrates and on Mo coated SLG substrates match with those of the standard kesterite structure obtained from the mineral data. Analysis of calculated and actual bond angles in the film on Mo coated SLG substrate showed a mismatch, while these were close enough in the film on glass substrate. The study indicates that it is important to adopt a different strategy for coating CZTS film on Mo coated SLG substrate, instead of adopting the same processing conditions used for coating the film on glass substrate.

7.2. Scope for future work

Relying on the investigations carried out, it is possible to extend the study for further efficiency improvement in CZTS solar cell. In the present study, higher efficiency was observed with lower absorber thickness, and hence further study is required to optimise minimum thickness required for efficient CZTS cell. The solar cells in this study were fabricated without intrinsic ZnO layer and anti-reflection coating. The efficiency may be increased by incorporating

there layers in the device structure. A few theoretical models predict that ZnS is not a suitable buffer layer for CZTS system, due to a high spike in the band alignment, which will act as a barrier for electron transport across the interface. In addition to this, further studies on the interfacial properties of the various layers have to be studied thoroughly for optimum performance of the cell. Towards other applications, Cu_2ZnSnS_4 is useful for photosensing applications and also for DSSC and perovskite based solar cells.